

**An Investigation into the Influence
of Nucleation Factors
on Yeast F-actin Structure and Organisation**

By Sarah R. Stevenson (née Gratton)

A thesis submitted for the degree of Doctor of Philosophy

School of Biosciences, Faculty of Science
The University of Sheffield, United Kingdom

September 2021



The
University
Of
Sheffield.

Abstract

The actin cytoskeleton is a ubiquitous feature of eukaryotic cells capable of performing diverse cellular functions in response to the needs and specialisms of the cell. The core component of the actin cytoskeleton is the globular protein actin, which reversibly polymerises into filaments (F-actin). The cytoskeleton undergoes continuous reorganisation, and its regulation is performed on many levels, including isoform variation, post-translational modifications, interaction with actin binding proteins, local ionic conditions, and ATP hydrolysis. Actin nucleation – the formation of new filaments – undergoes tight spatiotemporal regulation, directed by a set of actin binding proteins called nucleators. There is evidence from cell-based studies that actin nucleators define not only the spatiotemporal nature of a new actin network, but also the properties of the actin network they establish. The collective action of discrete nucleators allows the generation of distinct actin networks in a common cytoplasm. This project used cryogenic electron microscopy (cryo-EM) to investigate the hypothesis that the influence of actin nucleators on actin filaments has a structural basis, with nucleators influencing the structure of the actin filaments themselves. Our chosen actin nucleator for this work was the endocytic protein Las17, which functions at actin patches at the cortex of the budding yeast *Saccharomyces cerevisiae*. Our use of actin from the same species allowed structural characterisation of actin filaments from *S. cerevisiae*, which has been studied only at low resolution until now. Our investigation re-assesses previous reports that F-actin from *S. cerevisiae* has greatly reduced inter-strand connectivity and a more open nucleotide-binding cleft than F-actin from vertebrate skeletal muscle. An additional, unexpected outcome of this project was the discovery of actin bundling as a novel *in vitro* functionality of the polyproline rich region of Las17.

Acknowledgements

Thank you to my supervisor Prof. Kathryn Ayscough for her academic guidance of the project, and patient reassurance when needed.

I would also like to thank the following people for their input into the project.

For Las17 Work (The University of Sheffield)

Dr Ellen Allwood, Dr John Palmer, Dr Iwona Smaczynska-de Rooij, Lewis Hancock

For Electron Microscopy Work (The University of Sheffield)

Dr Svet Tzokov, Prof. Per Bullough, Dr Jason Wilson, Dr Julien Bergeron, Alex Parker

For Other Work in this Project

The University of Sheffield:

Dr Andrew Peden (Advisor), Dr Nic Mullin (Atomic Force Microscopy), Dr Mark Collins (Mass Spectrometry)

The University of Warwick:

Prof. Mohan Balasubramanian, Dr Tomo Hatano, Dr Andrejus Suchenko

On a personal note, I would like to thank the friends and family who supported me over the last 4 years, particularly my parents Jude and Robin. Thank you to my friends Ollie, Rob and Sam for reminding me that there is life outside work (and for putting up with my moaning about various PhD-related disasters!). I was very lucky to go through the PhD experience alongside my lab family Mona Nazemi, Adam Carlton, Stella Christou, and of course Ben Stevenson, who was there for me every step of the way.

Table of Contents

Abstract.....	1
Acknowledgements.....	2
Table of Contents.....	3
List of Tables.....	8
List of Figures.....	8
Abbreviations & Acronyms.....	11
1. Thesis Introduction.....	13
1.1 General Introduction to Actin.....	13
1.1.1 The Cytoskeleton.....	13
1.1.2 The Diverse Functions of the F-actin Cytoskeleton.....	13
1.1.3 Actin is a Highly Conserved but Versatile Building Block.....	15
1.1.4 Making a New Actin Filament: Nucleation.....	18
1.1.5 Actin Filament Dynamics.....	18
1.1.6 ATP Hydrolysis.....	19
1.2 Solving Actin Structure.....	20
1.2.1 Early insights into Actin Filament Structure.....	20
1.2.2 Initial Atomic Model Estimates for F-actin.....	21
1.2.3 Implications of the ‘Resolution Revolution’ for F-actin Structure.....	22
1.2.4 Obtaining 3D Information from Cryo-EM Data.....	24
1.3 Actin Structure.....	26
1.3.1 Features of the Actin Monomer.....	26
1.3.2 Polymerisation: The Monomer to Protomer Transition and ATP Hydrolysis.....	27
1.3.3 A Tilted Polymerisation Intermediate?.....	28
1.3.4 The Helical Symmetry of F-actin.....	28
1.3.5 Protomer-Protomer Contacts.....	30
1.4 Actin Binding Proteins: Architects of the Actin Cytoskeleton.....	33
1.4.1 Actin Binding Protein Strategies.....	33
1.4.2 Tethering Proteins and Cytoskeletal Linkers.....	35
1.4.3 Myosins.....	35
1.4.4 Tropomyosins.....	36
1.4.5 Capping Proteins.....	37

1.4.6	Bundlers and Crosslinkers.....	38
1.4.7	Monomer Binding.....	39
1.4.8	Filament Severing.....	40
1.4.9	Nucleators and Nucleation Promoting Factors	41
1.5	The Actin Cytoskeleton of <i>S. cerevisiae</i>	44
1.5.1	A Yeast for Bakers, Brewers and Biologists.....	44
1.5.2	<i>S. cerevisiae</i> Actin Architectures and their Associated Nucleators	45
1.5.3	Arp2/3 and the Need for a Mother Filament.....	48
1.5.4	WCA-Independent Functions of Las17.....	49
1.6	Exploring the Influence of Actin Nucleators on Actin Filament Function.....	50
1.6.1	Nucleators Can Dictate which Actin Architectures Assemble	50
1.6.2	Do Nucleators Influence the Conformation of F-actin?.....	51
1.7	Aims of the Project.....	52
2.	Materials & Methods	54
2.1	Materials	54
2.1.1	Solution and Buffer Recipes.....	54
2.1.2	Culture Media Recipes.....	57
2.1.3	Software.....	58
2.2	Molecular Biology Methods	59
2.2.1	DNA Sequencing and Primer Synthesis Services.....	59
2.2.2	Plasmids used in this Study.....	59
2.2.3	Plasmid Purification	60
2.2.4	Primer Design for Making His-tagged Las17	60
2.2.5	Cloning Las17 Fragment Sequences into a New Vector	62
2.2.6	Primer Design for Site-Directed Mutagenesis of pPICZc- <i>ScAct1-thyβ4-8His</i>	63
2.2.7	Site-Directed Mutagenesis of pPICZc- <i>ScAct1-thyβ4-8His</i>	64
2.2.8	Linearised Plasmids for Transformation into <i>P. pastoris</i>	64
2.2.9	DNA Electrophoresis	65
2.3	Microbiology Methods	65
2.3.1	<i>E. coli</i> Strains	65
2.3.2	<i>E. coli</i> Liquid Media and Culture.....	66
2.3.3	Generation of Competent <i>E. coli</i>	66
2.3.4	Transformation of <i>E. coli</i>	66
2.3.5	Culture and Induction of BL21 and Rosetta 2 Strains	67
2.3.6	Making <i>E. coli</i> Glycerol Stocks.....	67
2.3.7	<i>P. pastoris</i> Strains.....	67

2.3.8	<i>P. pastoris</i> Culture	68
2.3.9	Induction of <i>P. pastoris</i> for Recombinant Actin Expression	68
2.3.10	Transformation of <i>P. pastoris</i>	68
2.3.11	Making <i>P. pastoris</i> Glycerol Stocks.....	69
2.4	Protein Purification and Modification Methods	70
2.4.1	Purification of Rabbit Actin.....	70
2.4.2	<i>P. pastoris</i> Cell Lysis	70
2.4.3	Preparation of a DNase I Column for Native Actin Purification	71
2.4.4	Crude Purification of Native Actin from <i>S. cerevisiae</i>	71
2.4.5	Crude Purification of Recombinant Yeast Actin from <i>P. pastoris</i>	73
2.4.6	Further Purification of Wildtype Actin by a Polymerisation Cycle ('Cycling')	73
2.4.7	Dialysis.....	74
2.4.8	Purification and Cleavage of GST-tagged Las17 Fragments	74
2.4.9	Desalting GST-cleaved Las17PP.....	75
2.4.10	Ni-Affinity Purification of His-tagged Las17 from <i>E. coli</i>	75
2.4.11	Size Exclusion Chromatography of His-Las17	76
2.4.12	Labelling His-Las17 with Nanogold.....	76
2.4.13	Determining Protein Concentration.....	76
2.5	Biochemical Methods	77
2.5.1	Polymerisation of Actin Filaments.....	77
2.5.2	Sedimentation Assays.....	78
2.5.3	Protein Electrophoresis (SDS-PAGE).....	79
2.5.4	Coomassie Staining.....	79
2.5.5	Western Blotting	80
2.6	Microscopy Methods.....	81
2.6.1	Electron Microscopy Sample Preparation	81
2.6.2	Preparing Negatively Stained Specimens	83
2.6.3	Screening and Data Collection of Negatively Stained Samples	83
2.6.4	Single Particle Analysis of Negatively Stained Specimens in CisTEM	83
2.6.5	Frozen Grid Preparation for Cryo-EM and Cryo-ET	84
2.6.6	Cryo-EM Data Collection and Image Processing for Single Particle Analysis.....	84
2.6.7	Building a Pseudoatomic Model for F-actin.....	86
2.6.8	Cryo-EM Analysis & Presentation Tools in Chimera.....	86
2.6.9	Tilt-Series Acquisition for Cryo-ET	87
2.6.10	Tomogram Generation and Segmentation.....	87
2.6.11	Atomic Force Microscopy	88
3.	Yeast Actin Purification and Mutagenesis	90

3.1	Introduction.....	90
3.1.1	Traditional Methods of Actin Purification.....	90
3.1.2	Expression and Purification of Recombinant Actin.....	92
3.2	Results	94
3.2.1	Purification of Yeast Actin Using DNase I.....	94
3.2.2	Troubleshooting Purification of Recombinant Actin from <i>Pichia</i> Host	98
3.2.3	Identifying Additional Chymotrypsin Cleavage Sites.....	100
3.2.4	Assessing Factors Affecting Chymotrypsin Cleavage	103
3.2.5	Cell Culture Amendments to Improve Yield.....	105
3.2.6	Contamination by Native <i>P. pastoris</i> Actin.....	108
3.2.7	Introducing Polymerisation-Impairing Mutations: The Concept.....	109
3.2.8	Site-Directed Mutagenesis	110
3.2.9	Subsequent Steps.....	111
3.3	Discussion	113
3.3.1	Choice of Purification Method.....	113
3.3.2	Practical Considerations for <i>Pichia</i> Cell Lysis	114
3.3.3	Suggested Improvements to Recombinant Actin Purity	115
3.3.4	Potential Applications of Polymerisation-Impaired Actin Mutants	116
4.	Solving Yeast F-Actin Structure with Cryo-EM.....	118
4.1	Introduction.....	118
4.2	Cryo-EM Sample Preparation and Data Collection.....	119
4.2.1	Optimising Sample Preparation and Data Collection Strategy.....	119
4.3	The Reconstruction Process	122
4.3.1	Reconstruction Pipeline	122
4.3.2	Motion Correction	123
4.3.3	CTF Estimation & Data Quality Assessment	125
4.3.4	Particle Picking and Extraction	126
4.3.5	2D Classification	129
4.3.6	3D Reconstruction	131
4.3.7	Further steps to Improve Resolution	134
4.3.8	Local Resolution.....	134
4.3.9	Homology Model Selection & D-loop Conformation.....	136
4.3.10	Map Rescaling: Retrospective Pixel Size Calibration	136
4.4	Discussion	140
4.4.1	Limiting Steps in Acquiring a High Quality Dataset	140
4.4.2	Quality Control Checks During Data Processing.....	140

5.	Analysis of Yeast F-actin Structure	142
5.1	Introduction.....	142
5.2	Results	144
5.2.1	Yeast F-actin Helical Symmetry Compared to Other Published Structures.....	144
5.2.2	Comparison of Rabbit Skeletal Muscle F-actin and Yeast F-Actin Maps	146
5.2.3	A Pseudo-Atomic Model For Yeast F-Actin.....	148
5.2.4	Model Validation.....	150
5.2.5	The Nucleotide Binding Cleft.....	151
5.2.6	Protomer-Protomer Interfaces in the Yeast F-actin Model	153
5.2.7	Phalloidin-binding Site.....	160
5.3	Discussion	162
5.3.1	F-actin Helical Parameters for Different Species.....	163
6.	Las17PP Bundles F-Actin <i>in vitro</i>	165
6.1	Introduction.....	165
6.1.1	Research Aims	165
6.1.2	The Polyproline Region of Las17	165
6.2	Results	168
6.2.1	A Cryo-EM Structure for Yeast F-actin Polymerised in the Presence of Las17PP	168
6.2.2	An Increased Las17PP Concentration Enhances Actin Polymerisation and Induces Filament Bundling 170	
6.2.3	Assessing the Proportion of F-actin integrated in Bundles	172
6.2.4	The N-terminal Half of the Las17 Polyproline Region is Sufficient to Induce Actin Bundling.....	175
6.2.5	Las17PP Bundling in the Presence of Salt	176
6.2.6	Characterisation of Las17PP-Induced Actin Bundles using TEM.....	177
6.2.7	Assessing Bundle Shape with Cryogenic Electron Tomography.....	181
6.2.8	Bundle Characterisation by Atomic Force Microscopy	184
6.3	Discussion	185
6.3.1	Findings from Single Particle Analysis	185
6.3.2	A Novel <i>in vitro</i> Ability of Las17PP	185
6.3.3	Implications About Bundle Organisation from AFM Data.....	186
6.3.4	Could Non-Specific Interactions Enable Las17PP to Bundle F-Actin?.....	187
6.3.5	Are PP Tracts and Arginine Pairs Involved in Las17PP-Mediated Actin Bundling?.....	188
7.	Final Discussion.....	189
7.1	Developments in Actin Purification	189
7.2	Further Steps Towards Understanding Yeast F-actin Structure	189
7.3	The Expanding Database of F-actin Structures	190

7.4	Implications for Las17 at Endocytic Sites	192
7.5	Towards Understanding Distinct Architectures in a Common Cytoplasm from the Perspective of Actin Nucleators	193
8.	References	195

List of Tables

Table 2.1:	Key software used for the methods described in this chapter.....	58
Table 2.2:	Plasmids used in this research.....	60
Table 2.3:	Primers for generating Las17 fragment inserts.....	61
Table 2.4:	Mutagenic primers used for site-directed mutagenesis and sequencing of pPICZc-ScAct1-thy β 4-8His.....	63
Table 2.6:	Yeast glycerol stocks used in this work.....	67
Table 2.7:	Resolving and stacking gel solution components.....	79
Table 2.8:	Antibodies used for Western blotting.....	81
Table 3.1:	Actin binding proteins in the crude purification product using DNase I affinity.....	97
Table 3.2:	The molecular weight (MW) of theoretical fragments that would be generated from the candidate chymotrypsin cutting sites in Figure 3.8.....	103
Table 5.1:	Helical Parameter Statistics. Mean \pm Standard Deviation.....	146

List of Figures

Figure 1.1:	Examples of cellular architectures of the actin cytoskeleton. Actin filaments play a diversity of roles in eukaryotic cells. Many of these roles involve membrane manipulation. For example, actin filaments constitute the structural core of cellular protrusions such as m	15
Figure 1.2:	Sequence identity between actin isoform protein sequences in different species.....	16
Figure 1.3:	Features of the actin monomer.....	27
Figure 1.4:	Parameters used to describe a helix.....	30
Figure 1.5:	Protomer-Protomer contacts within an actin filament.....	31
Figure 1.6:	Some of the common functions of actin binding proteins.....	34
Figure 1.7:	Formin- and Arp2/3-Associated Actin Architectures in <i>S. cerevisiae</i>	45
Figure 1.8:	The stages of endocytosis.....	48
Figure 2.1:	Illustration of where primers anneal to the full length Las17 sequence and the generated inserts.....	61
Figure 2.2:	Schematic of the steps followed to generate plasmids encoding His-tagged Las17 protein fragments.....	62
Figure 2.3:	Schematic of a high-speed actin sedimentation assay.....	78
Figure 2.4:	Fiducial markers for cryo-ET.....	82

Figure 3.1: DNase I and G-actin form a tightly bound 1:1 complex that can be disrupted by formamide.	91
Figure 3.2: The G-actin-thy β 4 fusion protein.	93
Figure 3.3: Crude purification product from DNase I affinity purification of native <i>S. cerevisiae</i> actin.....	94
Figure 3.4: Representative images of rabbit muscle F-actin and DNase I-purified yeast F-actin negatively stained for TEM.	95
Figure 3.5: Assessment of contaminants in the crude purification product using DNase I affinity.....	97
Figure 3.6: Assessing polymerisation-competence of purified recombinant actin.....	99
Figure 3.7: Samples taken throughout <i>Pichia</i> culture and actin purification, visualised by Coomassie blue stain and by Western blot.....	100
Figure 3.8: Potential chymotrypsin cleavage sites in the ScAct1-Thy β 4-8His fusion protein.....	102
Figure 3.9: Chymotrypsin digestion performed under different conditions and enzyme concentrations.	105
Figure 3.10: A Western blot (anti-actin) comparing different chymotrypsin stocks and incubation temperatures.	105
Figure 3.11: Induction of cultured <i>Pichia</i> in our lab was successful when adapted to incorporate measures for improved oxygenation.....	106
Figure 3.12: Purification intermediates at the University of Sheffield, using <i>Pichia</i> cultured, induced and broken at the University of Warwick.....	107
Figure 3.13: The actin purification product using cells cultured, induced and broken at the University of Warwick and purified at the University of Sheffield.....	108
Figure 3.14: Codon options for site-directed mutagenesis.....	110
Figure 3.15: Primers for making polymerisation-impaired actin mutants by site-directed mutagenesis.....	111
Figure 3.16: Plasmid linearization by PmeI.....	112
Figure 4.1: Foil holes suitable for data collection were most often found near the grid square edge.....	121
Figure 4.2: Pipeline used for reconstructing yeast F-actin in RELION 3.1.	123
Figure 4.3: An example of a trajectory plot for a micrograph movie that suffered relatively little motion between frames.	124
Figure 4.4: Bad trajectory traces were not necessarily indicative of bad micrographs.	124
Figure 4.5: Assessing Data Quality following CTF Estimation.	127
Figure 4.6: Picking helical segments for particle extraction.	128
Figure 4.7: Spiked artefacts in 2D Classes from a discarded dataset with high filament density.....	129
Figure 4.8: Indication of secondary structure in 2D classes.....	130
Figure 4.9: Template-free 3D initial model generation.....	131
Figure 4.10: 3D refinement from a cylindrical template: a map with extra density.....	132
Figure 4.11: 3D refinement from a cylindrical template: a map displaying dual polarity.....	133
Figure 4.12: 3D refinement of a 7.42 Å F-actin map from a 30 Å F-actin template.	134
Figure 4.13: Local resolution.....	135
Figure 4.14: D-loop conformation of yeast F-actin.....	136

Figure 4.15: Pixel Size Calibration.	138
Figure 4.16: FSC curve of the final rescaled postprocessed map.	139
Figure 5.1: Helical Symmetry of F-actin Maps.	145
Figure 5.2: Comparison of yeast and RSkM F-actin experimental maps.....	147
Figure 5.3: Overview of the 4.7 Å map and pseudo-atomic model for yeast F-actin.....	149
Figure 5.4: Ramachandran outliers in the yeast F-actin model.	151
Figure 5.5: ADP in the nucleotide binding cleft.....	152
Figure 5.6: The D-loop.....	155
Figure 5.7: The H-Loop.	156
Figure 5.8: An Inter-Strand Interaction Site.....	158
Figure 5.9: Two intra-strand Interaction sites between intra-strand neighbours.....	159
Figure 5.10: Salt bridges at the intra-strand interface in RSkM F-actin and yeast F-actin.	160
Figure 5.11: Phalloidin-binding site.....	161
Figure 6.1: Domain structure of Las17, with focus on the polyproline region.	166
Figure 6.2: FSC curve and final map of yeast F-actin polymerized in the presence of Las17PP.....	168
Figure 6.3: 3D Classification reveals extra density at the predicted binding site for Las17PP.....	169
Figure 6.4: Pairing TEM with a high-speed sedimentation assay to investigate the effect of a high Las17PP concentration on the polymerisation of F-actin.....	171
Figure 6.5: High-speed and low-speed sedimentation of actin incubated under different nucleating conditions.	172
Figure 6.6: Low-speed sedimentation of actin bundles in the presence of increasing concentrations of Las17PP ₃₀₀₋₅₃₆ in G-buffer.	174
Figure 6.7: Low-speed sedimentation of actin bundles in the presence of increasing concentrations of Las17PP ₃₀₀₋₄₂₂ in G-buffer.	175
Figure 6.8: Low-speed sedimentation of actin bundles in the presence of increasing concentrations of Las17PP ₃₀₀₋₄₂₂ in F-buffer. F-buffer is G-buffer with added KME.....	176
Figure 6.9: Filaments within the bundles are clearly visible when viewed at high magnification in negative stain TEM.	177
Figure 6.10: Actin filaments in Las17PP-induced bundles have a centre-to-centre spacing of ~7 nm.	178
Figure 6.11: 2D classification of Las17PP-induced actin bundles.	179
Figure 6.12: Frequency distribution of actin bundle thickness.....	180
Figure 6.13: Appearance of bundles in ice on lacy grids.....	182
Figure 6.14: Visualising Las17PP-induced F-actin bundles in 3D using Cryo-ET.....	183
Figure 6.15: Periodicity of an F-actin Bundle.....	184
Figure 6.16: Proposed Arrangements of F-actin in Las17PP-induced bundles based on the double-peaked line profile observed in AFM.	187
Figure 7.1: EMDB entries falling under the search term ‘F-actin’, arranged by year.	191

Abbreviations & Acronyms

For amino acids, the standard 3-letter code is used.

For chemicals, the standard chemical formulae are used unless listed below.

The full and abbreviated names of buffers and media can be found in sections 2.1.1 and 2.1.2.

aa	amino acid
ABD	actin binding domain
ABP	actin binding protein
ADP	adenosine diphosphate
AFM	atomic force microscopy
Arp	actin-related protein
ATP	adenosine triphosphate
ATPase	adenosine triphosphatase
BSA	bovine serum albumin
CC	correlation coefficient
CCD	charge-coupled device
CMOS	complementary metal-oxide semiconductor
cryo-EM	cryogenic electron microscopy
CTF	contrast transfer function
D-loop	DNase I-binding loop
DNA	deoxyribonucleic acid
DNase	deoxyribonuclease
EM	electron microscopy
EMDB	electron microscopy data bank
F-actin	filamentous, or fibrous (polymeric) actin
FH	formin homology
FSC	Fourier shell correlation
FT	Fourier transform
G-actin	globular (monomeric) actin
GST	glutathione S-transferase
H-bond	hydrogen bond
H-loop	<i>Formerly 'hydrophobic loop' - refer to section 1.3.5</i>
HSP	high-speed pelleting
iBAQ	intensity based absolute quantification
Las17PP	polyproline region of Las17
LN2	liquid nitrogen
LSP	low-speed pelleting
MAP	microtubule associated protein
MT	microtubule

MW	molecular weight
MWCO	molecular weight cut-off
NMR	nuclear magnetic resonance
NPF	nucleation promoting factor
ns	non-significant
OD600	optical density measured at 600 nm
PCR	polymerase chain reaction
PDB	protein data bank
PI	protease inhibitor
Pi	phosphate
PIP2	phosphatidylinositol (4,5)-bisphosphate
PP	polyproline
PPII helix	poly-L-proline type II helix
PTM	post-translational modification
RSkM	rabbit skeletal muscle
SD	subdomain
SDM	site-directed mutagenesis
SDS-PAGE	sodium dodecyl sulfate polyacrylamide gel electrophoresis
TEM	transmission electron microscopy
thy β 4	thymosin β 4
TIRF	total internal reflection fluorescence
Tpm _{acc}	acetylated tropomyosin
Tpm _{un}	unacetylated tropomyosin
tRNA	transfer ribonucleic acid
VT	vinculin tail
WASH	WASP and Scar homologue
WASP	Wiscott Aldrich syndrome protein
WAVE	WASP-family verprolin homologue
WCA	WH2-central-acidic
WH	WASP-homology
WIP	WASP Interacting Protein
WT	wild-type

1. Thesis Introduction

1.1 General Introduction to Actin

1.1.1 The Cytoskeleton

The cytoskeleton is an intricate network of protein polymers that coordinates cellular organisation. The core elements of the cytoskeleton are filament-forming proteins. In eukaryotes, the major cytoskeletal proteins are actin and tubulin, which are the building block proteins of cytoskeletal filaments called actin filaments and microtubules, respectively. Actin and tubulin are both highly conserved, and the filaments they form are found extensively throughout eukaryotic organisms and cell types. Actin-like and tubulin-like proteins also make up the cytoskeletons of prokaryotic organisms. Metazoans (multicellular animals) additionally possess a third class of filaments called intermediate filaments, which are formed from a diverse family of proteins whose members include keratin, desmin and vimentin as well as the lamins of the nucleoskeleton. The different cytoskeletal networks interact with each other in a highly co-ordinated manner to enable connectivity between different areas of the cell. This thesis is concerned with the actin cytoskeleton, which will be introduced in this chapter in more detail.

1.1.2 The Diverse Functions of the F-actin Cytoskeleton

Actin is an abundant protein that has a monomeric ‘globular’ form (G-actin) and a polymeric ‘filamentous’ form (F-actin), which exist in a dynamic and highly regulated equilibrium. Actin filaments (also called microfilaments) are thin and flexible, with a diameter of ~7 nm. The ability of actin to dynamically and reversibly polymerise provides propulsive force for motility and manipulation of cell shape. Actin filaments are typically found at the cell cortex, with many roles involving the manipulation of membranes (Figure 1.1). However there are exceptions, notably their role as the thin filaments in sarcomeres; the highly specialised contractile units of muscle in which actin was first discovered by Straub and colleagues in the early 1940s. Nucleation of an actin filament from a pool of actin monomers is initiated on a local basis by proteins called actin

nucleators, and this occurs at numerous sites throughout the cytoplasm. Many actin filaments have a rapid turnover, but others serving a more structural role can be longer-lived and span several μm in length (composed of hundreds to thousands of actin molecules).

One way in which force generation can be achieved by the actin cytoskeleton is through directional polymerisation of filaments against a surface (such as protein complexes in a membrane). In protrusions called lamellipodia at the leading edge of a migrating cell, the rapid turnover of branched actin filaments pushes on the cell membrane to drive cell migration (reviewed in Ridley, 2011). Similarly, a dynamic network of short, branched actin filaments drives membrane invagination during endocytosis in yeast (section 1.5). During infection by the bacteria *Listeria monocytogenes*, the parasite hijacks the actin machinery of its eukaryotic host to propel itself through the host cytoplasm (Kocks *et al.*, 1992).

Actin filaments can also serve a more structural role. Membrane protrusions such as stereocilia and microvilli have a structural core composed of parallel bundles of F-actin attached laterally to the protruding plasma membrane (reviewed in Pelaseyed and Bretscher, 2018). Actin filament bundles can serve as tracks for intracellular transport via interaction with the motor protein myosin (reviewed in Titus, 2018). This evolutionarily ancient partnership between actin and myosin can also serve as a driver of contractility. Contractile actomyosin structures include the sarcomeres of striated muscle tissue (reviewed in Gautel and Djinić-Carugo, 2016) and contractile rings that, among other functions, can separate dividing cells during cytokinesis (reviewed in Schwayer *et al.*, 2016). While this thesis will focus on the roles of actin in the context of the cytoskeleton, it should be noted that there is also a growing body of evidence for a variety of functions for monomeric and filamentous actin in the nucleus (reviewed in Kelsch and Tootle, 2018).

Numerous actin binding proteins (ABPs) modulate the properties of actin filaments (see section 1.4 for an overview). Actin filaments and their tightly controlled regulation by ABPs are the primary focus of this thesis and will be covered in detail in subsequent sections of this chapter and the chapters that follow.

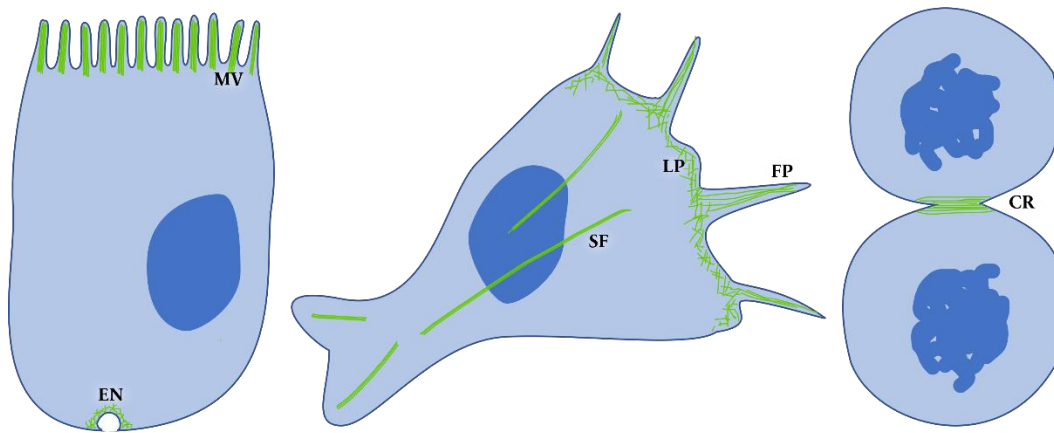


Figure 1.1: Examples of cellular architectures of the actin cytoskeleton. Actin filaments play a diversity of roles in eukaryotic cells. Many of these roles involve membrane manipulation. For example, actin filaments constitute the structural core of cellular protrusions such as microvilli (MV) and filopodia (FP), assist membrane invagination for endocytosis (EN), and – working with the motor protein myosin – constrict the plasma membrane at the interface of dividing cells by the formation of a contractile ring (CR). Other cellular roles of actin include providing pushing forces at the leading edge of migrating cells by forming motile branched networks called lamellipodia (LP), and forming bundles called stress fibres (SF) that increase resistance to mechanical stress.

1.1.3 Actin is a Highly Conserved but Versatile Building Block

Actin is an ATPase, with each monomer bound to one nucleotide at a deep ATP-binding cleft that separates the protein into two globular domains. Binding of ATP or its hydrolysed form ADP is stabilised by a divalent cation in the cleft near the terminal phosphate of the nucleotide (either Ca^{2+} or Mg^{2+}). It is a member of a wider protein superfamily of ATPases which share the same characteristic protein fold. Members of the actin superfamily are widespread throughout all domains of life, and other members include Hsp70/DnaK family chaperones and prokaryotic actin-like proteins (Arps). The prokaryotic Arps are considered to be specialists (forming one polymer for one purpose, e.g. plasmid separation). Consequently, they exhibit considerable sequence and structural diversity. In contrast, a single actin isoform has the potential to contribute to a large number of cell functions. Despite its evolutionarily ancient origins, actin shows a remarkable degree of sequence conservation between distantly related eukaryotes with, for example, over 75% sequence identity shared between actin isoforms from humans, yeast, protozoan parasites and grasses (Figure 1.2). To provide a sense of this high degree of sequence conservation in the context of evolutionary time, the skeletal muscle actin of mammals and birds - which diverged more than 300 million years ago - have identical sequences.

Despite this high degree of sequence conservation, even subtle alterations to the actin sequence can tailor actin to the requirements of the cell. For instance, mammals and birds have 6 actin isoforms, and while two of these (β -cytoplasmic and γ -cytoplasmic) are ubiquitously expressed, the remaining four (α -skeletal, α -cardiac, α -smooth and γ -smooth) are specialised for their role in the contractility of muscle cells. α , β and γ in this naming system refers to their migration during isoelectric focussing, which resulted in clustering into three groups (Vandekerckhove and Weber, 1978a). The variability between these actin isoforms is concentrated at the N-terminus. For example, the only four residues that differ between β and γ cytoplasmic actin are within the 9 most N-terminal residues of the sequence (residues 1, 2, 3, and 9).

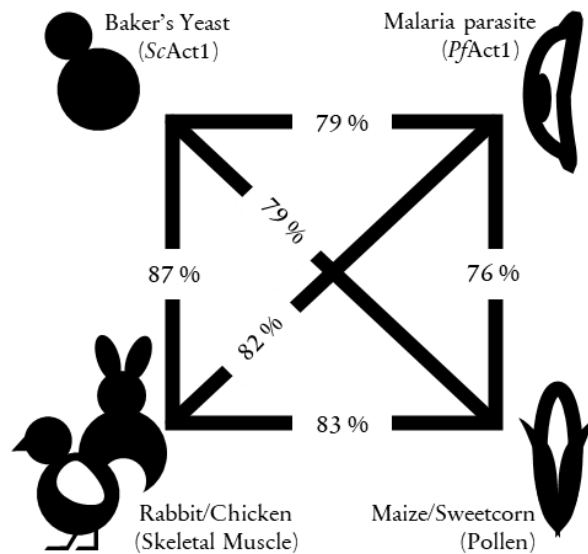


Figure 1.2: Sequence identity between actin isoform protein sequences in different species. High resolution structures of F-actin from these species have been solved by cryo-EM. The isoform or tissue used for purification is stated in brackets. Analysis of published F-actin structures is a topic of Chapter 5. Sequence alignment was performed using NCBI BLAST (Johnson *et al.*, 2008).

Actin dynamics can also be modulated by post-translational modifications (PTMs). Effects of a PTM can include altering protein folding, actin-actin interactions, actin-ligand interactions, or actin-ABP interactions. In some organisms, including vertebrates, two modifications, acetylation and arginylation, compete for the modification of the N-terminus, but acetylation is the more common N-terminal modification. Due to the positioning of the N-terminus on the exterior of the filament,

such modifications are predicted to exert their effects by altering actin-ABP interactions. A known example is the strengthening of the actin-myosin interaction by N-terminal acetylation (Abe *et al.*, 2000). As an example of a different type of modification, His73 is a residue located near the cleft that is commonly methylated (although not in *S. cerevisiae* actin; the isoform studied in this project), and its presence or absence has been found to alter the flexibility and stability of F-actin, possibly by slowing phosphate (Pi) release.

Redox modifications of actin are known to alter its properties, but the nature and effects of these modifications are greatly varied. A cysteine near the C-terminus (Cys374) is the most susceptible residue to spontaneous oxidative modification. Accordingly, actin storage buffers contain the reducing agent dithiothreitol (DTT) to prevent the consequences of Cys374 modification, which include disulphide bond formation between two actin monomers (Ishiwata, 1976). *In vivo*, oxidation of actin in response to oxidative stress has been found to stabilise actin-spectrin networks that result in irreversibly sickled red blood cells (Shartava *et al.*, 1995). Cells also use targeted redox modifications to regulate the cytoskeleton. For example, oxidation of Met44 of F-actin by the flavoprotein MICAL can induce rapid de-polymerisation by circumventing protection against cofilin severing (Hung *et al.*, 2011; Wioland *et al.*, 2021). This is of physiological importance, for example, in the disassembly of the contractile ring at the end of cytokinesis (Frémont *et al.*, 2017). Several other covalent modifications of actin have been identified, including phosphorylation, ADP-ribosylation, and nitrosylation, but much remains to be understood (reviewed in Terman and Kashina, 2013; Varland, Vandekerckhove and Drazic, 2019).

In addition to isoform variation and PTMs, actin owes much of its remarkable functional plasticity to the large and diverse set of binding partners that influence when and where it can polymerise, and how filaments associate with each other. This is the topic of section 1.4, which will provide an overview and examples of some of the ways in which ABPs modulate actin function.

1.1.4 Making a New Actin Filament: Nucleation

The formation of a new actin filament from a pool of monomers occurs by a condensation reaction. This means a certain number of actin molecules must come together in a relatively stable ‘seed’ before polymerisation can occur. This is because actin monomers have a low affinity for each other, but a much higher affinity for an actin filament end. It has been shown recently by X-ray scattering that the minimum number of subunits required to make a stable actin filament is five and therefore the last unstable intermediate (known as a nucleus) is a tetramer (Oda *et al.*, 2016). The formation of a nucleus is known as nucleation. This process is energetically unfavourable because actin dimers and trimers are unstable and therefore very short-lived. In cells, the process is facilitated by actin binding proteins known as actin nucleators that allow rapid nucleation under tight spatiotemporal control. Nucleators are discussed further in section 1.4.9.

In vitro, actin can be stored in a monomeric state in a low-salt buffer known as ‘G-buffer’, which creates an environment that is unfavourable for polymerisation. Monomeric actin in G-buffer can be nucleated by the addition of salt (typically KCl). Nucleation becomes favourable because ions from the dissolved salts shield electrostatic repulsion between actin monomers (Oda *et al.*, 2016). The concentration of G-actin also affects the rate of polymerisation, with higher concentrations resulting in both faster nucleation and elongation. Physiological salt concentrations (~150 mM KCl) and actin concentrations (~50-200 μM) are high enough for spontaneous nucleation of actin to occur so rapidly that almost all the actin in the cell would polymerise in a few seconds (Pollard, 2016), but this is prevented from happening by regulation from actin binding proteins, which collectively ensure rapid continuous turnover of the actin cytoskeleton (section 1.4).

1.1.5 Actin Filament Dynamics

Individual actin molecules are referred to as monomers in G-actin, but protomers in F-actin. Within an actin filament, the helically arranged actin protomers are all orientated in the same direction, conferring an overall polarity. As a result of this polarity, the two ends of an actin filament have different properties, most notably different rates of polymerisation, with a fast-growing ‘plus’ end and a slow-growing ‘minus’ end. Actin building blocks can dissociate from either end of the

filament, resulting in depolymerisation if the rate of monomer removal exceeds the rate of monomer addition. An equilibrium between polymerisation at the plus end and depolymerisation of the minus end results in a process known as treadmilling, in which the filament undergoes continuous turnover but maintains the same overall length (Pollard and Borisy, 2003).

The structural basis for the difference in plus and minus end dynamics is a tilted conformation of the protomer capping the minus end of the filament. This tilted conformation permits extra protomer-protomer contacts, which prevents the end protomer dissociating too easily, while simultaneously reducing accessibility of this end of the filament to new protomers joining (Narita *et al.*, 2011). Consequently, compared to the barbed end, the pointed end of an actin filament requires a much higher concentration of G-actin in order to elongate. This threshold concentration for actin elongation is referred to as the ‘critical concentration’.

1.1.6 ATP Hydrolysis

It has long been known that ATP is a requirement of actin polymerisation, that polymerisation of ATP-G-actin results in ATP hydrolysis to form ADP-G-actin, and that polymerisation of ADP-G-actin is highly unfavourable (Straub and Feuer, 1950). It is now also understood that conformational changes in F-actin upon polymerisation activate the ATPase activity of actin (section 1.3.2). The hydrolysis of ATP occurs rapidly upon polymerisation, but release of the γ -phosphate (Pi) is not immediate, resulting in ADP-Pi in the nucleotide cleft (Carrier, 1990). Because one end of the filament elongates more rapidly than the other, this results in a gradient of bound nucleotide along the length of the filament, with ADP in the cleft of the oldest (‘mature’) sections of the filament, ADP-Pi in newer sections, and a small number of ATP-bound protomers at an actively elongating filament end (Bryan and Rubenstein, 2005). ATP hydrolysis is irreversible, and nucleotide exchange only occurs in the monomeric form, facilitated by the protein profilin (section 1.4.7). However, phosphate release is reversible if enough Pi is available in solution (Carrier, 1990).

Alteration of the nucleotide in the cleft – by hydrolysis, phosphate release, or phosphate re-association – propagates subtle structural changes to regions of the protein exposed to the filament exterior. This confers age-dependent properties as a gradient along the length of the filament, so

ATP hydrolysis in the context of actin polymerisation has been referred to as a ‘molecular clock’. These subtle hallmarks of filament age can be sensed by some actin binding proteins, for example allowing selective disassembly of older regions of the filament by ABPs in the ADF/cofilin family (section 1.4.8).

Following disassembly, ADP-bound monomers rapidly undergo nucleotide exchange in order to replenish the pool of polymerisation-competent G-actin. Interfering with this actin monomer recycling system can be catastrophic for the cell, as demonstrated by the use of filament-stabilising toxins phalloidin and jasplakinolide (Pospich *et al.*, 2020) and the actin sequestering and depolymerising toxin latrunculin A (Ayscough *et al.*, 1997; Fujiwara *et al.*, 2018).

1.2 Solving Actin Structure

1.2.1 Early insights into Actin Filament Structure

In 1949, Rozsa, Szent-Györgyi and Wyckoff used TEM to view metal shadowed actin filaments that had been reconstituted *in vitro*. They observed very long, non-branching filaments of a little less than 10 nm in diameter that did not further fray into thinner filaments at their ends. It was not possible to make out details of the fine structure from these early micrographs, but in some areas they observed a periodicity every 30 nm or so. At the time, they proposed filaments were composed of ellipsoidal rodlets - each 30 x 10 nm in size - assembled end-to-end. In the 1960s, negative stain TEM studies were able to reveal that actin filaments have a helical nature (Hanson and Lowy, 1963; Huxley, 1963). Together, these studies presented evidence that F-actin was composed of two strands wound round the same helical axis, with the double-stranded helix exhibiting a periodicity of ~35 nm. The strands were chains of roughly spherical globular subunits that repeated every 5.5 nm along each strand, giving the strands a beaded appearance. There were approximately 13 of these subunits in each repeat of the double-stranded helix, and all subunits exhibited the same polarity, making the filaments polar as a result. Images of negatively stained samples cannot be used to deduce the handedness of a helix because projections cannot convey all the necessary positional information. To combat this problem, an alternative sample preparation method – the mica-replica

technique – was used, which makes it possible to distinguish which side of the filament is attached to the supporting surface. In this way, the double-stranded helix of F-actin was found to be right-handed (Depue and Rice, 1965).

1.2.2 Initial Atomic Model Estimates for F-actin

High resolution biomolecular structure determination is dominated by three techniques: X-ray crystallography, nuclear magnetic resonance (NMR) spectroscopy and cryogenic electron microscopy (cryo-EM). X-ray crystallography produces a diffraction pattern from a crystallised specimen to find out the relative positions of atoms. Cryo-EM produces enlarged projected images of a frozen hydrated specimen to map areas of high electron density. NMR spectroscopy produces information about the spin properties of atoms to determine their chemical environment. All three of these techniques have very high resolution in the sub-nanometer range. The unit of resolution for these techniques is ångström (Å), which is equivalent to a tenth of a nanometer.

The three techniques fill slightly different niches in the field of structural biology, where the nature of solved structures ranges from peptides to whole viruses. X-ray crystallography has persisted as the dominant technique and can routinely achieve very high resolution (<3 Å), but it is limited to molecules that can form crystals. Actin filaments cannot crystallise in a manner amenable to this technique, meaning their structure cannot be studied this way. F-actin can however form ordered parallel arrays called paracrystals, which have allowed some structural insights from a technique called X-ray fibre diffraction (some of which are mentioned below; Holmes *et al.*, 1990; Oda *et al.*, 2009). NMR spectroscopy does not rely on crystallisation, but this technique is limited to small proteins (up to 30 kDa), making it also unsuitable for studying F-actin structure. Cryo-EM is applied to relatively large (typically >50 kDa) molecules and complexes which are not amenable to crystallisation, making it suitable for studying F-actin structure. However, until the relatively recent ‘resolution revolution’ (section 1.2.3), cryo-EM was greatly limited in resolution, particularly when applied to flexible molecules with low contrast such as F-actin.

Therefore, in the years before cryo-EM was capable of solving filament structure to high resolution, efforts turned to solving the structure of the actin monomer. The tendency of monomers to polymerise in conditions necessary for crystallography presented its own challenges, so there were at least three research groups working on solving the structure of monomeric actin by the mid-1980s (reviewed in Egelman, 1985). In 1990, the first G-actin structure was finally published, in complex with DNase I (Kabsch *et al.*, 1990). From the atomic model of the actin monomer, the first atomic structure of an actin filament was modelled by combining the monomer crystal structure with X-ray diffraction data of filaments to 8.4 Å (Holmes *et al.*, 1990). Though many research groups continued to investigate F-actin structure, the initial atomic model underwent little refinement until Oda and colleagues achieved higher resolution X-ray fibre diffraction (3.3 Å radial and 5.6 Å along the equator) and realised that a protomer within an actin filament has a more flattened form than G-actin (Oda *et al.*, 2009). A cryo-EM structure of F-actin was also solved in this study to complement the X-ray fibre diffraction data, but this was limited to 13.8 Å, from which details such as secondary structures cannot be resolved.

F-actin is a technically challenging sample to work with owing to its flexibility and low contrast in vitreous ice. A breakthrough for F-actin was the first direct visualisation of actin filament secondary structure, which was achieved with a 6.6 Å cryo-EM map of rabbit skeletal muscle F-actin (Fujii *et al.*, 2010). This was made possible through meticulous sample preparation and the use of a liquid helium-cooled specimen stage and an energy filter in the microscope.

1.2.3 Implications of the ‘Resolution Revolution’ for F-actin Structure

In the last decade, cryo-EM has undergone transformational advances due to the culmination of new hardware for more sensitive and rapid data collection, increased storage and faster data processing, and increasingly sophisticated and accessible software for data processing that allowed more reliance on automation (reviewed in Kühlbrandt, 2014, which first coined the term ‘resolution revolution’ to describe these advances).

A key hardware development was a new type of detector for storing data as digital information. The new complementary metal-oxide semiconductor (CMOS) detector represented an alternative to traditional charge-coupled device (CCD) detector. CCDs rely on the conversion of electrons to photons, and then back to electrons, whereas CMOS detectors cut out these conversion steps and use the electrons directly (which is why they are commonly referred to as ‘direct detectors’). Crucially, this enables a very fast readout, which allows motion correction of distortion caused by beam damage (Li *et al.*, 2013; Kühlbrandt, 2014). A major limit in cryo-EM is that the electron beam damages the sample, and therefore restricts the amount of information that can be obtained from any one macromolecule. Images from beam damaged specimens are very noisy as a result. Collecting a movie and correcting for motion-induced blurring before the frames are added together enables the collection of a lot more information from the short exposure time (1-2 s) than a static image. It also allows differential weighting of the contributions made by the information in each image to the sum of aligned images. This is beneficial because frames collected towards the end of the exposure are images of the sample when it has suffered the most beam-damage. Beam damage disproportionately affects the fine features (high spatial frequencies) compared to coarse features (low spatial frequencies). Assigning low weighting to high frequency information in images collected towards the end of the exposure prevents blurring from damaged fine features, while still contributing contrast to coarse features in the image. CMOS detectors are also very thin – much more so than CCD detectors – so the image does not suffer so much from blurring by electron scattering.

At the time this project started in 2017, the first ‘near-atomic’ (4.7 and 3.7 Å) resolution structures of F-actin had just been solved (Galkin *et al.*, 2015; Von Der Ecken *et al.*, 2015) and the University of Sheffield had recently acquired a 200 kV cryogenic electron microscope. Now in 2021, over 40 structures have been solved to <4 Å resolution using this technique. At present, there is still some way before atomic resolution can be achieved for F-actin, but it has been demonstrated for another large protein complex; apoferritin (Nakane *et al.*, 2020). The highest resolution structure for skeletal muscle F-actin to date is 2.9 Å (Pospich *et al.*, 2021). As discussed in Chapter 5, structural studies of F-actin have been skewed heavily towards vertebrate skeletal muscle actin over other actin isoforms.

1.2.4 Obtaining 3D Information from Cryo-EM Data

Cryo-EM is a variant of transmission electron microscopy (TEM) where samples are suspended in an ice layer thin enough for electrons to pass through (<300 nm). Importantly, the freezing process is so rapid that the water in solution does not have time to form ice crystals. The result is vitreous (glass-like) ice that preserves the specimen in a near-native state (Adrian *et al.*, 1984). In Cryo-EM/TEM, the sample is visualised by passing an electron beam through the sample and a series of lenses. Therefore, the resultant image is a magnified projection of the specimen. While an individual projection cannot confer 3D information about the specimen, a series of projections covering a wide range of projection angles can, subject to processing. There are different approaches to reconstructing 3D information from a set of projection angles. One approach is tomography. This uses images collected from the same specimen by physically tilting the sample in the microscope between images to obtain a series of different projection angles. This technique is fairly limited in resolution (>10 Å) because the sample suffers from beam damage with repeated imaging. It is most suitable for larger, more robust, specimens. This technique was used for the work in 6.2.7, applied to examine the shape and dimensions of a thick actin bundle.

An alternative method of obtaining multiple projection angles is to make a sample with several identical copies of a specimen, arranged at different angles in the ice layer. This way, each area of the sample needs only to be imaged once, and the projected images will not suffer loss of information from beam damage. This method, called single particle analysis, is suitable for a range of biological specimens, from viruses at the largest end of the scale to individual globular proteins >40 kDa at the smallest end of the scale so far (Herzik *et al.*, 2019). The ‘particles’ in single particle analysis are individual images containing a single molecule of interest. They are obtained first by identifying the coordinates of features of interest within the micrograph (a process called particle picking) and then generating images of a set size around the picked co-ordinates to produce a set of images of identical size, each containing a view of a single particle (a process called particle extraction). Particles are grouped into equivalent views in a process called 2D classification which uses a cross-correlation algorithm to discern common features and, when a match is found, to find the best image alignment. The aligned particles in each 2D class are averaged together to generate a view of the macromolecule with greatly improved signal-to-noise. At this stage, the user can assess

whether there is a sufficient range of views of the macromolecule to proceed with processing. Additionally, false or damaged particles contributing to poor quality classes can be eliminated at this stage.

Each 2D class represents a 2D projection from a different viewing angle and identifying how these views are aligned relative to each other ('angle assignment') can be used to reconstruct a 3D map of the macromolecule in a process called 3D refinement. During 3D refinement, the dataset is divided into two subsets which are reconstructed independently of each other (each making a 'half map'). Back-projections of a low-resolution user-provided template map with similarity to the macromolecule of interest can be used as a reference to aid the process. 3D reconstruction is an iterative process that refines the reconstruction with every cycle. At the end of refinement, the resulting half maps can be used to calculate a Fourier Shell Correlation (FSC) curve, which is an indication of how well the two half maps correlate with each other over a range of resolutions. While these processes are largely automated, user-input is important for assessing whether the resulting map is a true representation of the structure, or whether an incorrect structure has been converged upon. Additionally, noise that is consistent across both half maps can result in a falsely high-resolution estimate, so the user should check reported resolution against the features of the map, such as α -helices (resolved at better than ~ 9 Å), β -sheets (resolved at better than ~ 5 Å) and side-chains (resolved at better than ~ 3 Å). Once a suitable initial 3D map is generated, there are several steps that can be performed to improve the resolution.

Unlike globular proteins and complexes, it is not possible to view actin filaments from all projection angles (e.g. directly down the helical axis). However, owing to their helical symmetry, a projection of a segment of filament is able to give a good coverage of projection angles from a single view of the specimen. As long as the helical parameters are known (or at least estimated well), projections of a helical filament can be used to reconstruct 3D information. The first 3D structure to be solved from EM data, the tail of a T4 bacteriophage, used helical reconstruction (De Rosier and Klug, 1968; DeRosier and Moore, 1970). Chapter 4 covers the process of helical reconstruction applied to yeast F-actin.

1.3 Actin Structure

1.3.1 Features of the Actin Monomer

The actin monomer is a highly conserved ~42 kDa globular protein comprised of around 375 amino acids (exact length is isoform specific but does not vary by much). The folded protein has the approximate dimensions of 5.5 x 5.5 x 3.5 nm, giving it a cuboid-like shape. The protein fold has been categorised into four subdomains (SD1-SD4; Figure 1.3), with the N and C-termini both located in subdomain 1.

G-actin binds ATP (Straub and Feuer, 1950) and has a high-affinity nucleotide binding site in a deep cleft located between SD2 and SD4 (Kabsch *et al.*, 1990). In the absence of excess nucleotide, G-actin becomes irreversibly inactivated, indicating the bound nucleotide is essential for the stability of the protein (Asakura, 1961). The phosphates from the adenine nucleotide and nearby acidic residues of the cleft (Asp11, Gln137, Asp154) make a hydrophilic pocket that harbours a single divalent cation (Kabsch *et al.*, 1990), which can be Ca^{2+} or Mg^{2+} . G-actin crystal structures show the cleft in closed (Rould *et al.*, 2006) and open states (Chik *et al.*, 1996), demonstrating a hinge-like flexibility which is important for nucleotide exchange. On the opposite side of the monomer to the cleft is a shallow groove between SD1 and SD3 that is the binding site for several ABPs. In the filament, the cleft is oriented toward the pointed/minus end, and the binding groove, or barbed-end groove, is oriented towards the barbed/plus end of the filament. The 'barbed' and 'pointed' naming convention stems from the stacked arrowhead appearance of F-actin decorated with myosin (Moore *et al.*, 1970). The 'plus' and 'minus' end naming convention is based on the dynamic properties of each end and is explained in section 1.1.5. Other distinct features of the protein backbone are the H-loop (residues ~263-272, located between subdomains 3 and 4 near the base of the cleft) and the DNase I binding loop (D-loop; residues ~38-52 in subdomain 2, extending from one 'corner' of the protein). These distinctive features are indicated in Figure 1.3. The D-loop, H-loop and N-terminus of G-actin are highly mobile, and remain so in the filament (Galkin *et al.*, 2015).

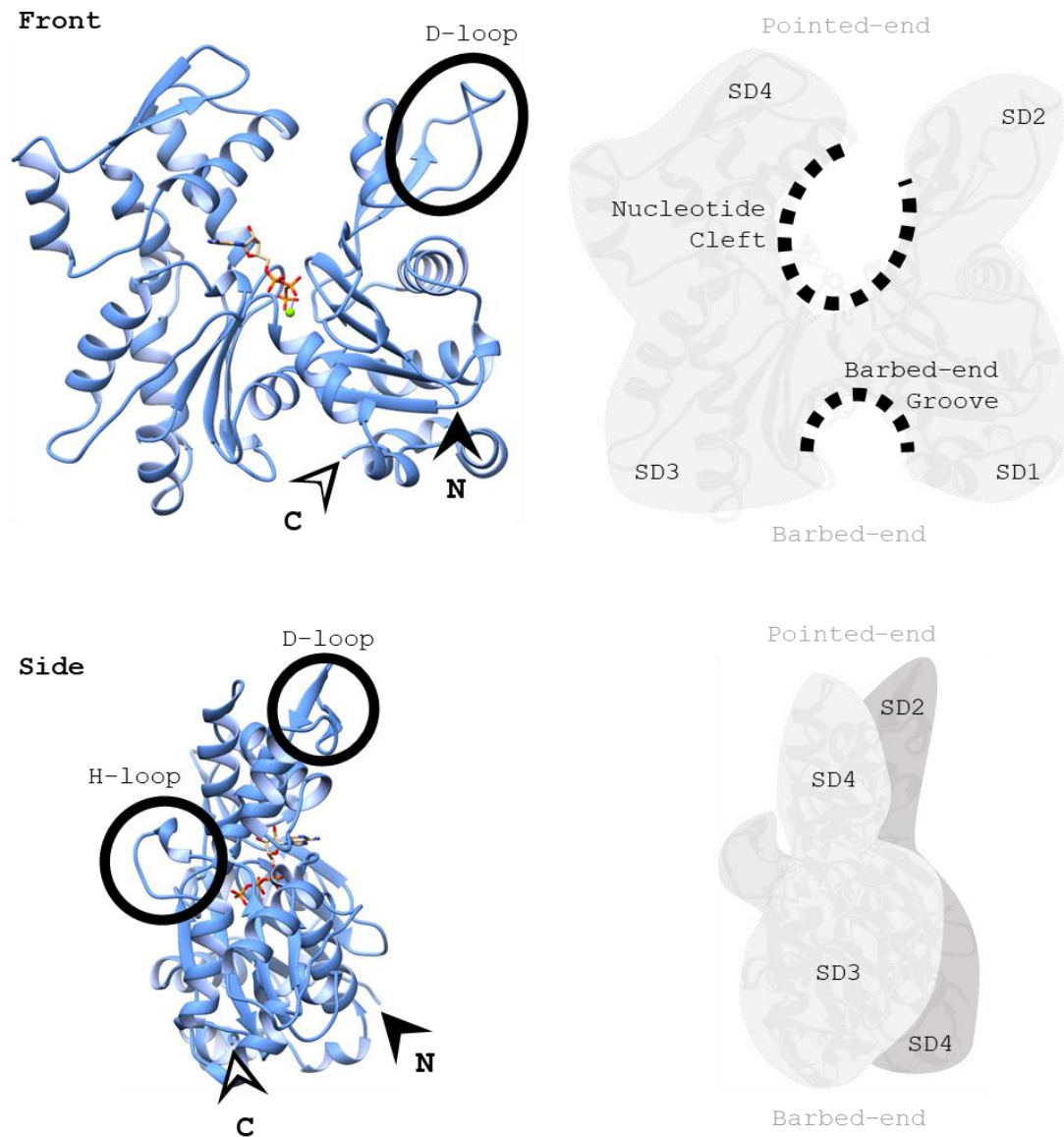


Figure 1.3: Features of the actin monomer. The protein is shown from two different angles, as both a ribbon structure (left) and a simplified diagram (right). ATP (stick model, coloured by element) and Mg^{2+} (green sphere) are also displayed. The structure shown is the *S. cerevisiae* actin monomer from PDB ID: 1YAG. Positions of the subdomains and key features are indicated.

1.3.2 Polymerisation: The Monomer to Protomer Transition and ATP Hydrolysis

Upon incorporation into a filament, an actin monomer undergoes a conformational change that can be thought of as flattening. This is achieved by the relative rotation of the two major domains of the protein found on either side of the cleft (SD1+SD2, and SD3+SD4) by approximately 20° (Oda *et al.*, 2009).

This conformational change activates ATP hydrolysis by a subtle reorganisation of the active site that increases its catalytic activity by several-thousand fold (Chou and Pollard, 2019). A key factor in this increased catalytic activity is the repositioning of Gln137 and His161 relative to the γ -phosphate of ATP (Oda *et al.*, 2009). This is because these residues each anchor a water molecule that plays an active role in the nucleophilic attack on the γ -phosphate during ATP hydrolysis (Vorobiev *et al.*, 2003; Merino *et al.*, 2018). The rate of hydrolysis is dependent on the identity of the cation occupying the cation binding site in the cleft, with Mg^{2+} -bound F-actin hydrolysing ATP at a rate of 0.3 s^{-1} , and Ca^{2+} -bound F-actin hydrolysing ATP at 0.05 s^{-1} ; a rate 6 times lower (Blanchoin and Pollard, 2002). As well as flattening of the molecule, another notable change upon polymerisation is the extension of the D-loop (Oda *et al.*, 2009), which is a major player in inter-filament contacts (see 1.3.5).

1.3.3 A Tilted Polymerisation Intermediate?

It has been proposed previously that F-actin has an alternative ‘tilted’ state with weaker intra-strand interactions, and that this state may represent an early stage of polymerisation (Orlova *et al.*, 2004; Galkin *et al.*, 2010, 2015). This tilted state, but not the canonical state of a mature filament, is comparable with an antiparallel actin dimer that has been observed upon cross-linking a solution of G-actin, and has been found capable of nucleating F-actin (Millonig *et al.*, 1988; Bubb *et al.*, 2002). Galkin, Orlova and colleagues from the Egelman lab also predict that several disease-causing mutations of actin would disrupt the protomer-protomer interfaces of the tilted F-actin state (while having little involvement in the protomer-protomer interactions of the canonical F-actin state). The protomer-protomer contacts described in the next section are for the canonical state of F-actin seen in most structural studies.

1.3.4 The Helical Symmetry of F-actin

From a simplified mathematical perspective, a helix is a curve continually progressing around and along a helical axis (aligned with the z-axis) in the same direction, with a fixed rotation per unit of

translation along the helical axis, and a fixed radius (Figure 1.4A). However, actin is a helix made up of discrete units (actin protomers) repeating at regular intervals, so rather than defining its helical symmetry by the radius and pitch, parameters are used that can provide information about the relative positioning of adjacent protomers. These parameters are the helical rotation or ‘twist’ (the degree and direction of rotation around the helical axis) and the axial rise (the distance of translation along the helical axis). The axial rise is always considered as the distance moved forwards along the helical axis, so is always a positive value, but the twist can have either a positive or negative value. Where the twist value is positive, the helix is described as a ‘right-handed’ helix, and where the twist value is negative, the helix is described as a left-handed helix.

An additional parameter describes how many helices are contained within the structure, or in other words how many strands there are. F-actin can be described either as a double-stranded (‘2-start’) or a single-stranded (‘1-start’) helix (Figure 1.4B). If considered as a 1-start helix, it is a left-handed helix with a twist of $\sim -167^\circ$, axial rise of $\sim 27.5 \text{ \AA}$, and a pitch of $\sim 59 \text{ \AA}$. However, F-actin can also be thought of as a double-stranded helix with two protofilaments (or strands) turning around each other. If considered this way, F-actin is a 2-start helix, with each strand having a twist of $\sim +26^\circ$, an axial rise of $\sim 55 \text{ \AA}$, and a pitch of $\sim 365 \text{ \AA}$. Owing to the large difference in pitch, the 1-start helix is often referred to as the short-pitch helix, while the 2-start helix is often referred to as the long-pitch helix. These parameters are important for the work in Chapter 4, which exploits the symmetry of actin to perform helical reconstruction on cryo-EM data (section 1.2.4).

The helical parameters stated above are the typical parameters for bare (i.e. with no bound ABPs) vertebrate skeletal muscle F-actin. However, F-actin has structural plasticity that allows some intrinsic variation in twist, while maintaining a constant axial rise (Egelman *et al.*, 1982). It is also known that the helical twist of F-actin can be altered by external factors. Cooperative binding of several cofilin molecules to decorate a region of filament results in a helical twist change of $\sim 5^\circ$ (-166.7° to -162°). This shortens the cross-over length of the two protofilaments from $\sim 36.5 \text{ nm}$ to $\sim 27.0 \text{ nm}$ (McGough *et al.*, 1997). This conformational change weakens intra-strand contacts of the D-loop and subdomain 1 of neighbouring protomers (section 1.3.5), allowing increased flexibility (Galkin *et al.*, 2011). This change in twist has been shown to alter the interactions of F-actin. For

example, it excludes the binding of phalloidin (McGough *et al.*, 1997) a cyclic heptapeptide toxin which binds at the interface of three actin protomers (Drubin *et al.*, 1993; Pospich *et al.*, 2020).

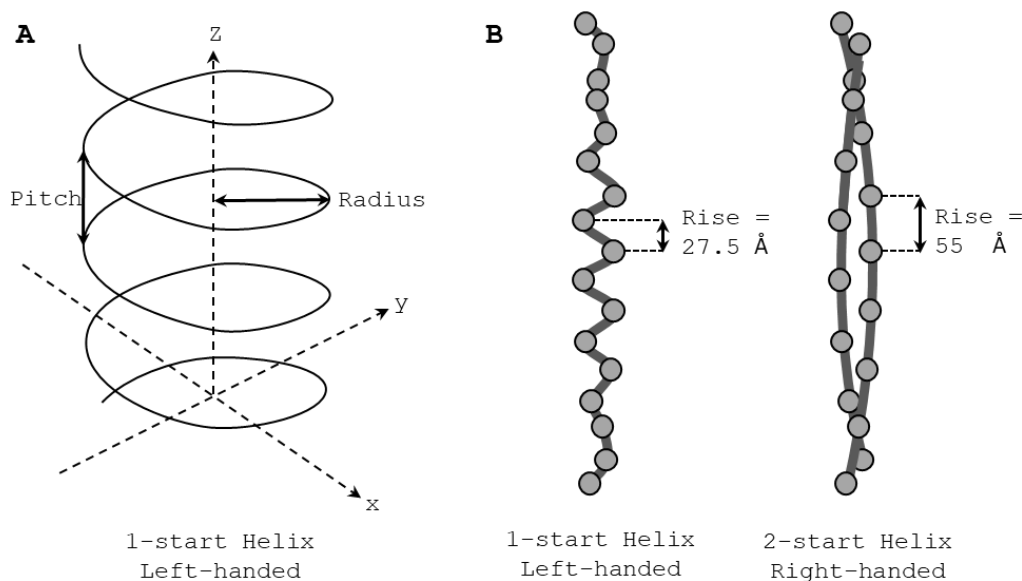


Figure 1.4: Parameters used to describe a helix. **A)** Graphical depiction of a simple continuous helix. Radius is the distance between the helical (z) axis and the path of the helix, while pitch is the distance travelled along the helical axis before one 360° turn is completed by the path of the helix. The example shown is a left-handed helix (meaning the rotation follows an anticlockwise direction with progression along the z -axis) and 1-start (meaning there is only a single helical path). **B)** Diagrammatic depiction of the two ways of describing the symmetry of F-actin: as a 1-start or a 2-start helix. Helical paths are indicated by lines and equivalent positions within actin protomers are indicated with circles. Axial rise (the distance travelled along the helical axis to reach an equivalent position in the next protomer on the helical path) is annotated.

1.3.5 Protomer-Protomer Contacts

An individual protomer contacts four neighbouring protomers in the filament (Figure 1.5A). Two of these neighbouring protomers are within the same strand: one making contacts with its pointed end and one making contacts with its barbed end. These contacts are often termed the ‘intra-strand interface’, or ‘long-pitch helix interactions’ or ‘longitudinal contacts’. The other two neighbouring protomers are from the opposite strand. The strands are staggered by approximately half a protomer’s width, so that the intra-strand interface between two protomers is level with the centre of a protomer on the opposite strand. The contacts that form between protofilaments are often termed the ‘inter-strand interface’, or ‘short-pitch helix interactions’ or ‘lateral contacts’.

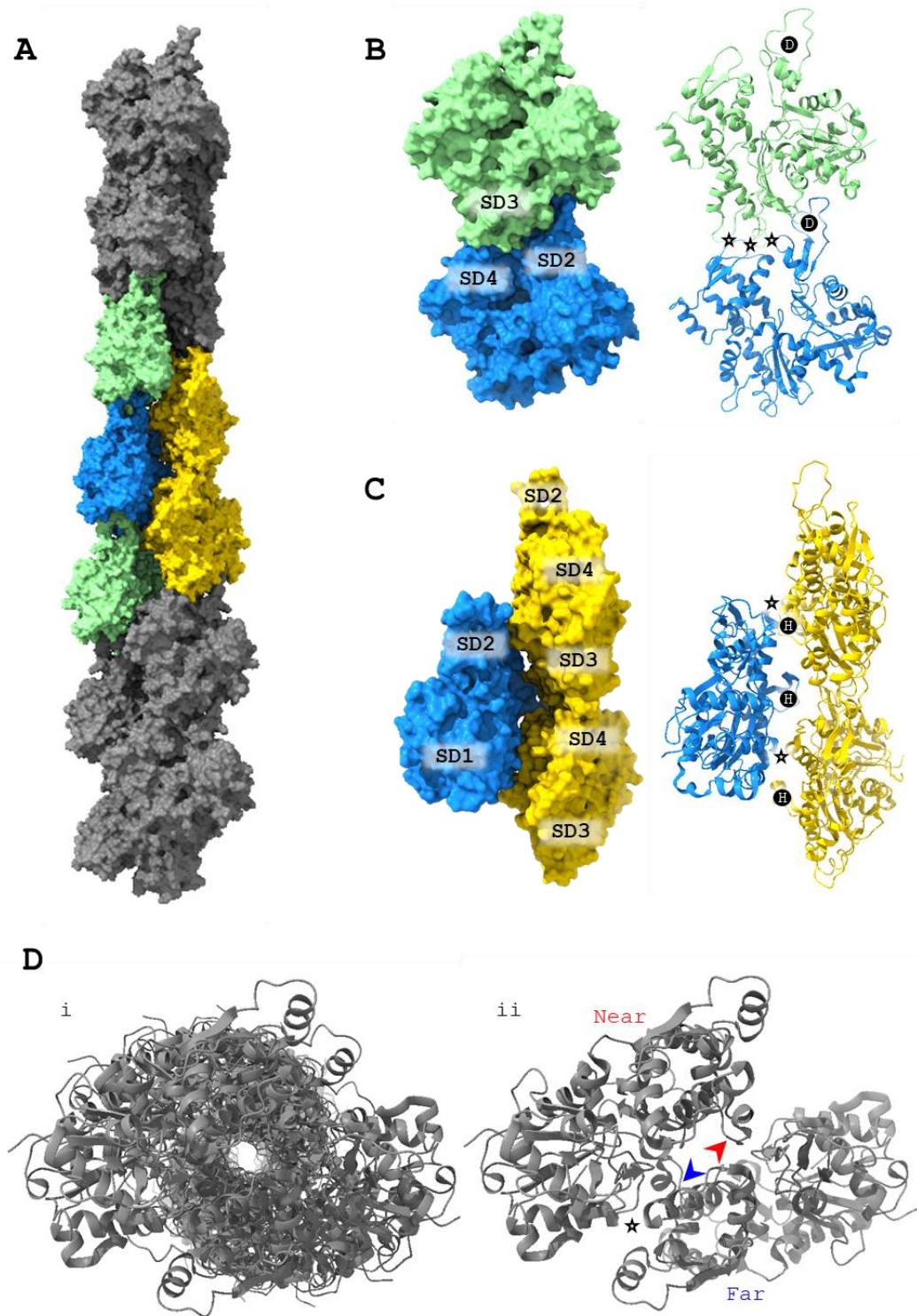


Figure 1.5: Protomer-Protomer contacts within an actin filament. **A)** Surface view of a short actin filament highlighting one protomer (blue), the protomers it contacts within the same protofilament (green) and the protomers it contacts in the opposite protofilament (yellow). **B)** The intra-strand interface. The D-loop, which mediates multiple intra-strand contacts, is indicated with 'D' and other SD2/4-SD3 contact sites are annotated with a star. **C)** The inter-strand interface. The H-loop is indicated with 'H', and the additional SD1-SD4 polar contact site is annotated with a star. **D)** A filament viewed from the pointed end with i) the same number of protomers as part **A** and ii) only the top two protomers. The H-loop of the nearest (pointed-end) protomer is labelled with a red arrowhead and the H-loop of its inter-strand neighbour is labelled with a blue arrowhead. The additional SD1-SD4 polar contact site is annotated with a star.

Intra-Strand Interactions (Longitudinal Contacts)

Intra-strand connections occur between SD2/SD4 at the barbed-end of one protomer and SD3 at the pointed-end of its neighbour (Figure 1.5B). The large flexible D-loop in SD2 (residues 38-50) is of key importance for the SD2-SD3 interaction, forming several contacts with the neighbouring protomer. The D-loop has been found to adopt different conformations depending on the bound nucleotide, which affects the specific residues involved in the intra-strand interaction (Merino *et al.*, 2018; Chou and Pollard, 2019). SD3 additionally forms polar contacts with a loop in SD2 adjacent to the D-loop, and with SD4.

Longitudinal contacts between protomers are similar in actin-related proteins in archaea and bacteria, which differ greatly in sequence but have a strongly conserved actin fold (Stoddard *et al.*, 2017). In contrast, the nature of inter-strand contacts can vary greatly, to the extent that some bacterial actin-like filaments exhibit a different arrangement of the strands relative to each other, such as the unstaggered two-stranded filaments of helical MamK (Löwe *et al.*, 2016) and non-helical MreB (van den Ent *et al.*, 2014).

Inter-Strand Interactions (Lateral Contacts)

Lateral contacts between the protofilaments are weaker than the longitudinal contacts connecting protomers within the same protofilament. The low occurrence of inter-strand connections results in the appearance of a gap running down the centre of the filament between the two strands (Figure 1.5D). Superimposition of monomer and protomer models of actin has demonstrated that subunit flattening upon polymerisation is important for permitting inter-strand contacts (Chou and Pollard, 2019).

A key contributor to the inter-strand interface is the H-loop, which projects across the space between the strands towards the SD2-SD3 intra-strand interface of its opposite neighbours (Figure 1.5C&D). The H-loop forms associations with the opposite protofilament, but without making close contact. There is evidence from crosslinking experiments that flexibility of the H-loop within the mature filament is necessary for filament elongation (Shvetsov *et al.*, 2008; Galkin *et al.*, 2015). Despite its largely hydrophilic properties, the H-loop was originally given the misleading name ‘hydrophobic plug’, or ‘hydrophobic loop’. This stems from speculation made at a time before

filament structure could be solved directly that the loop might rearrange to a conformation that allows hydrophobic interaction with the opposite strand (Holmes *et al.*, 1990).

On the opposite side of the protofilament interface, there is additionally a polar contact between SD1 of one protomer and SD4 of the opposite protomer positioned closer to the barbed end (Galkin *et al.*, 2015; Ren *et al.*, 2019)(Figure 1.5C&D).

1.4 Actin Binding Proteins: Architects of the Actin Cytoskeleton

1.4.1 Actin Binding Protein Strategies

Actin binding proteins associated with the actin cytoskeleton oversee the spatiotemporal regulation of actin polymerisation and its arrangement into architectures such as bundles, elastic meshes, parallel arrays alternating with myosin bundles, or branched networks. ABPs can also influence the physical properties of actin filaments, such as stiffness and stability. ABP functions include monomer sequestering, nucleotide exchange, nucleation, elongation, capping, bundling, cross-linking, and severing, with many ABPs performing more than one of these functions. Enhancing and suppressing the activity of specific ABPs confers tunability of the actin cytoskeleton. This is achieved through variation of several factors, such as regulatory proteins, autoinhibition, lipid binding, and the local chemical environment (e.g. ions, pH). For instance, many actin binding proteins are sensitive to Ca^{2+} , the cytoplasmic concentration of which can vary according to cellular responses to the external environment. In another example, several ABPs alter their activity in response to binding the phospholipid phosphatidylinositol (4,5)-bisphosphate (PIP_2), which is an intermediate in several cell signalling pathways: PIP_2 binding to the monomer-binding profilin, or severing proteins cofilin and gelsolin, inhibits the activity of these ABPs by competitively (profilin and cofilin) or indirectly (gelsolin) inhibiting their actin binding sites. Other ABPs, including the nucleation promoting factor N-WASP and the formin nucleator Dia2, are positively regulated by PIP_2 (Senju *et al.*, 2017). The complex interplay of ABPs and their regulatory factors means the outcome of an interaction between actin and one of its binding proteins can vary depending on

the local cytoplasmic environment. This section will showcase a few examples of the influence of ABPs on actin, and a general overview can be found in Figure 1.6. More comprehensive coverage of ABPs can be found elsewhere (Winder and Ayscough, 2005; Pollard, 2016).

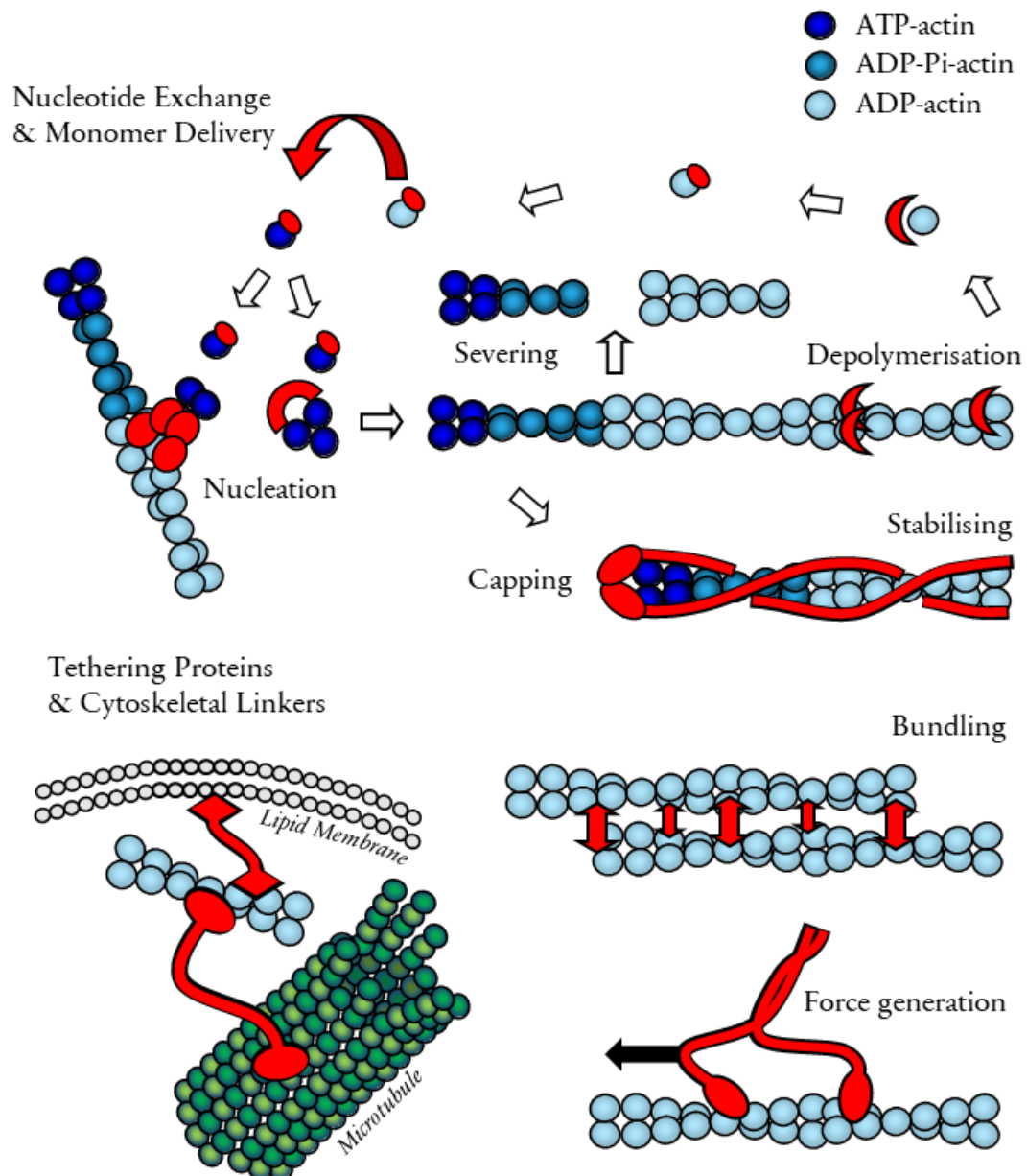


Figure 1.6: Some of the common functions of actin binding proteins. Actin binding proteins (ABPs) have many ways of regulating actin filament organisation and the equilibrium between the monomeric and filamentous states of actin. Since many ABPs perform more than one role, this illustration focuses on examples of ABP functionality rather than specific ABPs.

1.4.2 Tethering Proteins and Cytoskeletal Linkers

Some ABPs can tether F-actin to membranes. Examples include utrophin and its muscle-specific homologue dystrophin, which are part of plasma membrane-bound complexes (Keep, 2000). Another example is vinculin, which can simultaneously bind F-actin and focal adhesion proteins at the plasma membrane (Humphries *et al.*, 2007). Some ABPs can bind membranes directly. For example, the WH1 domain in the N-terminal portion of WASP proteins can bind lipids (Allwood *et al.*, 2016) while the C-terminal WH2 domain binds ATP-G-actin monomers. This enables accumulation of polymerisable G-actin near the plasma membrane. Alternatively, when unoccupied by monomeric actin, the WH2 domain can weakly bind the actin filament barbed end (Bieling *et al.*, 2018). This may allow intermittent tethering of filaments to the plasma membrane.

There is also extensive crossover between the ABPs of the actin cytoskeleton and the microtubule associated proteins (MAPs) of the tubulin cytoskeleton, with several proteins being both ABPs and MAPs. For example, crosslinking of F-actin and microtubules (MTs) is mediated by filament side-binding proteins such as plectin, Tau and Map2. Plectin also links to the intermediate filaments (Karashima *et al.*, 2012), facilitating connectivity between all three cytoskeletal filament types in metazoa. Other proteins, such as moesin, link the plus end of MTs to the cortical actin cytoskeleton. A great number of other proteins have roles facilitating coordination between F-actin and MTs and are reviewed in Dogterom and Koenderink, 2019)

1.4.3 Myosins

Actin has evolved an effective partnership with a class of ABPs called myosins, which form a superfamily of motor proteins analogous to the MT-associated kinesin and dynein motor protein superfamilies, all of which use ATP hydrolysis for force generation on a cytoskeletal track (reviewed in Lee Sweeney and Holzbaur, 2018). Together, actin and myosin can form contractile architectures such as the sarcomeres of muscle tissue (recently investigated on a structural level in great detail; Wang *et al.*, 2021) or the cytokinetic rings of animal cells, amoeboid cells, and budding and fission yeast (reviewed in Schwayer *et al.*, 2016). Alternatively, bundles of actin can be used by cargo-carrying myosin dimers as cytoskeletal highways for local transport, complementing the

generally more long-range transport mediated by kinesin and dynein using MT tracks (Titus, 2018). Myosins have a head and tail region. The tail region is used for anchoring and multimerization, while the head powers movement. The myosin head has a globular motor domain which binds actin and hydrolyses ATP. This is connected to the rest of the protein via a 'lever arm' which effectively amplifies the movements within the motor domain. An ATP hydrolysis cycle allows directional force generation between F-actin and myosin as follows:

1. ADP-Pi myosin has weak affinity for F-actin. Upon myosin binding actin, Pi is released.
2. Pi release strengthens binding of myosin to actin and simultaneously induces a conformational change where the motor domain folds in towards the lever arm: this generates directional tension on the actin filament and moves either the myosin or the F-actin, depending on which is more anchored. This force-generating movement is known as the power stroke.
3. Myosin remains strongly bound to F-actin in its contracted conformation, and ADP is released over time.
4. ATP binding causes dissociation of the actin-myosin interaction.
5. ATP hydrolysis restores the original extended conformation and the cycle repeats.

Dimerisation or bundling of myosin molecules that act independently of each other allows the myosin complex to remain associated with F-actin throughout the ATP hydrolysis cycle. There are several different myosin classes, each of which is specialised to particular cell roles (reviewed in Hartman and Spudich, 2012). The myosin motor domain binds F-actin at the interface between two adjacent actin protomers in the same protofilament (long pitch helix), making contacts with SD1, SD2 and SD3 (Behrmann *et al.*, 2012).

1.4.4 Tropomyosins

Tropomyosin is a two-stranded α -helical coiled-coil protein that binds along both sides of an actin filament. The path of a single tropomyosin dimer follows one of the two long-pitch helices of F-actin, making contacts with seven protomers in the same protofilament. Several molecules of

tropomyosin can form a longer polymer along the side of an actin protofilament by overlapping at their ends (Greenfield *et al.*, 2006), each with its N-terminus closest to the barbed end of the filament. The precise contact sites of tropomyosin with F-actin vary depending on the presence of troponin, myosin and Ca^{2+} , as well as the pH: the path of tropomyosin binding along the long pitch helix can shift between two main states (~ 2.3 nm apart) depending on these factors (Behrmann *et al.*, 2012; Von Der Ecken *et al.*, 2015). Fungi and animals express tropomyosins, but while budding and fission yeast express just two isoforms (Tpm1 and Tpm2), mammals have almost 40 tropomyosin isoforms from the alternative splicing of four genes (Geeves *et al.*, 2015). Tropomyosin regulates F-actin in an isoform-specific manner by altering its interactions with ABPs, for example by protecting F-actin from severing proteins and selectively recruiting, activating or blocking different myosin isoforms (reviewed in Gunning *et al.*, 2015). Tropomyosins are known to protect F-actin from severing by cofilin. There is some evidence to suggest that, rather than simply sterically blocking access to the filament surface, tropomyosins can influence actin protomer-protomer interfaces (D-loop and H-loop conformations) in a way that interferes with or counters the conformational changes induced by cofilin (Ostrowska-Podhorodecka *et al.*, 2020).

1.4.5 Capping Proteins

By binding to the end of an actin filament, capping proteins can control the rate of polymerisation of a filament end. Most capping proteins limit the association or dissociation of actin subunits at the end of the filament to which they bind. One notable exception is the formins – best known for their nucleation and elongating activity – which remain associated with the barbed end of a filament they have nucleated and either promote rapid elongation or restrict barbed-end growth depending on their conformational state and the effect this has on the terminal protomers at the barbed end of the filament (Aydin *et al.*, 2018; further details in section 1.4.9). The majority of barbed end capping proteins serve to restrict the number of free barbed ends for polymerisation to help maintain the G-actin pool. For example, the heterodimeric ‘capping protein’, which is expressed broadly across *Eukarya*, caps F-actin by binding the two protomers exposed at the barbed end; one from each of the long-pitch helical strands (Yamashita, 2003). Another example is the

severing protein gelsolin, which can remain associated with the new barbed end generated from the severing of a longer filament (reviewed in Nag *et al.*, 2013). The removal of barbed-end caps is one way in which a cell can upregulate actin polymerisation. Capping proteins that target the slow-growing pointed end can prevent depolymerisation and further promote directional growth at the faster growing barbed end of the filament. Examples include the muscle protein tropomodulin which caps the pointed end by wrapping around the three terminal subunits (Rao *et al.*, 2014), and the more ubiquitously expressed Arp2/3 actin nucleator complex which caps the pointed end of a filament it has nucleated. Capping a filament at both ends can enable the maintenance of filaments with a constant length in structures where this is important, such as sarcomeres and stereocilia.

1.4.6 Bundlers and Crosslinkers

Bundling and crosslinking of actin is mediated by proteins or protein oligomers (usually dimers) with two or more distinct actin binding sites. The distance between the actin binding sites in the crosslinker and their relative orientation determines the nature of the actin architecture. Fascin is a small globular protein with two distinct actin binding sites, and fimbrin has two adjacent actin binding domains (ABDs,) and therefore these proteins can organise actin filaments into compact parallel actin bundles. Other mediators of tight actin bundling include transgelin (Scp1 in yeast; Winder, Jess and Ayscough, 2003) and the focal adhesion protein vinculin (Jockusch and Isenberg, 1981). In contrast, α -actinin is an anti-parallel dimer with several nm separating its actin binding sites, so the resulting actin architecture is loose bundles of F-actin (~40 nm spacing) with mixed polarity. Tight and loose bundlers of actin promote more binding by similar bundling proteins, while inhibiting bundling by others, which enables sorting of discrete actin bundles with distinct properties (Winkelman *et al.*, 2016).

Looser networks of F-actin are linked by cross-linking proteins. Filamin is a long flexible molecule with an actin binding domain at one end and a dimerization domain at the opposite end, allowing the resulting V-shaped dimer to create a loose flexible meshes of F-actin (reviewed in Nakamura, Stossel and Hartwig, 2011). Rod-shaped spectrin tetramers, with actin binding sites at each end, are typically 150–250 nm in length. The interaction between actin and spectrin can produce strikingly

different architectures in different cellular contexts. Spectrin forms a network with very short actin filaments in erythrocytes (Pan *et al.*, 2018), and highly ordered parallel arrays of spectrin separate rings of F-actin that follow the circumference of the axons of nerve cells (Xu *et al.*, 2013). As a consequence of the weak actin binding of most ABDs, cross-linking and bundling proteins dissociate and reassociate. This allows plasticity of the cell over time, but stiffness and elasticity in response to sudden force (reviewed in Pollard, 2016).

1.4.7 Monomer Binding

In most well-studied eukaryotic cells, almost all of the G-actin in the cytoplasm is bound to a small (~14 kDa) highly conserved globular protein called profilin. Profilin family proteins bind at the barbed end of the actin monomer, preventing association with the pointed end of the filament. The bound monomer can however join the barbed end of the filament, which weakens its interaction with profilin and allows elongation to continue. Profilin plays an important role in delivery of actin to nucleators for polymerisation, binding both formins and the Arp2/3 complex (Machesky *et al.*, 1994; Chang *et al.*, 1997), but of the two nucleators it favours formins (Suarez *et al.*, 2015).

Profilin also promotes dissociation of ADP from G-actin by inducing an opening of the nucleotide binding cleft, thereby promoting nucleotide exchange (Vinson *et al.*, 1998). An additional way in which profilin assists nucleotide exchange is by displacing another broadly expressed ABP called cofilin, which blocks nucleotide exchange when bound to the barbed-end groove of G-actin. Other roles of cofilin are discussed further in the next section. Mammalian cells additionally express an ABP called thymosin β 4 (thy β 4), which is a 42-residue peptide that stretches around G-actin to sterically block the barbed and pointed ends of the monomer with its N-terminal and C-terminal alpha helices, respectively (see Figure 3.2 in Chapter 3). In these cells, thy β 4 competes with profilin for control of the G-actin pool, resulting in a greater degree of monomer sequestration. Leukocytes and platelets have particularly high expression of thy β 4, which serves to sequester a large pool of G-actin for the rapid and extensive actin polymerisation events triggered in these cells upon their activation (Safer *et al.*, 1991).

1.4.8 Filament Severing

Severing F-actin exposes a greater number of filament ends. This can favour either more net polymerisation or more net depolymerisation, depending on other factors, such as whether the barbed ends of the filaments are capped. One of the key ABPs for influencing filament turnover in this way is a family of highly conserved proteins called cofilins (alternatively called actin depolymerising factor; ADF). Cofilin is a very small (~15 kDa) globular protein that binds G-actin 1:1, or slots between two adjacent protomers on the same protofilament of F-actin (Tanaka *et al.*, 2018). Partial cooperative decoration of an actin filament with cofilin results in severing. Cofilin decoration induces a local twist change that destabilises the interface between the decorated and bare sections of the filament (Huehn *et al.*, 2018). Because severing is caused by the twist discrepancy in two neighbouring regions of filament and not by the altered twist itself, saturation of an actin filament with cofilin actually stabilises filaments by imposing a uniform twist along its entire length (McGough *et al.*, 1997). Another family of severing ABPs is the gelsolin family, which are large proteins with multiple actin binding domains that have a fold resembling cofilin. Gelsolins bind the barbed-end groove of actin protomers, which disrupts the protomer-protomer interactions of the filament (reviewed in Nag *et al.*, 2013). As mentioned earlier, after severing, gelsolin can remain attached to the barbed end, acting as a capping protein. Interestingly, there is a splice variant of gelsolin (plasma gelsolin) that is secreted into the bloodstream to scavenge F-actin released by dead or damaged cells (Lind *et al.*, 1986). In addition to specialist severing proteins, some formins have also been found to have F-actin severing activity (Harris *et al.*, 2004; Gurel *et al.*, 2014).

1.4.9 Nucleators and Nucleation Promoting Factors

When actin polymerisation is needed, ABPs called actin nucleators recruit monomers from the G-actin pool and lower thermodynamic barriers acting against polymerisation. Nucleators are diverse in their sequence, structure and nucleation mechanisms.

Formins

Formins are large multidomain proteins that form homodimers to nucleate and elongate actin filaments. They are primarily classified by a highly conserved domain called the FH2 domain which is responsible for dimerization and actin binding. In the homodimer, an antiparallel association of the FH2 domains results in a ring-like structure with actin binding sites spaced apart by flexible linkers. With a capacity for binding at least two actin monomers simultaneously, the FH2 ring can stabilise actin dimers or trimers, which would otherwise quickly dissociate. Stabilising these polymerisation intermediates therefore increases the likelihood of forming an actin nucleus by the addition of another actin monomer in the cytosol. In most formins, another domain called the FH1 domain is found upstream of the FH2 domain. The FH1 domain contains several polyproline repeats and is thought to have an extended, disordered structure. The polyproline repeats can specifically bind profilin, allowing capture of profilin-actin complexes as building blocks for elongation. The formin dimer ‘steps’ onto the new barbed end as it elongates, allowing processive capping (Moseley *et al.*, 2004; Shemesh *et al.*, 2005). The two barbed-end terminal subunits are related to each other around a tilted helical axis by a twist of -180° rather than -166.7° and an axial rise of 28 Å rather than 27.5 Å (Otomo *et al.*, 2005). This formin-induced twist has been implicated as a ‘gating’ mechanism used by formins to make monomer addition less favourable (Aydin *et al.*, 2018), rather than the formerly proposed ‘open’ and ‘closed’ state model where formin could permit or block monomer addition depending on adopting a literal open or closed conformation (Otomo *et al.*, 2005).

Arp2/3

The Arp2/3 complex is a multimer with 7 different globular protein sub-units. Two of these subunits (Arp2 and Arp3) have a high degree of structural similarity to actin monomers (Machesky *et al.*, 1994). In the inactive state of Arp2/3, Arp2 and Arp3 are separated by other subunits, but

upon Arp2/3 complex activation, these two subunits are brought into a conformation that mimics an actin dimer. The active conformation of Arp2/3 in complex with F-actin has recently been studied at high resolution (Shaaban *et al.*, 2020). The pseudo-dimer can contribute towards the formation of an actin nucleus, and therefore reduces the number of actin molecules required for nucleation. The Arp2/3 complex requires the assistance of other proteins termed nucleation promoting factors (NPFs) to adopt the active conformation. NPFs also have G-actin binding sites that enable them to deliver monomers to the activated Arp2/3 complex for nucleation. There are a large number of NPFs for Arp2/3, each associated with different cellular contexts.

A major class of NPFs are the WASP superfamily members, which perform their NFP role using a conserved set of C-terminal domains, together referred to as 'WCA'. This is composed of one or more G-actin binding WASP homology 2 (WH2 or W) domains, and the Arp2/3-binding central (C) and acidic (A) domains. The Central and acidic domains bind Arp2/3 and facilitate the conformational change required for its activation, while WH2 domains bind G-actin (or very weakly to the barbed end of F-actin). WH2 domains are intrinsically disordered until they come into contact with actin, at which point the N-terminal portion of the domain arranges into an amphipathic α -helix that fits into the binding groove (Renault *et al.*, 2013). The WASP superfamily encompasses five protein families, grouped according to common features and associated functions of their N-terminal domains: Wiscott Aldrich Syndrome Protein (WASP); WASP-family verprolin homologue (WAVE/Scar); WASP and Scar homologue (WASH) and junction-mediating regulatory protein (JMY); reviewed in Campellone and Welch, 2010).

In most circumstances, the Arp2/3 complex has to bind to a pre-existing actin filament (referred to as a mother filament) in order to induce the active conformation for formation of a new filament. The result is a branch junction of 70° between the mother and nascent filaments. Other ABPs can influence the stability of these F-actin branches, some (like cortactin) promoting their stability, and others (like cofilin) promoting their dissociation. Arp2/3 can remain bound to a dissociated branch as a pointed end cap. There are however some exceptions to the branching mode of Arp2/3 nucleation. The NPF Spin90 and its homologues (Dip1 in fission yeast) enable Arp2/3 to nucleate

a new actin filament without the need for a mother filament (Wagner *et al.*, 2013; Shaaban *et al.*, 2020).

Actin Nucleation by Other ABPs

The last two decades has seen the discovery of a growing number of proteins identified as having actin nucleating capabilities, although some have received more attention than others. The group receiving most interest comprises proteins with tandem WH2 domains: the *Drosophila* neural protein Spire (Quinlan *et al.*, 2005), the vertebrate neural protein Cordon-bleu (Ahuja *et al.*, 2007), and the p53 cofactor and WASP superfamily NPF JMY (Zuchero *et al.*, 2009). The proteins have three (Cobl, JMY) or four (Spire) WH2 domains in their C-terminal regions. With each adjacent WH2 domain able to bind an actin monomer, these proteins can bind multiple actin monomers simultaneously and support the formation of actin dimers, trimers and tetramers.

Several other actin binding proteins, dimers of these proteins, or fragments of these proteins, have demonstrated the ability to nucleate a pool of G-actin in buffer conditions that do not normally favour polymerisation. This list includes the globular head of heavy meromyosin (Cooke and Morales, 1971), the smooth muscle proteins caldesmon and fesselin (Gałązkiewicz *et al.*, 1985; Beall and Chalovich, 2001), a two-module fragment of the giant muscle protein nebulin (Chen *et al.*, 1993), the tropomodulin-related muscle protein Leiomodin (Chereau *et al.*, 2008), the tail region of vinculin (Wen *et al.*, 2009), the tumour suppressor protein adenomatous polyposis coli (Okada *et al.*, 2010), the polyproline region of yeast WASP Las17 (Urbanek *et al.*, 2013), and the lymphocyte transgelin TAGLN2 (Kim *et al.*, 2018). Most of these proteins have been demonstrated to abolish the lag phase of actin polymerisation in buffer conditions favourable to polymerisation, demonstrating their nucleation ability is relevant at physiological salt concentrations (Gałązkiewicz *et al.*, 1985; Chen *et al.*, 1993; Beall and Chalovich, 2001; Wen *et al.*, 2009; Haglund *et al.*, 2010; Urbanek *et al.*, 2013; Kim *et al.*, 2018).

The mechanisms of nucleation and ways of binding actin have proven to be diverse. While the aforementioned proteins may not all perform this actin nucleating role *in vivo*, the diversity of proteins with actin nucleating ability indicates that this functionality has evolved many times independently throughout evolution. This provides an indication of what actin nucleation

mechanisms may have been used by primitive cells before the evolution of complex molecular machines like formins and the Arp2/3 complex. It is also entirely possible that many of these less ubiquitously expressed ‘alternative’ actin nucleators perform this nucleating role *in vivo* to provide additional local control of highly specialised actin architectures in particular cell locations or tissues. ‘Unconventional’ actin nucleators are already known to operate effectively *in vivo* in some contexts: some parasitic bacteria are able to commandeer the actin cytoskeleton of their host for their own motility by expressing actin nucleators on their surfaces (Galkin *et al.*, 2002; Haglund *et al.*, 2010).

1.5 The Actin Cytoskeleton of *S. cerevisiae*

1.5.1 A Yeast for Bakers, Brewers and Biologists

Much of our fundamental knowledge of the actin cytoskeleton is derived from biochemical and genetic studies using the budding yeast *Saccharomyces cerevisiae*, a member of the fungus kingdom that is commonly used as a model organism across several biological fields. This yeast species has also been used for fermentation in beer production and as a leavening agent in bread for centuries, earning it the common names ‘brewer’s yeast’ and ‘baker’s yeast’. To divide, diploid ‘mother’ cells grow one or more buds into which they transport DNA, organelles and other cellular material. When the bud has everything it needs for independent survival, it is severed (Hartwell, 1974). F-actin is required for multiple aspects of this process. This yeast has proved to be a useful model organism for studying eukaryotic cellular processes, in part owing to its ease of culture and manipulation in a laboratory setting. Another key reason is the relative simplicity of this unicellular organism compared to a multicellular organism with tissue-specific expression. Owing to its simplicity and popularity as a model organism, *S. cerevisiae* was the first eukaryotic organism to have its genome sequenced (Dujon, 1996), which reinforced its usefulness to scientific research. Another key reason for the popularity of this organism is that its cellular processes have several similarities with our own, and therefore can give us insight into the underlying factors of many human diseases.

1.5.2 *S. cerevisiae* Actin Architectures and their Associated Nucleators

The spatiotemporal variation of F-actin architectures throughout the cell cycle of *S. cerevisiae* was first elegantly captured using rhodamine-phalloidin and light microscopy (Amberg, 1998). This species has only a single actin gene (*ACT1*), which encodes a single isoform. Three distinct F-actin architectures form during the life cycle of a budding yeast, each with distinct localisations and functions (Figure 1.7B). While all three actin architectures are composed from the same actin isoform, each has a characteristic profile of ABPs (reviewed in Mishra, Huang and Balasubramanian, 2014). Two of the F-actin architectures - patches and cables – can be seen forming and disassembling throughout the cell cycle, while a third architecture – a contractile ring – forms at the bud neck when the budding cell is preparing for cell division and disassembles when the bud has been severed.

These three actin architectures are associated with different nucleators. *S. cerevisiae* has three major nucleators: the two genetically redundant but functionally distinct formins Bni1 and Bnr1, and the Arp2/3 complex (Figure 1.7A). The formins and Arp2/3 compete for a limited pool of G-actin in a finely balanced equilibrium controlled by several factors.

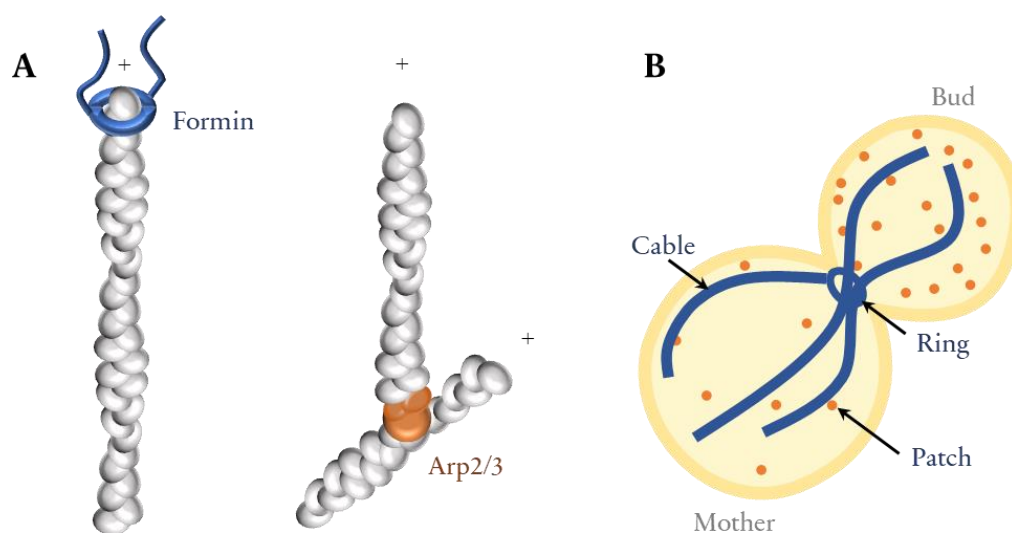


Figure 1.7: Formin- and Arp2/3-Associated Actin Architectures in *S. cerevisiae*. A) Diagram of actin filaments nucleated by a formin (left) and by Arp2/3 (right). The plus/barbed end of each filament is indicated by a '+' symbol. B) Diagram of a budding yeast cell preparing for cytokinesis. At this stage of the cell cycle, all three actin architectures co-exist in the cytoplasm: the contractile actomyosin ring at the bud neck, actin cables and endocytic actin patches, which are most concentrated in the bud. The actin architectures depicted are coloured according to their associated actin nucleator; formins (blue) or Arp2/3 (orange).

Formin-Associated Actin Architectures

Actin cables are long bundles of F-actin that serve as tracks for intracellular transport. There are two major networks of cables. These cables are found near the cell cortex and polarised along the mother-bud axis, one spanning the length of the mother cell and the other spanning the length of the bud. Each of these cable networks is nucleated by a specific actin nucleator: the formin Bnr1 remains tethered to the bud neck throughout the cell cycle where it nucleates actin filaments for the cables projecting into the mother cell, while the closely related formin Bni1 localises to the bud cortex for nucleation of cables in the bud compartment (Buttery *et al.*, 2007). In preparation for cell division, Bni1 relocates to the bud neck and both formins contribute to the actin network that forms the contractile ring that serves to constrict the bud neck in order to sever the bud from the mother cell. Cable and ring architecture has been extensively reviewed in both budding and fission yeast (Mishra *et al.*, 2014).

Arp2/3-Associated Actin Architectures

Formins are not involved in actin patch formation. Instead, the key nucleator linked to actin patches is the Arp2/3 complex. Actin patches are so called because of their punctate appearance when fluorescently labelled actin (or another patch component) is viewed in light microscopy. These are the result of dynamic bursts of localised actin polymerisation at endocytic sites, where these branched actin networks serve to facilitate membrane invagination. Cortical actin patches are a feature that appear to be unique to fungi. Most of our knowledge comes from studies in budding and fission yeast, but this punctate arrangement of actin has been observed at the endocytic sites of filamentous fungi as well as yeast (Berepiki *et al.*, 2011). Disruption of actin polymerisation by monomer sequestering or filament stabilising drugs completely impairs yeast endocytosis, demonstrating that a dynamic actin network is essential for endocytosis to occur (Ayscough, 2000). This absolute requirement for actin in yeast endocytosis has been demonstrably linked to turgor pressure, which poses resistance to membrane invagination (Aghamohammadzadeh and Ayscough, 2009). In contrast, actin polymerisation is only a requirement for invagination of mammalian cell membranes when local membrane tension is high due to osmotic swelling or mechanical stretching (Boulant *et al.*, 2011). Interestingly, plant cells – which have even higher

turgor pressure than yeast cells – have evolved an alternative strategy that does not utilise actin for endocytic invagination (Narasimhan *et al.*, 2019).

The lifetime of detectable F-actin at an endocytic patch is approximately 15-20 seconds, spanning invagination to scission; the final stages of endocytosis (Kaksonen *et al.*, 2003). Prior to the invagination event, however, several other proteins are recruited to lay the foundations for actin assembly, beginning as much as 2 minutes before actin is detected (Weinberg and Drubin, 2012). Over 60 different proteins are involved in endocytosis, localised to the endocytic site at the cell membrane in waves of recruitment. The earliest proteins to arrive are coat proteins, which arrive in stages referred to as early, mid and late (Figure 1.8). Actin-network associated proteins can first be detected around the same time as the late coat proteins are recruited. This includes the Arp2/3 NPFs – Las17, Myo3 and Myo5 - and their regulators. The majority of actin-binding proteins – including the Arp2/3 complex, the NPFs Myo3 and Myo5, the bundling proteins Sac6 and Scp1 and cofilin - are first detected along with actin itself. Finally, scission proteins (the amphiphysin family proteins Rvs161 and Rvs167) can be detected for the last ~10 seconds of endocytosis. The actin binding proteins recruited to endocytic sites prior to F-actin detection are the NPF Las17, followed by verprolin (yeast WASP Interacting Protein; WIP). For a summary of protein recruitment to endocytic patches, see Weinberg and Drubin, 2012; Goode *et al.*, 2015; Lu *et al.*, 2016.

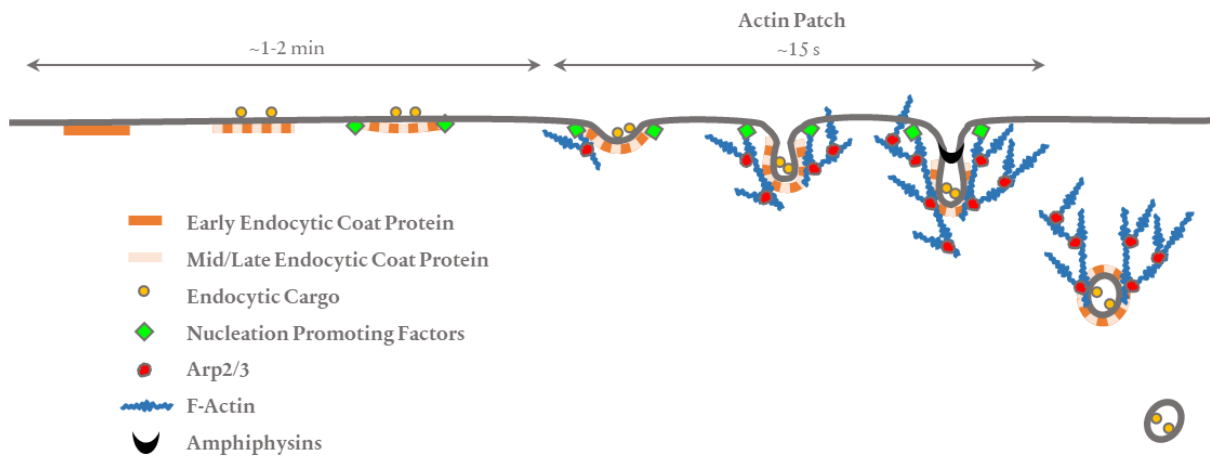


Figure 1.8: The stages of endocytosis. Coat proteins assemble at the membrane over a period of 1-2 minutes, joined in the later stages by nucleation promoting factors. A rapid burst of branched actin polymerisation is triggered by the arrival of Arp2/3. Over the next 15 seconds, the membrane invaginates until scission is induced by amphiphysins. Following scission, the actin network and vesicle coat disassemble. Bundling and severing of filaments also occurs in the actin network (not shown).

1.5.3 Arp2/3 and the Need for a Mother Filament

As mentioned in section 1.4.9, Arp2/3 nucleates actin by binding a pre-existing ('mother') filament and seeding a new filament as a branch off that mother filament. There is therefore a need for actin filaments to be present at the endocytic site prior to nucleation by Arp2/3. Unlike mammalian cells, *S. cerevisiae* does not possess a cortical actin network that could provide mother filaments to act as substrates for Arp2/3, nor does it express a known homologue to the NPF Dip-1/Spin-90 that enables Arp2/3 to nucleate linear actin filaments *de novo*. This begs the question: where do the mother filaments come from for endocytosis in *S. cerevisiae*? It has been proposed that short, capped filaments severed by cofilin from actin patches may diffuse through the cell cortex to new endocytic sites (Chen and Pollard, 2013). However, it could be argued that this passive mechanism of mother filament 'capture' at endocytic sites doesn't fit well with the fast turnover of actin patches, or the tightly regulated nature of the actin cytoskeleton. Another possible solution is the presence of another patch-associated nucleator that could nucleate actin filaments *de novo*. Even with very low *de novo* actin nucleation activity, only a very small number of actin filaments would be required as an initial substrate for Arp2/3 nucleation because Arp2/3 itself would rapidly amplify the number of mother filaments available.

1.5.4 WCA-Independent Functions of Las17

Since Las17 arrives ~20s earlier than Arp2/3 at endocytic sites (Kaksonen *et al.*, 2003; Sun *et al.*, 2006; Picco *et al.*, 2015) and has been demonstrated to nucleate actin *in vitro* (Urbanek *et al.*, 2013; section 1.4.9), this patch protein is a clear candidate for an *in vivo* nucleator of mother filaments.

Las17 is the most potent NPF for Arp2/3 at cortical actin patches, a function mediated by its WCA domain. However, yeast expressing only a truncated version of the protein missing the acidic domain (or even the entire WCA region) present only a mild phenotype and have apparently normal actin patch organisation, owing to functional redundancy with the other patch NPFs; Myo3 and Myo5 (Sun *et al.*, 2006; Galletta *et al.*, 2008). It is therefore surprising that, in contrast to the mild phenotype of the WCA-deleted Las17 truncation, Las17 null cells exhibit a severely altered actin filament organisation. Here, cortical actin patches are completely abolished, large clusters of aberrant F-actin can be seen in the cytosol, secretory vesicles accumulate and bud growth is slowed or defective (Li, 1997; Allwood *et al.*, 2016). Taken together with the mild phenotype of removing just the WCA region, this indicates regions within the portion of Las17 spanning from the N-terminus up to the WH2 domain have roles of great importance to the regulation of the actin cytoskeleton, particularly within the bud. A small number of actin patches can still be seen in the mother cell of Las17 knock-out yeast, but not the bud, where full-length Las17 is essential for local patch formation. Additional evidence of the importance of Las17 beyond its WCA region is that full length Las17 is a more potent activator of Arp2/3 than WCA alone (Rodal *et al.*, 2003).

Two pairs of arginine residues within the polyproline region of Las17 (Las17PP) have been identified as having great importance for G-actin binding (Feliciano *et al.*, 2015). As well as severely compromising the ability of Las17PP to bind actin, mutagenesis of these residues renders Las17 unable to nucleate actin *de novo* (Allwood *et al.*, 2016). Polyproline tracts within Las17PP have also been demonstrated to have functional importance, but for actin elongation rather than actin nucleation (Urbanek *et al.*, 2013; Allwood *et al.*, 2016). A model has been proposed whereby the adjacent arginine pairs bind actin monomers simultaneously to promote actin nucleation, and the polyproline tracts bind the nascent filament, enhancing their stability and retaining them at the

endocytic site (Allwood *et al.*, 2016). One aim of this project is to further investigate the interaction of Las17PP with actin, which is the topic of Chapter 6.

1.6 Exploring the Influence of Actin Nucleators on Actin Filament Function

1.6.1 Nucleators Can Dictate which Actin Architectures Assemble

As indicated in section 1.5.2, actin architectures are associated with particular nucleators. A striking example of the ability of actin nucleators to specialise in particular actin architectures comes from a study performed in the fission yeast *Schizosaccharomyces pombe*, which expresses two formins: For3 and Cdc12. These formins localise to distinct locations within the cell: For3 to the growing cell poles during interphase, where it nucleates F-actin for dynamic bundles that project into the cytoplasm, and Cdc12 to the cell division plane during cytokinesis, where it nucleates F-actin for a contractile cytokinetic actomyosin ring.

The actin architectures generated locally by each of the formins were known to have distinctly modified tropomyosin variants associated with them. This yeast expresses only a single tropomyosin (Cdc8), but it has an acetylated and unacetylated form. The N-terminally acetylated tropomyosin (Tpm_{ace}) binds F-actin much more tightly than the unacetylated version (Tpm_{un}) and consequently has more influence on the stability and myosin recruitment of actin filament. Tpm_{ace} localises to the cytokinetic actomyosin ring nucleated by Cdc12, and the Tpm_{un} localises to the cytoplasmic bundles nucleated by For3 at the growing cell poles. Remarkably, when Cdc12 (the ring-associated formin) was re-localised to the cell poles (in a For3 knock-out strain), the actin filaments nucleated resembled interphase cables (normally nucleated by For3), but they were decorated by the acetylated formin normally only seen on filaments of the cytokinetic ring (Johnson *et al.*, 2014). Other properties of these filaments - faster actin polymerisation rate, recruitment of ring-specific proteins - were also more characteristic of the cytokinetic ring.

The reverse localisation experiment was equally compelling: when For3 was localised to the cytokinetic ring in a Cdc12-disrupted strain, an F-actin ring was able to form with normal contraction kinetics, but its structural integrity was severely compromised, resulting in a high occurrence of ring collapse and unsuccessful cytokinesis. This study conclusively demonstrates that the formins dictate which variant of tropomyosin associates with the filaments they nucleate. The exact mechanism for this is not yet understood, but it is possible that For3 and Cdc12 generate conformationally distinct actin filaments (i.e. affecting more than just the terminal subunits, as described above), the structure of which can be sensed by tropomyosin isoforms.

In another demonstration of nucleating factors dictating the ABP population of an actin network, incubation of full-length Las17 immobilised on beads in a *S. cerevisiae* cytoplasmic extract resulted in bead-associated dendritic actin networks that were found to have the ABP composition of actin patches (Michelot *et al.*, 2010). Incredibly, the bead-linked actin networks did not associate with other ABPs such as formins or tropomyosins that are associated with distinct *S. cerevisiae* actin architectures (actin cables and a cytokinetic ring). This indicates a high degree of selectivity of the filaments nucleated at the bead surface for patch-associated F-actin binding partners. Therefore, it appears that Arp2/3 – and, given its known *in vitro* actin nucleating ability potentially La17 – nucleates actin filaments that are disfavoured by ABPs associated with formin-nucleated actin architectures.

1.6.2 Do Nucleators Influence the Conformation of F-actin?

Following these observations in budding and fission yeast that distinct actin networks are associated with particular nucleators, it has been proposed that nucleators might be leaving a molecular ‘fingerprint’ of the origin of a filament (Michelot *et al.*, 2010; Johnson *et al.*, 2014). It has further been proposed that this fingerprint takes the form of structurally distinct conformations of F-actin (Johnson *et al.*, 2014). Such a conformational fingerprint would be able to alter the affinity of the filament to several ABPs, favouring those that are associated with the actin architecture associated with that particular actin nucleator. The influence of actin nucleators on actin filament structure is particularly interesting because it represents the very earliest opportunity to assign an

actin filament to a particular actin architecture. Subsequent selective recruitment of ABPs may then serve to reinforce and amplify this initial fingerprint.

While formins are known to influence the conformation of the barbed end terminal protomers (section 1.4.9), their effect on the rest of the filament structure is unknown, as is the structural effect of most other known nucleators. As listed in section 1.4.9, one of the other proteins found capable of *de novo* actin nucleation *in vitro* is the tail region of vinculin (VT). Incubating G-actin with VT induces the formation of actin bundles, seemingly bypassing the nucleation of individual filaments, even at relatively low VT concentrations. There is also evidence to suggest that actin filaments saturated with VT have altered geometry, as assayed by altered emission profiles from overlapping fluorescence dyes conjugated to F-actin (Wen *et al.*, 2009). Though this has not yet been confirmed by structural analysis, this appears to be an example of an ABP nucleating actin in a way that directly modifies F-actin structure.

1.7 Aims of the Project

We aimed to test the hypothesis that actin nucleators exert a conformational fingerprint on F-actin, using the actin-nucleating polyproline region of *S. cerevisiae* N-WASP homologue Las17, and summary of our structural findings is presented at the start of Chapter 6. Through working with Las17, we also aimed to build on previous work by the Ayscough lab in which its actin nucleation capability was identified and further characterised (Urbanek *et al.*, 2013; Allwood *et al.*, 2016; Tyler *et al.*, 2016). Further biochemical characterisation of the interaction between Las17PP and actin *in vitro* is the topic of Chapter 6.

We decided to use purified actin from *S. cerevisiae* for our work since this the physiologically relevant actin isoform for Las17. Use of the yeast actin isoform for a high-resolution structural study introduced another novel aspect to our research, since no fungal actin filaments have previously been solved to relatively high resolution: the amalgamation of structural research on F-actin to date is overwhelmingly skewed towards a vertebrate actin isoform that is exclusively expressed in skeletal muscle actin for its highly specialised role in sarcomeres. An additional aim of this project was

therefore to solve and characterise the structure of yeast F-actin to high resolution, with reference to the canonical skeletal muscle actin structure. This is the topic of Chapters 4 and 5, and the purification of yeast actin is the topic of Chapter 3. For this project, we were able to take advantage of the recent increase in accessibility of studying F-actin structure using cryo-EM owing to the timely purchase of a cryo-EM microscope fitted with a direct electron detector.

Aims of the Project

- Purify yeast actin for structural work and biochemical assays.
- Further characterise the interaction between Las17PP and actin *in vitro*.
- Test, for the actin nucleating fragment of Las17, the hypothesis that actin nucleators can directly influence F-actin conformation.
- Investigate yeast F-actin structure at high resolution.

2. Materials & Methods

2.1 Materials

2.1.1 Solution and Buffer Recipes

Standard lab chemicals were purchased largely from Sigma Aldrich, Thermo Fisher Scientific and AnalaR NORMAPUR. It is noted below which stocks were made at 10x concentrations. These 10x stocks also included 1.5 mM NaN₃ added to the stock solution if it was to be stored for more than a week. All of the following recipes, listed alphabetically, describe the working (1x) concentration and are dissolved in water.

*pH was adjusted with HCl

†pH was adjusted with NaOH

Binding buffer

For purification of His-tagged actin from Pichia pastoris.

10 mM imidazole (pH 7.4*), 10 mM HEPES (pH 7.4+), 300 mM NaCl, 2 mM MgCl₂, 3.5 mM β-ME, 1 mM ATP (pH 7+), 1 mM PMSF.

ATP and PMSF were added on the day of use.

Blocking buffer

For antibody staining.

5% milk in TBST. Stored refrigerated.

Cleavage buffer (high salt)

For GST-tag removal by PreScission protease.

50 mM Tris pH 7, 300 mM NaCl, 1 mM EDTA, 1 mM DTT.

DTT was added on the day of use.

Cleavage buffer (low salt)

For GST-tag removal by PreScission protease.

50 mM Tris pH 7, 150 mM NaCl, 1 mM EDTA, 1 mM DTT.

DTT was added fresh on the day of use.

Coomassie stain

For staining SDS-PAGE gels.

40% methanol, 10% acetic acid, 80 mg/L Coomassie Blue R-250.

Coomassie destain

For destaining SDS-PAGE gels.

40% methanol, 10% acetic acid.

Coupling buffer

For coupling of DNase I to Affi-Gel.

100 mM HEPES (pH7.2+), 80 mM CaCl₂, 1 mM PMSF.

PMSF was added on the day of use.

G-buffer

For G-actin storage. (1x shown here, but made as a 10x stock)

10 mM Tris (pH 7.5*), 0.2 mM CaCl₂, 0.2 mM ATP (pH 7+), 0.5 mM DTT.

ATP and DTT were added on the day of use.

Gold-labelling buffer

For labelling His-Las17 with Nanogold.

150 mM NaCl, 20mM Tris (pH7.6*).

KME *(1x shown here, but made as a 10x stock)*

For inducing actin polymerisation.

50 mM KCl, 1 mM MgCl₂, 1 mM EGTA, 10 mM Tris (pH 8.0*).

Laemmli sample buffer (2x)

For loading samples for SDS-PAGE.

4% SDS, 10% β-ME, 20% glycerol, 0.1 M Tris (pH 6.8*).

A small amount of bromphenol blue solid was used to obtain a bright blue colour.

PBS

Phosphate buffered saline. (1x shown here, but made as a 10x stock)

137 mM NaCl, 2.7 mM KCl, 8 mM Na₂HPO₄, and 2 mM NaH₂PO₄.

With these relative quantities of monobasic and dibasic sodium phosphate, the pH of the 1x solution is pH 7.4.

Resuspension Buffer

For purification of GST-tagged Las17 fragments.

PBS, 300 mM NaCl, 1 mM MgCl₂, 1 mM MnCl₂.

SDS-PAGE Running Buffer

For resolving proteins by electrophoresis. (1x shown here, but made as a 10x stock)

250 mM Glycine, 0.1% SDS, 25 mM Tris (pH 8.6*).

Start buffer

For purification of His-tagged Las17 from E. coli.

20 mM Na₂HPO₄, 500 mM NaCl, 20 mM imidazole (pH 7.4*).

TAE

Tris-acetate-EDTA buffer

20mM AcOH, 1mM EDTA, 40mM Tris (pH 8.3*).

TBST

Tris-buffered saline with 0.1% Tween.

150 mM NaCl, 0.1% Tween, 20 mM Tris (pH 7.5*).

Transfer Buffer

For Western blotting.

19.2 mM glycine, 20% methanol, 2.5 mM Tris (pH 8.3*).

2.1.2 Culture Media Recipes

All media was sterilised by autoclaving prior to use (121°C, ≥15 psi). For solid media, 2% agar was also included.

MGY

Minimal glycerol medium.

1.34% YNB, 1% glycerol and 0.00004% biotin.

MM

Minimal methanol medium.

1.34% YNB, 0.00004% biotin, 0.5% methanol.

YPD

Yeast extract peptone dextrose medium.

1% yeast extract, 2% peptone, 2% glucose.

For **YPDS**, include 1 M sorbitol.

2xYT

Yeast extract tryptone (2x concentration).

10 mg/mL yeast extract, 16 mg/mL tryptone, 5 mg/mL NaCl.

2.1.3 Software

Table 2.1: Key software used for the methods described in this chapter.

Software			
Name	Appears in text as...	Source/Developer(s)	Reference
Amira	Amira	Thermo Scientific™	-
A plasmid Editor (ApE, v2.0.55)	ApE	M. Wayne Davis	-
AutoCTF	-	FEI, Thermo Fisher Scientific	-
CisTEM	CisTEM	Grigorieff Lab, University of Massachusetts Medical School	(Grant <i>et al.</i> , 2018)
EMAN2	EMAN2	Ludtke Lab National Center for Macromolecular Imaging, Baylor College of Medicine, Houston	(Tang <i>et al.</i> , 2007)
EPU 2	EPU	FEI, Thermo Fisher Scientific	-
FIJI	FIJI	Open source	-
Gctf	Gctf	Kai Zhang, MRC Laboratory of Molecular Biology, Cambridge	(Zhang, 2016)
Gwyddion	Gwyddion	David Nečas and Petr Klapetek, Department of Nanometrology, Czech Metrology Institute	(Nečas and Klapetek, 2012)
Image Lab 3.0	Image Lab	Bio-Rad	-
IMOD / eTomo	IMOD	David Mastronarde, Rick Gaudette, Sue Held, Jim Kremer, Quanren Xiong, Suraj Khochare, and John Heumann, University of Colorado	(Ahmed <i>et al.</i> , 2013; Mastronarde and Held, 2017)
ISOLDE	ISOLDE	Tristan Croll, Cambridge Institute for Medical Research, University of Cambridge	(Croll, 2018)
MotionCor2	MotionCor2	University of California, San Francisco (UCSF) Resource for Biocomputing Visualization, and Informatics	(Zheng <i>et al.</i> , 2017)
Python-based Hierarchical ENvironment for Integrated Xtallography (Phenix)	Phenix	Paul Adams group (Berkeley Lab), Randy Read group (University of Cambridge), Jane & Dave Richardson group (Duke University), Tom Terwilliger group (Los Alamos National Laboratory). Funded by NIH General Medical Sciences	(Afonine <i>et al.</i> , 2018)
REgularized LIkelihood Optimization (v 3.0 and 3.1)	RELION	Scheres Lab, MRC Laboratory of Molecular Biology, Cambridge	(Scheres, 2012; He and Scheres, 2017)
TIA (Tecnai Imaging & Analysis)	-	FEI, Thermo Fisher Scientific	-
Tomography 4.0	TEM Tomography	FEI, Thermo Fisher Scientific	-
UCSF Chimera	Chimera	University of California, San Francisco (UCSF) Resource for Biocomputing Visualization, and Informatics	(Pettersen <i>et al.</i> , 2004)
UCSF ChimeraX	ChimeraX	University of California, San Francisco (UCSF) Resource for Biocomputing Visualization, and Informatics	(Goddard <i>et al.</i> , 2018; Pettersen <i>et al.</i> , 2021)
Warp	Warp	Cramer Lab, Max Planck Institute of Molecular Physiology, Dortmund	(Tegunov and Cramer, 2019)

2.2 Molecular Biology Methods

2.2.1 DNA Sequencing and Primer Synthesis Services

DNA sequencing was performed by the Medical Research Council Protein Phosphorylation and Ubiquitylation Unit DNA Sequencing and Services, University of Dundee. For some of the work focussed on mutagenesis of pPICZc-*ScAct1-thyβ4-8His*, this service was additionally used for the generation of custom primers used for sequencing. All other primers were ordered through Eurofins Genomics.

2.2.2 Plasmids used in this Study

Glutathione S-transferase (GST)-Las17PP fragments used were from the Ayscough lab plasmid (pKA) collection (Table 2.2). His-tagged Las17 plasmids were made by cloning fragments of Las17 sequence from pKA606 into pKA850, a vector containing a 6xHis-tag. This is described in section 2.2.4. The pPICZc-*ScAct1-thyβ4-8His* plasmid was obtained directly from Mohan Balasubramanian (University of Warwick), but it is also available on AddGene (cat. number #111148, Hatano et al., 2018). The coding sequence (optimised for expression in *Pichia pastoris*) consists, from 5' to 3', of *S. cerevisiae ACT1*, a linker sequence of 14 amino acids, *Homo sapiens thyβ4*, and a His-tag composed of eight consecutive histidine residues. Mutagenised versions of pPICZc-*ScAct1-thyβ4-8His* were generated using site-directed mutagenesis (section 2.2.7).

Table 2.2: Plasmids used in this research.

pKA	Protein Product	Vector	Selection Agent	Origin/Reference
606	Las17-His	pRS313	100 µg/mL Ampicillin	RC
566	GST-Las17(300-422)	pGEX6P-1	100 µg/mL Ampicillin	RC
670	GST-Las17(300-536)	pGEX6P-1	100 µg/mL Ampicillin	RC
671	GST-Las17(300-633)	pGEX6P-1	100 µg/mL Ampicillin	JT
850	His-Vps1	pCRT7_Nt_TOPO	100 µg/mL Ampicillin	IS
1280	His-Las17(300-422)	pCRT7_Nt_TOPO	100 µg/mL Ampicillin	SRG
1281	His-Las17(300-536)	pCRT7_Nt_TOPO	100 µg/mL Ampicillin	SRG
1282	His-Las17(300-633)	pCRT7_Nt_TOPO	100 µg/mL Ampicillin	SRG
1289	ScAct1-Thyβ4-His	pPICZc	100 µg/mL Zeocin	Hatano <i>et al.</i> , 2018
1311	ScAct1(A204E, P243K)-Thyβ4-His	pPICZc	100 µg/mL Zeocin	SRG
1312	ScAct1(K291E, P322K)-Thyβ4-His	pPICZc	100 µg/mL Zeocin	SRG

2.2.3 Plasmid Purification

Methods for bacterial transformation and culture are described in section 2.3. For plasmid purification from transformed DH5- α or TOP10 cells, 5 mL overnight culture was harvested by centrifugation and plasmid DNA was purified using the commercially available QIAprep Spin Miniprep Kit (Qiagen #27104). Briefly, the cell pellet was subjected to alkaline lysis in the presence of RNase A, after which the pH was neutralised to allow re-annealing of plasmid DNA. Cell debris was removed by centrifugation and plasmid DNA in the supernatant was extracted by its affinity to silica resin, washed, and then eluted in water or in the elution buffer provided in the kit (10 mM Tris-Cl, pH 8.5). The double-stranded DNA concentration was measured using a NanoDrop (Thermo Scientific™). To isolate plasmid DNA from mixtures containing protein (e.g. after PmeI restriction digest,) a PCR Purification Kit was used (Qiagen #28104), splitting the mixture over multiple columns if the predicted plasmid concentration exceeded the column capacity.

2.2.4 Primer Design for Making His-tagged Las17

Primers (Table 2.3) were designed to have complementarity sequences to the Las17 sequence at their 3' end and to the digested new host vector at their 5' end (Figure 2.1). One forward primer

was suitable for all three fragment lengths since all three started at the 300th codon in the Las17 sequence. Different reverse fragments were used to generate the three different fragment lengths (codons 300-422, 300-536 and 300-633). The stop codon for full-length Las17 is located immediately after amino acid 633, so the reverse stop codon (TTA) was included in the primer designed for the 300-633 fragment. For the shorter fragments (300-422 and 300-536), a reverse stop codon was incorporated into the primer design (Table 2.3). In order to increase the melting point (T_m) of these primers, additional cytosine and guanine residues were incorporated at the 5' end. An additional base was incorporated between the BamHI site and the Las17 sequence in OKA1502 to prevent a frameshift.

Table 2.3: Primers for generating Las17 fragment inserts. pKA606 (see Table 2.2) was used as the template for the Las17 DNA sequence. Primers were designed for annealing with a vector (pKA850) that had been digested by BamHI and HindIII. Sequences are annotated as follows: uppercase = complementary to the Las17 sequence, red = stop codon, green = HindIII recognition site, blue = BamHI recognition site.

OKA No.	Primer Name	Sequence (5'-3')	Length (b)	%GC	T_m
1502	Las17300 BamHI Fwd	cgcggatccaCAAGCTCCTTCAATGGGCATACCAC	35	57.1	74.2
1504	Las17422 HindIII Rev	ccc <aagctt< a="">tttagCTATTTGTCTGATATCCAAGGGGCGG</aagctt<>	40	42.9	71.4
1505	Las17536 HindIII Rev	ccc <aagctt< a="">ttagCCTCCGGATGTTGATGTAGCTGG</aagctt<>	36	47.5	72.5
1503	Las17633 HindIII Rev	ccc <aagctt< a="">TTACCAATCATCACCATTTGTCCATATCGTCATG</aagctt<>	42	52.8	72.9



Figure 2.1: Illustration of where primers anneal to the full length Las17 sequence and the generated inserts. The PCR products for each primer combination are shown below. Arrows indicate the 5'-3' direction of the primer. The 5' end of each primer is not complementary to Las17, as indicated by a slight curve in the shape at this end of the primer. Colour coding is the same as in Table 2.3.

2.2.5 Cloning Las17 Fragment Sequences into a New Vector

The following procedure was used to generate three new plasmids: His-Las17(aa300-422), His-Las17(aa300-536) and His-Las17(aa300-633). These plasmids were allocated the identifiers pKA1280, pKA1281, and pKA1282, respectively, in the KA lab plasmid collection (Table 2.2). For each new plasmid, the Las17 fragment of interest amplified by PCR (from pKA606), using primers designed to anneal to a BamHI cut site upstream, and to a HindIII cut site downstream of the Las17 fragment sequence. The pCRT7_Nt_TOPO vector, which includes an upstream 6xHis tag, was liberated from a His-Vps1 plasmid in the collection (pKA850) by restriction digest with BamHI and HindIII in CutSmart buffer (New England BioLabs #B7204S), then the Las17 fragment was introduced along with ligase enzyme. A graphic summary of the procedure is shown in Figure 2.2. To validate successful cloning, newly cloned plasmids were transformed into DH5 α and plated out on 2xYT agar containing 100 μ g/mL ampicillin. Transformants were allowed to grow overnight at 37°C, then 4 colonies per plasmid were picked, then plasmid was purified using a Miniprep kit. Purified plasmids were sent off for sequencing and the results were analysed using the software ApE for sequence validation.

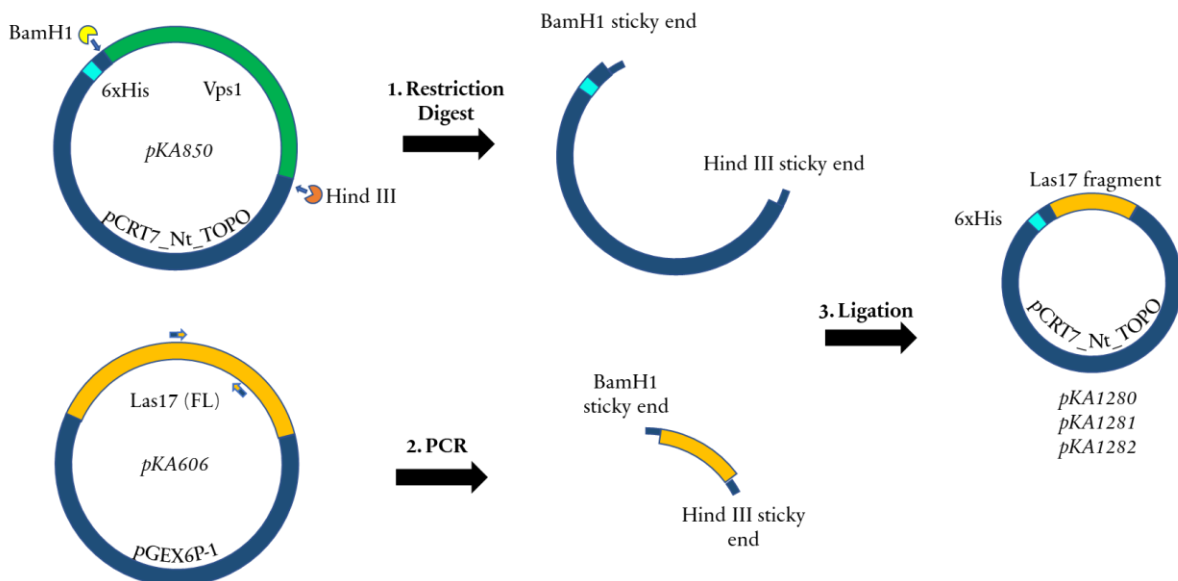


Figure 2.2: Schematic of the steps followed to generate plasmids encoding His-tagged Las17 protein fragments.

2.2.6 Primer Design for Site-Directed Mutagenesis of pPICZc-ScAct1-thyβ4-8His

Primers were designed to conform with the following criteria: forward (fwd) and reverse (rev) primers must both contain the desired mutation, which should be in the middle of the primer with ~10-15 bases either side; 25-45 bases in length; melting temperature (T_m) $\geq 78^\circ\text{C}$; guanine and cytosine content (%GC) $\geq 40\%$; last base in the sequence is a C or G. The chosen primers are shown in Table 2.4.

To account for the effect on the mismatch between primer and template on the melting temperature, T_m was calculated using the following equation, where %mistake = % of bases that differ from the template sequence, and n = primer length:

$$T_m = 81.5 + 0.41(\%GC) - (675/n) - \%mistake$$

Table 2.4: Mutagenic primers used for site-directed mutagenesis and sequencing of pPICZc-ScAct1-thyβ4-8His. The codons targeted for mutagenesis are underlined, with base substitutions indicated by bold text.

Actin I (Pointed-end mutant)

SDM Round	OKA No.	Primer Name	Sequence (5'-3')	Length (b)	%GC	T_m
1	1635	A204E fwd	CTCCTTCTCCACTACT <u>GAG</u> GAAAGAGAGATCGTCAG	36	50	78
	1636	A204E rev	CTGACGATCTCTCTTTCTCAGTAGTGGAGAAGGAG			
2	1637	P243K fwd	CCATTGAAAAGTCTTACGAATTG AAG GACGGTCAGGTCATCACTATTGG	49	43	79
	1638	P243K rev	CCAATAGTGATGACCTGACCGTC CTT CAATTTCGTAAGACTTTTCAATGG			

Actin II (Barbed-end mutant)

SDM Round	OKA No.	Primer Name	Sequence (5'-3')	Length (b)	%GC	T_m
1	1639	K291E fwd	GACGTGGACGTCAGAG GA AGAGCTGTACGGTAACATC	36	53	79
	1640	K291E rev	GATGTTACCGTACAGCTCT TC TCTGACGTCCACGTC			
2	1641	P322K fwd	GAGATCACTGCTTTGGCT AA ATCCTCCATGAAGGTCAAG	36	46	78
	1642	P322K rev	CTTGACCTTCATGGAGGAT TT AGCCAAAGCAGTGATCTC			

2.2.7 Site-Directed Mutagenesis of pPICZc-*ScAct1-thyβ4-8His*

Residues impairing actin filament polymerisation by mutations in either the barbed- or pointed-end of actin were identified from the literature (Chen *et al.*, 2013). To generate each polymerisation-impaired mutant, the pPICZc-*ScAct1-thyβ4-8His* plasmid was subjected to two successive rounds of site-directed mutagenesis using the QuikChange Lightning Site-Directed Mutagenesis Kit (Agilent Technologies #210518). Briefly, thermal cycling was used to denature the template DNA, allow mutagenic primer annealing, and primer extension by a high-fidelity DNA polymerase. The template DNA was then digested using the enzyme DpnI, which selectively targets methylated and hemimethylated DNA. Finally, the mutagenised plasmid was transformed into competent *E. coli* cells for nick repair and amplification. Each polymerisation-impaired actin mutant plasmid was generated by two successive rounds of SDM. To generate the pointed-end mutant plasmid (pKA1311), the *ScACT1* sequence was first targeted for the A204E mutation (using primers OKA1635 and OKA1636), then successfully mutated plasmid was additionally targeted for the P243K mutation (using primers OKA1637 and 1638). To generate the barbed-end mutant plasmid (pKA1312), the *ScACT1* sequence was first targeted for the K291E mutation (using primers OKA1639 and 1640), then successfully mutated plasmid was additionally targeted for the P322K mutation (using primers OKA1641 and 1642).

2.2.8 Linearised Plasmids for Transformation into *P. pastoris*

pKA1311 and pKA1312 were each linearised using PmeI in CutSmart buffer (New England BioLabs #R0560S and #B7204S, respectively) for 1 hr at 37°C. A small sample of each agarose gel was run to ensure that no uncut plasmid DNA remained before PmeI was heat-inactivated at 65°C for 20 mins. Linearised DNA was extracted using a PCR Purification Kit. Next, ethanol precipitation was performed to remove all salt from the DNA and this step could simultaneously be used to concentrate DNA if necessary. The purified DNA was precipitated by the addition of 0.1 volumes of 3 M NaOAc and 3 volumes ice-cold 100% EtOH followed by incubation for 1 hr at -80°C. Precipitated DNA was pelleted by centrifugation (30 mins, 18,000 x g, 4°C) and the pellet was washed in ice-cold 70% EtOH (10 mins, 18,000 x g, 4°C). Pellets were air-dried and resuspended

in 5-10 μL dH_2O ready for transformation into *P. pastoris*. It was important to elute into dH_2O rather than into another elution buffer because the DNA must be completely free of salts for electroporation.

2.2.9 DNA Electrophoresis

Agarose solid was dissolved in warmed TAE buffer to make a 1% agarose gel stock to be melted for each use. For each gel, 40 mL melted agarose gel was cooled to below 50°C before the addition of 1-3 μL 10 mg/mL EtBr. The mixture was poured into a cast with an appropriately sized comb inserted and allowed to set. Once set, the gel was submerged in TAE buffer. DNA samples were mixed with DNA loading buffer in a 1:3 ratio before being loaded into wells using a gel-loading tip. A DNA hyperladder covering a suitable kb range was loaded for reference. To run the gel, 100 V was applied, and the position of the dye front was used to determine when to stop the run. Gels were imaged using a UV transilluminator or a Gel Documentation System (Bio-Rad).

2.3 Microbiology Methods

2.3.1 *E. coli* Strains

For plasmid amplification, plasmids were generally transformed into chemically competent DH5- α cells, with the following exceptions: XL10-Gold Ultracompetent Cells from the QuikChange Lightning SDM Kit were used for plasmid amplification immediately following site-directed mutagenesis, and TOP10 cells were sometimes used instead of DH5- α for some of the *Pichia* plasmid work. For protein expression, plasmids were transformed into chemically competent BL21 or Rosetta™ 2 cells (Novagen™ #71400).

2.3.2 *E. coli* Liquid Media and Culture

For a small volume of culture, a 30 mL universal container was filled with 5-10 mL sterile 2xYT with an appropriate antibiotic and inoculated with a single colony from solid media or a swab from a glycerol stock. For a large volume of culture, conical flasks were filled with 2xYT liquid media to no more than 50% capacity and autoclaved with a foam bung and foil cap protecting the flask opening. The appropriate antibiotic was added on the day of use from a frozen 1000x stock. Freshly transformed cells on agar plates were harvested using a cell scraper and resuspended in the liquid media. Cells were grown at 37°C with shaking at a speed of 180 rpm.

2.3.3 Generation of Competent *E. coli*

Initially, chemically competent strains were purchased commercially. To replenish DH5- α , BL21 and Rosetta competent cell stocks in-house, a 100 mL culture was grown up in 2xYT liquid media to $OD_{600} = 0.4-0.6$. Cells were harvested by gentle centrifugation (3000 x g, 10 min, 4°C). The cell pellet was resuspended in 10 mL ice-cold 100 mM $CaCl_2$ and incubated on ice for at least 10 mins. Cells were pelleted as above and resuspended in 2 mL ice-cold 70 mM $CaCl_2$ with 15% glycerol. The cell suspensions were dispensed into 100 μ L aliquots and immediately flash frozen in LN_2 . Competent cells were stored at -80°C until immediately before use.

2.3.4 Transformation of *E. coli*

1 μ L plasmid DNA was incubated with 25 μ L freshly thawed competent cells for 30 mins on ice. Cells were heat-shocked at 42°C for 40 seconds and then placed immediately back on ice for 2 mins. Cells were resuspended in 2xYT liquid media and allowed to recover at 37°C with shaking for approximately 1 hr before plating out on solid 2xYT containing the appropriate antibiotic for resistance, and additionally 25 μ g/mL chloramphenicol if Rosetta cells were used to maintain the plasmid encoding rare tRNAs.

2.3.5 Culture and Induction of BL21 and Rosetta 2 Strains

Cells were cultured in 2xYT as described above to $OD_{600} = 0.6-0.8$. Protein expression was then induced by the addition of IPTG to 1 mM, and cells were cultured overnight with shaking at 37°C or 17°C. Cells were harvested the next morning by centrifugation at 5,000 x g for 10 mins. Pellets were either used for protein purification immediately or stored at -20°C.

2.3.6 Making *E. coli* Glycerol Stocks

A single colony of transformed cells was picked and grown up overnight in a small volume of liquid media. 800 μ L overnight culture was mixed with 800 μ L sterile 25% glycerol in a cryovial and stored at -80°C.

2.3.7 *P. pastoris* Strains

An X-33 *P. pastoris* strain stably transformed with *ScACT1* (Hatano *et al.*, 2018), was obtained from Mohan Balasubramanian (University of Warwick). *Pichia* colonies have the appearance of smooth white glossy domes when grown on YPD agar plates.

Table 2.5: Yeast glycerol stocks used in this work.

KAY number	Parent Strain	Stable Insert	Source
1945	Pichia X-33	N/A	Thermo Scientific™ (#C18000)
1946	Pichia X-33	<i>ScAct1-thyβ4-8His</i>	(Hatano <i>et al.</i> , 2018)

2.3.8 *P. pastoris* Culture

Pichia strains were revived from glycerol stocks by streaking out a swab of frozen cells onto YPD agar plates and incubating the inverted plates at 30°C for 2-3 days. For culture in liquid broth, a swab of cells was inoculated into YPD or MGY in a conical flask (filled to no more than 50% of its volume capacity) and incubated at 30°C with shaking at a speed of 220 rpm. For most of the *Pichia* work performed for this thesis, guidance was taken from the EasySelect™ *Pichia* Expression Kit Instruction Manual (Invitrogen).

2.3.9 Induction of *P. pastoris* for Recombinant Actin Expression

To initiate liquid culture, a scraping of cells from YPD agar was inoculated into 50 mL MGY and cultured overnight (section 2.3.8). Next morning, a small volume of the overnight culture was used to inoculate 200 mL MGY to an OD₆₀₀ of 0.2, which was then cultured for a further 4-6 hrs. Next, the MGY culture was scaled up once more, this time split over two 2 L flasks each containing 1 L MGY with starting OD₆₀₀ of 0.02. The final MGY culture was grown overnight and monitored until it reached OD₆₀₀ = 1.2 - 1.5 the next day. Cells were then pelleted by centrifugation at 6000 x g at 25°C for 10 min. The pellet was washed once by resuspending in sterilized water before re-pelleting and re-suspending into a volume of MM that could be split evenly between four 2 L baffled flasks (500 mL per flask). The content of each flask was topped up with MM to 500 mL and cells were then cultured for 1.5 - 2 days. 0.5 % methanol was added after the first 24 hrs. Cells were pelleted as above, yielding approximately 10 g pelleted cells per 1 L liquid culture. The pellets were pooled (~20 g total) and resuspended in ~15 mL dH₂O. The concentrated cell suspension was pipetted drop-wise into liquid nitrogen to form frozen beads.

2.3.10 Transformation of *P. pastoris*

Electroporation was performed by another member of the KA lab (EGA), following guidance from the EasySelect™ *Pichia* Expression Kit Instruction Manual (Invitrogen). First, electrocompetent cells were generated. For this, X-33 cells (Invitrogen™) were streaked out on YPDS solid medium

and then cultured in increasing volumes of YPD liquid medium until a 500 mL culture with OD₆₀₀ 1.3-1.5 was obtained. Cells were pelleted and resuspended in successive steps with the following solutions: 1) 500 mL ice-cold, sterile water, 2) 250 mL ice-cold, sterile water, 3) 20 mL ice-cold 1 M sorbitol, 4) 1 mL ice-cold 1 M sorbitol. For each transformation, 80 µL of the electrocompetent cell suspension was transferred to a 0.2 cm electroporation cuvette, mixed with 5-20 µg linearised plasmid (section 2.2.8) and then incubated for 5 mins on ice. The electroporation device used was a GenePulser (Bio-Rad) with the following settings: charging voltage 1,500 V; capacitance 25 µF; resistance 200 Ω. For the 0.2 cm cuvette, these settings generated a pulse of ~10 ms with a field strength of ~7,500 V/cm. Immediately after the pulse, 1 mL ice-cold 1M sorbitol was added to the cuvette and transferred to a sterile tube for incubation at 30°C without shaking. Cells were then spread on YPDS plates containing 100 µg/mL Zeocin (Gibco™ #R25001) for incubation at 30°C for 2-3 days until colonies formed. A selection of colonies was picked for further analysis: each colony was streaked onto a separate YPDS plate containing 100 µg/mL Zeocin.

2.3.11 Making *P. pastoris* Glycerol Stocks

Cells were streaked for single colonies on YPD agar and grown at 30°C until colonies were visible. Single colonies were streaked in a small patch at the centre of a fresh YPD plate (1 colony per plate) and incubated at 30°C until the inoculated patch of agar was dense with *Pichia* growth. A cell spreader was used to streak the central patch of cells over the entire agar surface and the plate was incubated overnight at 30°C. All growth from one plate was scraped into a cryovial and resuspended in YPD + 15% glycerol to make a concentrated cell suspension. Glycerol stocks were flash-frozen in LN₂ and stored at -80°C.

2.4 Protein Purification and Modification Methods

2.4.1 Purification of Rabbit Actin

Actin was routinely purified by other lab members (EGA, JP, AH) from rabbit skeletal muscle-derived acetone powder. The method used is the same as described in former publications from the KA lab (Urbanek *et al.*, 2013; Allwood *et al.*, 2016; Tyler *et al.*, 2021). More information about the principles of the method can be found in the introduction of Chapter 3.

2.4.2 *P. pastoris* Cell Lysis

Small-Scale Cell Lysis of Culture Samples

A pellet from 1 mL culture was resuspended to 200 μ L in a 1 x binding buffer. 300 μ L acid-washed glass beads were added to the resuspended cells and cells were broken by ten 30 second rounds of vortexing with 2 mins on ice between each round. Following breakage, an extra 200 μ L ice-cold binding buffer was added to each sample and the beads were pelleted by a brief spin in a benchtop centrifuge. The sample was harvested from off the beads and transfer to a pre-cooled tube. If necessary, this process was repeated until there were no residual beads in the cell lysate. 10 μ L or more of the cell lysate was mixed 1:1 with 2x Laemmli sample buffer.

Lysis using a French Press

The equipment used was a FRENCH[®] Press (Thermo #FA-032). A 10 g cell pellet was resuspended in binding buffer up to 35 mL (this is the maximum capacity for the French press). The cell suspension was loaded into a French press pressure cell with a 1-inch diameter plunger and the apparatus was sealed. A small amount of sample was pushed out via the sample tube to ensure all air was removed from the pressure cell, before the apparatus was assembled onto the French Press stage. The French press was operated at 30,000 psi while the tap was opened gradually to release pressure slowly, aiming for the sample to exit the sample tube outlet into a collection tube (placed on ice) in a steady drip. The sample in the collection tube was then reloaded into the pressure cell for a second round of lysis.

Lysis using a Freezer Mill

Frozen beads of cell suspension from the previous induction steps (section 2.3.9) was transported to the University of Warwick on dry ice. 6 L culture yielded approximately 150 g material. Freeze grinding could only accommodate 50 g material at a time, so the following process was repeated as many times as necessary to grind all of the starting material.

50 g frozen cell suspension was loaded into a large grinding vial that had been pre-cooled with LN₂. This was inserted into a freezer mill containing a LN₂ bath. Duration of the grinding was 1 min with 14 cycles/s. The grinding was repeated 30 times at 1 min intervals. LN₂ was re-filled every 10 cycles of grinding. Once grinding was complete, the grinding vial was kept at room temperature until the lysate started to melt before the vial was opened.

2.4.3 Preparation of a DNase I Column for Native Actin Purification

200 mg DNase I was dissolved in 10 mL DNase I coupling buffer and dialysed (section 2.4.7) overnight against coupling buffer. Next day, 25 mL Affi-Gel activated affinity chromatography media (Affi-Gel 10; Bio-Rad #1536099) was applied to a filter funnel fitted to a vacuum line, then washed five times with 30 mL ice-cold dH₂O, then another five times with 30 mL ice-cold coupling buffer. The washed Affi-Gel was mixed into the dialysed DNase I solution and incubated on a rocker for 3 hrs at 4 °C. The DNase I Affi-Gel was poured into a chromatography column with a bed volume of 25 mL, then was washed with 15 bed volumes of coupling buffer (375 mL total). The column was stored in coupling buffer with 1.5 mM NaN₃. Care was taken not to let the Affi-Gel dry out at any point throughout the steps described.

2.4.4 Crude Purification of Native Actin from *S. cerevisiae*

Frozen cell lysate was prepared using a cell disruptor before the start of the project, using commercial baker's yeast cakes as a source of *S. cerevisiae*. For each purification, 100 g frozen cell lysate droplets were thawed in 100 mL G-buffer but with added PI cocktail (cOmplete™ EDTA Free Protease Inhibitor Cocktail; Roche #05056489001), and without ATP. Once thawed, the lysate was

kept cold throughout the purification procedure (4°C refrigeration or on ice). The lysate was split between four 50 mL ultracentrifuge bottles, adding extra G-buffer if necessary to ensure no bottle was less than 80% full. The lysate was centrifuged at high speed to pellet cell debris (> 100,000 x g, 1 hr, 4°C). The lysate supernatant was filtered through successively finer filters: first through glass wool (optional) if pieces of debris were visible, then through a 0.45 µm syringe or vacuum filter and finally a 0.22 µm syringe or vacuum filter.

The filtered lysate supernatant was loaded into a DNSae I-Affi-Gel column that had been pre-equilibrated with G-buffer. This work was carried out in a cold-room so that the column and buffer temperature was maintained at 4°C. Note: for preparation of the wash and elution buffer, deionised formamide was allowed to warm to room temperature before opening and handling in a fume hood. For the loading, wash and elution steps, the next buffer was added or the flow was stopped while there was still a small amount of residual liquid above the Affi-Gel bed to ensure it wasn't exposed to air at any point. The column was washed with 1) 20 mL G-buffer 2) 20 mL G-buffer with 10% deionised formamide and 3) 20 mL G-buffer with 10% deionised formamide and 0.2 M NH₄Cl. Actin was eluted from the column with G-buffer containing 50% deionised formamide. Eluate was collected in fractions into tubes already containing 4 mL G-buffer to dilute the formamide concentration of the buffer. 5 mL eluate was collected per fraction.

Protein-containing fractions were assessed by mixing a 2 µL sample of each fraction with 10 µL droplets of 20% Bradford reagent on parafilm over white paper to clearly visualise the subtle colour change to blue where protein was present. An optional step here was to run samples of each fraction on an SDS-PAGE gel to assess the presence of cofilin (~21 kDa), which was more likely to be found in the earlier fractions owing to its smaller size compared to actin. Selected fractions were pooled and dialysed (section 2.4.7) against G-buffer overnight to remove formamide. Dialysed actin was concentrated to 0.5-1 mL using a 30k MWCO spin-concentrator. The concentration was assessed using a NanoDrop (section 2.4.13) and concentrated further if necessary, aiming for ~20-30 µM actin.

2.4.5 Crude Purification of Recombinant Yeast Actin from *P. pastoris*

This protocol is adapted from the method described in Hatano *et al.* (2018) and can be used for wild-type actin and polymerisation-impaired mutant actin. For cells broken using a freezer mill, approximately 50 g frozen lysate powder (the amount of cell lysate harvested from 2 L induced cell culture) was thawed in 50 mL 2x binding buffer. For cells broken by French press, the starting material for purification already contained binding buffer and totalled 35 mL. This quantity of lysate is equivalent to only 1 L induced cell culture, which is half the quantity of cells compared to the freezer mill lysate for which the method is written. Therefore, the volumes in the following purification method were halved if cell lysate from the French press was used.

Cell lysate was centrifuged at 5000 x g for 5 min at 4°C to remove intact cells and debris, then the supernatant was further cleared by centrifugation at 21,000 x g for 1 h at 4°C. The lysate supernatant was passed through a 0.22 µm vacuum filter and incubated with 1 mL Ni resin (HisPur™ Ni-NTA Resin; Thermo Scientific™ #88221) at 4°C for 1-1.5 hrs. The resin was pelleted by centrifugation at 4°C at 1,500 x g for 5 min and washed with a total of 200 mL ice-cold 1x binding buffer. The Ni resin was then washed with a total volume of 450 mL ice-cold G-buffer. The resin was resuspended to 40 mL in ice-cold G-buffer containing 5 µg/mL TLCK-treated chymotrypsin (Sigma-Aldrich #C3142-10MG, or Promega #V1061) and incubated overnight at 4°C. The chymotrypsin was inactivated by addition of PMSF to 1 mM and incubated for 30 min with on ice, with occasional agitation. The resin suspension was loaded into an open column and the eluate was collected into a tube. The eluate was concentrated using a 30k spin concentrator. The final volume adjusted to 900 µL with ice-cold G-buffer for cycling (section 2.4.6).

2.4.6 Further Purification of Wildtype Actin by a Polymerisation Cycle ('Cycling')

For wild-type actin, the crude purification product (from the native or recombinant methods described above in sections 2.4.4 and 2.4.5) could be further purified by cycling. 100 µL 10 x KME was added to the 900 µL actin solution and incubated on a roller at room temperature for 1 hr to induce actin polymerization. The 1 mL polymerised actin was transferred to a clean centrifugation tube for the MLA-80 rotor, and actin filaments were pelleted by ultracentrifugation at >100,000 x

g for 1 hr, 4°C. The supernatant was decanted off, and the pellet was washed once with 1 mL G-buffer before being resuspended in 0.5 mL ice-cold G-buffer. Resuspended F-actin was depolymerised by dialysis (section 2.4.7) against 1 L G-buffer for 2 days. After dialysis the depolymerised actin was collected in a cold tube and any remaining filaments or aggregates were pelleted by ultracentrifugation at >100,000 x g for 30 min, 4°C. The supernatant was harvested and transfer to pre-cooled microcentrifuge tube on ice. The protein concentration of the purification could be analysed using a NanoDrop at this stage (section 2.4.13). Further concentration was achieved using a 30k MWCO spin-concentrator, aiming for approximately 20-30 µM. The purification product was dispensed into 10 µL and 100 µL aliquots, which were flash-frozen in LN₂ and stored at -80°C or -20°C.

2.4.7 Dialysis

Dialysis Tubing Preparation

14k MWCO 19 mm diameter dialysis tubing was used for dialysis in most instances. This pore size is small enough to retain both actin (~42 kDa) and DNase I (~31 kDa). Sections of dialysis tubing were prepared by incubation in dialysis membrane cleaning solution (2% NaHCO₃, 1 mM EDTA) at 80°C for 1 hr. Cleaned tubing washed in water before transfer to storage in 20% EtOH.

Dialysis for Buffer Exchange

Dialysis tubing was sealed at one end, washed in water and stored in G-buffer before use. Protein solution was carefully loaded into one or more dialysis tubes before the other end was sealed. The loaded tubing was floated in 1 L of the desired buffer with gentle continuous stirring for up to 2 days, changing the buffer at least twice a day.

2.4.8 Purification and Cleavage of GST-tagged Las17 Fragments

The cell pellet from 2 L induced Rosetta cells was resuspended in 10 mL resuspension buffer with 1x PI cocktail. The cell suspension was sonicated in three rounds (1 min each), with gentle agitation between rounds. Cell debris was removed by centrifugation (20,000 x g, 40 min, 4°C). 400 µL

Glutathione Sepharose[®] 4B bead suspension (GE Healthcare #GE17-0756-01) was transferred to a clean 15 mL Falcon and washed in PBS with 300 mM NaCl. Washed beads were resuspended in the cleared cell lysate for 30 min at 4°C with gentle agitation. The beads were pelleted and the supernatant discarded, then beads were washed as follows: 3 washes with ice-cold PBS containing 1% Tween and 300 mM NaCl, 3 washes with ice-cold PBS, 2 washes with ice-cold high salt cleavage buffer and 2 washes with ice-cold low salt cleavage buffer. Washed GST-Las17-bound sepharose beads were incubated in 300 µL low salt cleavage buffer with PreScission Protease (GE Healthcare #GE27-0843-01) for 6-8 hrs at 4°C with gentle agitation. Following this incubation, beads were sedimented and the supernatant was harvested and either desalted straight away or stored at -20°C and desalted later (section 2.4.9).

2.4.9 Desalting GST-cleaved Las17PP

A PD MiniTrap G-25 column (GE Healthcare) was equilibrated with G-buffer and all liquid was allowed to enter the resin bed completely before the next steps. Up to 500 µL purified Las17PP was added and allowed to enter the resin bed. If less than 500 µL protein solution had been added, the additional volume was then made up with G-buffer and allowed to enter the resin bed completely. 1 mL G-buffer was used to elute the protein, and the buffer-exchanged protein was collected. A 3k MWCO spin-concentrator was used to concentrate the eluate to a volume of ≤ 200 µL. The concentrated purification product was dispensed into 5-10 µL aliquots and stored at -20°C

2.4.10 Ni-Affinity Purification of His-tagged Las17 from *E. coli*

The cell pellet from 2 L induced BL21 or Rosetta culture was resuspended in 10 mL Start buffer with added PI cocktail. The cell suspension was sonicated in three 1-min rounds, with gentle agitation between rounds. Cell debris was removed by centrifugation and the supernatant was further cleared by filtration before loading onto a pre-equilibrated Ni column (His-trap HP nickel column; GE Healthcare). The column was washed with Start buffer containing PI cocktail and increasing concentrations of imidazole (20 mM, 80 mM, 100 mM, 120 mM, 500 mM). Flow-

through for each wash was kept in separate tubes on ice for up to 2 hrs until the contents of each fraction had been analysed on a Coomassie stained SDS-PAGE gel. Fractions containing relatively pure His-Las17 were pooled and concentrated using a 10k MWCO spin-concentrator to ~1 mL.

2.4.11 Size Exclusion Chromatography of His-Las17

A little over 0.5 mL filtered Ni-affinity purified His-Las17 was injected into the 0.5 mL loading loop of an AKTA fitted with a Superdex-200 10/300 GL column (GE Healthcare #17517501), pre-equilibrated with gold-labelling buffer. The sample was run through the column at 0.4 mL/min at 4°C and collected in 0.5 mL fractions. Samples of each fraction were run on an SDS-PAGE gel to identify the fractions containing His-Las17. The selected 3-5 fractions were pooled and concentrated using a 10k MWCO spin-concentrator to ≤ 150 μ L. The concentrated purification product was dispensed into 5-10 μ L aliquots and stored at -20°C.

2.4.12 Labelling His-Las17 with Nanogold

1.8 mm diameter gold particles (Ni-NTA-Nanogold[®], Nanoprobes #2080-3ML) and His-Las17 were diluted 5x in gold-labelling buffer to give final concentrations of ~2 μ M gold and ~1 μ M His-Las17. This was incubated for 15 mins at room temperature with gentle agitation to allow the labelling reaction to take place. This was followed by a 15 min incubation on ice with Ni-resin to remove unlabelled protein. After pelleting the Ni-resin, the supernatant was diluted 1:2 in 20 mM Tris pH 7.6 (to dilute the NaCl concentration in the buffer from 150 μ M to 50 μ M and concentrated using a 10k MWCO spin-concentrator.

2.4.13 Determining Protein Concentration

Measuring Total Protein Concentration

Before aliquoting, protein concentration of actin purification products was assessed using a NanoDrop. A wavelength of 290 nm was used to account for ATP in the buffer, which absorbs at 280 nm. The absorbance reading was converted into a concentration using the following formula:

$$\text{Concentration (M)} = \frac{A_{290}}{\text{Ext. coef. (mL/mg/cm)} \times \text{Mr (Da)}}$$

where for actin the extinction coefficient is 0.63 mL/mg/cm and the Mr is approximately 42,000 Da. Therefore:

$$\text{Concentration } (\mu\text{M}) = \frac{A_{290}}{0.0264}$$

Estimating Protein Concentration by Densitometry

Since NanoDrop readings reflected total protein concentration, any impurities present resulted in a misleadingly high concentration estimate for the purification product. For this reason, to obtain the concentration of a protein stock for use in biochemical assays, an alternative approach was taken which could account for impurities. A sample of the purification product was run on an SDS-PAGE gel with a range of actin standards of known concentration. The gel was then stained with Coomassie blue stain (section 2.5.4) and imaged ≤ 10 min after adding destain solution (before the Las17 bands could fade) and again after ≥ 30 mins (better signal-to-noise for actin bands). The Las17 bands of interest were measured against a calibration curve made by plotting the measurements of the actin standards in Image Lab. The molecular weight discrepancy between a Las17 fragment and actin standards was compensated for by multiplying the measured concentration of Las17 by $\text{actin(MW)}/\text{Las17(MW on gel)}$; this is larger than the theoretical MW owing to the high proline content of Las17PP).

2.5 Biochemical Methods

2.5.1 Polymerisation of Actin Filaments

Freshly prepared G-buffer was used to dilute G-actin and any nucleating agents (KME or Las17) to the desired concentrations, with a final sample volume of 20-30 μL . Where used, KME was added from a 10x stock. Alternatively, actin polymerisation was induced by the addition of a purified Las17 fragment to the desired concentration. Polymerisation was allowed to occur at room temperature for approximately 1 hr.

2.5.2 Sedimentation Assays

To sediment filamentous F-actin, but not monomers, tubes containing 20-30 μ L actin solution were centrifuged at 279,000 x g for 15 mins at 4°C. Following centrifugation, a gel-loading pipette tip was used to carefully remove the supernatant and transfer it to a new tube. To sediment actin bundles but not unbundled filaments or monomers, the actin solution was centrifuged at 20,000 x g for 15 mins at 4°C. A volume of G-buffer equal to that of the removed supernatant was used to resuspend the pellet (Figure 2.3). Both supernatants and resuspended pellets were mixed 1:1 with 2x Laemmli sample buffer and analysed by SDS-PAGE followed by Coomassie staining. Bands were quantified by densitometry in Image Lab.

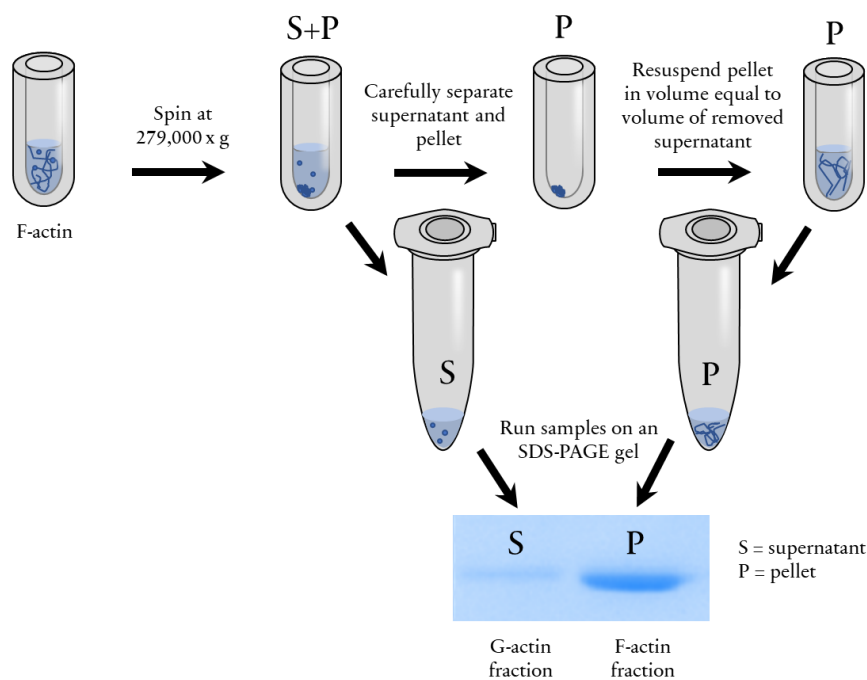


Figure 2.3: Schematic of a high-speed actin sedimentation assay.

2.5.3 Protein Electrophoresis (SDS-PAGE)

To cast gels, 100 μ L ammonium persulfate and 5 μ L TEMED were mixed into 10 mL 10%, 12.5% or 15% resolving gel solution (made up as shown in Table 2.6). The mixture was poured into an assembled SDS-PAGE gel casting frame (1.0 mm Mini-PROTEAN[®] Tetra Cell; Bio-Rad). The resolving gel mixture was topped with a thin layer of isopropanol as a levelling agent and allowed to set. Once set, the isopropanol was decanted off. 50 μ L APS and 15 μ L TEMED were then mixed into 5 mL 5% stacking gel solution (Table 2.6) and the mixture was poured on top of the resolving gel. A 15-well 1.0 mm comb was inserted before the gel was allowed to set.

Table 2.6: Resolving and stacking gel solution components.

	Resolving			Stacking
	10%	12.5%	15%	5%
Acrylamide	2.50 mL	4.15 mL	5.00 mL	0.800 mL
Gel Stock Solution (see main text)	3.75 mL	3.75 mL	3.75 mL	0.625 mL
Water	3.65 mL	2.00 mL	1.20 mL	3.525 mL

All protein samples were prepared by mixing with an equal volume of 2x Laemmli sample buffer. A heat block set to 100°C was then used to boil the samples for 3 mins. Boiled samples were cooled before being loaded into the gel.

Set gels were inserted into an SDS-PAGE Gel Tank (Mini-PROTEAN[®] Tetra Cell; Bio-Rad) and submerged in SDS-PAGE running buffer before the comb was removed. A gel-loading tip was used to apply either 5 μ L protein ladder (Bio-Rad #1610377) or 14 μ L sample to each well. A voltage of 120 V was applied until the dye front had passed through the stacking gel into the resolving gel, then the voltage was increased to 150-180 V. The run was stopped when the dye front reached the bottom of the resolving gel.

2.5.4 Coomassie Staining

Gel cases were cracked open and gels were submerged in Coomassie stain for approximately 40 mins, with gentle agitation on a rocker. To destain, the stain was decanted off and the gel was

transferred into Coomassie destain, incubating and refreshing the solution as many times as necessary to clearly make out protein bands. Gels were imaged using a Gel Documentation System (Bio-Rad).

2.5.5 Western Blotting

Gel cases were cracked open and the gel was submerged in transfer buffer along filter paper and sponges cut to size (8 cm x 10 cm). A 7 cm x 9 cm rectangle of polyvinylidene fluoride (PVDF) membrane was soaked in 100% methanol before being submerged in transfer buffer. The gel and PVDF membrane were sandwiched between the filter paper, and this in turn was sandwiched between the sponges. This assembly was inserted into the tank along with an ice pack, and the remaining space was filled with TBST. To run the transfer, a constant voltage of 100 V was applied and maintained for 75 mins.

Following transfer, the PVDF membrane was carefully transferred to a clean 50 mL Falcon, with the side that had been against the gel facing into the centre. For the following steps, incubations used an automated roller to ensure even exposure of the membrane to the blocking and antibody solutions. The membrane was incubated in blocking buffer for at least 30 mins. Next, the blocking buffer was decanted off and replaced with primary antibody (diluted in blocking buffer to a suitable working concentration; Table 2.7) for 1 hr at room temperature, or alternatively overnight at 4°C. The membrane was washed 3 times by 10-min incubations with TBST before the membrane was incubated with secondary antibody (diluted in blocking buffer to a suitable working concentration; Table 2.7) for 1 hr at room temperature. The membrane was washed in TBST as before.

Luminol solution was mixed 1:1 with peroxide solution (ECL™ Prime Western Blotting System kit; GE Healthcare #GERPN2232) and this was repeatedly pipetted over the PVDF membrane to ensure good coverage. The membrane was imaged straight away using the Chemi High-Resolution setting on a Gel Documentation System (Bio-Rad). The membrane was imaged again using a custom setting to obtain an image of the protein ladder, and this was superimposed on the image of the bands.

Table 2.7: Antibodies used for Western blotting. All antibodies are immunoglobulin G (IgG). Secondary antibodies were labelled with horseradich peroxidase (HRP).

Type	Target	Label	Raised in	Dilute 1 in...	Notes
Primary	Actin	None	Rabbit	300	Sigma A2066
Primary	Las17	None	Rat	10,000	'Rat2'
Secondary	Rabbit IgG	HRP	Goat	10,000	-
Secondary	Rat IgG	HRP	Goat	10,000	-

2.6 Microscopy Methods

2.6.1 Electron Microscopy Sample Preparation

For most applications, no additional sample preparation was required after actin polymerisation (section 2.5.1). For salt-nucleated F-actin, 1 μ M G-actin was incubated for 1 hr in F-buffer (G-buffer with 1xKME; see 2.1.1). For Las17-nucleated F-actin, 4 μ M G-actin and 0.4 μ M His-Las17PP₃₀₀₋₅₃₆ were incubated for 1 hr in G-buffer. For actin bundles, 1 μ M G-actin and 1 μ M GST-Las17PP₃₀₀₋₅₃₆ were incubated for 1 hr in G-buffer.

For single particle cryo-EM, 3-4 μ L of the F-actin solution was applied directly onto a glow-discharged grid (sections 0 and 2.6.5). However, for cryogenic electron tomography (cryo-ET) of actin bundles, additional sample preparation was first required to introduce gold nanoparticles into the sample to act as fiducial markers for image alignment during the reconstruction process.

BSA-Coating Gold Colloids for Tomography

10 nm gold nanoparticles (Sigma-Aldrich #752584-25) were coated with bovine serum albumin (BSA) to reduce aggregation (Iancu *et al.*, 2007). 10 nm diameter gold nanoparticles were vortexed to resuspend, then 1 mL was transferred to a clean tube. The gold was pelleted by centrifugation at 18,000 x g for at least 20 min, then the cleared supernatant was carefully removed and discarded. The gold pellet was resuspended in 200 μ L 5 % w/v BSA and incubated at 4-23°C for 30 min. Following incubation, the gold was pelleted by centrifugation as before and washed once in dH₂O, then resuspended in 200 μ L dH₂O and stored at 4°C until ready for use.

Preparation of Samples Containing Fiducial Markers

Actin bundles were pelleted by centrifugation at 18,000 x g for 15 mins, after which 22 μ L supernatant was discarded, leaving a 3 μ L solution of concentrated actin bundles. No further steps were carried out until shortly before applying the sample to the first grid. This was necessary to minimise precipitation of the gold particles, which could occur in less than 10 mins of introducing gold into the sample (Figure 2.4). Immediately before loading sample onto the first grid, BSA-coated 10 nm gold was mixed 1:1 with 2x G-buffer, then 20 μ L was added to the concentrated bundles and mixed by pipetting. The solution colour was monitored before loading each grid, and the sample was discarded upon a subtle shift from red to purple (indicative of gold precipitation).

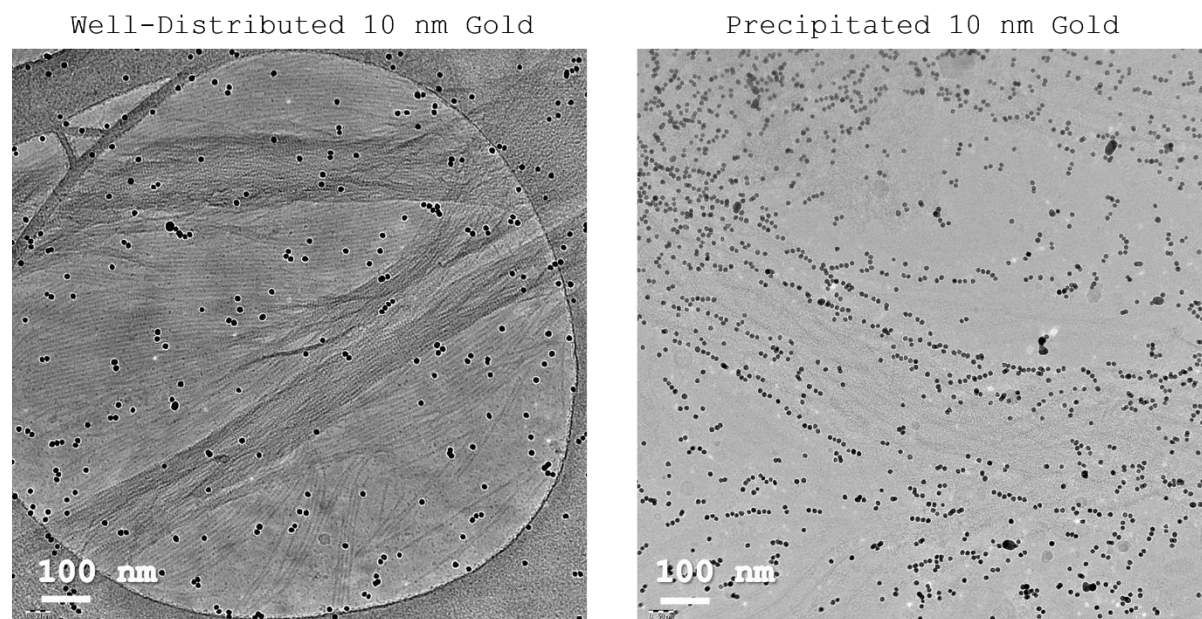


Figure 2.4: Fiducial markers for cryo-ET. 10 nm gold colloids were introduced to the sample very shortly before preparing frozen grids to avoid precipitation. The bundles appeared to have a looser arrangement after mixing with colloidal gold, with individual filaments seen spread throughout the ice. Precipitation could be seen by eye as a very subtle colour change of the sample solution from red to purple.

2.6.2 Preparing Negatively Stained Specimens

Carbon-coated grids were glow-discharged for 30 seconds in a Cressington 208 high vacuum carbon coater no longer than 30 mins prior to use. 3 μL polymerised actin was applied to the carbon-coated side of the grid. Sample was incubated on the grid for 60 seconds prior to blotting from the side with a torn edge of blotting paper. For the following wash steps, droplets were applied to the grid and then blotted off straight away. The grid was washed twice with dH_2O and once in 0.75% uranyl formate solution. Finally, the grid was incubated with a second droplet of uranyl formate for 20 s before blotting. Any liquid remaining on the grid was removed by suction before it was transferred to a grid box, Grid boxes were stored grid-side-down to protect them from light.

2.6.3 Screening and Data Collection of Negatively Stained Samples

Negatively stained samples were loaded into a CM100 TEM (Philips) with a LaB_6 source operated at 100 kV. Images were recorded on a 1k x 1k Multiscan 794 CCD camera (Gatan). Screening was performed at a range of magnifications spanning 700 to 21,000 x to locate actin filaments or bundles and to assess the quality of staining.

For data collection of bundled actin filaments, areas containing bundles with good staining were identified at low magnification. Then, in a nearby area free of specimen, the magnification was increased to 28,500 x and the defocus was set. Images were collected 'blindly' to minimise beam damage to the sample. Three defocus values were used for this dataset: -1000, -2000 and -3000 nm.

2.6.4 Single Particle Analysis of Negatively Stained Specimens in CisTEM

Micrographs were converted from .dm3 to .mrc format before being imported into CisTEM. The data had a pixel size of 7.2 \AA /pixel, and the spherical aberration of the microscope was 3.6 mm. CTF corrections was performed before 520 particles were picked manually. The box size was set to 84 pixels (604.8 \AA) and the mask radius was 280 \AA . 2D classification was performed with 8 classes and 20 iterations.

2.6.5 Frozen Grid Preparation for Cryo-EM and Cryo-ET

Holy carbon grids were glow-discharged for 30 seconds in a Cressington 208 high vacuum carbon coater no longer than 30 mins prior to use. Single particle analysis samples used 300 copper mesh R2/2 or R1.2/1.3 holy carbon grids (Quantifoil). Tomography samples used lacey carbon grids (EM Resolutions).

A Leica EM GP plunge-freezer was used for automated blotting and plunging. 3-4 μL sample was applied to the carbon-coated side of the grid and incubated for 60 seconds in the chamber (maintained at 15°C and 70-85% humidity). Automated blotting was performed on the uncoated side (backside) of the grid with blotting paper (Whatman no.1) for 3-6 s before immediate automated plunging into liquid ethane. In instances where a double-blotting step was used, 3-4 μL F-actin solution was applied to the carbon-coated side of the grid and manually blotted from the side, using a torn edge of blotting paper before a second sample application as described above. Frozen grids were transferred to LN_2 for clipping into cartridges and maintained in LN_2 for storage and all subsequent handling.

2.6.6 Cryo-EM Data Collection and Image Processing for Single Particle Analysis

Screening and data collection was performed in a Tecnai Arctica™ microscope (FEI) operated at 200 kV and fitted with a Falcon III detector (FEI). Atlas acquisition at low magnification (165x) to assess the ice-quality across the grid, and higher magnification screening was used to assess actin filament distribution. The magnification for data collection was based on a trade-off between resolution and field of view. Datasets in this thesis were collected at 53,000 x and 110,000 x magnification, giving a nominal pixel size of 2.04 Å and 0.98 Å, respectively. Data were collected in the form of micrograph movies with 80 frames, grouped pairwise into 40 fractions, in the software EPU. The electron dose was adjusted to approximately 1 $\text{e}/\text{Å}^2$ (100 e/nm^2) per fraction (~40 $\text{e}/\text{Å}^2$ total dose per exposure) by altering the exposure time or spot size. The data acquisition area was positioned to include at least 20% carbon film to ensure sufficient contrast for strong Thon rings for CTF fitting during data processing. Automated acquisition was run for 24-48 hrs. On-the-

fly processing was performed in Warp (Tegunov and Cramer, 2019) in order to monitor data quality in real-time.

The following steps were followed for two independent datasets. Raw micrograph movies were imported into RELION (Scheres, 2012) and reconstruction was performed by following the helical processing approach (He and Scheres, 2017). Key steps of this process are covered in Chapter 4, and additional details can be found below. Briefly, motion correction was performed using MotionCor2 and CTF estimation and correction was performed using Gctf. Particle coordinates were picked manually in RELION using the tool for helical segments. Particle extraction, 2D classification and generation and refinement of a 3D map, particle polishing and postprocessing were all performed in RELION.

Generation of templates for 3D Refinement

To generate a cylindrical template, RELION helix toolbox was used to define cylinder parameters and the dataset pixel size (2.04 Å in the example below).

```
relion_helix_toolbox --cylinder --o cylinder.mrc --boxdim 120 --  
cyl_outer_diameter 100 --angpix 2.04 --sphere_percentage 0.9 --width 5
```

To generate a homology model template from PDB ID: 6BNO, the following command was used to define model parameters:

```
relion_helix_toolbox --pdb_helix --i 6bno.pdb --o 6bno_helix.pdb --  
cyl_outer_diameter 0 --rise 28.11 --twist -166.65 --nr_subunits 8
```

This was converted into a density map (.mrc file) in EMAN2 using the program `e2pdb2mrc.py`, specifying the pixel size of the dataset (0.98 Å in the example below) to ensure correct scaling, and introducing a lowpass filter of 15 Å.

```
e2pdb2mrc.py 6bno_helix.pdb 6bno_helix.mrc --apix 0.98 --box 250 --res 15
```

Calibration of Pixel Size

The final 3D refinement output map was postprocessed using pixel sizes ranging from the nominal pixel size (0.98 Å) to 0.93 Å. The true pixel size was identified by performing real-space refinement on each map in Phenix to identify the rescaled map with the highest correlation coefficient to an

F-actin homology model (PDB ID: 5ONV). The postprocessed map with 0.945 Å was used as the final map.

2.6.7 Building a Pseudoatomic Model for F-actin

The modelling steps using ISOLDE were performed in part by Professor Per Bullough (University of Sheffield). A masked version of the map was used for modelling to ensure density attributable to solvent noise did not influence backbone or sidechain positioning. A single homologous model protomer (PDB ID: 5ONV) was docked into the map by rigid-body fitting. Residues that differed in the yeast actin primary sequence were mutagenised. Additionally, Hic73 (methylated His) from the homology model was changed to His73 in the yeast model.

An iterative modelling approach was applied for the generation of a short model filament, beginning with a single protomer. First, flexible fitting of the model protomer was performed automatically over the entire chain length using ISOLDE in Chimera X. ISOLDE automatically detects and avoids atomic clashes. Ramachandran outliers were then adjusted manually if an improvement could be made without introducing clashes or unfavourable rotamers. Next, three copies of the new protomer model were docked into the experimental map and subjected to another round of flexible fitting to ensure clashes at the protomer-protomer interfaces were accounted for and avoided, again making manual alterations where improvements could be made.

2.6.8 Cryo-EM Analysis & Presentation Tools in Chimera

Cropping a Map

To crop a map, the 'Region Bounds' and 'Subregion Selection' features from the 'Volume Viewer' tool were used. Region and subregion bound values were adjusted in x, y and z by adjusting the values directly or adjusting bounds by dragging the boundary cube faces in the display window. 'Crop' was run once the regions were positioned.

Rigid Body Fitting & Map Correlation

A map or model was roughly aligned manually with a reference map before automatic alignment was performed using the 'Fit in Map' tool. If two maps were aligned this way, the correlation value

calculated could be found in the 'Fit in Map' window. For map-map correlation (section 5.2.2), maps were cropped to cover the same region to restrict the correlation calculation to areas common to both maps.

Detecting Hydrogen Bonds and Salt Bridges in Chimera

The 'FindHBond' tool was used to detect hydrogen bonds with following H-Bond Parameter options: intra-model only (if multiple models were open); inter-molecule only (to limit H-bond detection to residues from different protomers); relax H-bond constraints by 0.4 Å and 20°. To detect only H bonds classed as salt bridges, charged functional groups were first selected using the command `select Ng+ | N3+ | N2+ | O2- | O3-`, and the option 'only find H bonds with both ends selected' was ticked in addition to the parameters listed above.

2.6.9 Tilt-Series Acquisition for Cryo-ET

Screening and data collection were performed in a Tecnai Arctica™ microscope (FEI) operated at 200 kV and fitted with a Falcon III detector (FEI). An atlas was acquired to assess the ice-quality across the grid, and higher magnification screening was used to assess actin bundle and gold nanoparticle distribution. Bundles that could be clearly visualised over a range of tilt angles without obstruction were selected for data collection. The Tomo software (FEI) was used to set up automated data acquisition of tilt series, with the data acquisition magnification set to 16,000 x (pixel size = 6.63 Å). Automated tilt series acquisition was set up in the TEM Tomography software. A series of 61 images with 2° rotation intervals was set up, spanning 120° (-60° to +60°, beginning at 20°). The exposure time per tilt angle was 0.52 s, and 20 frames were collected per exposure, grouped into fractions of 2 frames. A total dose of 100 e/Å² was used for the full tilt series.

2.6.10 Tomogram Generation and Segmentation

The software package IMOD was used to generate a tomogram from the tilt series data. Briefly, an initial coarse alignment was performed, then coordinates of fiducial markers were identified and tracked across the tilt series. Next, fine alignment was performed using the fiducial markers as

reference points. Finally, the aligned tilt series was cropped in the x, y and z-axis to restrict the reconstruction volume to the feature of interest before tomogram reconstruction was performed by weighted back projection. Segmentation to generate a 3D model was performed in Amira using the brush tool to manually select regions corresponding to the actin bundle every few slices of the tomogram.

2.6.11 Atomic Force Microscopy

Atomic force microscopy (AFM) sample preparation and data collection was performed by Nic Mullin (University of Sheffield). Briefly, 1 μM G-actin was polymerised with 1 μM Las17PP in G-buffer (total vol. $\sim 25 \mu\text{L}$) at room temperature for ~ 1 hr.

Muscovite mica (Agar Scientific) was punched into 11 mm diameter discs and glued to a glass slide. The top surface was cleaved with adhesive tape and functionalised by incubating a 50 μl drop of poly-L-ornithene (P3655, Sigma Aldrich) in aqueous solution (100 $\mu\text{g}/\text{ml}$) on the surface for 1 minute, followed by 5x1 ml rinses with HPLC grade water (Sigma Aldrich) and blow drying under a stream of HEPA filtered nitrogen. 10 μl of the polymerised actin solution was incubated on the functionalised mica for 30 minutes, then rinsed with 3 x 200 μl of G buffer and imaged immediately without drying.

Imaging was performed under G buffer, using a NanoWizard 3 Ultra AFM (JPK instruments/Bruker) operating in AC mode. Fastscan-D cantilevers (nominal stiffness 0.25 N/m, nominal resonant frequency 100 kHz (in liquid)) were tuned to a free amplitude of approximately 1-2 nm at a frequency just below resonance. Scanning was performed at relative setpoint of 65-90 %. The free amplitude, setpoint and feedback gains were optimised while imaging. Images were captured at line rates of 0.5-2 Hz with 256-1024 pixels along the long axis. In some cases, the scan angle was adjusted to align the fast scan axis with the long axis of the actin bundles to improve tracking and minimise the influence of drift on measurements of the periodicity. The height, height sensor, error signal and phase channels were recorded in both trace and retrace directions.

The data (.jpk format) was analysed in Gwyddion software. All measurements were made on the height sensor channel in the trace direction. Before any measurements were taken, mean plane subtraction was performed to ensure the mica surface was aligned along a flat plane. For width and height, line profiles 1 pixel in width were generated across areas of the image containing individual bundles. Bundle height was measured as the distance between background and peak height, and bundle width was measured as the width of the base of the peak. For periodicity, a line was drawn lengthways along a bundle and the generated profile was characterised by inter-peak distance.

3. Yeast Actin Purification and Mutagenesis

3.1 Introduction

3.1.1 Traditional Methods of Actin Purification

A good quality preparation of purified actin is of particular importance for single particle cryo-EM (Chapter 4) as it is a highly sensitive technique that resolves structures to a sub-nanometer resolution. This chapter covers the generation of purified yeast actin for use in the biochemical and structural work described in the following chapters.

At the time this project began, actin was routinely purified from rabbit skeletal muscle tissue in our lab, so this was available as a resource for some of the early optimisation work with EM sample preparation and biochemical assays with Las17 fragments. Vertebrate (typically rabbit or chicken) skeletal muscle is historically and currently by far the most commonly used source of purified actin owing to the abundance of actin in this tissue. Actin and myosin dominate the machinery of muscle contraction, with actin making up approximately 22% of the protein mass in myofibrils, and myosin making up 43% (Yates *et al.*, 1983). In the context of the whole muscle cell, actin is estimated to make up ~15% of the total protein content (Varland *et al.*, 2019) and exists largely in actomyosin complexes.

The modern method for actin purification from muscle tissue has changed little from the original procedure developed in the 1940s by Straub and colleagues (Pardee and Spudich, 1982). Early steps of the procedure denature any proteins that are not stabilised in actomyosin complexes by dehydrating muscle in acetone. Later steps exploit the effect of salt concentration on the equilibrium between the monomeric and polymeric state of actin: high salt concentration favours the insoluble F-actin state and, conversely, low salt concentration favours the soluble G-actin state. Consequently, depending on the salt concentration in the buffer, centrifugation can be used either to separate F-actin from soluble material, or to separate G-actin from insoluble material. The shift of G- to F-actin and back again is known as cycling.

While actin is still a major protein in most eukaryotic cells, the abundance of actin found in muscle is highly unusual and represents an extreme case. In the majority of eukaryotic cells, actin is estimated to make up ~1-3% of the protein mass (Varland *et al.*, 2019). Additionally, a lower proportion of actin in non-muscle cells is locked in stable actomyosin complexes. The method used for purifying muscle actin is therefore unsuitable for non-muscle sources.

A traditional method for purifying non-muscle actin exploits the interaction between DNase I and G-actin to allow affinity purification (Schafer *et al.*, 1998). G-actin and DNase I form a tight 1:1 complex (Mannherz *et al.*, 1975) and in fact this was used to obtain the first atomic structure of G-actin (Kabsch *et al.*, 1990; Figure 3.1A). To harvest G-actin, the actin-DNase I complex can be disrupted with the chemical formamide (Figure 3.1B). An elution buffer with $\leq 40\%$ formamide does not impair the assembly competence of actin or its ability to re-associate with DNase I (Zechel, 1980). Once actin is eluted from immobilised DNase I, cycling can be used to further improve the purity if necessary.

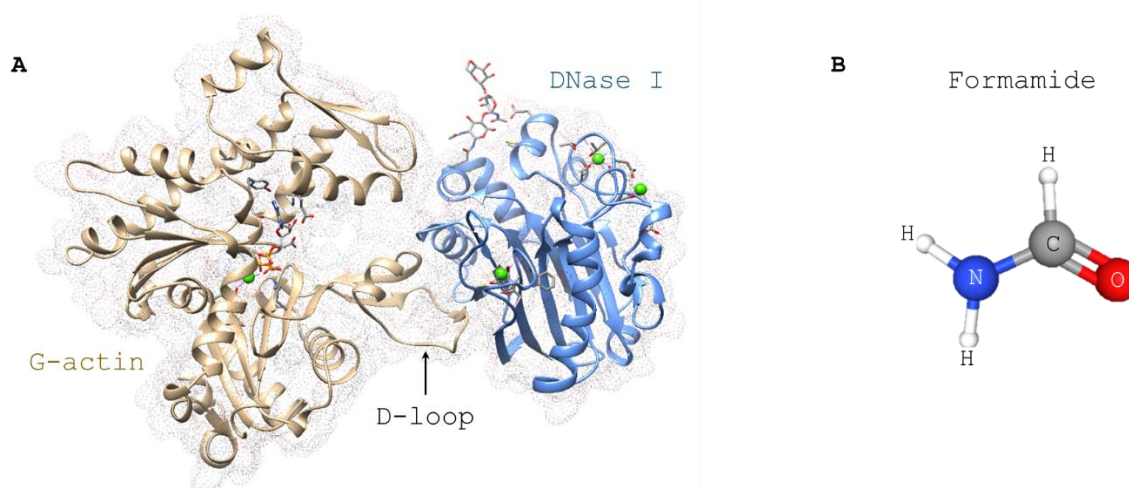


Figure 3.1: DNase I and G-actin form a tightly bound 1:1 complex that can be disrupted by formamide. A) The structure of actin bound to DNase I. PDB ID: 1ATN (Kabsch *et al.*, 1990). Protein backbones are shown as ribbons, protein surface as a dotted mesh, small molecule ligands as ball and stick models and metal ions as green spheres. The DNase I binding loop (D-loop) is indicated. B) Formamide is used in DNase I affinity purification of actin to liberate the monomeric actin from the immobilised DNase I. PubChem CID: 713.

3.1.2 Expression and Purification of Recombinant Actin

At the early stages of this project, *S. cerevisiae* actin was purified from commercially available baker's yeast using the DNase I method. However, we encountered difficulties obtaining a sufficient yield of functional actin, as will be described later in this chapter. The timely publication of a new and versatile method of recombinant actin purification (Hatano *et al.*, 2018) prompted our shift to this method for the purification of native *S. cerevisiae* actin.

This alternative purification method uses the methylotrophic budding yeast *Pichia pastoris* as the host for recombinant actin expression. *P. pastoris* is well-established as a recombinant protein expression system that exploits this organism's ability to metabolise methanol as its sole carbon source by substantially upregulating expression of a protein called alcohol oxidase I from the gene *AOX1* (Higgins, 1995, EasySelect™ *Pichia* Expression Kit User Manual, Invitrogen). In the *Pichia* recombinant expression system, the gene sequence for a recombinant protein is integrated downstream of an *AOX1* promoter so that its expression is also induced by the presence of methanol. The recombinant protein in this case is *S. cerevisiae* actin connected at its C-terminus via a linker sequence to human thymosin β 4 (thy β 4), which is in turn linked to a polyhistidine sequence (His-tag). When this fusion protein is expressed, the thy β 4 sequesters the recombinant G-actin, preventing interactions with both the barbed and pointed end of the monomer (Figure 3.2A). Crucially, the bound thy β 4 makes the recombinant actin unavailable for polymerisation with the native pool of *Pichia* G-actin. This is designed to prevent native actin appreciably co-purifying with the recombinant actin when nickel resin is used to pull down the His-tagged fusion protein. Next, instead of eluting the actin-thy β 4 complex from the nickel resin, chymotrypsin cleavage is used to liberate actin from the fusion protein. Chymotrypsin can cleave immediately after the last residue in the actin sequence (Phe375; Figure 3.2B), meaning the purification product has the exact primary sequence of natively expressed actin in *S. cerevisiae*, with no additional residues.

This chapter addresses establishing this method of expressing and purifying recombinant *S. cerevisiae* actin from *P. pastoris* in our own lab and outlines how the benefits of this system have been exploited to generate mutant actin proteins for further studies. Additionally, the purity of the actin product obtained using this method is scrutinised by mass spectroscopy, and a sequence modification in the thy β 4-His linker is proposed in the interests of removing off-target chymotrypsin cleavage sites.

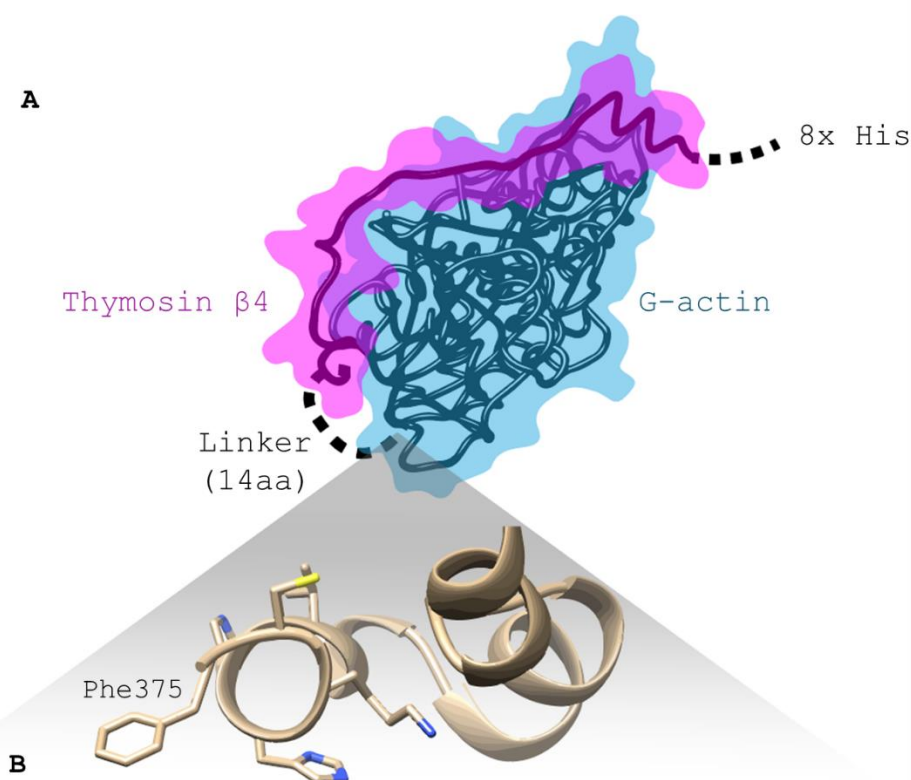


Figure 3.2: The G-actin-thy β 4 fusion protein. A) Backbone structure of *P. pastoris* G-actin fused to human thy β 4. Dashed lines stand in for stretches of missing structural information. The D-loop of G-actin is absent from the backbone but has been factored into the surface representation (top-right). PDB ID: 4PL7 (Xue *et al.*, 2014). B) C-terminal residues of *S. cerevisiae* G-actin with side-chains 370-375 displayed. The terminal phenylalanine at position 375 is indicated: this residue is recognised by chymotrypsin for proteolytic cleavage, liberating G-actin from the rest of the fusion protein. PDB ID: 1YAG (Vorobiev *et al.*, 2003).

3.2 Results

3.2.1 Purification of Yeast Actin Using DNase I

During the early stages of this project, the DNase I affinity purification method was used to purify actin from commercially available baker's yeast. Following the DNase I purification, actin was the most prevalent protein present but several other bands spanning a large range of molecular masses could be seen on a Coomassie-stained gel (Figure 3.3). This level of purity was acceptable for biochemical studies but was not optimal for electron microscopy in which contaminants could be visualised as well as filamentous actin. The appearance of negatively stained rabbit muscle F-actin in transmission electron microscopy (TEM) was used for comparison. At high magnification (39,000x), the helical arrangement of protomers was just about visible for rabbit actin filaments but was obscured by impurities on the yeast actin filaments (Figure 3.4).

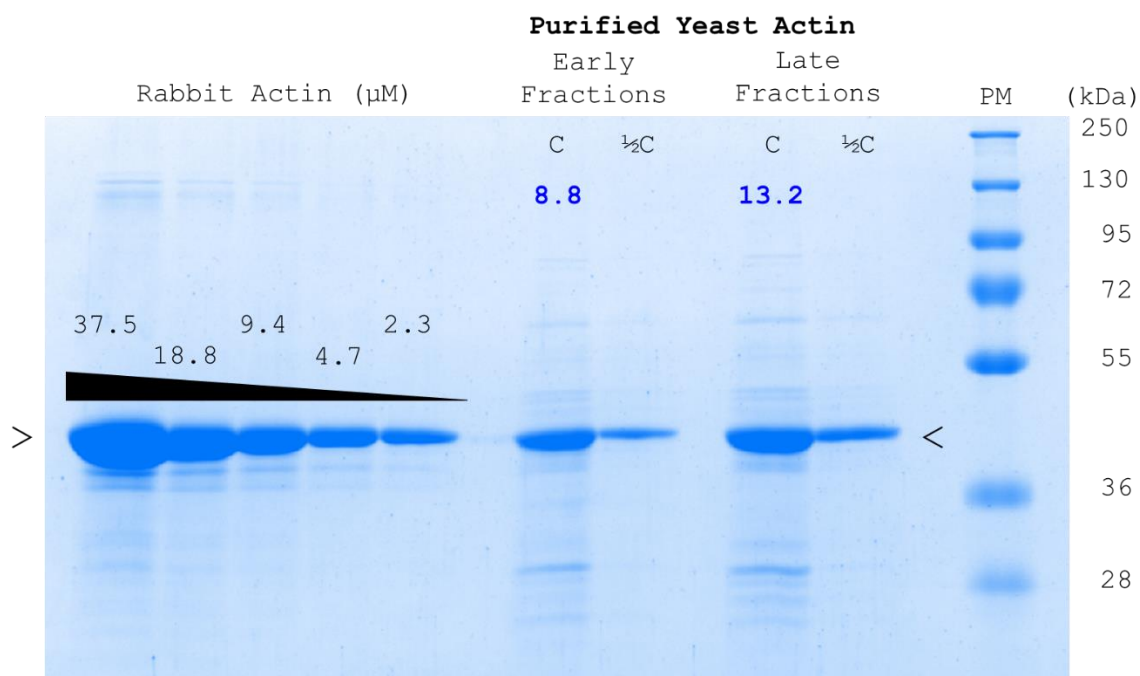


Figure 3.3: Crude purification product from DNase I affinity purification of native *S. cerevisiae* actin. Actin is the predominant band in the purification product, but several additional bands are also visible. This preparation was split into early and late fractions at the elution stage, but the purification product appears highly similar in terms of the yield of actin and impurities present. C = undiluted, $\frac{1}{2}\text{C}$ = diluted 2x. A dilution series of rabbit skeletal muscle actin was used for reference when assessing the concentration of the yeast actin purification product by densitometry. The estimated concentration (μM) of actin in the undiluted purification product is labelled in blue text.

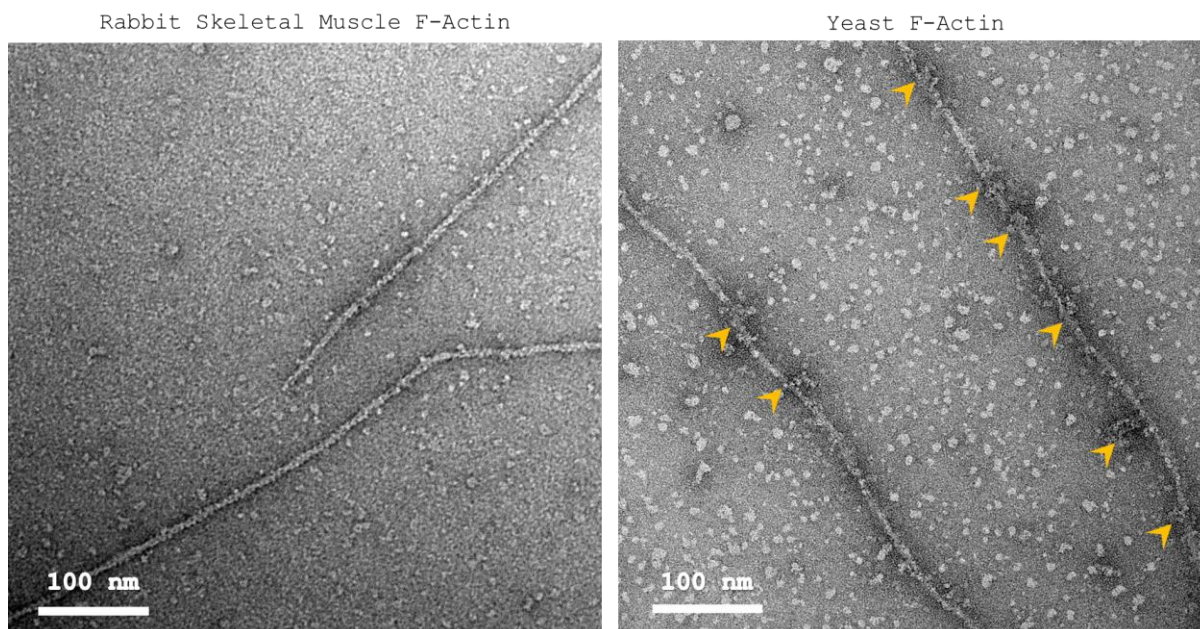


Figure 3.4: Representative images of rabbit muscle F-actin and DNase I-purified yeast F-actin negatively stained for TEM. Impurities in the yeast actin preparation (purified using DNase I affinity with no additional cycling steps) were visible both on the filaments themselves, in which details of the helical arrangement of protomers was completely obscured, and in the background where globular features are both larger and more abundant than the example prepared using rabbit skeletal muscle actin. Yellow arrowheads point to large aggregates on the yeast actin filaments that have retained more stain than surrounding features.

The impurities in the yeast actin purification product were further investigated using intensity based absolute quantification (iBAQ). This is a label-free method for quantifying proteins using mass spectroscopy and, like other mass spectroscopy methods, this relies upon the detection of proteolytic fragments (peptides) from a digested protein sample. Unlike other methods, iBAQ corrects for over-representation of proteins that produce more peptides upon digestion. This works by summing the intensity for all of the peptides detected for an identified protein, then dividing this total by the number of theoretical peptides for this protein (Schwanhüusser *et al.*, 2011). The digestion enzyme used will have a known specificity, so the theoretical peptides can be worked out from the protein sequence by identifying cleavage sites for this enzyme.

The crude actin purification product from DNase I affinity purification was revealed to have a purity of 60.93%. While this means that 39.07% of the purification product consisted of proteins other than actin, the breakdown of impurities revealed that each individual impurity was only present at very low quantities (Figure 3.5). For example, the top contaminant – Glyceraldehyde-3-

phosphate dehydrogenase 3 (TDH3) – made up only 5.05% of the purification product. The contaminants with the next highest ranking, starting with the highest, were: Alcohol dehydrogenase 1 (ADH1, 2.70%); Enolase 2 (ENO2, 2.13%); Phosphoglycerate kinase (PGK1, 1.49%); Fructose-bisphosphate aldolase (FBA1, 1.26%); Phosphoglycerate mutase 1 (GPM1, 1.25%); Pyruvate decarboxylase isozyme 1 (PDC1, 1.10%); Cofilin (COF1, 1.03%); Alpha-glucosidase MAL12 (MAL12, 1.00%); and Peptidyl-prolyl cis-trans isomerase (CPR1, 0.98%).

Only one of the top 10 contaminants is a recognised actin-binding protein: the actin filament severing protein cofilin (COF1). The presence of cofilin in the preparation is not ideal since this protein is known to alter the properties of actin filaments, but at this low level it should be limited to low severing activity. Severing requires the co-operative binding of several cofilin molecules to near saturation (1 cofilin:1 protomer) on a stretch of F-actin to invoke a local discrepancy in twist. Its effects on the twist of actin filaments have been demonstrated to occur at the interface between decorated and undecorated stretches of F-actin, and are not propagated beyond the neighbouring protomers (Huehn *et al.*, 2018). Table 3.1 contains the full list of other actin binding proteins detected in the crude purification product.

To increase the purity, the crude purification product was subjected to an additional polymerisation cycle. However, these additional purification steps also resulted in a significant loss of actin from approximately 0.504 mg (26 μ M in 450 μ L) to approximately 0.122 mg (7 μ M in 400 μ L). This equates to an 86% loss of actin. Since the additional purification step selects for polymerisation-competent actin that can dynamically assemble into filaments and depolymerise into monomers according to the buffer conditions, this marked loss in purified actin product indicates that much of the original DNase I purified actin was non-functional.

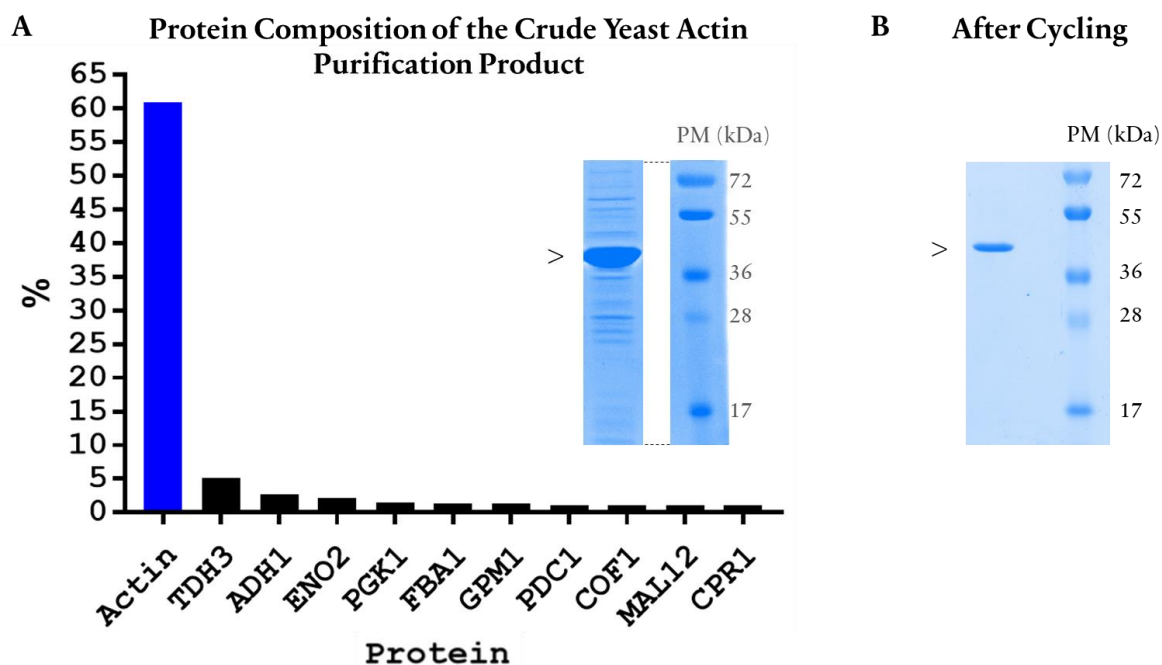


Figure 3.5: Assessment of contaminants in the crude purification product using DNase I affinity. A) iBAQ was performed on the crude yeast actin purification product from DNase I affinity purification. iBAQ scores of each protein were converted into a percentage of the total score for all proteins. The percentages for actin and the 10 highest-scoring contaminants are shown (refer to main text and Table 3.1 for full names). A Coomassie-stained SDS-PAGE gel with a sample from the same preparation is inset. B) A Coomassie-stained SDS-PAGE gel of the purification product after a polymerisation cycle. Black arrowheads mark the band corresponding to actin on each gel.

Table 3.1: Actin binding proteins in the crude purification product using DNase I affinity.

Protein	Gene	iBAQ Score	% of total
Cofilin	COF1	18629000	1.0265
Twinfilin-1	TWF1	6194500	0.3413
Profilin	PFY1	3869700	0.2132
Verprolin	VRP1	572400	0.0315
Tropomyosin-1	TPM1	448160	0.0247
Calmodulin	CMD1	327320	0.0180
F-actin-capping protein subunit beta	CAP2	293340	0.0162
Actin-binding protein	ABP1	226600	0.0125
Fimbrin	SAC6	158720	0.0087
Myosin light chain 1	MLC1	107610	0.0059
Actin-related protein 2/3 complex subunit 2	ARC35	89619	0.0049
Actin-related protein 2	ARP2	68968	0.0038
F-actin-capping protein subunit alpha	CAP1	58358	0.0032
Actin-interacting protein 1	AIP1	51984	0.0029
Actin-related protein 2/3 complex subunit 4	ARC19	29285	0.0016
Actin-related protein 3	ARP3	25280	0.0014
Actin-related protein 2/3 complex subunit 1	ARC40	22395	0.0012
Coronin-like protein	CRN1	13701	0.0008

Further optimisation of this procedure was unfortunately not possible owing to additional technical difficulties that resulted in consistently poor yield from subsequent purifications using the DNase I method. This was suspected to be due to degradation of the immobilised DNase I because the methodology remained unchanged from previous, higher yielding attempts. Spin-concentrating the product to a smaller volume could not compensate for the low yield because the final volume was then too low for the experimental demand. Attempts to replenish the column with new DNase I were apparently ineffective as low yields continued (data not shown). Since purified *S. cerevisiae* actin was a necessity for the work planned for this project, it was necessary to either carry out a thorough diagnostic investigation on the DNase I procedure, or to try an alternative purification method. The latter option was chosen due to the timely publication of a method for rapidly purifying recombinant actin isoforms to high purity using a *P. pastoris* expression system (Hatano *et al.*, 2018).

3.2.2 Troubleshooting Purification of Recombinant Actin from *Pichia* Host

To enable the purification of recombinant *S. cerevisiae* actin from *Pichia pastoris*, the required *Pichia* strain (X-33 stably integrated with pPICZc-ScAct1-thy β 4-8His) was kindly provided by the lab that had published the method (Hatano *et al.*, 2018; Balasubramanian lab, University of Warwick). This was the strain they had used to test and optimise the published method, so we could be certain it expressed and purified well under the right conditions. One aspect of the method we could not replicate was the method of cell breakage. Since we did not have local access to a freezer mill, a French press was used instead for breakage of cells in suspension at room temperature. Though the initial purification product was polymerisation-competent and appeared to be relatively pure (Figure 3.6), the yield was much lower than expected. The published method indicated the yield from 2 L induced culture (~20 g cell pellet) had been high enough to feasibly spin-concentrate the purified actin product to 100 μ M. In contrast, starting with an 8 g cell pellet, the adapted protocol had yielded only 12 μ M actin when concentrated into a volume smaller than 150 μ L. Even taking into account the difference in starting material, this was unexpectedly low and made further concentration of the product unfeasible.

To diagnose the potential causes of protein loss, samples that had been taken throughout the culture and purification process were separated by SDS-PAGE and visualised by Coomassie blue staining (Figure 3.7). The chymotrypsin cleavage step was identified as a major stage of protein loss because of a marked difference in the observed versus the expected ratio between fully liberated actin (resulting from chymotrypsin cleavage at the target site) and partially liberated actin (resulting from off-target chymotrypsin cleavage somewhere in the linker-thyβ4-linker-8His sequence) (Figure 3.7, lanes E and F, blue and red arrowheads). A Western blot in the published method revealed the ratio of these bands to be approximately 1:1. In contrast, our cleavage product was heavily skewed towards the partially liberated actin. This meant that most of the recombinant actin that had been expressed had retained additional residues from the fusion protein due to off-target chymotrypsin cleavage.

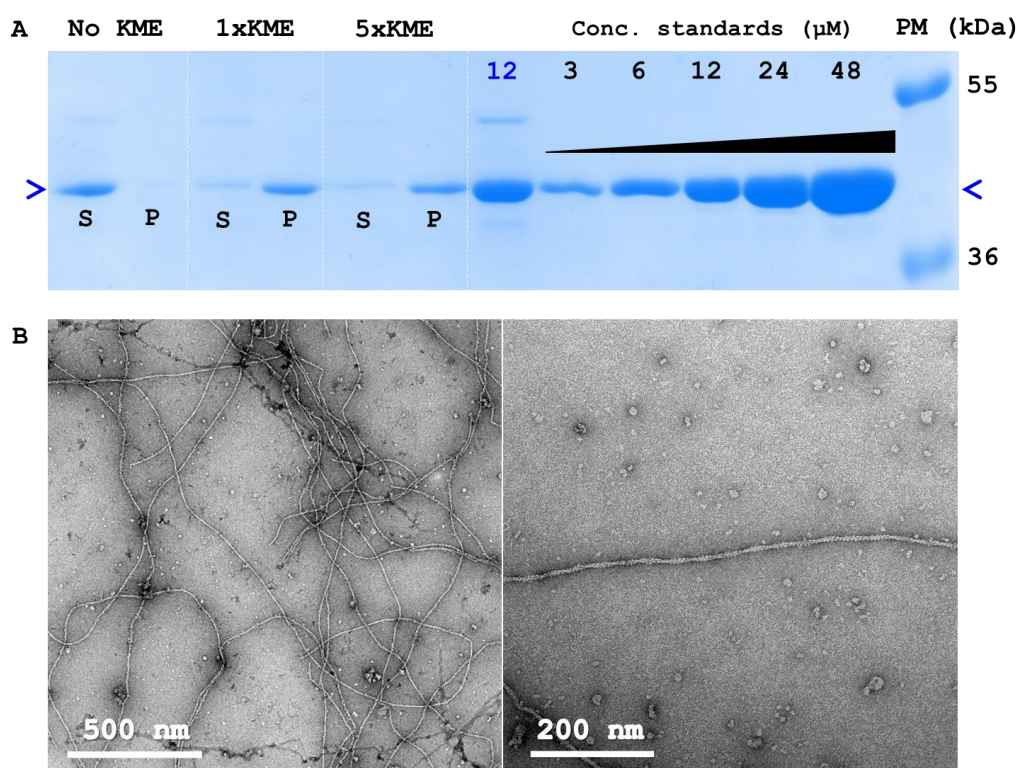


Figure 3.6: Assessing polymerisation-competence of purified recombinant actin. **A)** The supernatant (S) and pellet (P) from purified actin incubated in G-buffer ('no KME'), and following the addition of KME, or a 5x concentrated KME solution. Samples were spun at >100,000 x g which causes F-actin to pellet while G-actin remains in the supernatant. Coomassie-stained SDS-PAGE gel. **B)** TEM of negatively stained F-actin polymerised from the purification product.

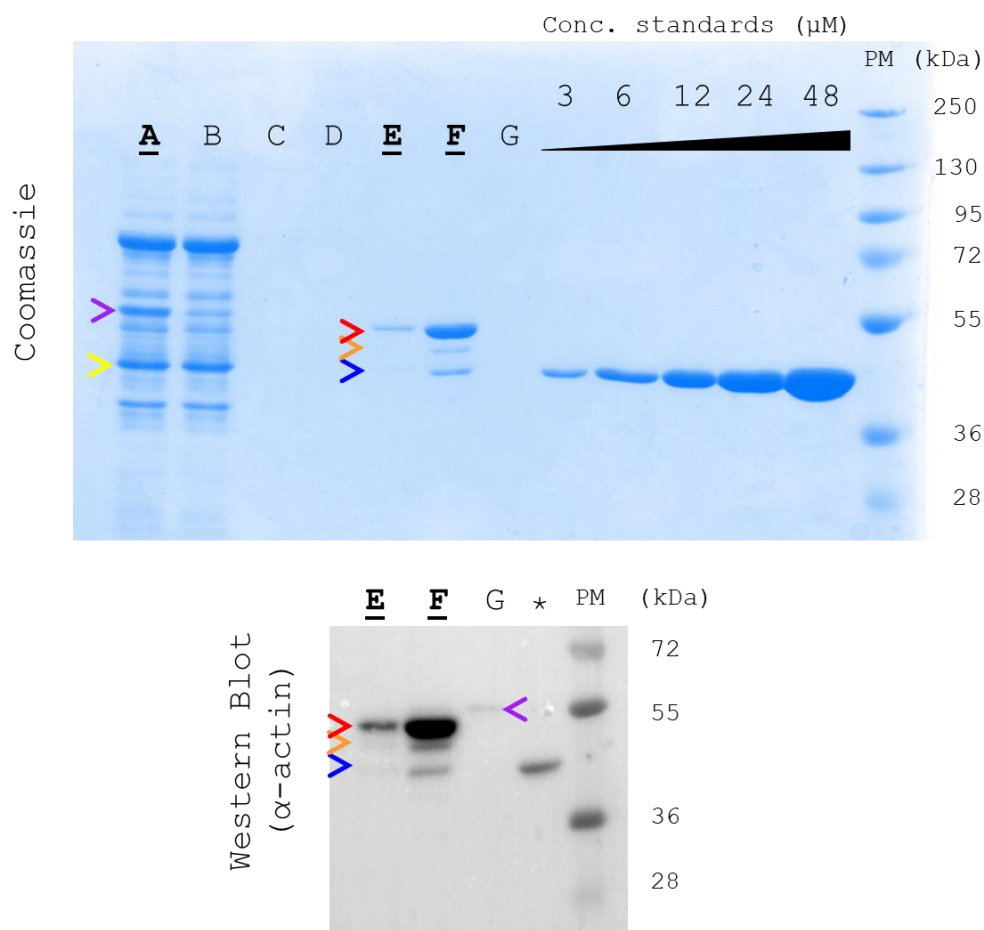


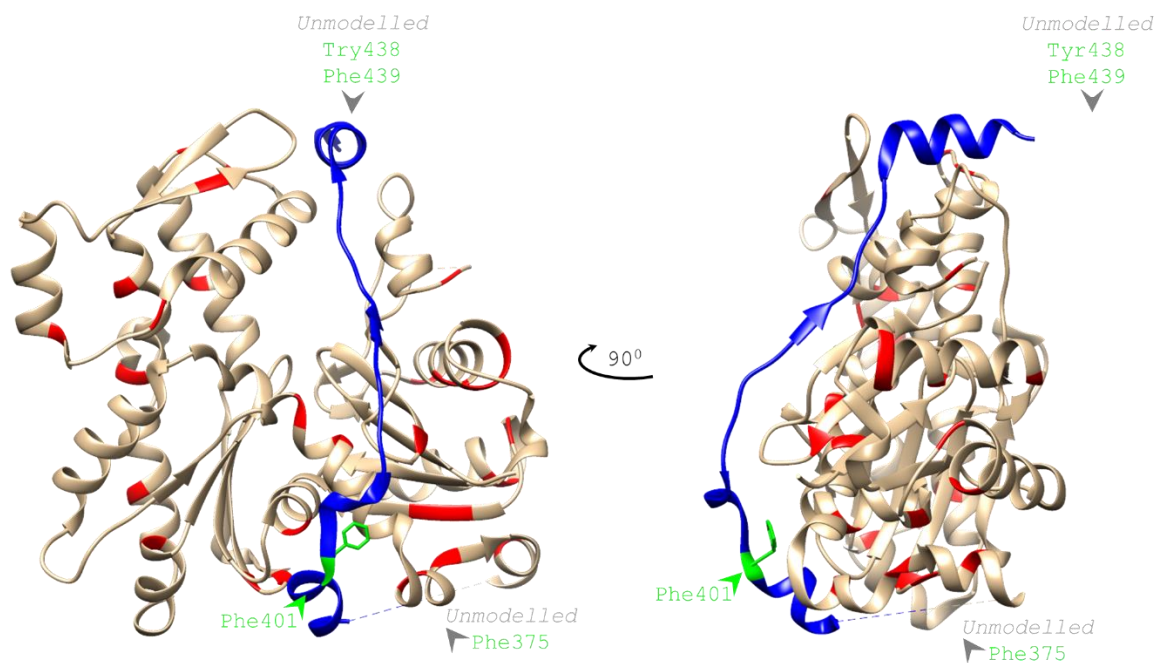
Figure 3.7: Samples taken throughout *Pichia* culture and actin purification, visualised by Coomassie blue stain and by Western blot. Bold underlined letters indicate samples that were carried forward into the next step (i.e. everything else was discarded as a waste product **A**) Filtered supernatant, **B**) Column flow-through, **C**) Beginning of binding buffer wash, **D**) Beginning of G-buffer wash, **E**) Protein liberated from nickel resin by chymotrypsin cleavage, **F**) Concentrate, **G**) Proteins retained on the Ni-NTA resin after chymotrypsin cleavage. *) Purified native *S. cerevisiae* actin, for reference. Arrowhead colouring corresponds to **Table 3.2**, except for the yellow arrowhead, which is putatively native *P. pastoris* actin.

3.2.3 Identifying Additional Chymotrypsin Cleavage Sites

To assess the efficiency of chymotrypsin cleavage, any protein that remained bound to the nickel resin was eluted and run on a gel (lane G, Figure 3.7). A band corresponding to the full-length fusion protein was only faintly detectable by Western blot, indicating that very little fusion protein remained totally uncleaved. Therefore, it was evident that the key issue at the chymotrypsin cleavage stage of the purification was with specificity rather than efficiency of the enzyme. It should be noted that bands for thyβ4-8His (~5 kDa) were not in the resolving range of this gel.

In addition to the ~42 kDa actin band, two extra bands were detected in the liberated cleavage product. These bands stained with anti-actin antibody in Western blot (Figure 3.7) and ran at a higher molecular weight than actin, confirming their identity as partially cleaved fusion products. Accordingly, the chymotrypsin was hypothesised to cleave other sites between the target site at Phe375 and the His-tag. Potential chymotrypsin cleavage sites for high-fidelity chymotrypsin were identified from the amino acid sequence of the fusion protein using the ExPASy PeptideCutter tool (Gasteiger *et al.*, 2005; Figure 3.8). Three of the identified sites (positions 401, 438 and 439) were located between Phe375 and the His-tag. The theoretical molecular mass of fragments that would be liberated from the Ni resin from cleavage at each site was calculated using the ExPASy Compute pI/Mw tool (Gasteiger *et al.*, 2005; Table 3.2), and this demonstrated that cleavage at either 438 or 439 would generate a cleavage product with an Mw of 48.2 kDa, while cleavage at 401 would generate a 44.2 kDa. This fitted well with the extra bands in the cleavage product.



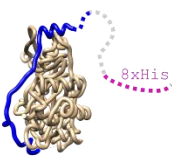









The larger partially cleaved fusion protein was detected in the final cycled product, but at a greatly depleted level compared to before cycling, relative to the fully liberated actin product (data not shown). Co-polymerisation of the partially cleaved fusion with fully liberated actin should be minimal since the full length thy β 4 remains intact, but given the partially cleaved fusion protein was present several times in excess of fully liberated actin in the crude purification product (lane F, Figure 3.7), it is unsurprising that some was retained after the cycling steps, most likely due to not being entirely washed off the F-actin pellet.



Enzyme	No. Cleavages	Positions of Cleavage Sites															
Chymotrypsin (high specificity)	32	21	53	79	86	90	91	124	127	132	133	143	166	169	188	198	200
		218	223	240	255	262	279	294	337	340	352	356	362	375	401	438	439

Figure 3.8: Potential chymotrypsin cleavage sites in the ScAct1-thyβ4-8His fusion protein. Potential cleavage sites for high specificity chymotrypsin were identified in the sequence of ScAct1-thyβ4-8His using the ExPASy PeptideCutter tool (Gasteiger *et al.*, 2005). These sites were labelled on the ribbon model in red if they occur before the target cleavage site at 375 in the primary sequence, or green if they occur afterwards. The ribbon model is an actin-thyβ4 fusion complex (PDB ID: 4PL7), with *P. pastoris* actin coloured beige and human thyβ4 coloured blue. Some sections of the model are missing because they were not resolved by X-ray crystallography: grey arrowheads indicate approximately where cleavage sites are in these missing sections. The same model is displayed here at two different angles.

Table 3.2: The molecular weight (MW) of theoretical fragments that would be generated from the candidate chymotrypsin cutting sites in Figure 3.8. MW was calculated using the ExPASy Compute pI/Mw tool (Gasteiger *et al.*, 2005). Actin is depicted in beige and thyβ4 in blue. A dashed line represents the C-terminal portion of thyβ4 and the His tag that were missing from the model. Other missing sections of the model (D-loop, actin C-terminus, 14aa linker and thyβ4 N-terminus) have not been added.

<u>Label</u>	<u>Description</u>	<u>Front View</u>	<u>Side View</u>	<u>Cleave After</u>	<u>MW</u>
	Full-Length Fusion Protein			N/A	50.1 kDa
	Larger Truncated Fusion Protein			Tyr438 Phe439	48.2 kDa
	Smaller Truncated Fusion Protein			Phe401	44.2 kDa
	Fully Liberated Actin			Phe375	41.7 kDa

3.2.4 Assessing Factors Affecting Chymotrypsin Cleavage

A number of factors were examined for their effect on chymotrypsin digestion: the buffer conditions used for chymotrypsin cleavage, the chymotrypsin concentration, the chymotrypsin stock used and the time/temperature of incubation.

Alterations to the G-buffer composition to match the published method did not affect the cleavage product band profile (Figure 3.9, lanes A and C). A condition using G-buffer without DTT was also tested (lane B) because this chemical reducing agent was known to be incompatible with certain laboratory reagents, but no difference was observed. A band corresponding to the uncleaved fusion protein appears only in the lane for the HEPES G-buffer (the buffer composition used by Hatano *et al.*, 2018), but this is suspected to be due to some Ni-resin contaminating the sample rather than the result of full-length fusion protein having disassociated from the resin.

An additional condition was run in parallel to determine whether using a concentration of chymotrypsin several times in excess of the recommended 5 µg/mL would increase the amount of fusion protein cleaved at the target site (Phe375). Using 100 µg/mL chymotrypsin (in the Tris-based G-buffer with DTT) did result in a denser band for fully liberated actin, but the proportion of this to other cleavage products remained similar (lane D, Figure 3.9). Two additional bands with a molecular weight lower than actin indicate that cleavage sites within the actin sequence were also targeted as a result of the increased chymotrypsin concentration. Using this higher level of chymotrypsin for a full-scale purification was not seen as feasible or worthwhile since it is an expensive reagent and a 20-fold increase in enzyme concentration had only resulted in a ~2-fold improvement in yield of the intended product.

A new chymotrypsin stock was purchased to rule out the possibility that the initial batch was performing poorly because it had partially denatured. Chymotrypsin from both stocks performed equally (Figure 3.10). At the same time, different temperatures and durations of digestion were tested, but also had no perceivable impact on the efficiency or specificity of digestion (Figure 3.10).

None of the conditions tested had replicated the ~1:1 ratio of actin:Tyr438/Phe439-cleaved fusion protein seen in the published method, indicating there was a problem with our method at an earlier stage of the process. Focus therefore turned to the cell culture stage.

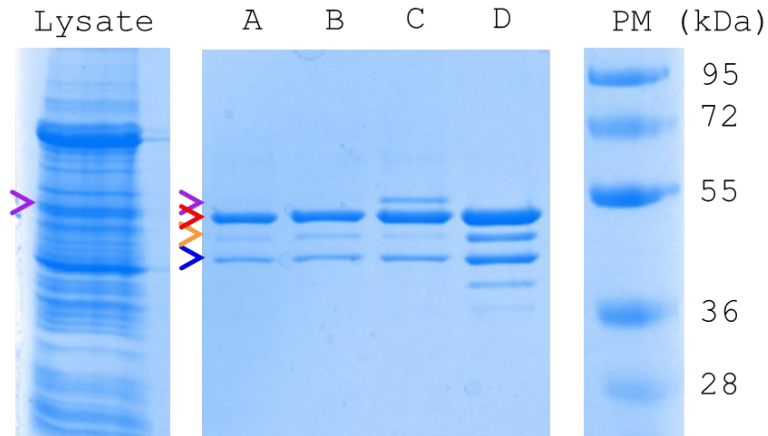


Figure 3.9: Chymotrypsin digestion performed under different conditions and enzyme concentrations. **A)** 5 $\mu\text{g}/\text{mL}$ in Tris G-buffer (conditions used in initial purification attempt), **B)** 5 $\mu\text{g}/\text{mL}$ in Tris G-buffer lacking DTT, **C)** 5 $\mu\text{g}/\text{mL}$ in HEPES G-buffer (conditions used in Hatano *et al.*, 2018) and **D)** 100 $\mu\text{g}/\text{mL}$ in Tris G-buffer. The resin was pelleted and the supernatant harvested following overnight incubation at 4 °C. Arrowhead colouring corresponds to Table 3.2.

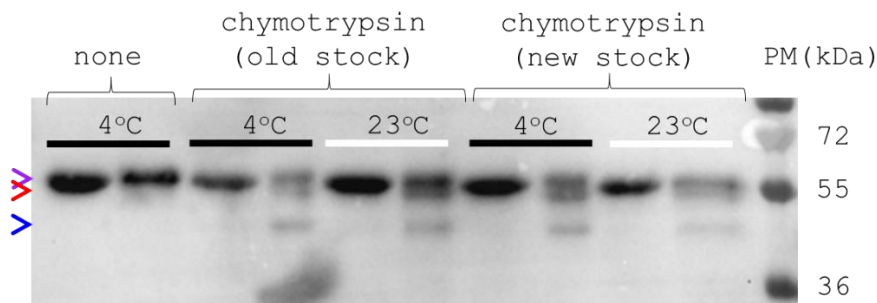


Figure 3.10: A Western blot (anti-actin) comparing different chymotrypsin stocks and incubation temperatures. Each condition has a sample for uncleaved and cleaved fusion protein (left and right lanes, respectively). Black lines indicate an incubation temperature of 4 °C and white lines an incubation at room temperature. Arrowhead colouring corresponds to Table 3.2.

3.2.5 Cell Culture Amendments to Improve Yield

Creating the correct cell culture environment required further clarification from the authors of the methods paper (Hatano *et al.*, 2018), and they kindly provided a demonstration in their lab at the University of Warwick. It transpired that the low actin yield we had experienced was due to insufficient oxygenation of the culture medium during methanol induction. The practicalities to ensure sufficient oxygenation were outlined in a source referenced by the paper (EasySelect™ *Pichia* Expression Kit User Manual, Invitrogen), but were not explicitly stated in the published method which we had used as a guide.

Oxygenation is of high importance during induction because it is required for the first step of methanol metabolism, which is the oxidation of methanol to formaldehyde by alcohol oxidase 1 using molecular oxygen (Vonck *et al.*, 2016). In addition to using high shaking speed (220 rpm), key practical measures to ensure sufficient aeration are 1) using baffled flasks to maximise turbidity and 2) ensuring the liquid level is no more than 10-30 % of flask volume. When these additional measures were incorporated in our protocol, Western blotting revealed that actin expression was comparable to that in a sample cultured in the lab of the authors (Figure 3.11).

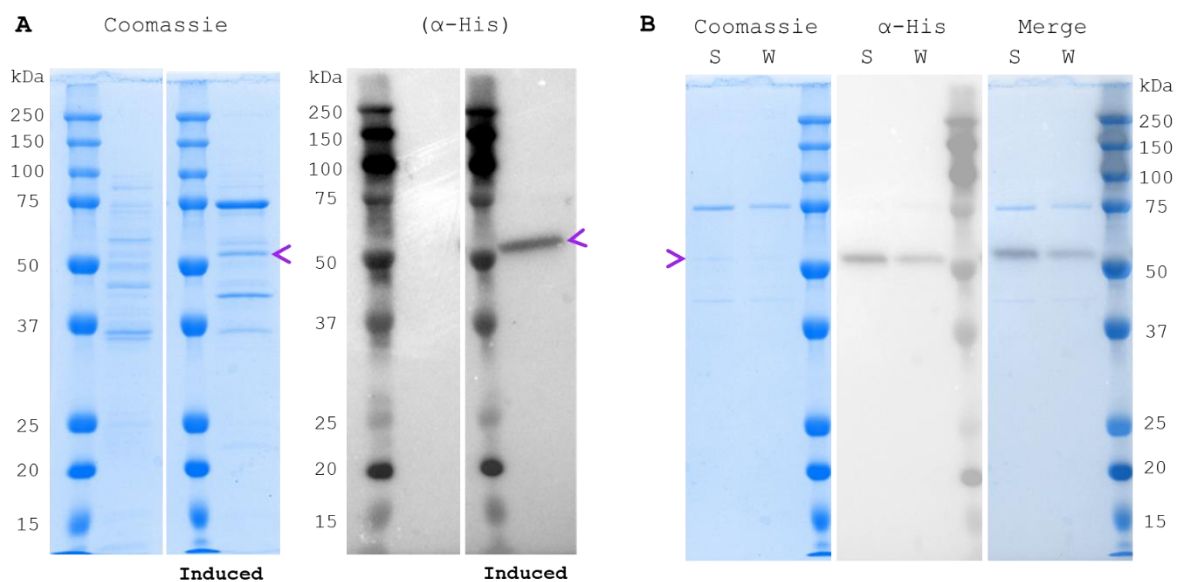


Figure 3.11: Induction of cultured *Pichia* in our lab was successful when adapted to incorporate measures for improved oxygenation. A) Before and after induction in our lab in Sheffield, shown by Coomassie blue staining and Western blot with an α -His antibody. In this case, 1 mL samples taken from the culture before and after induction were broken by vortexing with glass beads. B) The intensity of the band for ScAct1-thy β 4-8His in induced cell lysate from cells cultured and induced in our lab in the University of Sheffield (S) was comparable to that in induced cell lysate from cells cultured and induced at the University of Warwick (W). Cells from both conditions were broken in the freezer mill at the University of Warwick.

A thick band corresponding to the ~51 kDa full-length fusion protein was observed for the Ni-bound protein prior to chymotrypsin cleavage (Figure 3.12, lane C). However, interestingly, this band was not detectable among other bands in the cell lysate (lane A) and evidence of its depletion could not be seen by comparison with the unbound protein removed from the Ni-resin (lane B). The lysate band profile in general looks very different to the lysate from cells broken using a French press in Figure 3.7. This is not surprising as the French press lyses cells by disrupting the plasma membrane and cell wall to release cytosolic proteins. Consequently, most membrane proteins and

proteins in organelles, including the nucleus, will be pelleted and removed along with cell debris and therefore will be absent in the lysate. In contrast, freeze-grinding shears all parts of the cell non-discriminately and consequently will solubilise a higher proportion of cellular proteins. It therefore makes sense that the higher background from the freeze-ground lysate masked the fusion protein band. Notably, despite the higher background, the band for alcohol oxidase 1 (~72 kDa) was greatly enhanced in the freezer mill lysate. This is a good indicator of stronger induction of the *AOX1* promoter compared to the poorly oxygenated culture conditions we had used before.

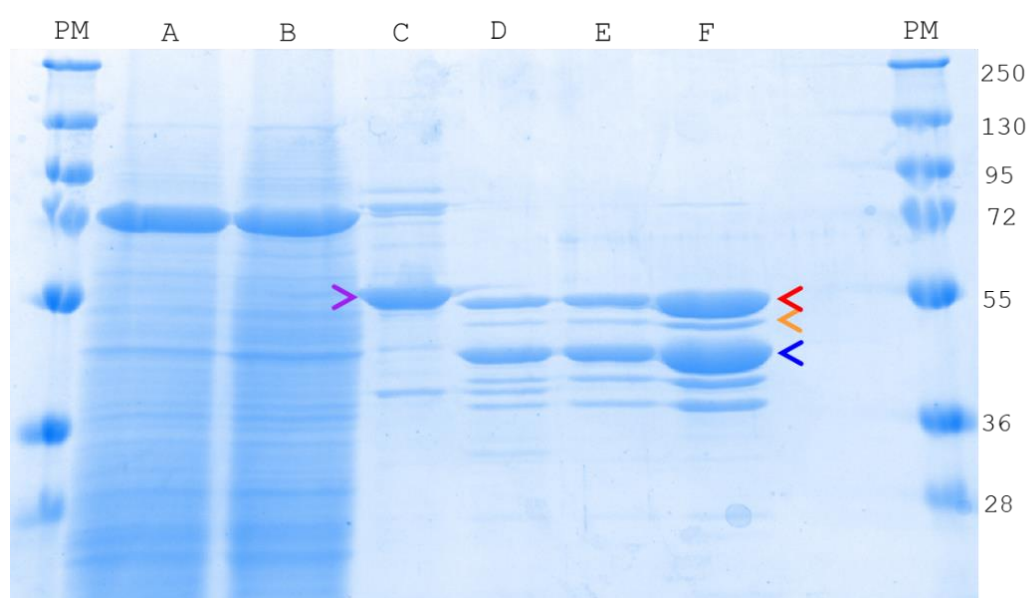


Figure 3.12: Purification intermediates at the University of Sheffield, using *Pichia* cultured, induced and broken at the University of Warwick. This gel shows initial purification steps (pre-cycling). **A)** Whole cell lysate, **B)** Depleted cell lysate (recovered after incubation with Ni-NTA resin), **C)** Nickel-resin bound proteins before chymotrypsin cleavage, **D)** Nickel resin and liberated proteins after chymotrypsin cleavage, **E)** Liberated proteins after chymotrypsin cleavage, **F)** Partially concentrated. This time the bands corresponding to the larger partially liberated fusion protein (red arrow) to fully-liberated actin (blue arrow) were observed at the expected ratio of approximately 1:1.

The purification steps were almost identical to our adapted version. It was, however, noted that the authors used more stringent wash steps before chymotrypsin cleavage to ensure all protease inhibitors are removed. After incorporating the above practicalities into our culture and purification method, the band patterning in the product following chymotrypsin cleavage was as expected; with a ratio between fully liberated actin and the larger truncated fusion protein close to 1:1 (Figure 3.12). The freezer mill was used for cell breakage of both preparations to remove cell

breakage as a variable. After the cycling step, the final purification product was quantified as 25 μM , in a volume of $\sim 950 \mu\text{L}$ (Figure 3.13). This was found to be polymerisation-competent and assembled filaments that appeared largely free of debris when examined by TEM, indicating it was suitable for progression to cryo-EM (Chapter 4).

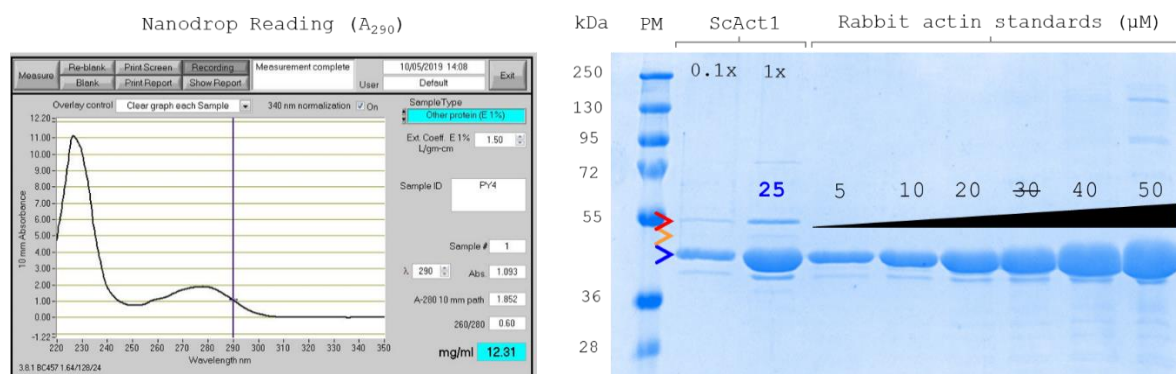


Figure 3.13: The actin purification product using cells cultured, induced and broken at the University of Warwick and purified at the University of Sheffield. Absorbance at 290 nm (left) indicated the purification product contained 12.31 mg/mL protein, which is equivalent to approximately 29.5 μM actin. However, this is an overestimate as it includes impurities. The concentration of actin alone was calculated to be 25 μM (equivalent to approximately 10.5 mg/mL) by comparison to actin standards run on a Coomassie gel (left). The 30 μM standard was omitted from the calculation due to a pipetting error. The volume of the purification product was $\sim 950 \mu\text{L}$, and the starting material was 2 L methanol-induced *Pichia* culture.

3.2.6 Contamination by Native *P. pastoris* Actin

Using fully liberated *S. cerevisiae* actin in parallel lanes as a MW reference, we did not detect an obvious 42 kDa band for native *P. pastoris* actin among the Ni-NTA-bound proteins at the early stages of recombinant actin purification (Figure 3.12, lane C). The lack of a prominent 42 kDa band in the Ni-NTA bound fraction was the reasoning used by the authors of the published method to indicate that the native *Pichia* actin did not appreciably co-purify with the recombinant actin.

To better understand the composition of our purification product, we decided to verify the absence of native *Pichia* actin with a more sensitive method. Mass spectrometry was used to ascertain whether actin from the *Pichia pastoris* host (Q9P4D1, ACT_KOMPG) was present in the final purified product as well as the intended *S. cerevisiae* actin (P60010, ACT_YEAST). 48 unique peptides were detected for *S. cerevisiae* Act1, while 9 unique peptides were detected for *Pichia* actin. Unfortunately, this does indicate that the purification product consists of a mix of actin isoforms.

However, these two yeast actin isoforms have 94% sequence identity, which is a much higher degree of conservation than the difference between *S. cerevisiae* and vertebrate α -actin (87% identity). Also, given the ratio of unique peptides as an approximation for the abundance of the different actin isoforms present ($48/9 = 5.33$), the number of *S. cerevisiae* actin monomers was more than five-fold higher than the number of *Pichia* actin isoform monomers. Given the time limitations of the project and the difficulties already encountered with purification, it was decided to push ahead with the structural work, at least to get an initial structure on the in-house cryo-EM microscope.

3.2.7 Introducing Polymerisation-Impairing Mutations: The Concept

With the *Pichia* expression system now established in our lab, we next harnessed the system for the purification of mutant actin isoforms. Since the use of the thy β 4 fusion in the *Pichia* system prevents recombinant actin incorporating into the native actin cytoskeleton, mutant actin isoforms can be expressed without conferring toxicity on the host cell (Umeki *et al.*, 2019).

We were interested in the potential for polymerisation-impaired actin mutants as tools for *in vitro* assays to better understand the actin nucleating capability of Las17. We were aware of published work in which two polymerisation-impaired mutants had been used to mimic a tetrameric actin nucleus for a structural study of a nucleus-nucleator complex with the tandem-WH2 domain actin nucleator Spire (Chen *et al.*, 2013). This work could not have been performed with wild-type actin because the actin nucleus has only a fleeting existence: once the nucleus is formed, it rapidly seeds the polymerisation of a new filament. Since one mutant actin was unable to interact with actin monomers at its barbed (plus) end, and the other was unable to interact with actin monomers at its pointed (minus) end, the mutant tetramer was prevented from forming a higher order structure than a tetramer. The presence of Spire stabilised the tetrameric state and permitted X-ray crystallography of the crystallised complex. We saw this pseudo-nucleus system as a potentially useful tool for studying the structure, nucleating activity and actin-binding of Las17PP. Other potential applications we have considered for these mutants are a topic of the discussion.

3.2.8 Site-Directed Mutagenesis

The actin mutants used by Chen *et al.*, 2013 used the *Drosophila melanogaster* 5C actin isoform (UniProtKB P10987; ACT1_DROME). This actin isoform shares 89% sequence identity with *S. cerevisiae*, and the target residues for mutation are conserved, making it likely that the mutations they had used would confer the same effect in *S. cerevisiae* actin. The mutant sequences were made by substituting specific residues for glutamic acid and lysine: pointed-end (A204E, P243K); barbed-end (K291E, P322K). Suitable codons are annotated in Figure 3.14 and the primers used are shown in Figure 3.15. Starting with the pPICZc-*ScAct1*-thy β 4-8His plasmid, each mutant plasmid was generated by two successive rounds of mutagenesis and verified by sequencing.

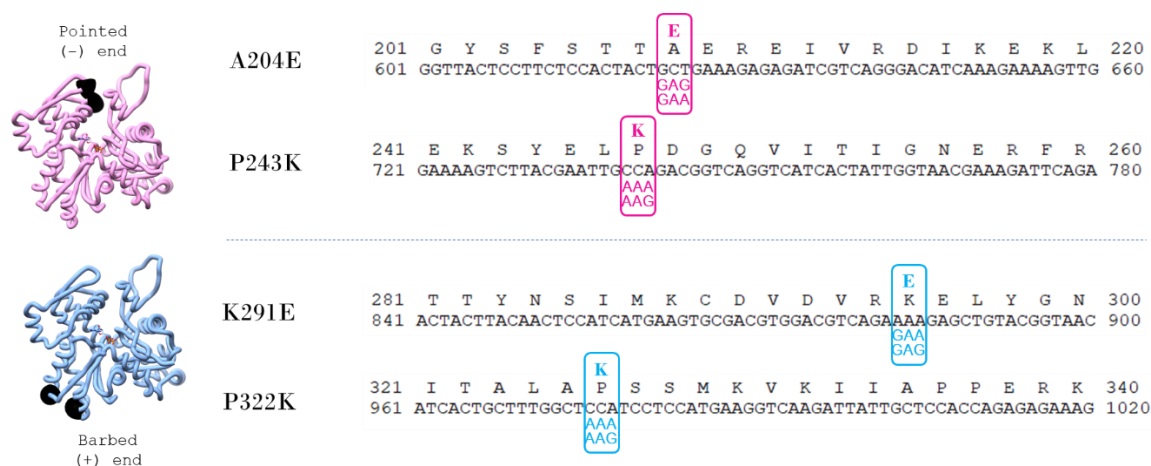


Figure 3.14: Codon options for site-directed mutagenesis. Sections of the *S. cerevisiae* Act1 protein sequence and DNA sequence as it is in the pPICZc-*ScAct1*-thy β 4-8His plasmid (codon-optimised for expression in *P. pastoris*). Codons targeted for mutagenesis target sites are ringed, with the mutant amino acid substitution shown above, and the *Pichia*-optimised codons that could generate this below the original sequence. The positions of the substitutions on the actin backbone are indicated by black spheres on the liquorice model of each mutant.

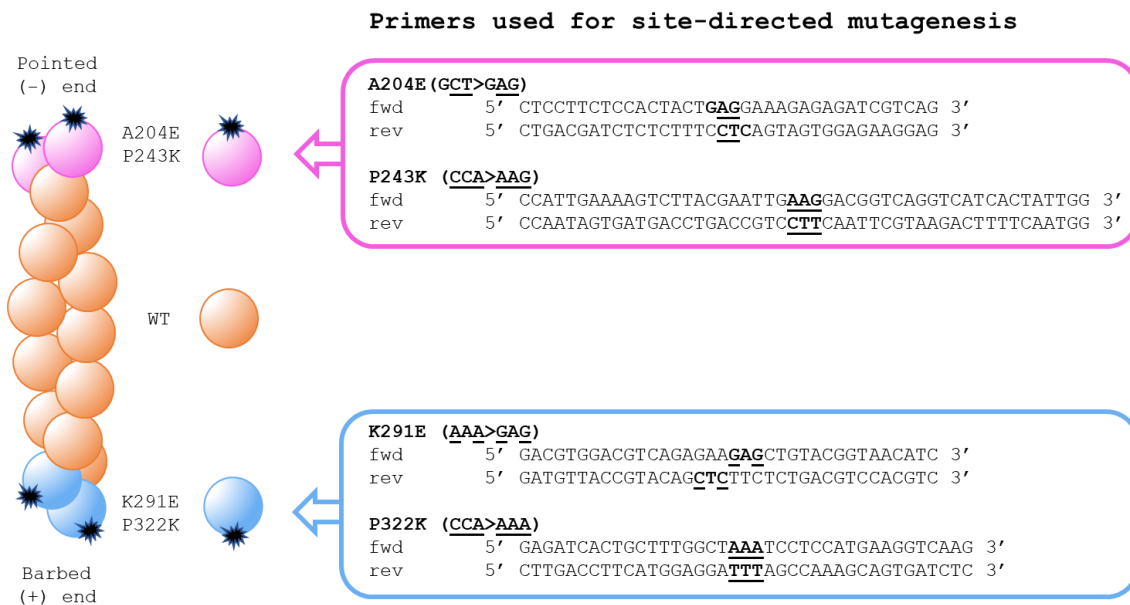


Figure 3.15: Primers for making polymerisation-impaired actin mutants by site-directed mutagenesis. Primers used for site-directed mutagenesis of the pPICZc-ScAct1-thy β 4-8His plasmid in order to create two new constructs, each encoding a different polymerisation-impaired actin isoform.

3.2.9 Subsequent Steps

The next step for each mutant plasmid was stable integration into the *P. pastoris* genome (using the Mut⁺ *Pichia* strain X-33). This required linearisation of each mutant plasmid at the *AOX1* locus, which was achieved with the restriction enzyme PmeI (Figure 3.16), as used for integration of the original wildtype ScAct1 plasmid (Hatano *et al.*, 2018). Transformation of *Pichia* by electroporation and the purification of both mutant actin isoforms was carried out by another lab member (EGA, KA lab).

The final step of the purification of wild-type (WT) actin is a polymerisation cycle to select for polymerisation-competent actin over impurities. However this was not possible for the mutant actin isoforms due to their inability to polymerise. Like the WT actin, the major impurities are partially-cleaved fusion proteins (see Figure 3.12). Improvements for the purity are a topic of the discussion. Yield was fairly low: ~13 μ M for B* and ~3 μ M for P*, in ~0.4 mL; compared to ~25 μ M wild-type actin in ~0.95 mL. The low yield might be due to using a cell homogeniser for cell breakage rather than a freezer mill since this equipment was not available to us at the time.

As an outcome of this work, *S. cerevisiae* versions of both polymerisation-impaired mutants can now be expressed through the *Pichia* expression system, although further improvements are required to improve the purity and yield. Both mutant actin isoforms were found to be non-polymerisable, as assayed by their retention in the supernatant in a high-speed pelleting assay (KA lab; data not shown; see Figure 3.6A for an example of assessing polymerisation competence using this assay).

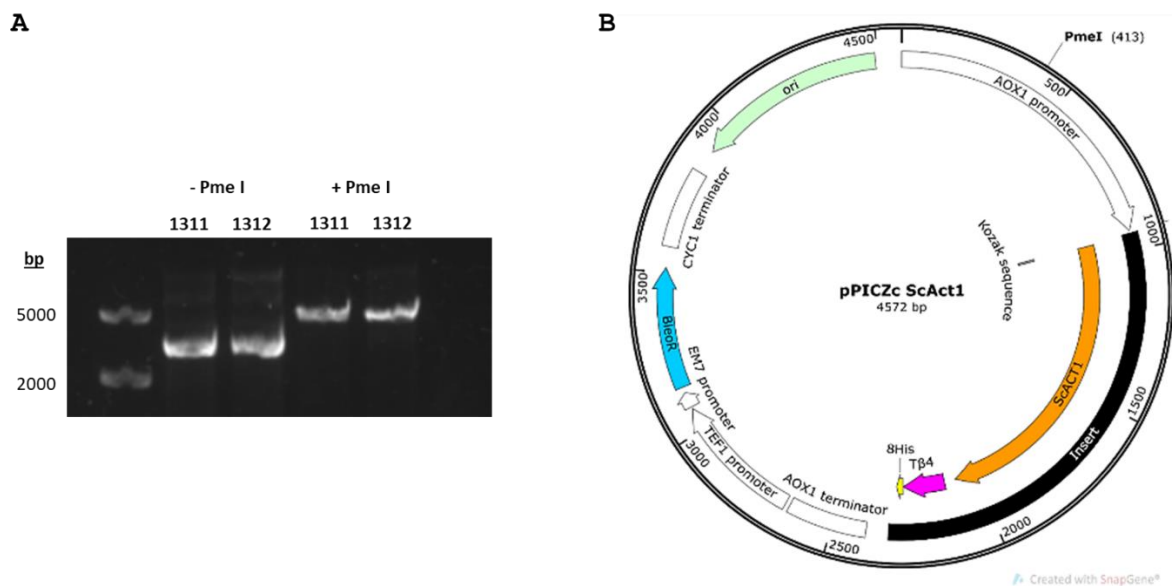


Figure 3.16: Plasmid linearization by PmeI. A) The digestion product migrated more slowly through a 1% agarose gel, indicating linearisation was successful. B) PmeI cuts the pPICZC-ScAct1-thy β 4-8His plasmid in the AOX1 promoter region. The plasmid map was created in SnapGene®.

3.3 Discussion

3.3.1 Choice of Purification Method

The traditional DNase I method of purification remains a valid and popular method for purifying native actin from non-muscle sources. However, after some initial success with the crude purification, we were unable to use this method to reliably produce sufficient actin for the experimental demands of this project. The problems we encountered were specific to our set-up: possibly due to a problem with our DNase I column. The sudden drop-off in yield between two sequential batches could be explained by the denaturation of the immobilised DNase I upon exposure to air, rather than a decrease in activity owing to repeated use which would be expected to cause a more gradual decline in yield. Following an unsuccessful attempt to replenish the DNase I column, it was decided that there was more value in exploring a novel purification method than optimising the set-up for this traditional native actin purification technique.

The alternative method for purifying non-muscle actin isoforms recombinantly from a *Pichia pastoris* expression system (Hatano *et al.*, 2018) worked well in our hands once the correct measures had been taken for ensuring sufficient aeration of cultured cells during induction. Our final adapted method is very similar to the original but customised to our available reagents and equipment. Rather than simply being an alternative to the DNase I method of purifying non-muscle actin isoforms, the recombinant method using *Pichia* offers a system with versatility. It can be applied to any actin isoform (e.g. from any tissue or species, wild-type or mutant), and it also has the potential for vast up-scaling if the users have access to an industrial fermenter. As we discovered from mass spectrometry analysis, a potential disadvantage of this method is contamination by *Pichia pastoris* actin, which transpired to be more of a problem than concluded in the published method. However, if successful, our suggested modification to improve yield (discussed below in section 3.3.3), would greatly enrich the purity of the recombinant actin isoform compared to the *Pichia* host actin isoform.

3.3.2 Practical Considerations for *Pichia* Cell Lysis

The freezer mill at the University of Warwick offered considerable advantages for large-scale *Pichia* cell lysis over the lysis methods available in our lab. Being able to break cells at a very high concentration allows high throughput: the freezer mill has the capacity to break cells from 20 g wet pellet at a time, compared with the French press which can only handle half this given the need for a relatively dilute cell suspension. Another important advantage offered by the freezer mill is that temperatures of -80°C or cooler are maintained throughout, which is low enough to suppress protease activity. A final advantage of the freezer mill over the French press is that it releases a much higher proportion of cellular protein, as evident from the much greater number of bands in the lysate from this method (Figure 3.12A) compared to the lysate from the French press (Figure 3.7A). This means any actin-thy β 4-8His sequestered within organelles will also be accessible for purification, rather than only what is available in the cytoplasm. For reasons listed above, our large-scale purifications took advantage of this machinery, hosted in the University of Warwick. However, the freezer mill equipment is expensive and requires specialist infrastructure to ensure proper ventilation. These considerations made it unfeasible to purchase the equipment for our own lab for the purpose of this PhD project.

For small volumes such as 1 mL culture samples taken for analytical purposes, breakage using glass beads and vortexing (with regular intervals on ice) proved to be an effective cell lysis technique. However, this was not suitable for the large volumes (30-150 mL) involved in a purification. We also trialled the use of a Waring blender to break frozen yeast droplets. The major limitation of this method was that the fine lysate powder easily escaped the apparatus, resulting in a significant loss of material (from 48 g yeast droplets we retained only 11 g of cell lysate). To make the droplets, the cell pellet had been resuspended 1 in 4 with water, so the remaining 11 g lysate was equivalent to only 2.75 g cell pellet (<30% of the minimum mass normally used for a single purification).

The project required a steady supply of wild-type *S. cerevisiae* actin, so a consistently good yield from a single purification batch was essential for the viability of the project. However, for instances where the purification product was used more sparingly in its applications, use of the French press or a cell homogeniser could be justified.

3.3.3 Suggested Improvements to Recombinant Actin Purity

Removal of Off-Target Chymotrypsin Cleavage Sites

Even with the purification protocol optimised to match the expected yields of the published method, there is a significant amount of protein loss (~50%) at the chymotrypsin cleavage stage of this method (Figure 3.12, lanes E and F). Our sequence-based examination of chymotrypsin cleavage sites on the recombinant fusion protein has indicated that the major off-target cleavage site is actually two adjacent cleavage sites: residues Tyr438 and Phe439 (Table 3.2). These residues are located in the flexible linker sequence connecting human $\text{thy}\beta 4$ with the 8xHis tag, so the residue identity is of little functional or structural importance. Therefore, we propose that the efficiency of this purification method could be greatly improved by mutating these residues to ones not targeted by chymotrypsin. With these cleavage sites removed, we expect a much greater portion of the fusion to experience on-target cleavage, after Phe375.

The remaining off-target cleavage site (Phe401 in the $\text{thy}\beta 4$ sequence) does not appear to be favoured by chymotrypsin, since the ~44 kDa band corresponding cleavage product was much less prevalent than the others. This is suggestive of this site only becoming available for cleavage if the $\text{thy}\beta 4$ temporarily dissociates from the fused actin, restricting accessibility for protease digestion. Removing the Tyr438/Phe439 off-target cleavage sites might result in increased cleavage at Phe401, but this is likely to be vastly outweighed by the increase in cleavage at the target site (Phe375). Based on the roughly equal abundance of cleavage products from on-target Phe375 and off-target Tyr438/Phe439, it is reasonable to predict that our suggested modification has the potential to roughly double product yield.

An interesting development from the authors of the recombinant actin method is the expansion of the capabilities of the method to allow the introduction of specific post-translational modifications (Hatano *et al.*, 2020). With the foreseeable increase in demand for this method of actin purification, our suggested modification to increase on-target chymotrypsin cleavage, if effective, could be of great benefit to the scientific community adopting this method.

Considerations for Improving Purity of Polymerisation-Impaired Mutant Actin Isoforms

As mentioned, further purification of actin by a polymerisation cycle ('cycling') step is effective for WT actin, but not possible for the polymerisation-impaired actin isoforms. Conversely, the tendency of WT actin to spontaneously polymerise makes it unsuitable for loading into a size-exclusion chromatography column. The mutants would not have this problem, and therefore it may be possible to separate the fully liberated mutant isoforms from impurities. The difficulty with this method for the mutant isoforms is that, like the WT actin, the major impurities are partially cleaved fusion proteins (see Figure 3.12F), which have very similar molecular masses that might not be easily resolved by gel filtration. Still, if our proposed method of removing the major off-target chymotrypsin cleavage sites is successful in greatly depleting what is currently the major contaminant, the *Pichia* expression system could be extremely effective for the production of high-purity polymerisation-impaired mutant actin isoforms. In light of the higher-than-expected contamination we detected from native *Pichia* actin, the inability of these mutant actin isoforms to polymerise could actually serve as an advantage for their further purification, since a cycling step could separate native (cycling) actin from mutant (non-cycling) actin.

3.3.4 Potential Applications of Polymerisation-Impaired Actin Mutants

The polymerisation-impaired mutant actin isoforms described in this chapter have been established to form an effective pseudo-nucleus in the presence of a stabilising actin nucleator (Chen *et al.*, 2013). Prior to that, the A204E/P243K mutant was used to obtain the first X-ray crystal structure of G-actin without bound proteins or non-physiological toxins or chemical modifications (Rould *et al.*, 2006).

Like X-ray crystallography, some biochemical assays require actin to remain in a monomeric state, and its tendency to spontaneously polymerise is disadvantageous. For example, other lab members have been experiencing artefacts from actin polymerisation when measuring the actin binding affinity of ABPs using micro-scale thermophoresis. Substituting wildtype actin for one of the polymerisation-impaired mutants would be expected to prevent these artefacts. Furthermore,

having the choice of two mutants would enable choice of the most appropriate one to use depending on the predicted actin binding site of the protein of interest.

We are also interested in the application of these polymerisation-impaired actin mutants as a tool for creating custom-length filaments, by altering the ratio of wild-type and mutant isoforms. This would rely on the mutants being able to act as dynamic capping proteins for WT actin filaments to generate a population of shorter filaments than in a WT-only population. This would have useful applications for cryo-EM because several short filaments would distribute more evenly in the thin ice layer than the same amount of actin in long filaments. Generating more filament ends would also facilitate further structural study of filament end conformation, building on the work of Narita *et al.*, 2006; Narita, Oda and Maéda, 2011, which has so far eluded high resolution structural interrogation.

4. Solving Yeast F-Actin Structure with Cryo-EM

4.1 Introduction

Due to high sequence conservation across actin isoforms within and between species, it has generally been assumed that the structure of F-actin is conserved to a high degree across eukaryotes. However, existing high-resolution structural data for F-actin still represents only a minute subset of Eukarya, with published high-resolution structures covering just two non-vertebrate species at the time of writing: the apicomplexan malaria parasite *Plasmodium falciparum* (Pospich *et al.*, 2017; Robert-Paganin *et al.*, 2021; Vahokoski *et al.*, *to be published*) and the grass family species *Zea mays* (maize or corn; Ren *et al.*, 2019). These structures have so far confirmed a high degree of structural conservation but have also revealed some subtle but significant structural differences that seem likely to account for functional differences in stability.

F-actin from the kingdom Fungi is so far unrepresented by high resolution structural data, and yet much of our fundamental knowledge of actin is derived from biochemical and genetic studies using the budding yeast *S. cerevisiae* ('baker's yeast'); a member of the fungus kingdom that is commonly used as a model organism across several biological fields. It is an example of an organism with only one actin gene (*ACT1*), with no reported isoform variation. Our direct structural knowledge of F-actin from this species has been previously limited to a small number of low-resolution reconstructions (Orlova *et al.*, 1997, 2001; Belmont *et al.*, 1999). These reconstructions tentatively indicated some structural differences in baker's yeast F-actin compared to α -skeletal muscle F-actin derived from rabbit tissue.

A primary aim of this project was to re-examine the comparison between yeast F-actin and vertebrate skeletal muscle F-actin. To allow detailed comparison, it was necessary to solve the structure of yeast F-actin to much higher resolution than had been previously achieved (~23 Å). The purified recombinant *S. cerevisiae* actin described in Chapter 3 was polymerized with KME and imaged using cryo-EM. This chapter focuses on the cryo-EM reconstruction process that was used to make the F-actin map.

Reconstruction was performed using the open-source computer program RELION (REgularized Likelihood Optimization; Scheres, 2012; Fernandez-Leiro and Scheres, 2017). This program integrates multiple automated processing steps required for single particle analysis of cryo-EM data, from pre-processing to refinement. The distinction of RELION is its Bayesian approach to aligning and classifying particles, which infers parameters from the data to calculate maximum likelihood. A key advantage of this approach is its accessibility to researchers new to the cryo-EM field, owing to the reduced reliance on user expertise compared to earlier methods. This said, informed user input is still fundamental to guide the reconstruction process, as incorrect parameters yield poor results. The latest versions of RELION (3.0 and 3.1) include a reconstruction pathway for macromolecules with helical symmetry (He and Scheres, 2017). Reconstruction of 3D objects from electron micrographs by helical reconstruction is covered in Section 1.2.4 of the Introduction Chapter.

4.2 Cryo-EM Sample Preparation and Data Collection

4.2.1 Optimising Sample Preparation and Data Collection Strategy

Actin filament concentration is difficult to measure directly, so G-actin concentration prior to polymerisation was used as a proxy to guide sample preparation. Actin concentration was optimized to determine the concentration which would most consistently result in a filament density that was relatively high, but with limited filament overlap. The optimal concentration was found to be 1 μM (~ 0.042 mg/mL) G-actin, provided grids were blotted from the back side (the front side being the carbon-coated face of the grid to which sample is applied). Early optimisation experiments revealed that blotting from the front side or both sides of the grid required much higher concentrations of actin (>5 - 10 μM), indicating a migration of filaments to the filter paper. Back-blotting was therefore adopted as the standard protocol for grid preparation.

A key difficulty with sample optimisation was that the filament distribution on a single cryo-EM grid was highly variable, ranging from areas of ice completely devoid of filaments to areas with

dense mats of filaments. An example of variation found within a single grid square is shown in Figure 4.1, and the variation over an entire grid was even more extreme. Since sample optimisation was made challenging by inconsistencies within and between samples, a data collection strategy was developed to maximise the amount of data that could be extracted from a less than optimal grid. It was observed that holes which had both thin ice and a sparse filament distribution were most likely to be found towards the grid square edge (Figure 4.1C). Therefore, at the template definition stage of automated acquisition set-up, the majority of foil holes selected were those close to the grid bar that appeared to have the thinnest ice. Problems that led to discarding datasets collected early on in the project included thick ice, poor particle distribution and beam damage. This was later circumvented by the use of on-the-fly pre-processing software Warp (Tegunov and Cramer, 2019), which provided a useful indication of issues – such as poor Thon rings due to thick ice (McMullan, Vinothkumar and Henderson, 2015) – as they arose in real time.

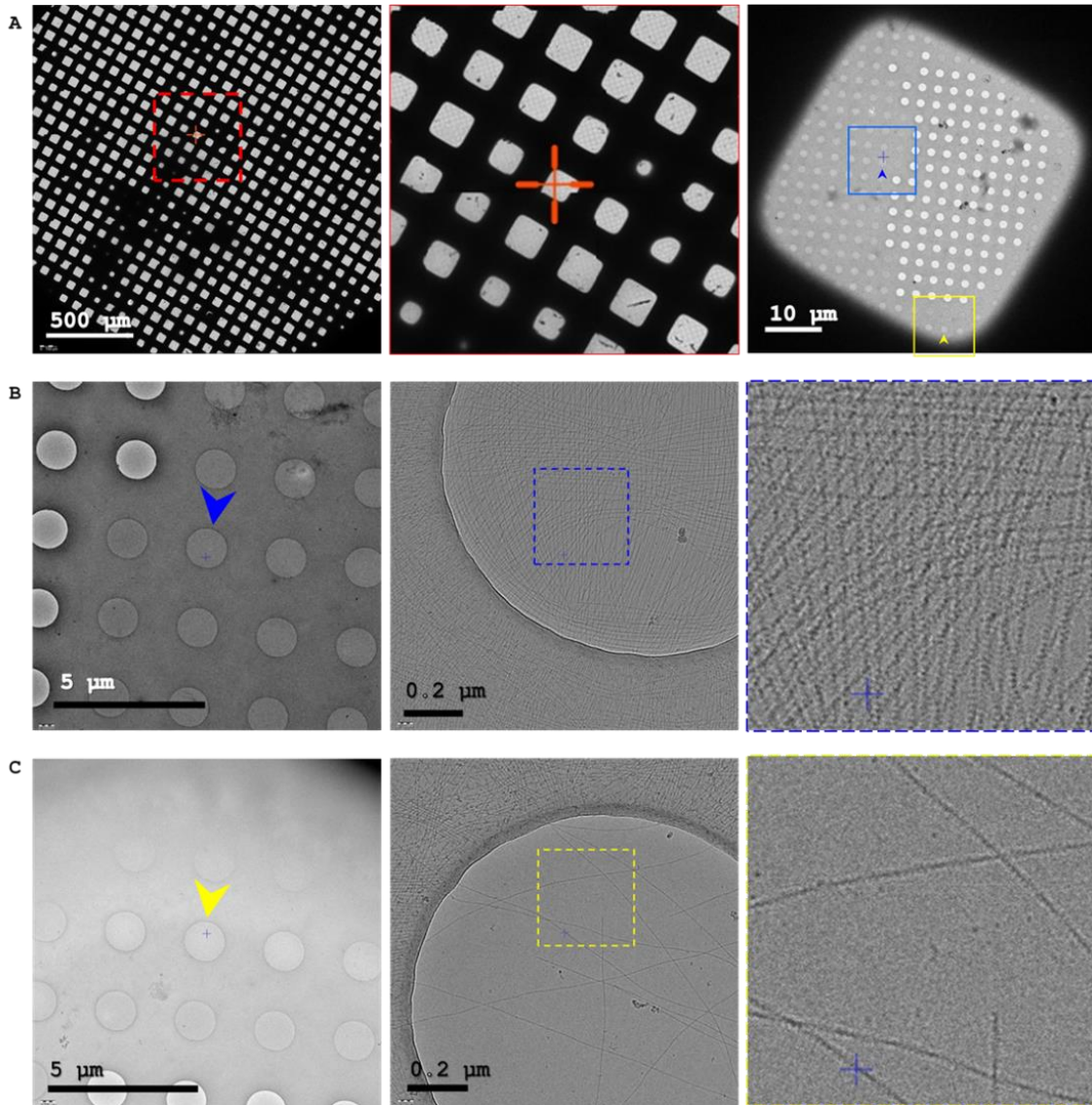


Figure 4.1: Foil holes suitable for data collection were most often found near the grid square edge. A) Low magnification views of a Quantifoil R1.2/1.3 grid loaded with F-actin polymerised from 1 μM G-actin by the addition of KME. An atlas of the grid composed of 8 x 8 images collected at 165x (left and enlarged central image), has a red cross positioned over the grid square screened in panels B and C (570x; right). Coloured arrowheads indicate the position of the individual foil holes shown in panels B and C. B and C) On the left, a higher magnification view of the ice holes (3,800x). The hole screened in the next image is indicated by an arrowhead. A microscope magnification of 39,000x was used for screening, which is high enough for filaments to be visible and allows a field of view wide enough to cover almost the entire foil hole. For all rows, the image on the right is an enlarged section from the middle image.

4.3 The Reconstruction Process

4.3.1 Reconstruction Pipeline

The dataset used for reconstruction was collected at 110,000 x microscope magnification from 2 grids over a 48hr period. Using motion-corrected preview images generated by the software EPU, 142 out of 409 micrograph movies were manually selected on the basis that they contained some non-overlapping regions of actin filaments and lacked major artefacts such as large ice crystals or tears in the carbon film. A number of micrographs were observed to have two-toned banding (as seen in Figure 4.5B). This was found to be due to intermittent problems with the camera control box that affected frame processing and transfer of processed frames to the storage server. Micrographs bearing this artefact were still used for particle picking where filaments could be seen clearly, but with care taken to avoid picking coordinates on the banding interface.

Figure 4.2 outlines the reconstruction pipeline followed for producing a 3D map in RELION 3.1. Not all of these steps contributed to the evolution of the map. For instance, 2D classification and local resolution were used to assess data and map quality, respectively. 3D classification was used to investigate potential variations within the dataset but, owing to the already relatively small size of the dataset (<42,000 particles), the resolution of an individual class from just a subset of this number of particles was limited. After an initial template-based 3D refinement, particle polishing slightly increased the resolution that could be achieved. Finally, owing to a discrepancy between the nominal and true pixel size, the map was rescaled by performing CTF refinement and postprocessed with the calibrated pixel size, as covered in section 4.3.10.

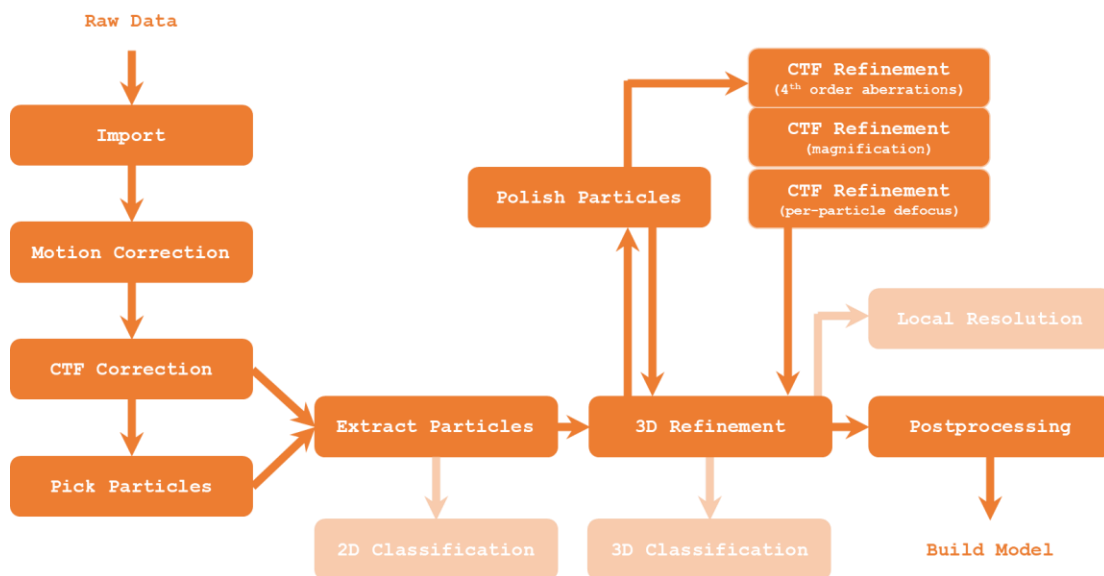


Figure 4.2: Pipeline used for reconstructing yeast F-actin in RELION 3.1. The paler shade of orange indicates steps that were performed but that did not contribute to the evolution of the map.

4.3.2 Motion Correction

The importance of motion correction for the processing of cryo-EM data is covered in section 1.2.3. Motion correction was performed using the program MotionCor2 (Zheng *et al.*, 2017). The micrographs (each 4000 pixels²) were divided into 25 ‘patches’ (5 x 5) for local motion tracking, and the motion trajectory plots in the generated logfile were used to make decisions about the quality of the dataset. An example of a typical plot representing a case in which there was little motion between frames is shown in Figure 4.3. It was decided not to discard any micrographs at this stage of processing because examination of a sample of plots with their corresponding motion-corrected micrographs revealed that atypical motion plots was not necessarily indicative of poor-quality micrographs (Figure 4.4).

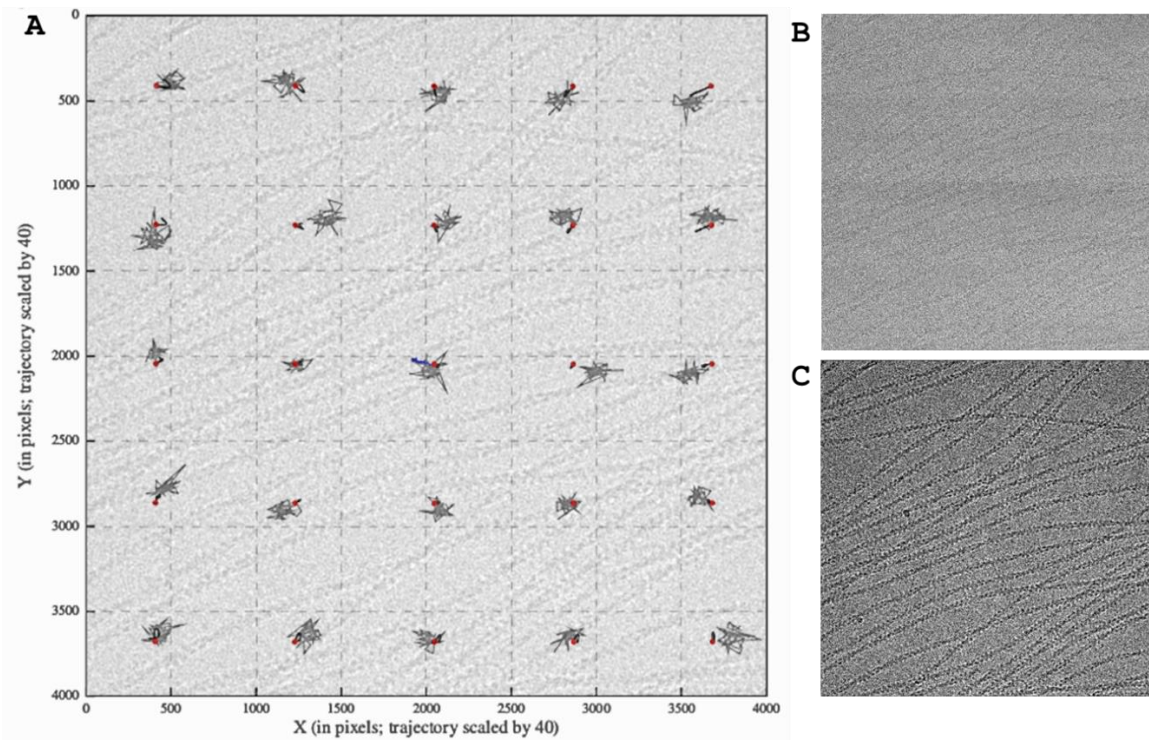


Figure 4.3: An example of a trajectory plot for a micrograph movie that suffered relatively little motion between frames. A) The trajectory plot, overlaying the corresponding motion-corrected micrograph. All trajectories are scaled by 40 relative to the values of the axes, so the motion appears exaggerated. B) A maximum intensity projection of the uncorrected movie frames. The image was smoothed and brightness and contrast settings were adjusted until features could be seen. C) The motion-corrected micrograph.

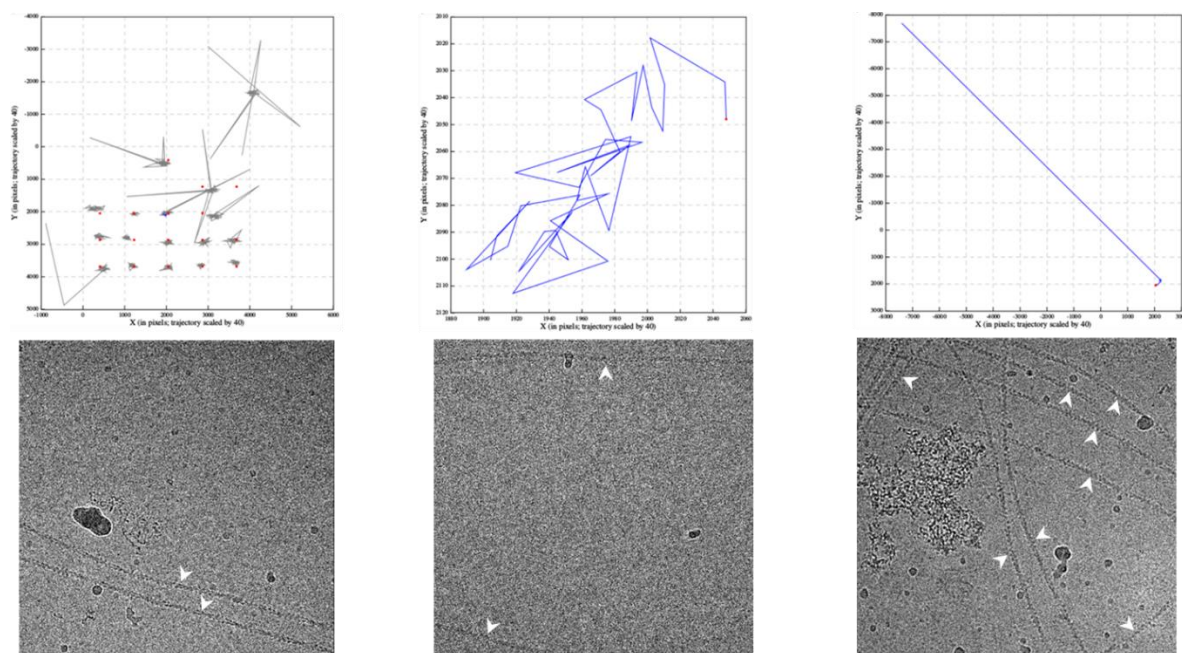


Figure 4.4: Bad trajectory traces were not necessarily indicative of bad micrographs. Examples where trajectory plots appeared to indicate a major problem with drift, but the micrographs were found to be acceptable for use in particle picking.

4.3.3 CTF Estimation & Data Quality Assessment

The Fourier transform of an electron micrograph appears as a series of bands ('Thon rings') rather than continuous signal because some of the information is missing, i.e. not all of the spatial frequencies are being represented (for examples, see Figure 4.5B&C). This patterning occurs because the image is modulated by the contrast transfer function (CTF) of the microscope, which effectively acts as a complicated band pass filter. While spatial frequencies with zero contrast cannot be recovered, those with negative contrast can be restored by changing their CTF value from negative to positive. This recovery of information is performed in a process called CTF correction. However, in order for CTF correction to work, it is necessary to accurately identify which spatial frequencies need to undergo phase-flipping. This is achieved by a process called CTF estimation, which involves fitting a theoretical CTF curve to the spatial frequency information in a micrograph. For the reasons described above, estimation of and correction for the CTF of every micrograph in a dataset is an essential step in high-resolution reconstruction.

CTF estimation and correction was performed using the program *Gctf* (Zhang, 2016) which uses cross-correlation to match simulated CTFs to the Thon rings of real data. Following CTF correction, RELION ranks each micrograph by multiple criteria and plots this information as histograms in a logfile. These histograms can be used to give an indication of whether a dataset is suitable for further processing (Figure 4.5). One of the most useful histograms generated profiles for the highest resolution detected in each micrograph in the dataset, which is calculated from the highest spatial frequency detectable in each micrograph after CTF estimation (*rlnCtfMaxResolution*). The histogram formed an approximately normal distribution around a peak of ~ 3.75 Å, with the highest resolution of the dataset ~ 2.5 Å. This indicated the dataset was suitable for processing because it contained high resolution information (better than 4 Å). The histogram also indicated that CTF estimation had worked well because the job did not incorrectly detect resolutions higher than the theoretical maximum, which was 1.96 Å (double the pixel size; according to the Nyquist-Shannon sampling theorem).

In addition to the histogram of maximum resolution, the logfile also includes histograms for CTF figure of merit (*rlnCtfFigureOfMerit*) and measured defocus (*rlnDefocusU*). The CTF figure of

merit provides a rough overview of micrograph quality within a dataset. Two extremes from the dataset have been shown here for illustration purposes. The FT with the lowest figure of merit has an outer speckled ring, which is a hallmark of cubic ice. This can be seen in the blotchy appearance of the accompanying micrograph (Figure 4.5B). The measured defocus range (focus values -3.5 to -0.5 μm ; Figure 4.5C) was larger than the nominal defocus range (focus values -2.6 to -0.8 μm). Defocus values too close to zero made particle picking difficult because low contrast made the filaments difficult to see, but micrographs collected close to focus were still used if possible.

4.3.4 Particle Picking and Extraction

In the context of particle picking, a ‘box’ is a cropped, square section of a micrograph that contains a single projected view of the object of interest (i.e. a single particle). When the object of interest is a helix, different views can be obtained by translation of the box along the helical axis. In this way, a single filament can generate a large number of particles (Figure 4.6). There are considerations to be made when defining box size and overlap. The box size (width) should be greater than the maximum filament width, which for actin is approximately 8 nm. The amount of overlap between boxes determines how many new asymmetric units are included per translation along the helical axis. A single asymmetric unit is equivalent to the helical rise. In F-actin, one asymmetric unit can be considered to be either a double-stranded (2-start) helix with the asymmetric unit being equal to one protomer (~ 5.5 nm in length along the helical axis) or a single-stranded (1-start) helix with the asymmetric unit being equivalent to half a protomer (~ 2.75 nm). For this work, the helical symmetry was treated as the latter. The symmetry of F-actin is covered in more detail in the Introduction Chapter, in section 1.3.4.

The chosen box size was ~ 24.5 nm (approximately three times the maximum filament width), with an inter-box distance of ~ 2.75 nm (0.5 protomers; 1 asymmetric unit) (Figure 4.6B). To define the helical axis for particle extraction, stretches of isolated actin filaments were picked manually by clicking to define the end points (coordinates) of a vector. Where filaments exhibited curvature, multiple straight lines were used (Figure 4.6A).

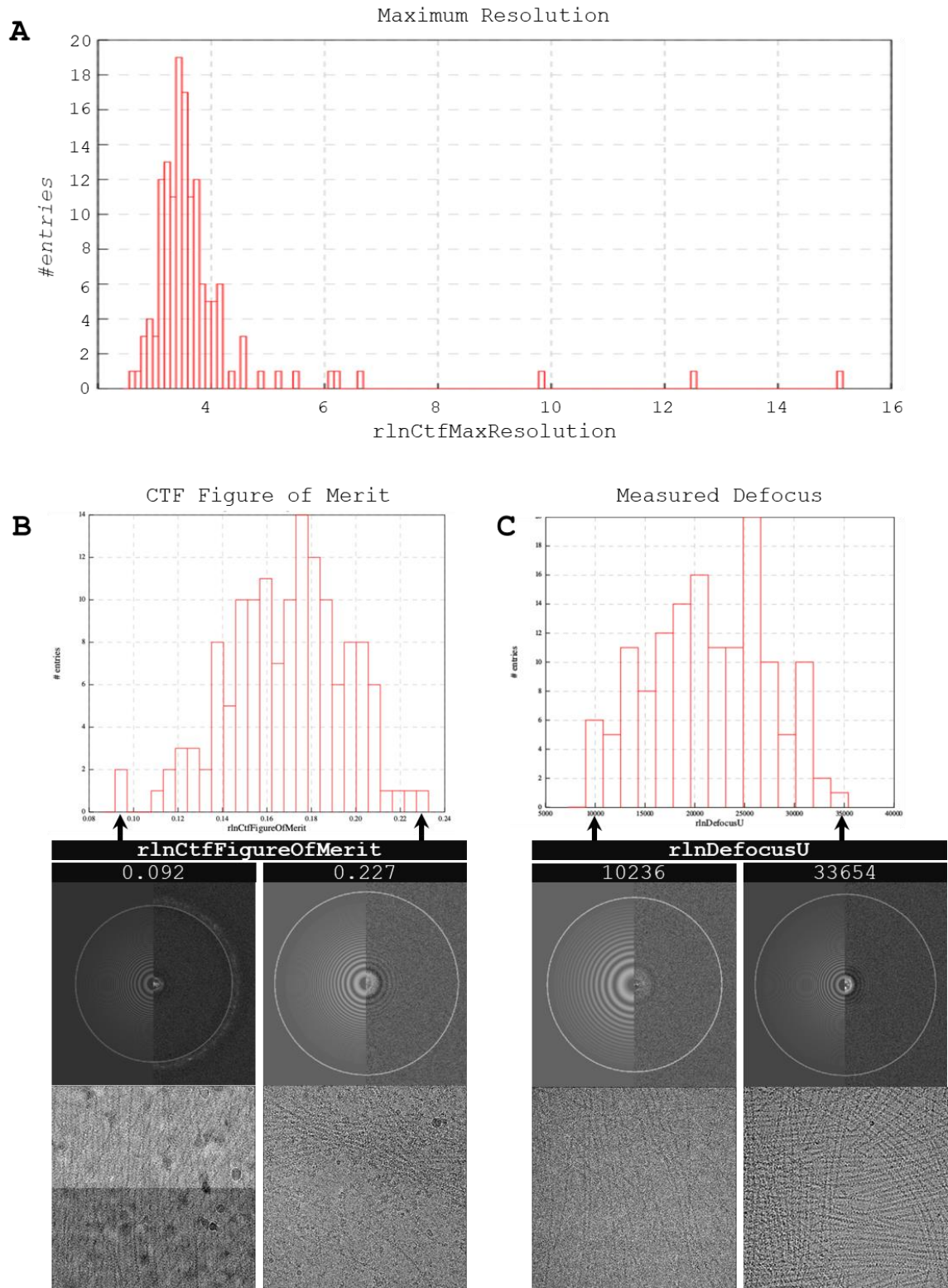


Figure 4.5: Assessing Data Quality following CTF Estimation. Histograms for **A**) maximum resolution detected **B**) the CTF Figure of Merit assigned by RELION **C**) measured defocus. All histograms display data for 142 micrographs of yeast F-actin, collected at 110,000 x microscope magnification. In **B**) and **C**), examples of micrographs with the lowest and highest scores are shown with their accompanying Fourier transform (right half) and simulated Thon rings from the simulated CTFs (left half).

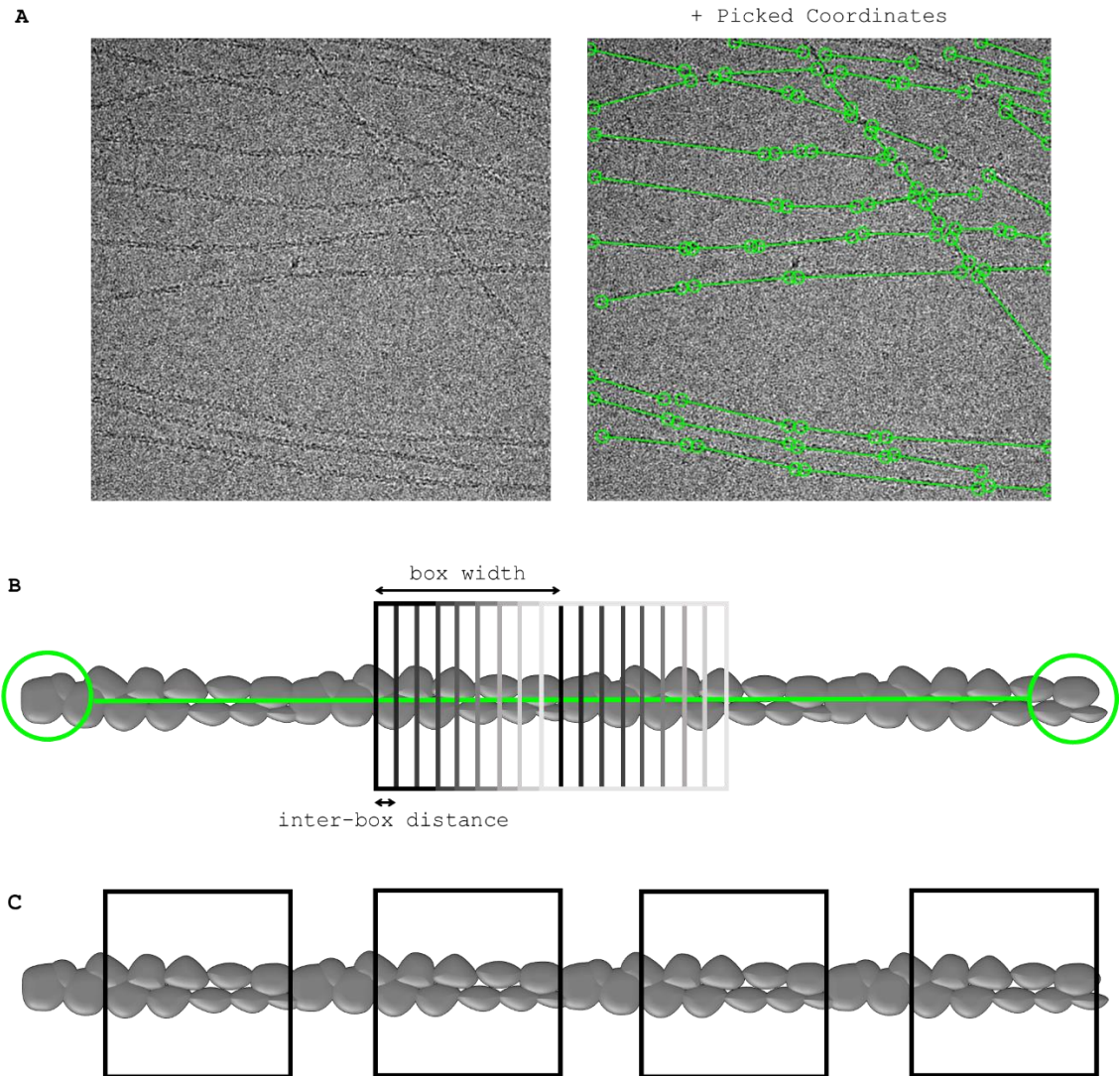


Figure 4.6: Picking helical segments for particle extraction. **A)** Examples of a micrograph with and without manually picked coordinates (green circles, connected pairwise by a straight line). The actin filaments exhibit a slight curvature, so multiple short vectors were used to closely trace the helical axis. **B)** Schematic of a short filament with picked coordinates. A selection of boxes for particle extraction is displayed towards the centre of the filament, each in a different shade of grey. Box width and inter-box distance for one of the boxes are indicated. **C)** Four of the boxes with equivalent views of the filament. These could be averaged together for 2D classification.

4.3.5 2D Classification

2D classification is an effective way of visually checking the quality of a dataset (see introduction section 1.2.4). At this stage, at least some of the averaged images should be consistent with knowledge of the specimen in terms of shape and symmetry; i.e. the structure should be recognisable. Other factors worth examining are the signal-to-noise ratio, the presence of artefacts and the level of detail that can be seen.

Artefacts are evident in the 2D classes in Figure 4.7 from a dataset that was found unsuitable for processing at this stage. The classes have a streaked appearance, with perpendicular spikes projecting out from the helical axis. This spiked effect is reminiscent of radial spikes, which are indicative of over-fitted noise (Henderson, 2013; Johnson, 2019). The micrographs in this dataset were densely packed with overlapping actin filaments, with very few isolated filaments for particle picking. The artefacts in the 2D classes confirmed that using overlapping filaments for particle picking was to be avoided, and this dataset was not fit to process further.

Datasets which included areas of lower filament density allowed particle picking of isolated actin filament segments. The resulting 2D classes were free of artefacts, with some indication of secondary structure (Figure 4.8).

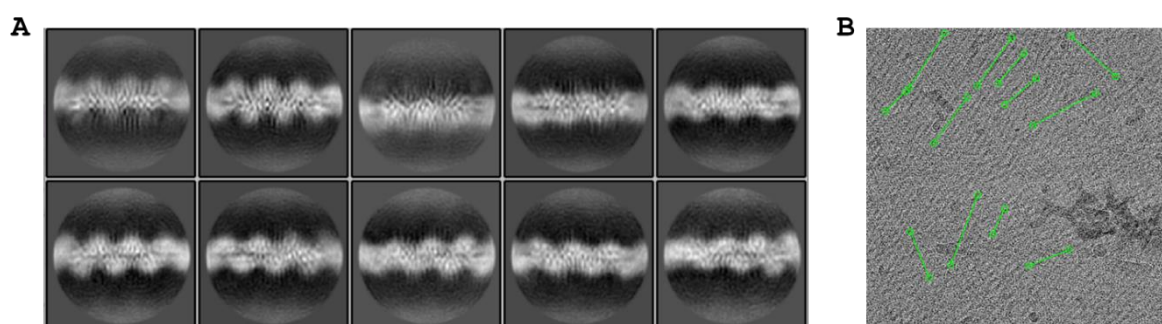


Figure 4.7: Spiked artefacts in 2D Classes from a discarded dataset with high filament density. A) Most of the 2D classes resemble actin filaments, with an observable twist and clearly defined protomers. However, all classes are affected by artefactual smearing in a perpendicular direction away from the helical axis, giving a 'spiked' appearance. B) A micrograph representative of this dataset, which has a very high filament density and consequently extensive filament overlap.

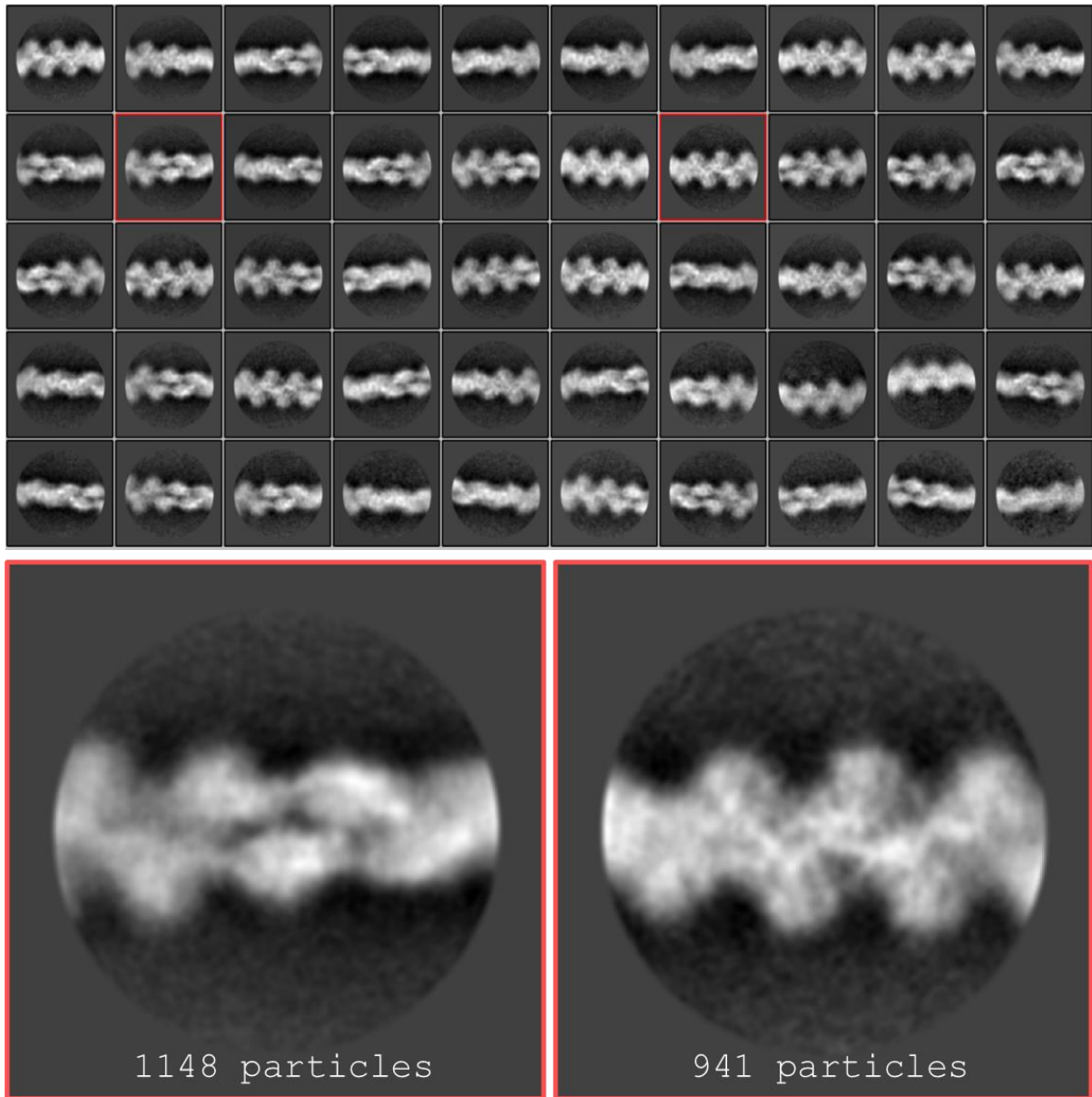


Figure 4.8: Indication of secondary structure in 2D classes. 50 2D classes generated from 41,793 particles. Red squares indicate the classes which are enlarged below, chosen because they are good examples of different views of the filament. The irregular dappled patterning on the filament, seen best on the 941-particle class, is indicative of secondary structure.

4.3.6 3D Reconstruction

A caveat of iterative 3D refinement is that it requires a starting template with approximately the same shape, size and symmetry of the molecule of interest in order to solve its structure. Since F-actin is structurally well-studied and consequently plenty of homologous structures were available to use as templates, this was not a hurdle for 3D reconstruction. However, templates can introduce bias, so other options were tested first. Optimisation of the reconstruction template was performed on a trial F-actin dataset collected at 53,000 x magnification (Figure 4.9 - Figure 4.11).

RELION has an 'Initial model' step that can be used in some cases to generate a 3D structure from the data in the absence of a template. This initial model can then be used as a reference map (template) for 3D refinement. However, this process was unable to produce a 3D model that resembled F-actin (Figure 4.9). Consequently, a different template had to be used for 3D refinement.

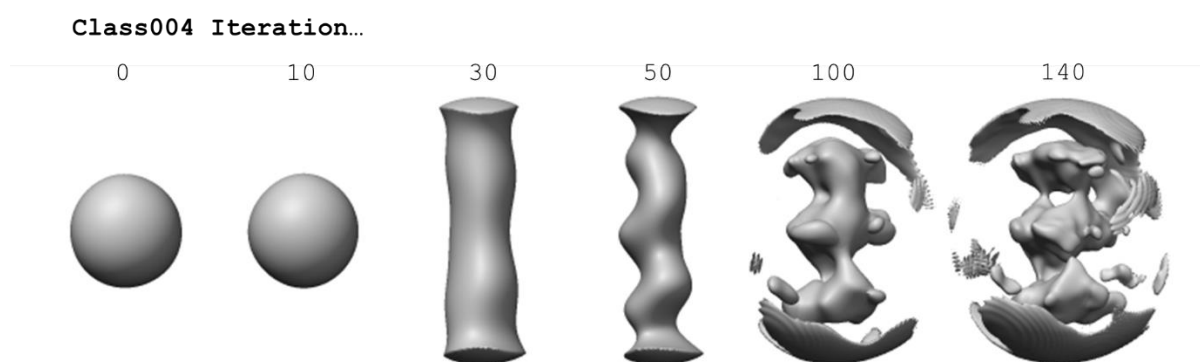


Figure 4.9: Template-free 3D initial model generation. *De novo* generation of a 3D model from the 2D particles failed to produce a suitable reference map for 3D refinement.

It has been demonstrated that in favourable cases, molecules with helical symmetry can be reconstructed using a cylinder as a template (He and Scheres, 2017). A simple template such as this ensures there is no bias in the resulting structure. An initial run with a cylinder template generated a structure that superficially resembled F-actin (Figure 4.10A). However, upon lowering the contour value threshold to reveal low density features, extra density was present that did not correspond to the 2D class averages (Figure 4.10B). The job was re-run with a smaller central Z

length (40%, reduced from 50%). The central Z length determines how much of each box is used to search for and impose helical symmetry, starting from the centre which suffers less from inaccuracies of orientation searches than the outer parts of the z-axis. This time the map appeared smeared (Figure 4.11), which can happen when the wrong helical symmetry is imposed (He and Scheres, 2017). This structure also lacked a distinct polarity, indicating that particles of opposite polarity may have been averaged together. Fitting a published skeletal muscle F-actin model into the density map supported this prediction, as the model fit equally well with opposite orientations. The best fit was obtained when both orientations were fit simultaneously, which together filled any empty density seen for each orientation alone (Figure 4.10B).

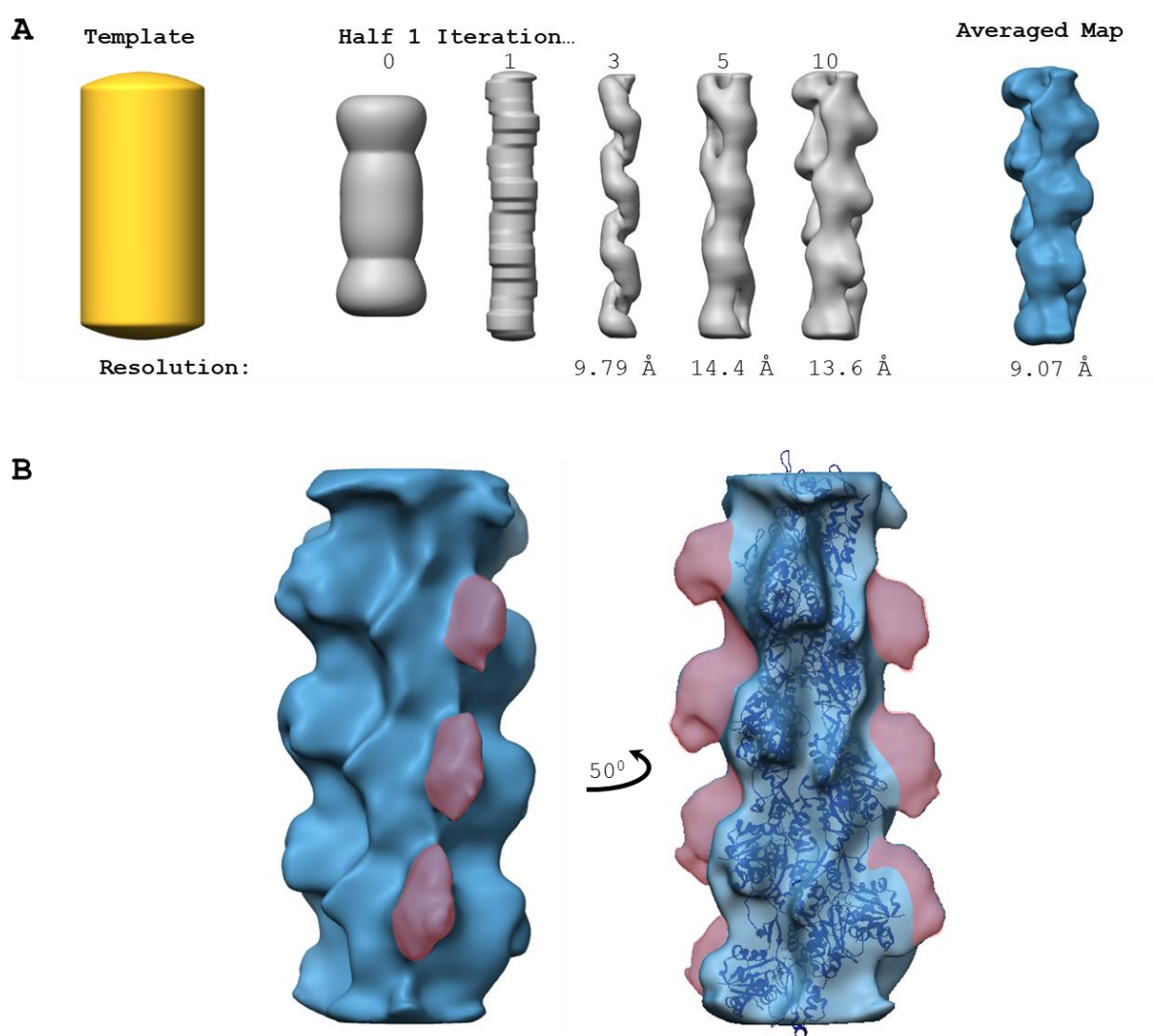


Figure 4.10: 3D refinement from a cylindrical template: a map with extra density. A) The cylindrical template (yellow), select iterations of one half-map (grey) and the final averaged map (blue). **B)** Increasing the threshold value revealed patches of density (pink) that did not correspond to F-actin when a model (navy ribbon structure; PDB 6BNO) was fitted into the map.

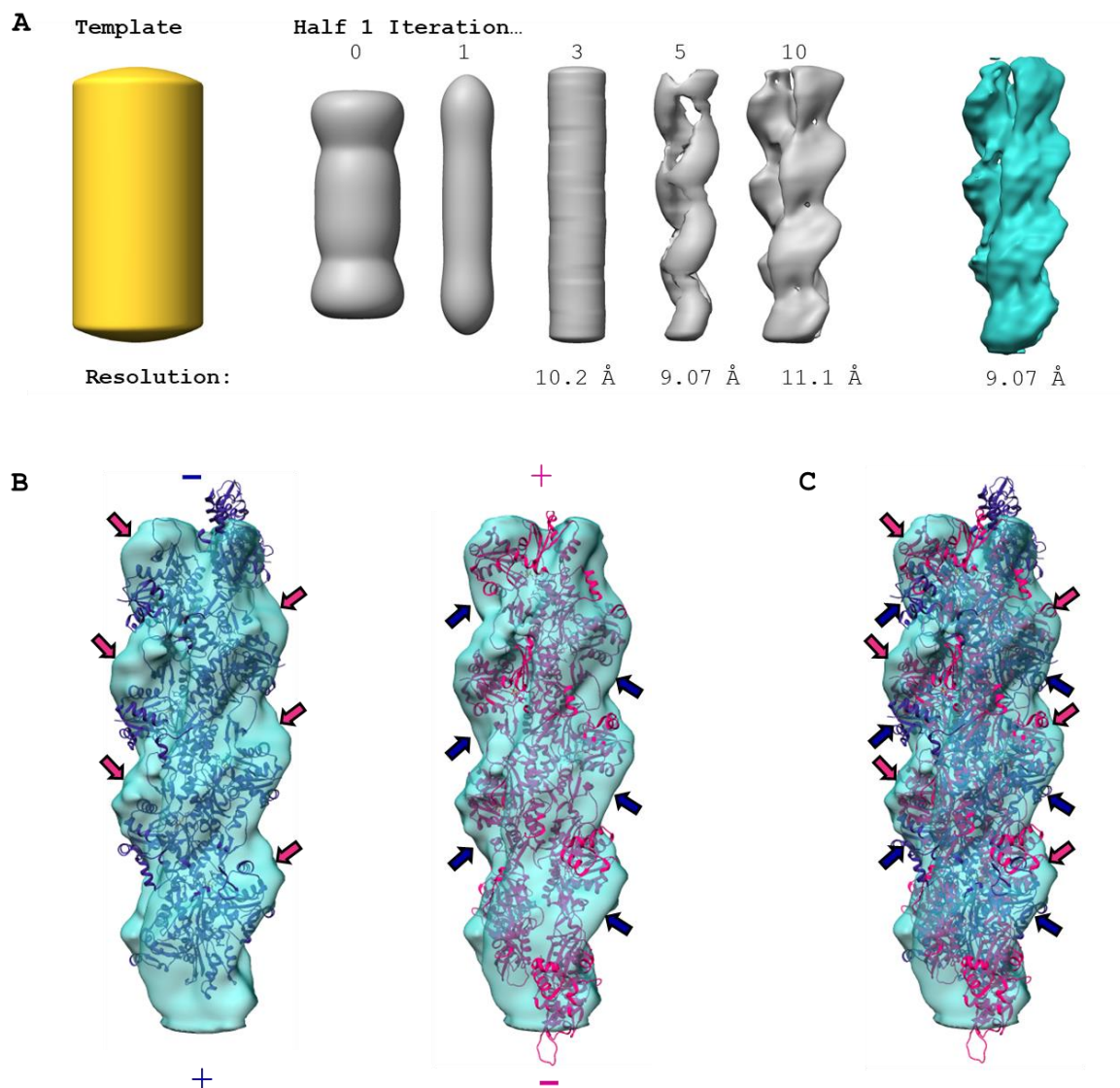


Figure 4.11: 3D refinement from a cylindrical template: a map displaying dual polarity. **A)** The cylindrical template (yellow), select iterations of one half-map (grey) and the final averaged map (turquoise). **B)** The F-actin model PDB 6BNO fits into this map in two orientations with opposite polarity. The barbed (+) and pointed (-) ends are indicated. Block arrows indicate regions of empty density. **C)** Most of the density becomes filled when both orientations of the F-actin model are fitted into the map simultaneously.

There was a clear need for a template with defined polarity, so a reference map was generated from a published F-actin model. The chosen model was F-actin from bare rabbit skeletal muscle F-actin that had been generated using a similar box size to ours so was approximately the same length as the maps generated from our data (PDB ID: 6BNO; Gurel *et al.*, 2017). A 30 Å initial low-pass filter was applied in RELION during 3D refinement to remove fine detail that could impose bias. 3D refinement using this low-passed F-actin template output a polar helical structure with visible

secondary structure elements, indicating the reconstruction had worked well (Figure 4.12). Secondary structure can only be resolved at resolutions higher than $\sim 9 \text{ \AA}$, which could not have been influenced by the 30 \AA reference map.

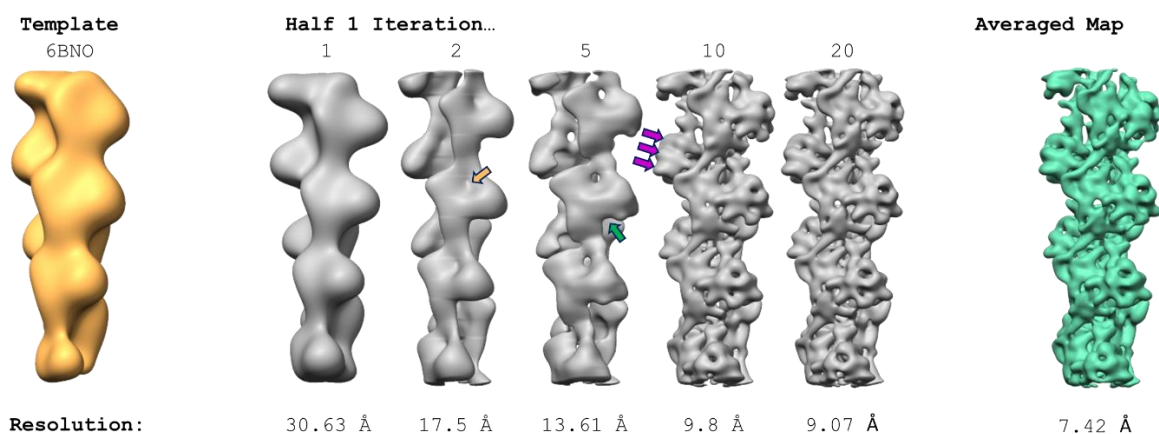


Figure 4.12: 3D refinement of a 7.42 \AA F-actin map from a 30 \AA F-actin template. The cylindrical template (yellow), select iterations of one half-map (grey) and the final averaged map (green) are shown. The cleft is well-defined as early as the second iteration (yellow arrow), and the binding groove is well-defined by the fifth iteration (green arrow). By the tenth iteration the α -helices of subdomain 1 have been resolved (purple arrows).

4.3.7 Further steps to Improve Resolution

The averaged map from the initial 3D refinement (shown in Figure 4.12) had a resolution of 7.42 \AA . Next, Bayesian polishing was performed on the extracted particles, which makes improvements to frame alignment. The 3D refine job using polished particles had a resolution of 6.81 \AA and this was further improved to 4.54 \AA by postprocessing, a procedure in which a mask is applied to remove solvent noise.

4.3.8 Local Resolution

The overall representative resolution value of the final postprocessed map is calculated from the FSC curve (see Figure 4.16). However, in reality, the local resolution of different parts of the map varies. For datasets A and B, a local resolution job was performed using RELION's implementation

to generate a temperature map, which was applied to the post-processed map in Chimera (Figure 4.13).

The map was found to have a local resolution range of 4.59-6.97 Å. The temperature maps indicated that the highest resolution was found at the core of the structure, while the lowest resolutions were found at the extremities. This is to be expected because imperfect alignment affects structures furthest from the alignment centre most severely, causing greater blurring. Areas of low local resolution can also be an indication of flexibility.

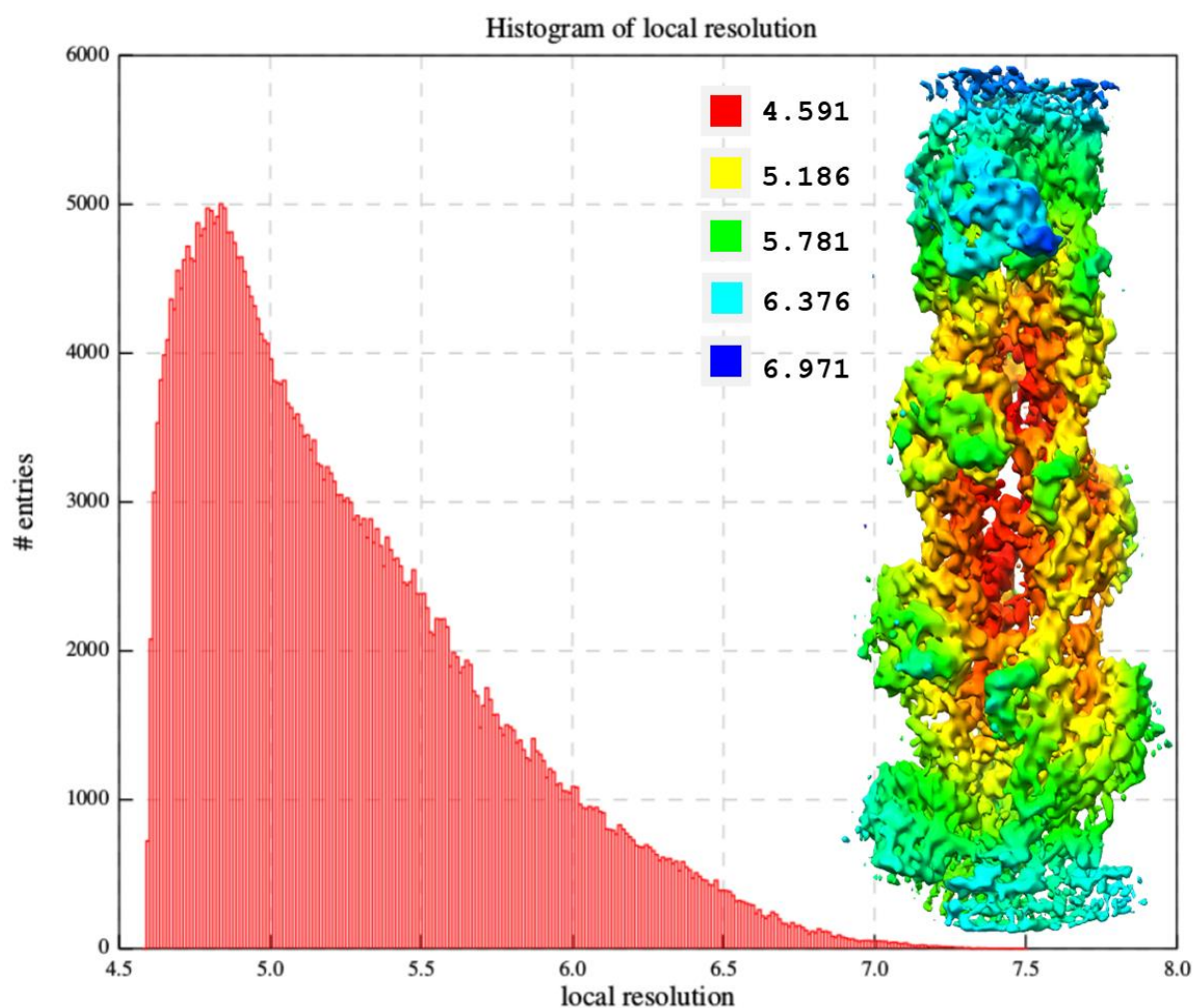


Figure 4.13: Local resolution. Local resolution histogram and temperature map for the polished, CTF-corrected map from the final 3D refinement job.

4.3.9 Homology Model Selection & D-loop Conformation

A homologous model of bare rabbit α -skeletal muscle F-actin in the ADP-bound state was used as a starting model (Merino *et al.*, 2018; PDB ID code: 5ONV). This model was chosen based on similarities to our yeast F-actin structure. Firstly, this model represents bare F-actin (i.e. there are no additional proteins or small molecules present other than ADP-Mg²⁺). Secondly, the density corresponding to the D-loop of our yeast F-actin model fitted well with the ‘closed’ D-loop conformation of this model (Figure 4.14).

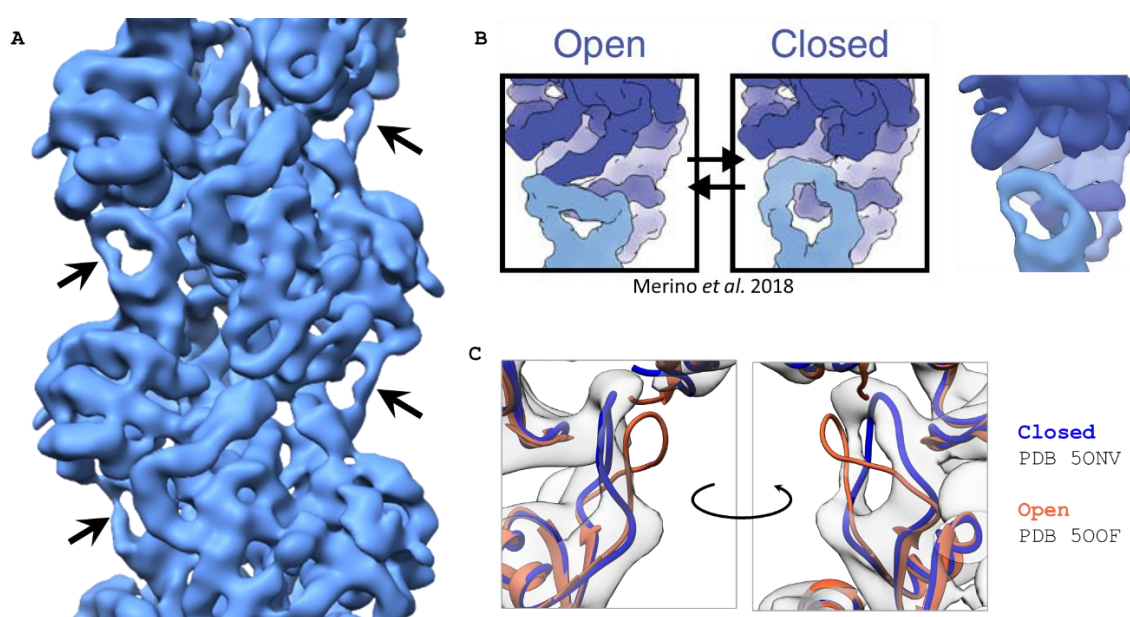


Figure 4.14: D-loop conformation of yeast F-actin. A) Arrows indicate the D-loop of each protomer in view. B) Illustrations of open and closed D-loops reproduced with permission from Merino *et al.* (2018), next to an equivalent section of the yeast F-actin map presented in a similar style for easier comparison. C) Two different views of the D-loop, fitted with the PDB models for an open (orange) and a closed (blue) D-loop. The closed conformation has the best overall fit. The yeast F-actin map is low-passed to 6 Å in all parts of this figure to improve clarity of the D-loop.

4.3.10 Map Rescaling: Retrospective Pixel Size Calibration

A single chain from PDB ID: 5ONV, corresponding to one protomer, was used for the initial modelling steps. This was docked into the map by whole-molecule rigid body fitting. The model protomer fitted the map reasonably well, however the map and the model were offset in many places, with the most pronounced differences in parts of the structure furthest from the centre of the map (Figure 4.15C). This indicated a discrepancy between the nominal and actual pixel size.

Correction of pixel size errors can be performed retrospectively in RELION (RELION, 2021). This is achieved by including a calibrated pixel size in the postprocessing job parameters. It is important to ensure that the 3D refine job used as the input has been preceded by CTF refinement for 4th order aberrations and then for per-particle defocus before 3D refine. Since the true pixel size was not yet known, a series of maps were created, with a calibrated pixel size ranging from the oversized nominal pixel size (0.98 Å) to 0.93 Å.

To ascertain the true pixel size, the original and downscaled maps were quantitatively assessed for map-to-model fit by plotting the masked correlation coefficient (CC_{mask}) against pixel size (Figure 4.15A). This strategy has been used effectively for higher resolution structures (Wu, Lander and Herzik, 2020), where the true pixel size can be clearly identified as the maximum of a broad peak. However, unsurprisingly for the relatively low resolution (4.65-4.9 Å) of the yeast F-actin maps, the plot did not present as a smooth peak, and differences between CC values with varying pixel size were subtle. However, rescaling the map to a pixel size within the range of 0.94 Å to 0.95 Å did result in an improved CC_{mask} from 0.72 to 0.73. An intermediate value (0.945 Å) was used as the best estimate of true pixel size. This was consistent with the true pixel size calculated independently by other lab members using an apoferritin dataset collected using the same microscope and magnification (personal communication). Modelling work therefore continued with the 0.945 Å map.

Calibration of the pixel size therefore resulted in a downscaling of 3.57 %. The rescaled map was qualitatively a greatly improved fit compared to the original map. Alpha-helices furthest from the helical axis showed the most notable improvement. Figure 4.15C shows residues 222-232 before and after rescaling as an example. In the rescaled map, the helix is shifted to the centre of map density and the helical register of the model is more clearly aligned with the map.

While rescaling was fundamental for the modelling steps to prevent artefactual distortion, it also impacted the measured helical symmetry of the map. Helical parameters in this section apply to when F-actin is treated as a 1-start helix (refer to Chapter 1, section 1.3.4). Before re-scaling, the yeast F-actin map was observed to have an unusually high axial rise (29 Å), but after re-scaling this was reduced to 27.5 Å, which is consistent with the previously calculated axial rise of yeast actin from

layer lines (Orlova *et al.*, 1997). The helical twist (-167.3° and -167.2° for datasets A and B, respectively), was unaltered following map rescaling. The helical parameters of yeast F-actin in the context of published F-actin structures are covered in Chapter 5, in section 5.2.1. The FSC curve of final masked map is shown in Figure 4.16.

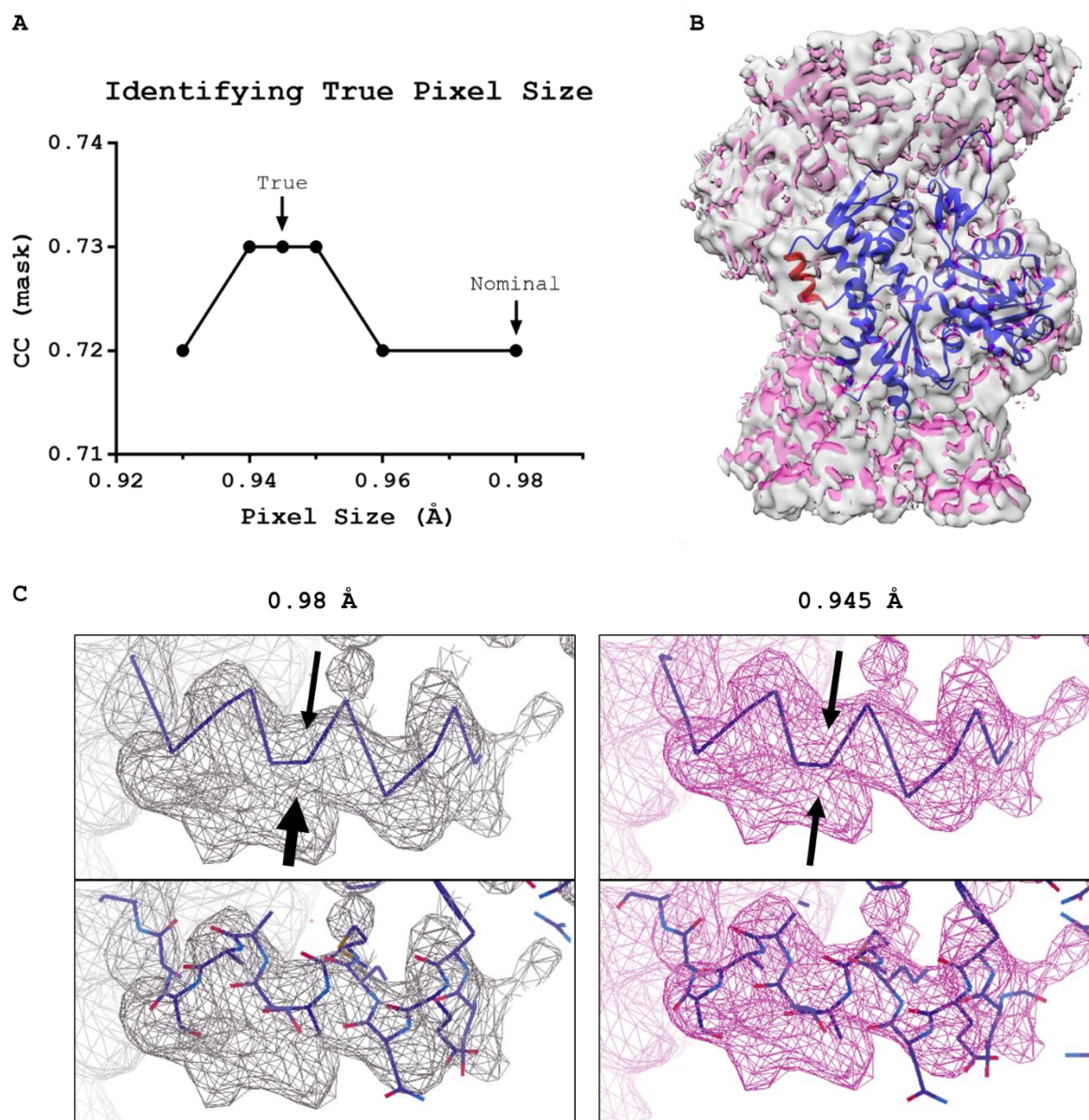


Figure 4.15: Pixel Size Calibration. A) Correlation coefficient values calculated from performing real-space refinement in Phenix. This was used to acquire an estimate of the true pixel size (0.945 \AA). CC_{mask} is an output from real-space refinement in Phenix calculated using only map values contained within a masked area around the model coordinates (Afonine *et al.*, 2018). B) Before (grey) and after (pink) rescaling. Red indicates the helix shown in part C. C) Helix corresponding to ~residues 222-232.

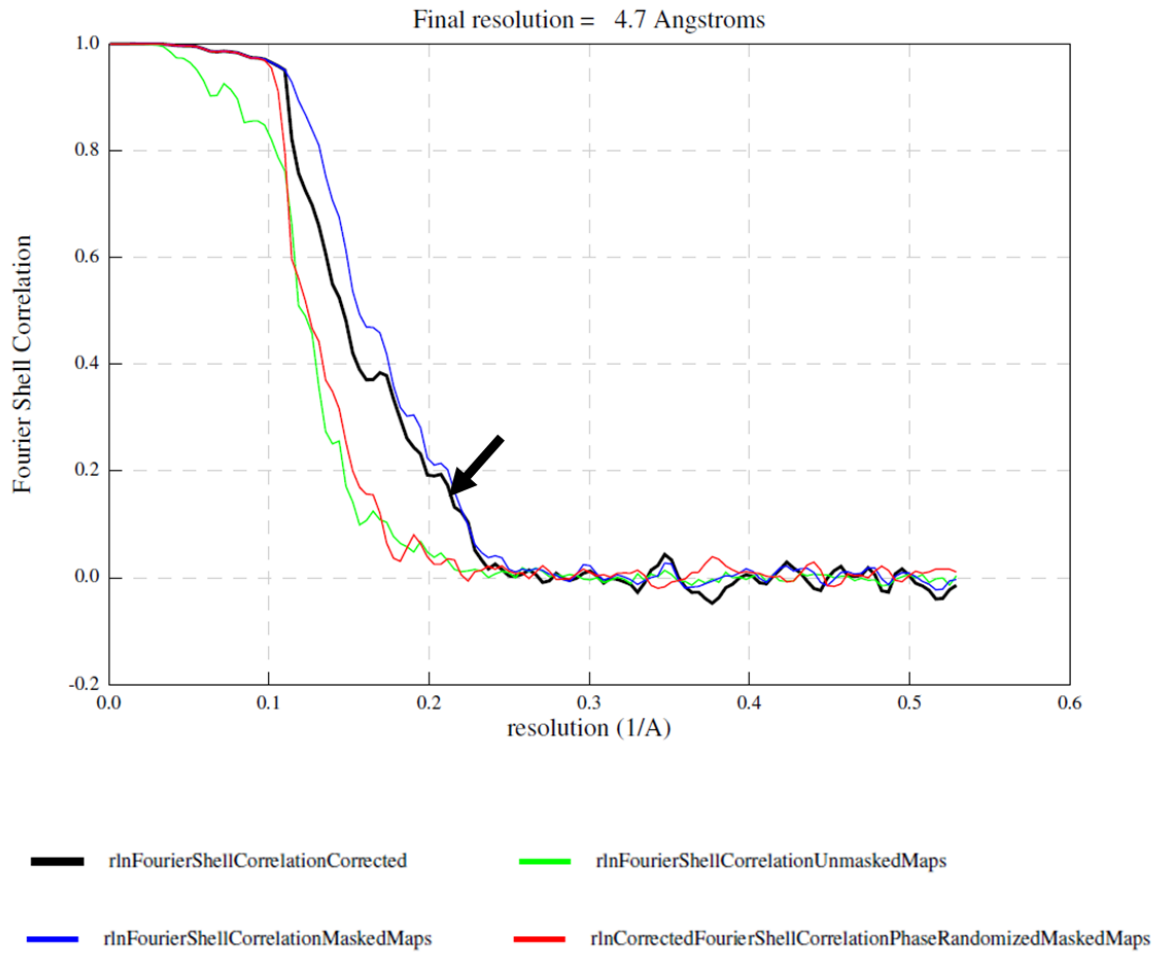


Figure 4.16: FSC curve of the final rescaled postprocessed map. The arrow indicates the point at which the corrected FSC curve (black) crosses the threshold value of 0.143, which is the traditional method for determining maximum map resolution (Rosenthal and Henderson, 2003).

4.4 Discussion

4.4.1 Limiting Steps in Acquiring a High Quality Dataset

Cryo-EM sample preparation was a key obstacle for this project, with inconsistent and unpredictable results making tactical optimisation extremely challenging. Grid preparation has greatly lagged behind the data collection and processing developments that have enabled the resolution revolution, having generally changed little since the technique was first developed by Adrian *et al.*, 1984. However, the cryo-EM world is constantly evolving, and recent years have seen exploration of innovative sample preparation techniques (reviewed in Weissenberger *et al.*, 2021).

Grids were only used for data collection if suitable areas were found during screening. However, screening often represented a ‘best-case’ scenario that was not widely replicated during data collection. This is because areas of the grid used for data collection had to be limited to a single exposure at high resolution in order to preserve high resolution information. In contrast, screening could afford multiple exposures in a small ‘sacrificial area’ of the grid to home in on an area with good filament distribution. Additionally, the heterogeneity of filament distribution meant that the screening area was not necessarily representative of other areas of the grid, and the requirement for ‘blind’ sampling meant that suitable areas could be missed during data collection.

With sample optimisation proving difficult, it was investigated whether micrographs with a non-optimal, dense actin filament distribution could be used for reconstruction. However it was clear that at the 2D classification stage that this data was unsuitable for further processing (Figure 4.7). It was therefore confirmed that only non-overlapping projections of specimens can be used effectively for data processing.

4.4.2 Quality Control Checks During Data Processing

This chapter has provided several examples of checks that can be made at different stages of data processing. We found that trajectory traces output from a motion correction job should not be used as a criterion for data subset selection, as they can be misleading. In contrast, histograms of

maximum resolution, figure of merit, and defocus from a CTF correction job are useful indicators of whether a dataset is suitable for processing further.

Comparing the examples of 3D refinement that did not work (Figure 4.10 and Figure 4.11) with the example that worked well (Figure 4.12), it can be seen that the first few iterations are a strong indicator of the success of the job. This proved to be a useful observation in terms of quality-control: examining the early iterations while the job is running can save a significant amount of time by bypassing the need to run each job to completion. 3D refinement jobs can take several hours to complete because, while early iterations take only a few minutes, later iterations can approach an hour each, which adds up when there are 15-25 iterations in total. If there is an erroneous input parameter (e.g. incorrect helical symmetry, sub-optimal central Z length) or there is an issue with the template (e.g. template is not on the same scale as experimental data, the axes of symmetry are not aligned, the template is unsuitable for the data), this will manifest as abnormalities in the early iterations and the job can be stopped for adjustment to be made.

5. Analysis of Yeast F-actin Structure

5.1 Introduction

S. cerevisiae possesses only a single actin isoform, so abolishing its expression has lethal consequences for the cell (Shortle *et al.*, 1982). This protein shares 87-89% sequence identity (94-96% sequence similarity) with vertebrate actin isoforms and X-ray crystallographic studies have found the G-actin structures to be highly similar (Vorobiev *et al.*, 2003). However, intriguingly, substitution of the yeast gene for the vertebrate β -cytoplasmic isoform severely disrupts cell function (Karlsson *et al.*, 1991), and it has even been reported that substitution for the vertebrate skeletal muscle isoform is lethal (McKane *et al.*, 2005). Direct comparison of dynamics *in vitro* have indicated that skeletal muscle actin but not yeast actin can be induced to polymerise by KCl in the absence of $MgCl_2$, that yeast actin nucleates more efficiently than skeletal muscle actin in certain ionic environments (Ca^{2+} -G-actin, $+MgCl_2$, no KCl), and that yeast F-actin exhibits increased fragmentation compared to skeletal muscle F-actin (Buzan and Frieden, 1996; Kim *et al.*, 1996). It has also been noted that yeast F-actin does not exhibit the Mg^{2+} -dependent stiffness/rigidity of skeletal muscle actin, possibly owing to a single residue substitution (E167A) that weakens the filament's interaction with a stiffness-associated cation (Kang *et al.*, 2012). Differences have also been observed between yeast and muscle F-actins in their interactions with some binding partners. For instance, yeast F-actin binds phalloidin more rapidly but more weakly than skeletal muscle actin (De La Cruz and Pollard, 1996) and has a lower affinity for muscle myosin, which it also activates more weakly (Greer and Schekman, 1982; Cook *et al.*, 1993).

The N-terminus has been found to be a region of concentrated sequence variation between actin isoforms (Vandekerckhove and Weber, 1978a, 1978b). The less negative charge of the yeast actin N-terminus compared to the muscle isoform equivalent has been found to greatly impair its interaction with myosin (Cook *et al.*, 1992). Substituting the yeast N-terminal acidic motif for the muscle equivalent was found to induce more rabbit-like activity (Cook *et al.*, 1993). The charge of the N-terminus alone cannot account for all functional differences observed between yeast F-actin

and skeletal muscle actin. The C-terminus (subdomain 1) and D-loop (subdomain 2) have also been implicated in functional differences between isoforms. Both these regions exhibit considerable flexibility and are important for intra-strand protomer-protomer interactions. Fluorescent and phosphorescent labelling of Cys-374 have indicated that the C-terminus of yeast F-actin is more flexible and more exposed to the surrounding environment than the C-terminus of skeletal muscle F-actin is (Prochniewicz and Thomas, 1999). The D-loop is susceptible to proteolytic cleavage by the protease subtilisin between Met47 and Gly48 of the D-loop (Schwyter *et al.*, 1989). The rate of subtilisin digestion of yeast F-actin is approximately 10-fold faster than muscle actin, indicating greater flexibility compared with the D-loop of the skeletal muscle isoform (Kim *et al.*, 1996). This has implications for the stability of the intra-strand interactions of yeast F-actin since the D-loop is the major contact site between neighbouring protomers within the same strand. Inducing crosslinking of cysteine residues in the D-loop to the C-terminus (via a disulphide bond between Cys42 and Cys374 in a Q41C mutant yeast actin) was found to alter the mechanical properties of yeast actin to have a greater resemblance to the less flexible skeletal muscle F-actin (Orlova *et al.*, 2001).

While there are now multiple published structures for skeletal muscle F-actin with resolution of 5 Å or better, the resolution of yeast F-actin structure has not been improved past ~20 Å (Orlova *et al.*, 1997, 2001; Belmont *et al.*, 1999). The key reported differences between this density map and a rabbit skeletal muscle F-actin map of comparable resolution were that yeast F-actin had reduced inter-strand connectivity as well as a more open nucleotide binding cleft (Orlova *et al.*, 1997). These observed differences have since been cited as explanations for the biochemical traits of yeast F-actin (e.g. Prochniewicz and Thomas, 1999; Boiero Sanders, Antkowiak and Michelot, 2020). However, these observations were based on maps in which the only features that could be resolved were individual protomers and the position of the ATP-binding cleft, and therefore require reinvestigation with the more advanced technology now available.

The structural information for yeast F-actin obtained by cryo-EM for this project is considerably improved in resolution, with detailed information such as the position and register of α -helices. Using our 4.7 Å map and a pseudoatomic model constructed from it, we investigated whether the

formerly reported differences between vertebrate skeletal muscle F-actin and yeast F-actin were consistent with our higher resolution structural data.

5.2 Results

5.2.1 Yeast F-actin Helical Symmetry Compared to Other Published Structures

We first examined the helical symmetry of our map. The axial rise of 27.6 Å for our yeast F-actin map was more or less consistent with the 27.5 Å canonical axial rise for actin, and with the 27.5 Å axial rise previously calculated for yeast actin from layer lines (Orlova *et al.*, 1997). In contrast, the helical twist of -167.3° is slightly more negative than the accepted value for vertebrate α -skeletal muscle F-actin (-166.7°). Broader analysis was required to establish whether this was significant. Therefore, to examine the extent of variation in helical parameters across published structures, analysis was performed on published maps to investigate the variation of helical parameters across the available published structures of bare F-actin. The following selection criteria were applied: 1) the map was available to download from the electron microscopy data bank (EMDB); 2) the resolution of the published map was 10 Å or better; 3) the F-actin was not bound to any ABPs. F-actin bound to small-molecules phalloidin, jasplakinolide or pyrene were included in the analysis because these have been found not to impact helical symmetry (Pospich, Merino and Raunser, 2020).

The helical parameters of 32 F-actin maps fitting the above criteria were measured in ChimeraX. This encompassed: 22 rabbit (*O. cuniculus*) and 6 chicken (*G. gallus*) skeletal muscle F-actin, 1 maize pollen (*Z. mays*) F-actin and 3 *P. falciparum* F-actin. The *S. cerevisiae* maps from the trial 53,000 x dataset and another dataset polymerised in the presence of Las17 (introduced in Chapter 6) were additionally included in this analysis, giving a total of 34 F-actin maps. Axial rise and helical twist were plotted separately, grouping the results by source species (Figure 5.1). The primary sequence of rabbit and chicken skeletal muscle actin is identical, but structures for these organisms were

plotted separately to account for the possibility of different post-translational modifications that could alter the properties of F-actin in each species.

An ordinary one-way analysis of variance (one-way ANOVA) with multiple comparisons was used to ascertain whether any of the helical parameters were significantly different between species. As expected, comparing the helical parameters of the two vertebrate skeletal muscle F-actins (which are identical in primary sequence) revealed the difference to be non-significant. None of the species had a significantly different axial rise, but F-actin from *P. falciparum* and *S. cerevisiae* were found to have a significantly more negative twist compared to the vertebrate skeletal muscle F-actins (Figure 5.1 and Table 5.1).

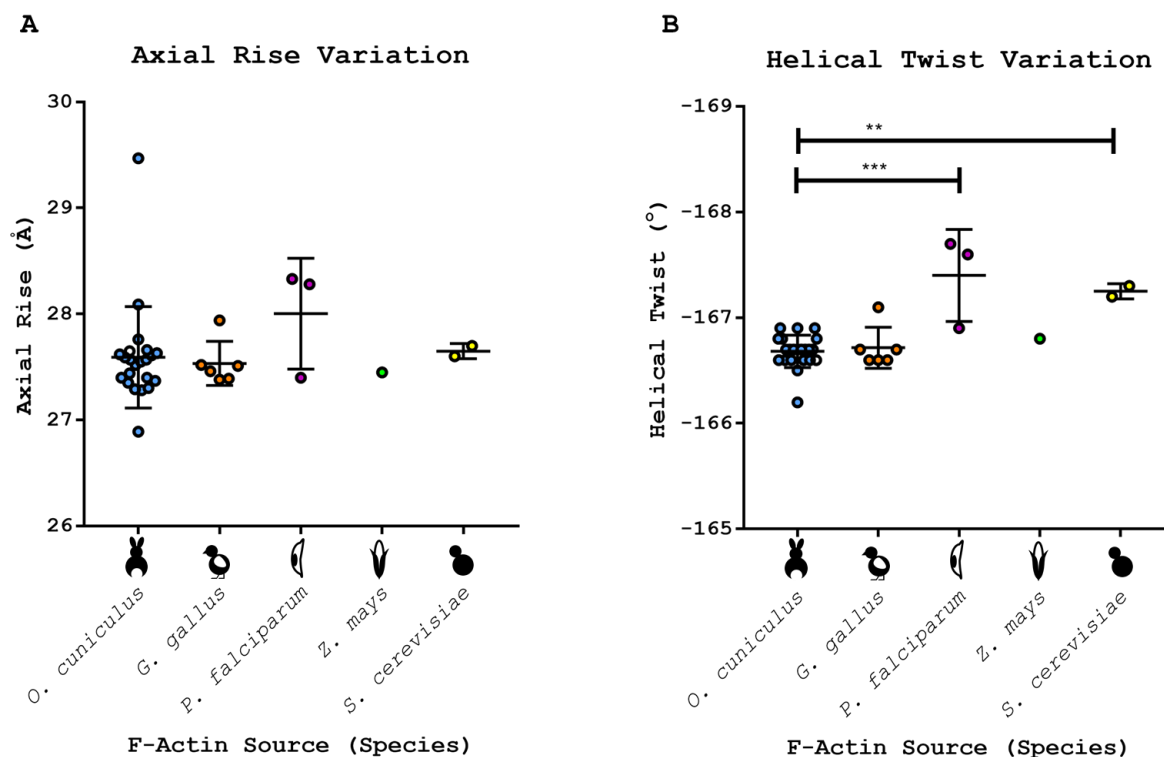


Figure 5.1: Helical Symmetry of F-actin Maps. A) Axial rise and B) helical twist of actin filament from different species. An ordinary one-way ANOVA with multiple comparisons was used to compare helical parameters between actin isoforms, and the full results are presented in Table 5.1. Isoforms found to have statistically different symmetry values to rabbit skeletal muscle actin are annotated with asterisks.

Table 5.1: Helical Parameter Statistics. Mean \pm Standard Deviation. The number of maps contributing to the average value is indicated (n).

F-actin Source (Species)	Axial Rise (\AA)	Statistically Significant Difference to...	n
	Helical twist ($^\circ$)		
<i>O. cuniculus</i> (Rabbit)	27.59 \pm 0.48	ns P. falciparum (<0.0001), S. cerevisiae (0.0033)	22
	-166.7 \pm 0.15		
<i>G. gallus</i> (Chicken)	27.53 \pm 0.21	ns P. falciparum (0.0002), S. cerevisiae (0.0154)	6
	-166.7 \pm 0.19		
<i>P. falciparum</i> (Malaria Parasite)	28.00 \pm 0.52	ns <i>O. cuniculus</i> (<0.0001), <i>G. gallus</i> (0.0002)	3
	-167.4 \pm 0.44		
<i>Z. mays</i> (Maize)	27.45 \pm 0.00	ns ns	1
	-166.8 \pm 0.00		
<i>S. cerevisiae</i> (Baker's Yeast)	27.65 \pm 0.07	ns <i>O. cuniculus</i> (<0.0033), <i>G. gallus</i> (0.0154)	2
	-167.3 \pm 0.07		

5.2.2 Comparison of Rabbit Skeletal Muscle F-actin and Yeast F-Actin Maps

Alignment of our 4.7 \AA yeast F-actin map with a published 4.1 \AA map for ADP-bound rabbit skeletal muscle actin ('RSkM actin'; EMDB-3835) revealed strong similarities between the experimental maps. EMDB-3835 was the map used to model PDB ID:5ONV, which we had identified as a suitable homology model for our structure based on its nucleotide state and D-loop conformation, as explained in the previous chapter (section 4.3.9). As well as being objectively similar (seen best in closely overlapping density at distinctive features such as α -helices and loops), the maps had a high correlation coefficient value of 0.93 (Figure 5.2). Notably, there was no evidence of the previously reported differences between RSkM and yeast F-actin: yeast F-actin had neither obviously reduced connectivity between protofilaments or a more open cleft conformation.

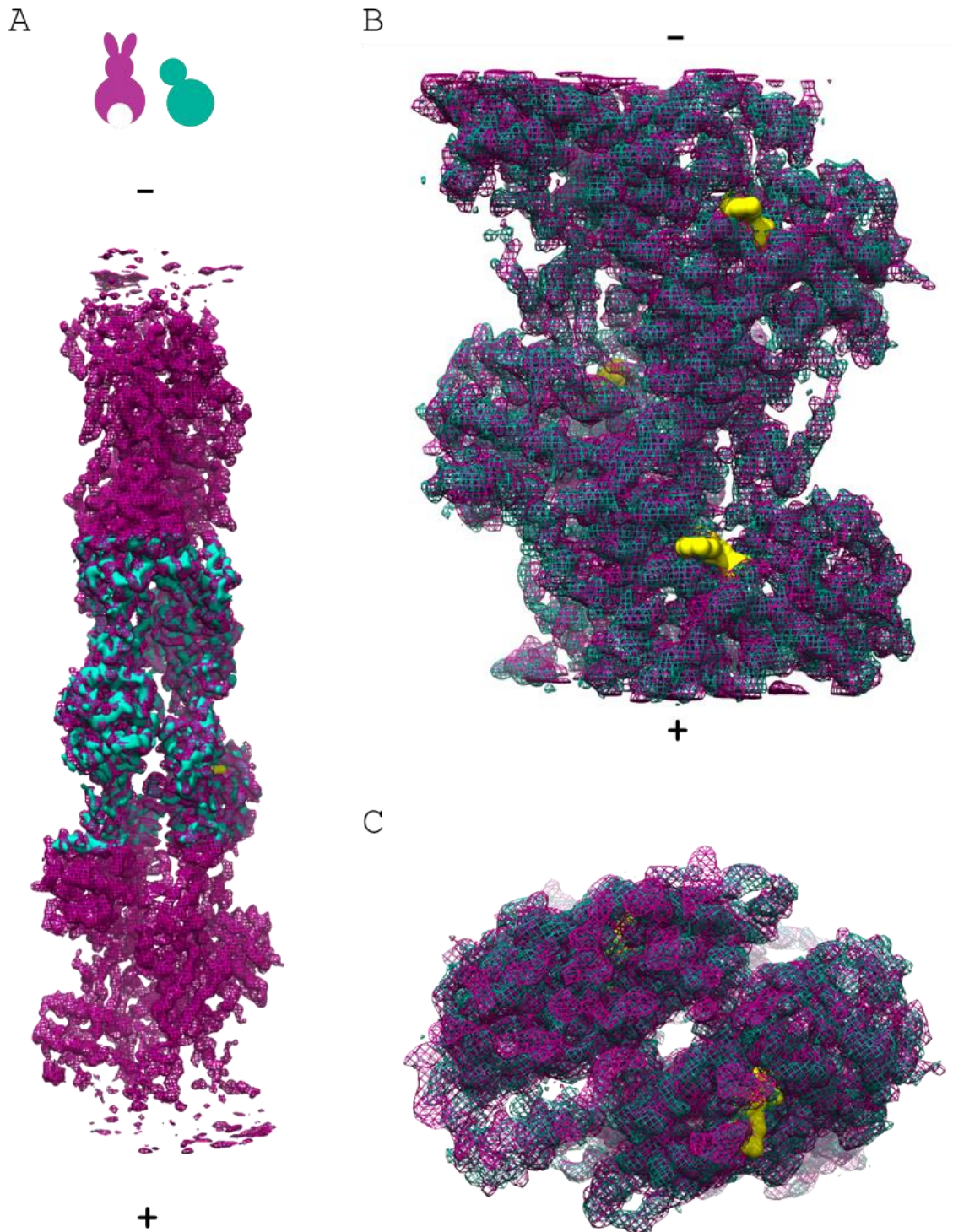


Figure 5.2: Comparison of yeast and RSkM F-actin experimental maps. **A)** Alignment of the 4.7 Å masked yeast F-actin map (turquoise) with the 4.1 Å RSkM F-actin map EMDB-3835 (pink). + and – indicate the barbed and pointed ends, respectively. **B)** EMDB-3835 was cropped to cover the same region as the masked yeast F-actin map before the correlation coefficient was calculated. Model ADP (yellow) from PDB ID: 5ONV has is displayed to indicate the position of the nucleotide-binding cleft. **C)** A cross-section of the cropped, aligned maps viewed from the pointed end.

5.2.3 A Pseudo-Atomic Model For Yeast F-Actin

Owing to the helical symmetry of F-actin, a central protomer and the neighbouring half of each adjacent protomer is sufficient to examine all inter-strand and intra-strand interactions. PDB ID: 5ONV was used as a homology model to construct a pseudo-atomic model consisting of 3 protomers with the yeast actin sequence. The map density allowed the positioning of α -helices with high confidence, and helical register could be refined using densities from bulky sidechains (Figure 5.3A). Our modelling approach (section 2.6.7) yielded three highly similar but unique protomers based on their local map density. These will be referred to as n, n+1 and n-1, with n as the central protomer, n-1 as the protomer positioned closer to the pointed (-) end and n+1 as the protomer positioned closer to the barbed (+) end (Figure 5.3B). Further improvements to the model were not pursued due to time constraints of the project and the limited resolution of the map. One possible route of further refinement considered was the possibility of imposing helical constraints during an additional round of real-space refinement to produce a model with identical model protomers.

Using the models as reference points, it was noted that the map density corresponding to the N and C termini of the actin fold was similar in the RSkM F-actin and yeast F-actin maps, with Val5 as the most N-terminal residue to be resolved and an absence of density for the aromatic ring of Phe375 at the C-terminus.

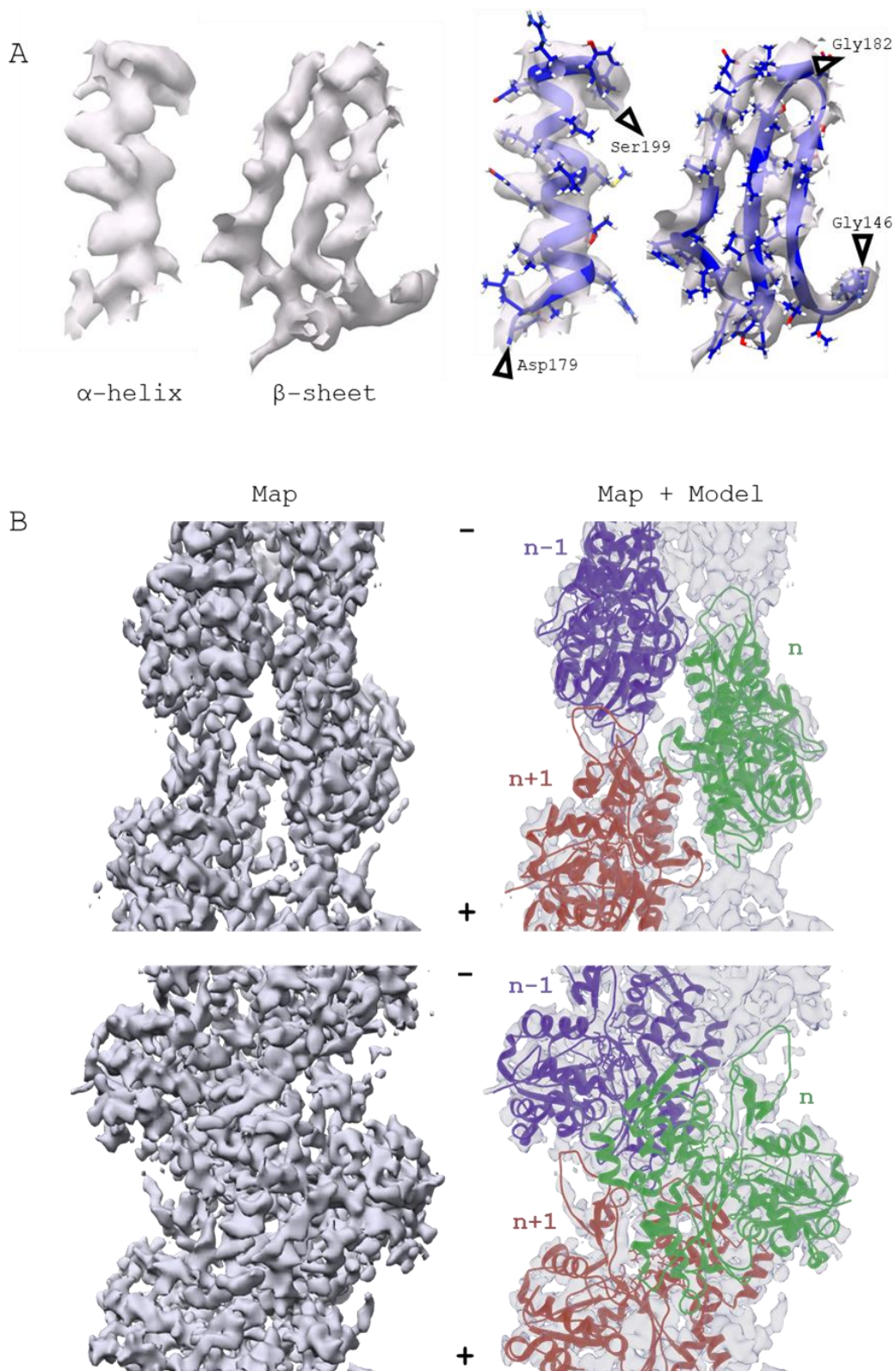


Figure 5.3: Overview of the 4.7 Å map and pseudo-atomic model for yeast F-actin. **A)** The map quality was high enough to resolve secondary structures and some sidechains. The first and last residues in each section of the model are labelled. **B)** Two different views of the map on its own (left) and fitted with the final model (right). Model protomers n, n-1 and n+1 are coloured green, purple and pink, respectively, and this colouring will be maintained throughout the rest of the chapter.

5.2.4 Model Validation

Our model does not contain atomic clashes since we used the ChimeraX extension ISOLDE for the modelling process, which automatically detects and avoids atomic clashes (Croll, 2018). Validation of our model in MOLPROBITY (Lovell *et al.*, 2003) revealed 8 Ramachandran outliers: Ala6 and Ala181 in protomer n-1, Arg39, Phe169, Gly197 and Lys336 in protomer n, and Gly48 and Asn252 in protomer n+1 (Figure 5.4). It was not possible to manually adjust the backbone in these locations without compromising other validation parameters or introducing bad geometry in neighbouring sections of the backbone. Gly48 (in the D-loop) is the only Ramachandran outlier that falls within a region of interest for this chapter (Figure 5.6C).

We note that the homology model (PDB ID: 5ONV) had a greater proportion of Ramachandran outliers in the backbone than our model, with 13 outliers per identical subunit, including 7 out of the 19 proline residues per protomer (Pro27, Pro38, Pro98, Pro112, Pro164, Pro264 and Pro367). The remaining outliers in that model were Met44, Ser52, Leu110, Ser199, Gln246 and Ser350. Ramachandran outliers are indicated in most figures when they occur in regions of interest for sections 6.2.5 and 6.2.6.

The MOLPROBITY analysis also scored our model poorly for rotamers, with 15 poor rotamers identified over the entire 3-protomer model (1.64%, goal <0.3%). However, given the limited resolution of the map, further adjustment of the model would be highly speculative and risked introducing clashes. No changes were made, therefore, to improve these unfavourable rotamers. This is accepted as a limitation of this model, which is the best fit for our experimental data.

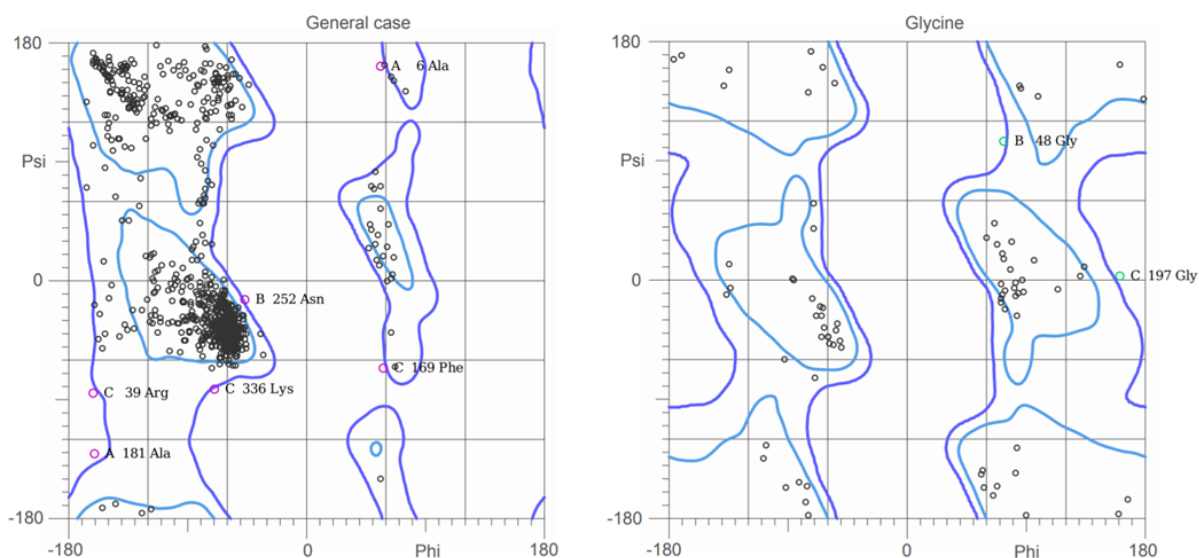


Figure 5.4: Ramachandran outliers in the yeast F-actin model. Ramachandran plots generated by MOLPROBITY and visualised with kinemage (Lovell *et al.*, 2003). The 8 outliers are annotated.

5.2.5 The Nucleotide Binding Cleft

The nucleotide binding cleft contained a density corresponding to ADP (Figure 5.5) and lacked any density corresponding to a γ -phosphate, indicating this structure represented the ADP state of F-actin. The cation (Mg^{2+}/Ca^{2+}) is not seen at the resolution of our map but its approximate position is shown for reference. Since flexible fitting had been performed independently for each of the 3 model protomers, we used this as an opportunity to establish which interactions between ADP and actin were most likely. As expected, each model cleft had a slightly different positioning of sidechains and profile of hydrogen bonds with ADP. 7 hydrogen bond partners were consistent across all three binding clefts and these are labelled in Figure 5.5B. Additionally, the approximate position of a salt bridge between α - PO_4 and Lys18 is annotated, which was also present in the RSkM F-actin model. All residues involved in the bonds described between actin and ADP are conserved in rabbit and yeast, and none are Ramachandran outliers in either model.

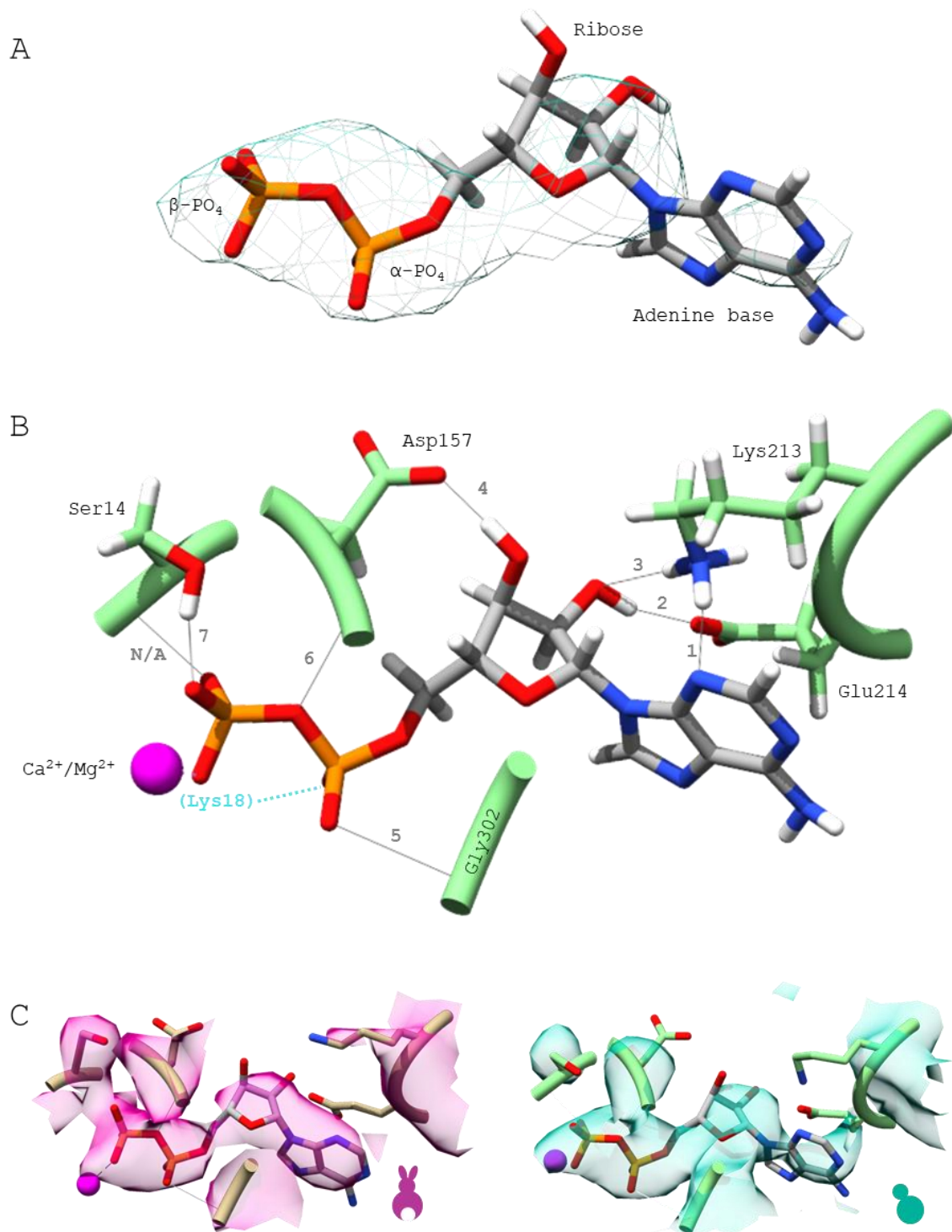


Figure 5.5: ADP in the nucleotide binding cleft. **A)** A model of ADP and corresponding density (mesh) from protomer n of the experimental map. **B)** The model of residues identified as forming hydrogen bonds with ADP in protomer n. The hydrogen bonds consistent across all three protomer models are numbered 1-7. The approximate position of a salt bridge between α - PO_4 and Lys18 is indicated by the dashed cyan line. The divalent cation ($\text{Ca}^{2+}/\text{Mg}^{2+}$) is represented by a magenta sphere. **C)** Comparison of the nucleotide binding cleft of RSKM (left) and yeast F-actin (right).

5.2.6 Protomer-Protomer Interfaces in the Yeast F-actin Model

The yeast F-actin model was next used to examine protomer-protomer interfaces in more detail in the context of the experimental map, and with direct comparison to the RSkM model and map (figures 5.6-5.9). This aim of this analysis is to assess whether any differences are detectable at this resolution between the filaments from the two isoforms, and to identify potential regions of interest for when a higher resolution structure is obtained in future. Protomer interfaces were chosen as the focus because small changes in these regions could have profound functional consequences for the filament.

D-loop Shape and Ramachandran Outliers

The major mediator of protomer-protomer contacts is the D-loop, which is positioned at both intra- and inter-strand interfaces and therefore contacts two neighbouring protomers. While the overall D-loop conformation appears to be similar, our map and model indicate a slightly distorted D-loop in F-actin compared to the rounded D-loop of RSkM F-actin (Figure 5.6). However, as a flexible region, the D-loop was poorly resolved in both RSkM and yeast F-actin maps and therefore both models are limited in their ability to accurately represent this loop. Notably, both models contain Ramachandran outliers in this region (Gly48 in yeast F-actin; Pro38, Met44 and Ser52 in RSkM F-actin).

Interactions of the D-loop

In our model, the D-loop of protomer $n+1$ forms two H-bonds with its intra-strand neighbour protomer $n-1$. These interactions are between residues at the top of the D-loop (Val45 and Ile43) with the sidechain hydroxyl group of Tyr143 and with the backbone of Phe196 of protomer $n-1$, respectively. Together, these H-bonds appear to ‘clamp’ the D-loop in place (Figure 5.6B). The RSkM F-actin model forms H-bonds between the equivalent residues but there is a substitution at position 43 (Val43 in RSkM), and in RSkM F-actin *two* H-bonds are formed between each of these pairs of residues. Another noticeable point of contact between these two protomers is formed between the complementary surfaces of the protruding Phe169 aromatic ring from $n-1$ and the interior of the D-loop from $n+1$ (Figure 5.6A). Importantly, in RSkM F-actin the aromatic sidechain

nestled in the D-loop is Tyr169, and its reactive hydroxyl group allows its position there to be further stabilised by an H-bond with Gln49.

The H-loop

In Figure 5.7B, the residues with closest proximity to the H-loop in our model are displayed: Arg39, His40, Ser201 and Thr202 from the inter-strand neighbour closest to the barbed-end of the filament, and His173 from the inter-strand neighbour closest to the pointed-end of the filament. This interface contains four substitutions between yeast and RSkM F-actin, and the prominent extra density at position 266 in the RSkM F-actin map is a clear indicator of the bulkier Phe at this position compared to Val in yeast (Figure 5.7C). However, it is not clear what the structural implications of these substitutions are based on the maps as the interface appears otherwise highly similar.

Arginine 39

In our model, Arg39 at the base of the D-loop of protomer n+1 forms a hydrogen bond with the main chain carbonyl at Gly268 in the H-loop of its inter-strand neighbour protomer n. Interestingly, Arg39 in the RSkM F-actin model does not form an H-bond with the H-loop. Instead, Arg39 in the RSkM F-actin model forms a salt bridge with Asp286 of protomer n-1 (Figure 5.6C). A very subtle difference in the positioning of Arg39 in these models therefore makes the difference between its involvement in an *inter*-strand interface or an *intra*-strand interface.

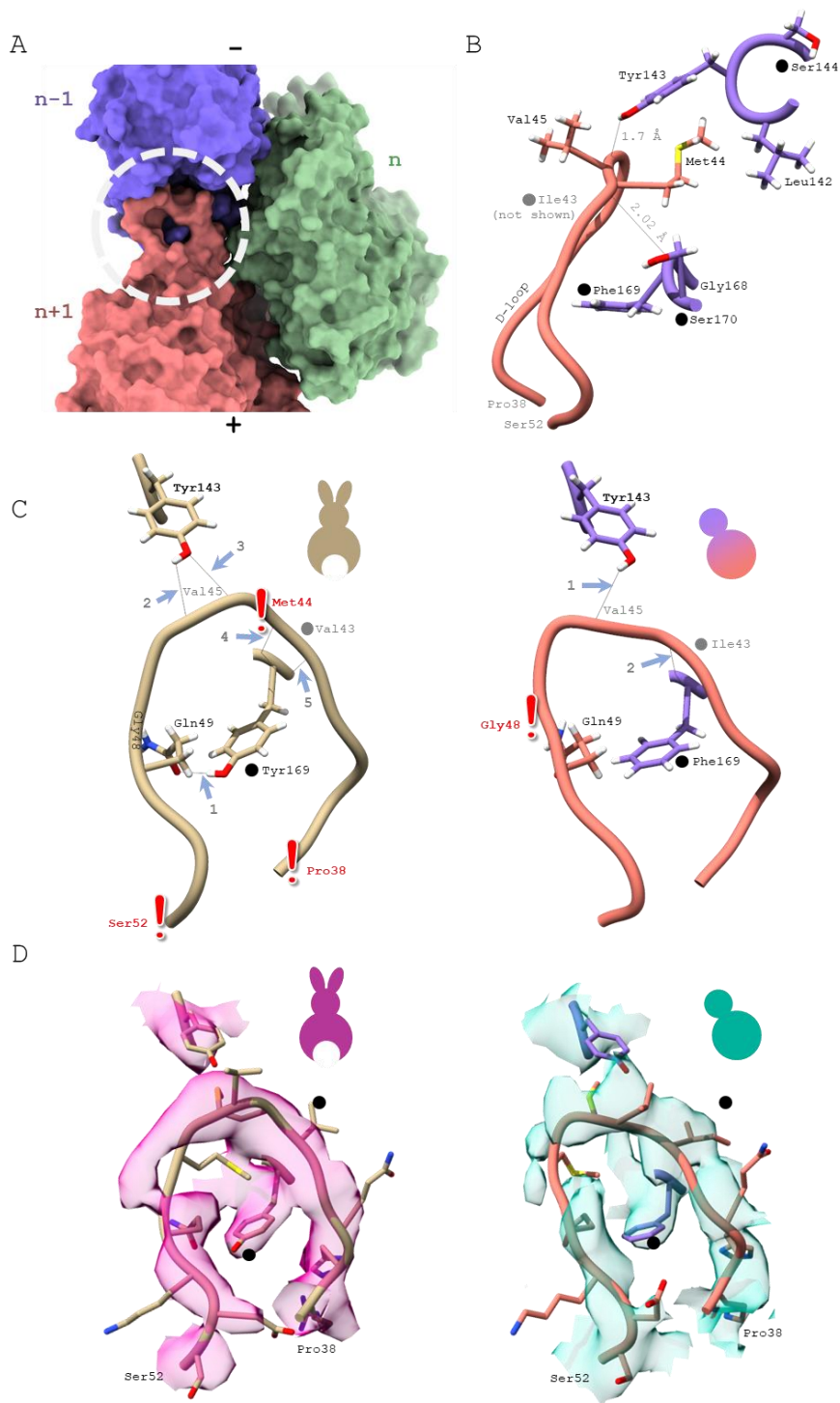


Figure 5.6: The D-loop. **A)** Surface view of the yeast F-actin model with the D-loop of one protomer circled. **B)** Side view of the yeast F-actin model D-loop displaying select residues (with hydrogens) and H-bonds. **C)** Comparison of D-loop models for RSkM F-actin (beige) and yeast F-actin (coloured to match the protomers in panel A). H-bonds in are indicated by arrows and numbered 1-5 in skeletal muscle F-actin, and 1-2 in yeast F-actin. Black/grey dots indicate amino acid substitutions between RSkM and yeast F-actin. Red exclamation marks indicate Ramachandran outliers. **D)** Both model D-loops (displaying all residues, without hydrogens) set in their corresponding density maps.

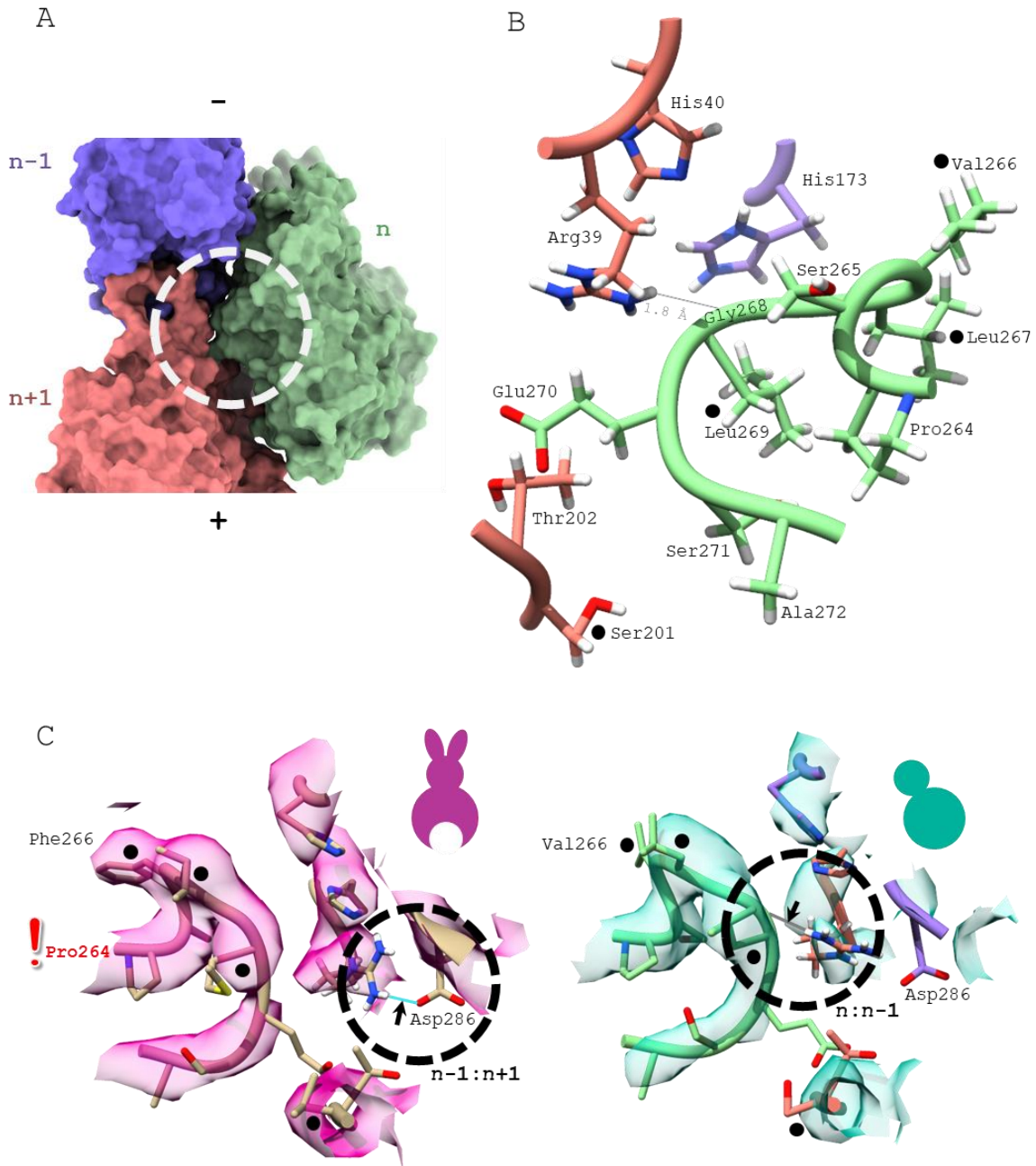


Figure 5.7: The H-Loop. **A)** Surface view of the yeast F-actin model with a circle indicating the interface between the H-loop (protomer n ; green) and residues in the opposite protofilament ($n+1$ and $n-1$; pink and purple protomers). **B)** The yeast F-actin model of residues involved in this interface. Hydrogens are displayed in order to show the hydrogen bond (length = 1.8 Å formed between Arg39 and Gly268, which is not seen in the protonated 5ONV model). Asp286 is not displayed. **C)** The RSkM model/map and the yeast F-actin model/map viewed from a different angle compared to panel **B**, with the H-loop of protomer n on the left. Arginine 39 is circled in both models and hydrogens for this residue are displayed. Arg39 forms an intra-strand salt bridge in RSkM between protomer $n-1$ and protomer $n+1$, while in yeast F-actin it forms an inter-strand H-bond between protomer n and protomer $n-1$. Black dots indicate amino acid substitutions between RSkM and yeast F-actin. Pro264 is a Ramachandran outlier in the RSkM F-actin model. The colouring of the yeast model backbone throughout this figure is consistent with the protomer colouring in panel **A**.

Other Protomer-Protomer Interfaces

Apart from the H-loop, the only other inter-strand interface is a hydrogen bond between the backbone hydrogen of Lys113 and the backbone oxygen of Glu195. This bond was conserved in our model, and of similar length (1.97 Å in the yeast F-actin model vs 2.17 Å in the RSkM F-actin model). An ionic interaction between the sidechains of these two residues is also known to be important (Wen *et al.*, 2013). In our model, these charged functional groups are separated by 6.5 Å, though the lack of clear density for these sidechains did not allow their positioning based on experimental data (Figure 5.8).

Intra-strand interfaces are slightly more extensive. SD3 forms intra-strand contacts with other regions of SD2 as well as the D-loop, and also with SD4. The SD3-SD4 contacts in our model are an H-bond between Arg290-Asp244 (conserved in RSkM F-actin) and two H-bonds between Ser324-Glu241 (Figure 5.9A-C). In RSkM F-actin, the equivalent is Thr324-Glu241, which is just a single H-bond. In addition to the D-loop (covered above), the SD3-SD2 contacts are Asp288-Arg62 and Asp288-Gly63 in both models (Figure 5.9D-F). Comparison of salt bridges in yeast and RSkM F-actin revealed salt bridges at the intra-strand interface that are missing in our yeast F-actin model: Asp286-Arg39 (covered above) and 2 bonds between Glu167 and Lys61 (Figure 5.10). In yeast actin, the residue at position 167 is Ala, which is smaller than Glu and uncharged.

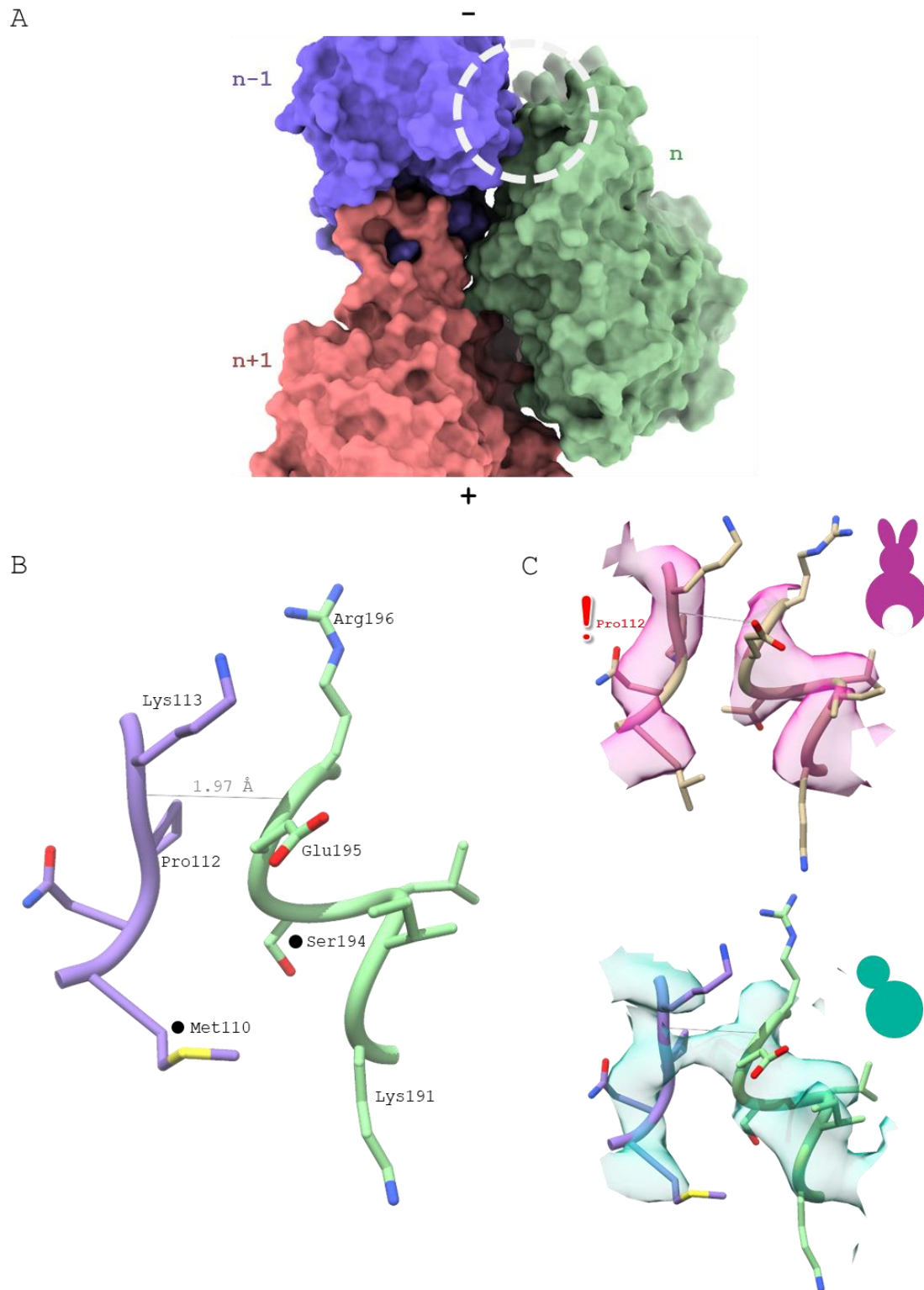


Figure 5.8: An Inter-Strand Interaction Site. A) Surface view of the yeast F-actin model with a circle indicating the interface between Lys113 and Glu195. B) The yeast F-actin model of residues at this interface. C) The yeast F-actin model overlaid with the RSkM F-actin model (beige) displayed in each of the experimental maps. Black dots indicate amino acid substitutions between RSkM and yeast F-actin. Pro112 is a Ramachandran outlier in the RSkM F-actin model. The colouring of the yeast model backbone throughout this figure is consistent with the protomer colouring in panel A.

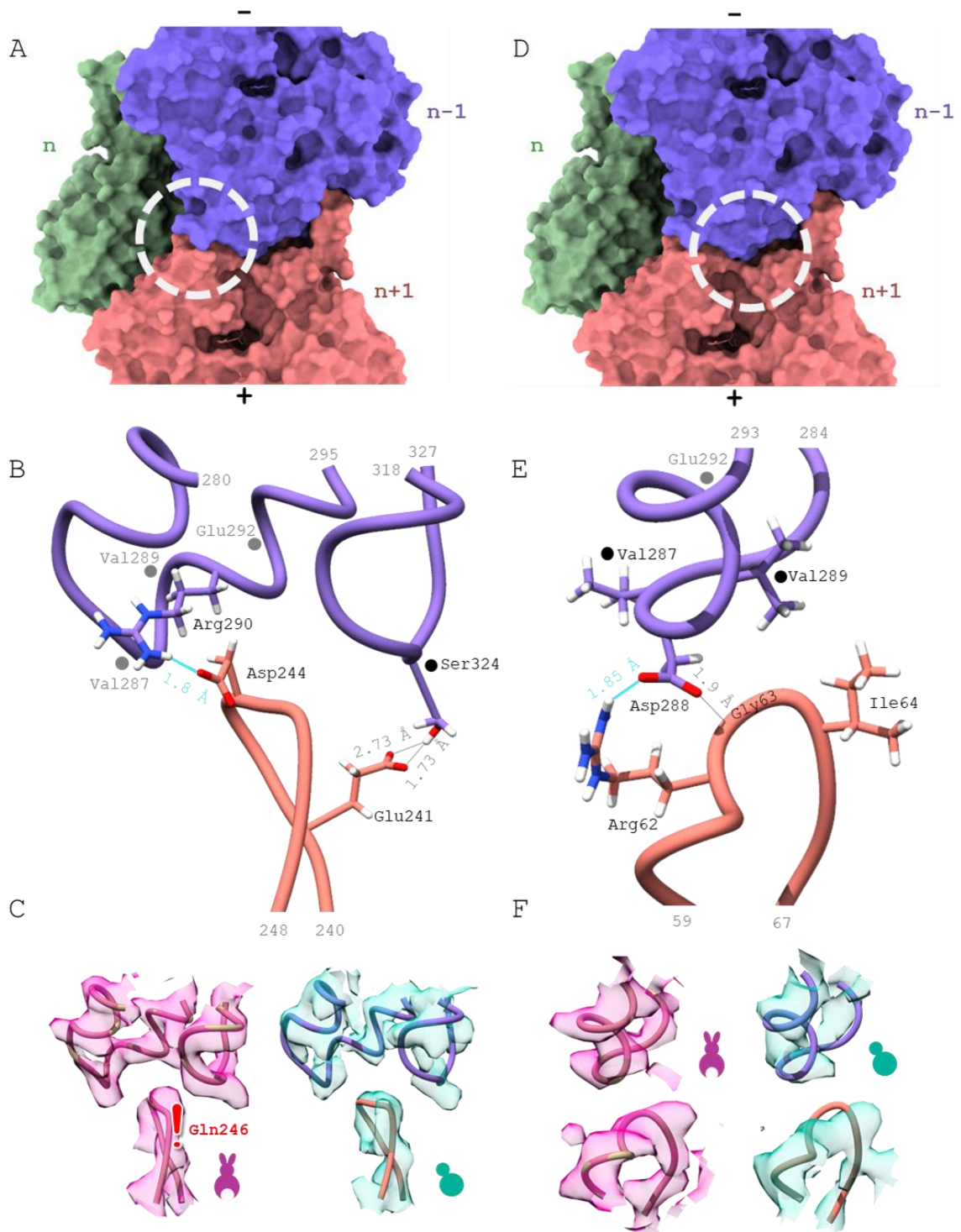


Figure 5.9: Two intra-strand Interaction sites between intra-strand neighbours. A & D) Surface view of the yeast F-actin model with a circle indicating the interface of interest. B & E) Model of residues involved in each interface, with select residues displayed. Black and grey dots represent aa substitutions of displayed and hidden sidechains, respectively. C & F) The model backbone set in the experimental map. A Ramachandran outlier in the RSkM F-actin model is indicated. The colouring of the yeast model backbone throughout this figure is consistent with the protomer colouring in Figure 5.3.

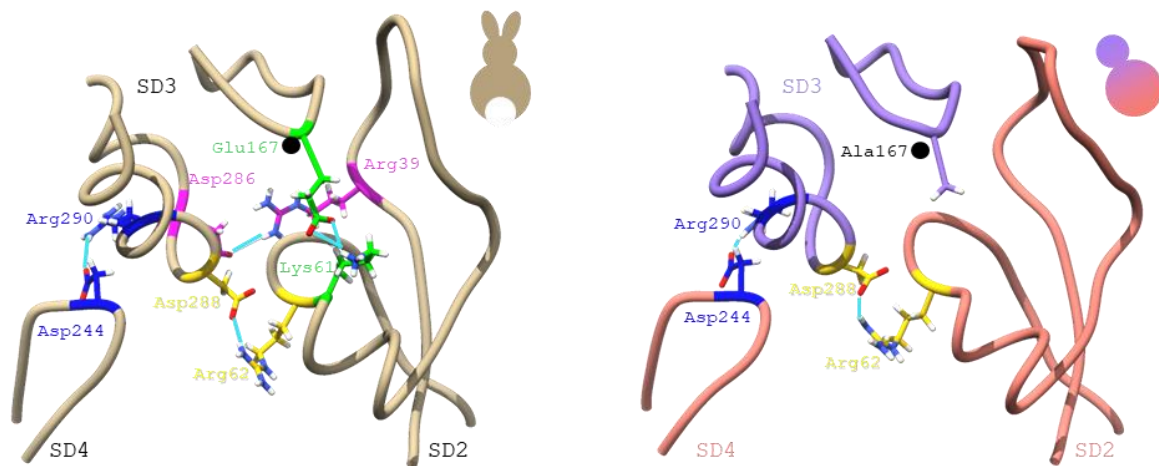


Figure 5.10: Salt bridges at the intra-strand interface in RSkM F-actin and yeast F-actin. Each pair of H-bonded residues is coloured differently to the model backbone (blue, pink, green or yellow). Salt bridges are represented by cyan lines. The substitution at position 167 is indicated by a black dot. The colouring of the yeast model backbone is consistent with the protomer colouring in Figure 5.3.

5.2.7 Phalloidin-binding Site

The phalloidin-binding site of F-actin is located in the interface between the protofilaments, on the opposite side to the H-loop (Figure 5.11A). Residues from three protomers face bound phalloidin, but phalloidin has most contact with the ϕ -loop (aa197-203) of one protomer ($n+1$ in our model) and the 73-75 loop of its inter-strand neighbour (n in our model) (Oda *et al.*, 2005; Das *et al.*, 2020; Pospich *et al.*, 2020). Yeast F-actin has been found to bind to phalloidin more rapidly than skeletal muscle actin, but with weaker affinity (De La Cruz and Pollard, 1996), so this region was examined in our model in comparison to our chosen homology model and map. One important difference between yeast and RSkM F-actin at the phalloidin-binding interface is the presence or absence of post-translational methylation of the His at position 73 to give 3-methylhistidine (Hic73). This PTM is known to be absent in yeast F-actin, so this was factored into our model (Kalhor *et al.*, 1999). Comparing the yeast and RSkM F-actin models indicated that Hic73 is in closer proximity to Lys284 (Figure 5.11B). The backbone positioning in residues near the phalloidin binding site was generally similar in our map compared to the RSkM actin map, but sidechains were poorly resolved in both maps and therefore no meaningful direct comparison could be made at a greater level of detail (Figure 5.11C).

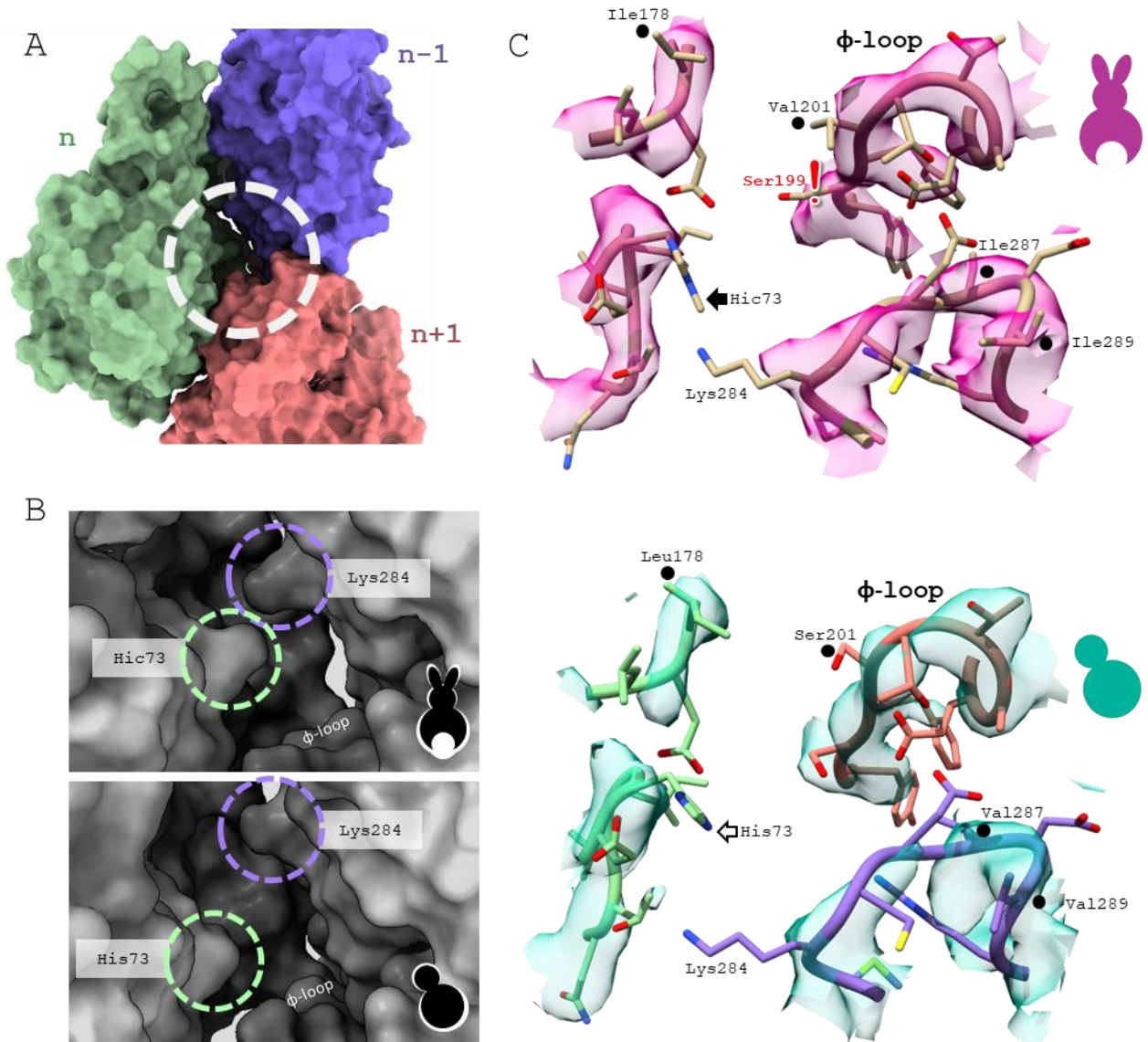


Figure 5.11: Phalloidin-binding site. **A)** Surface view of the yeast model with the phalloidin-binding site circled. **B)** Surface view of the RSkM F-actin (top) and yeast F-actin (bottom) model at the phalloidin binding site. Circles indicate the difference in relative positioning of His/Hic73 and Lys284. **C)** The models and corresponding density for the RSkM and yeast F-actin phalloidin binding sites, which includes the ϕ -loop. Substitutions and Ramachandran outliers are labelled with black dots and red exclamation marks, respectively. Also annotated is the methyl group of the methylated His (Hic) at position 73 of rabbit F-actin. Hydrogen atoms are not displayed.

5.3 Discussion

Our analysis of yeast F-actin structure at 4.7 Å resolution does not support conclusions from low resolution studies that yeast F-actin has a more open nucleotide binding cleft or significantly reduced inter-strand interactions (Orlova *et al.*, 1997, 2001; Belmont *et al.*, 1999). The map density of yeast F-actin and that of a published ADP-bound RSkM F-actin map (Merino *et al.*, 2018) were found to be highly similar.

A detailed comparison of RSkM and yeast F-actin using our pseudo-atomic model and the published homology model was performed to identify potential areas of interest to re-examine once a higher resolution structure for yeast F-actin is achieved. It is important to emphasise that this preliminary analysis is speculative, since the experimental map lacked the resolution to accurately position side-chains. This analysis highlighted some subtle differences between the yeast and RSkM models that may be indicative of weaker protomer-protomer interactions in yeast F-actin. Interestingly, these have greater implications for *intra*-strand interactions. One of these differences was the additional H-bonds of the RSkM F-actin D-loop. Of particular interest is the interaction of the D-loop with the residue at position 169. In yeast F-actin, Phe169-D-loop interaction is stabilised by van der Waals forces alone, whereas the Tyr169-D-loop interaction in RSkM F-actin is additionally stabilised by an H-bond to Gln49 enabled by the Tyr hydroxyl group. The remaining two extra H-bonds (a second bond for Val45-Tyr143 and Ile43-Phe169) appear to be lost in yeast F-actin because of subtle repositioning of the backbone, and since this region was poorly resolved in the maps it cannot be known for certain if this is a real difference between yeast and RSkM F-actins, or simply a difference in these models.

Another indication of potentially weaker intra-strand interactions in yeast F-actin compared to RSkM F-actin is the reduced number of salt bridges between SD3 of one protomer and SD2/4 of its barbed-end intra-strand neighbour. The Lys61:Glu167 salt bridge in RSkM F-actin was absent from yeast F-actin, which may be attributable to an amino acid substitution at position 176 (Ala167), which unlike Glu167 lacks oxygens in its sidechain. The other salt bridge missing from our yeast F-actin model was Arg39:Asp286. In the yeast F-actin model, Arg39 instead formed an

inter-strand interaction with the H-loop (Figure 5.7). The positioning of Arg39 in the two models was only slightly different. This raises the interesting possibility is that Arg39 may be able to switch between mediating *inter*-strand and *intra*-strand interactions within the filament by reorienting its side-chain. It should be stressed that the absence of a clear sidechain density in the maps did not allow unambiguous positioning, therefore it is unclear if the interaction of Arg39 truly differs between the isoforms. Refinement of the model sidechains with higher confidence will require improved experimental data.

5.3.1 F-actin Helical Parameters for Different Species

Our comparison of helical symmetry measurements from published structures has supported previous observations that axial rise is highly conserved across species (~ 27.5 Å), while twist is slightly more variable (Egelman *et al.*, 1982). F-actin from published *P. falciparum* structures and from our own yeast F-actin structures were found to have a significantly more negative twist (-167.4° and -167.3° , respectively) compared to actin from vertebrate α -skeletal muscle and *Z. mays*. The maintenance of a constant axial rise with a varied helical twist is seen upon decoration of F-actin by the severing protein cofilin: cofilin was observed to shorten the crossover length of the two actin protofilaments by 25%, but without altering the overall length of the filament (McGough *et al.*, 1997). Actin decorated with cofilin (cofilactin) has a helical twist of -162.1° (Galkin *et al.*, 2011), indicating that F-actin can withstand a considerable alteration to its twist. It has recently been confirmed that severing occurs at the interface between decorated and bare actin due to the stark difference in twist, but not because of the twist itself (Huehn *et al.*, 2018). As far as we are aware, no direct comparison has been made between the sensitivity to cofilin of yeast F-actin and skeletal muscle F-actin. Based on the findings of our work, it might be expected that yeast actin would have increased sensitivity to cofilin because the resultant twist difference between cofilactin and bare actin would be more extreme than in vertebrate α -actin (albeit only slightly).

The actin filament should not, however, be thought of as a static uniform molecule. The Egelman/Galkin group have published a body of work investigating structural heterogeneity in actin filament populations. Variations in the twist of F-actin were reported as early as the 1980s

(Egelman, Francis and Derosier, 1982). One of their more recent studies examined twist variability in cryo-EM samples, and found that filaments were fairly uniform in thin ice, but exhibited greater twist variability in thicker ice (Galkin *et al.*, 2015). Though ice thickness is difficult to measure quantitatively, our samples were noted to objectively have relatively thick ice. The twist range reported for vertebrate α -actin in the 1982 study was -167.14° to -166.15° , and the 2015 paper sorted filaments into -166° and -167° classes. The twist of yeast and *P. falciparum* F-actin is more negative than these values still, so the more extreme twist observed for these actin filaments may still be of functional significance.

6. Las17PP Bundles F-Actin *in vitro*

6.1 Introduction

6.1.1 Research Aims

The ability of the central polyproline-rich portion of Las17 (Las17PP) to bind and nucleate actin *de novo* – and the inability of Arp2/3 to nucleate actin in the absence of a pre-existing filament – raises the interesting possibility that Las17, not Arp2/3, might be the nucleator responsible for assembling the first actin molecules at the endocytic site into filaments (Urbanek *et al.*, 2013; Allwood *et al.*, 2016). One of the aims of this project was to determine whether Las17PP has any detectable influence on the structure of the F-actin it nucleates. An additional cryo-EM dataset was therefore collected for yeast F-actin polymerised in the presence of Las17PP₃₀₀₋₅₃₆, which is presented in this chapter.

An unexpected outcome of this work was the finding that, if present in high enough concentrations, Las17PP not only nucleated actin, but also bundled the filaments. The following chapter outlines the discovery and characterisation of this novel and previously unrecognised ability of Las17PP, and considers the potential physiological insights this provides. A variety of techniques was explored to investigate the organisation of actin and Las17 in these F-actin bundles. The results presented here build on the previous discovery and characterisation of the actin-binding capabilities of Las17PP by the Ayscough lab and others (Urbanek *et al.*, 2013; Feliciano *et al.*, 2015; Allwood *et al.*, 2016).

6.1.2 The Polyproline Region of Las17

Full length Las17 is comprised of 633 amino acids and has a MW of ~68 kDa. As is characteristic of WASP family proteins, the N-terminal portion of the protein contains a WH1 domain (~aa 14-123), while the C-terminal portion contains a WH2 domain (~aa 544-571) followed by central and acidic domains. The polyproline region is a central portion of the protein containing 9 runs of (usually

5) consecutive proline residues (referred to hereafter as ‘PP tracts’). These tracts have a regular structure called a poly-L-proline type II (PPII) helix, as seen in the only available model for Las17 structure based on direct experimental data (PDB ID: 1ZUK; aa350-360). PPII helices are left-handed helices repeating every 3 residues that have an extended structure compared to α -helices, i.e. a longer pitch and narrow radius (reviewed in Adzhubei, Sternberg, and Makarov 2013).

The Las17PP fragments used in this study span amino acids 300-536 and 300-422, which contain PP tracts 2-9, and 2-5, respectively (Figure 6.1). Every PP tract in the 300-536 region consists of 5 consecutive proline residues. The PP tracts occur throughout the length of this region with fairly regular spacing (23 ± 12 residues). In the full-length protein there is an additional PP tract (P1) consisting of 6 consecutive proline residues found at aa185-190, but this is a considerable distance from the other PP tracts and its inclusion is not a requirement for actin binding or the *de novo* nucleation and elongation capabilities of Las17PP.

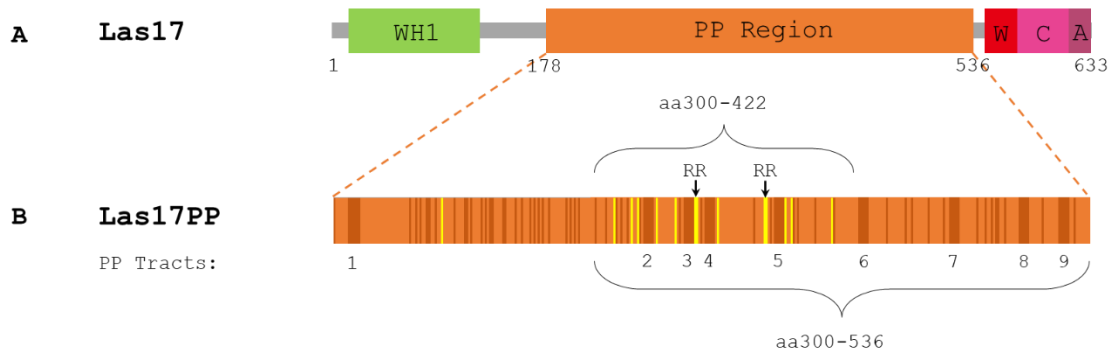


Figure 6.1: Domain structure of Las17, with focus on the polyproline region. **A)** The positions of the following domains in the primary structure of the protein are indicated: WASP-homology 1 (WH1), polyproline region (PP Region), WASP-homology 2 (WH2, here shortened to W), central (C) and acidic (A) domains are indicated. **B)** The polyproline region has been expanded and colour-coded to indicate the positions of proline residues (dark orange) and arginine residues (yellow). The polyproline tracts of 5 consecutive proline residues (PP tracts 2-9) or 6 consecutive proline residues (PP tract 1) are indicated. The arginine pairs (RR) identified as being important for G-actin binding are annotated. The purified Las17 fragments used in this project are aa300-536 and aa300-422.

Two pairs of arginine residues, one located 3 residues before PP tract 4 and the other located 3 residues before PP tract 5, have been demonstrated to contribute to G-actin binding by Las17 (Figure 6.1B). Simultaneously mutating both pairs from RR to AA weakens G-actin binding of Las17PP fragments six-fold, and severely diminishes *de novo* nucleation activity by these fragments *in vitro* (Feliciano *et al.*, 2015; Allwood *et al.*, 2016). *In vivo*, this mutation (RR,RR>AA,AA) in full-length Las17 was found to have relatively normal size and distribution of cortical actin patches, but Arp2/3 recruitment was delayed (Allwood *et al.*, 2016). In all assays, mutating just one arginine pair at a time resulted in intermediate effects between the WT and the mutant with both arginine pairs mutated, indicating the additive nature of these basic residues for actin binding.

Another feature of importance in the PP region are the PP tracts themselves. Simultaneously mutating P8 and P9 to PPPAA impaired Las17-mediated actin elongation *in vitro* (Urbanek *et al.*, 2013). Yeast expressing this mutant Las17 exhibited reduced stability of endocytic patch positioning in the plasma membrane, with increased lateral movement of early endocytic proteins prior to invagination. *In vitro* assays using a 28mer peptide containing only P8 and P9 demonstrated that these neighbouring PP tracts were able to elongate, but not nucleate actin. Expressing different length fragments of Las17PP containing different numbers of PP tracts indicated that a greater number of PP tracts promoted a higher rate of F-actin elongation (Allwood *et al.*, 2016). A greater number of PP tracts also promoted stronger actin binding (Urbanek *et al.*, 2013). Any C-terminal or N-terminal truncations of the 300-536 fragment that removed two or more of the PP tracts compromised actin binding and elongation compared to the full fragment.

While it has been possible to dissect some of the functions of specific residues in Las17PP, the functions of this region appear to be due to the collective action of multiple weak actin binding sites. The exact mechanisms by which Las17PP binds, nucleates and elongates actin filaments are still not well understood and require further investigation. The work described in this chapter introduces an additional *in vitro* capability of Las17PP, which may provide additional insight into how Las17PP mediates its interaction with G- and F-actin.

6.2 Results

6.2.1 A Cryo-EM Structure for Yeast F-actin Polymerised in the Presence of Las17PP

A cryo-EM dataset of 375 micrograph movies was collected for yeast F-actin polymerized in the presence of Las17PP₃₀₀₋₅₃₆ (in the absence of KME). The same processing steps were followed as for the KME-polymerised yeast F-actin dataset (Chapter 4) to produce a final map with 4.8 Å resolution, using 74,207 particles from 193 movies (Figure 6.2). The symmetry (27.7 Å axial rise and -167.2° twist) was almost identical to the map for KME-polymerised F-actin, and the two maps had a very high correlation coefficient of 0.96. No density corresponding to Las17PP was detected in the final map, however a possible density was detected in a low-resolution map from 3D classification.

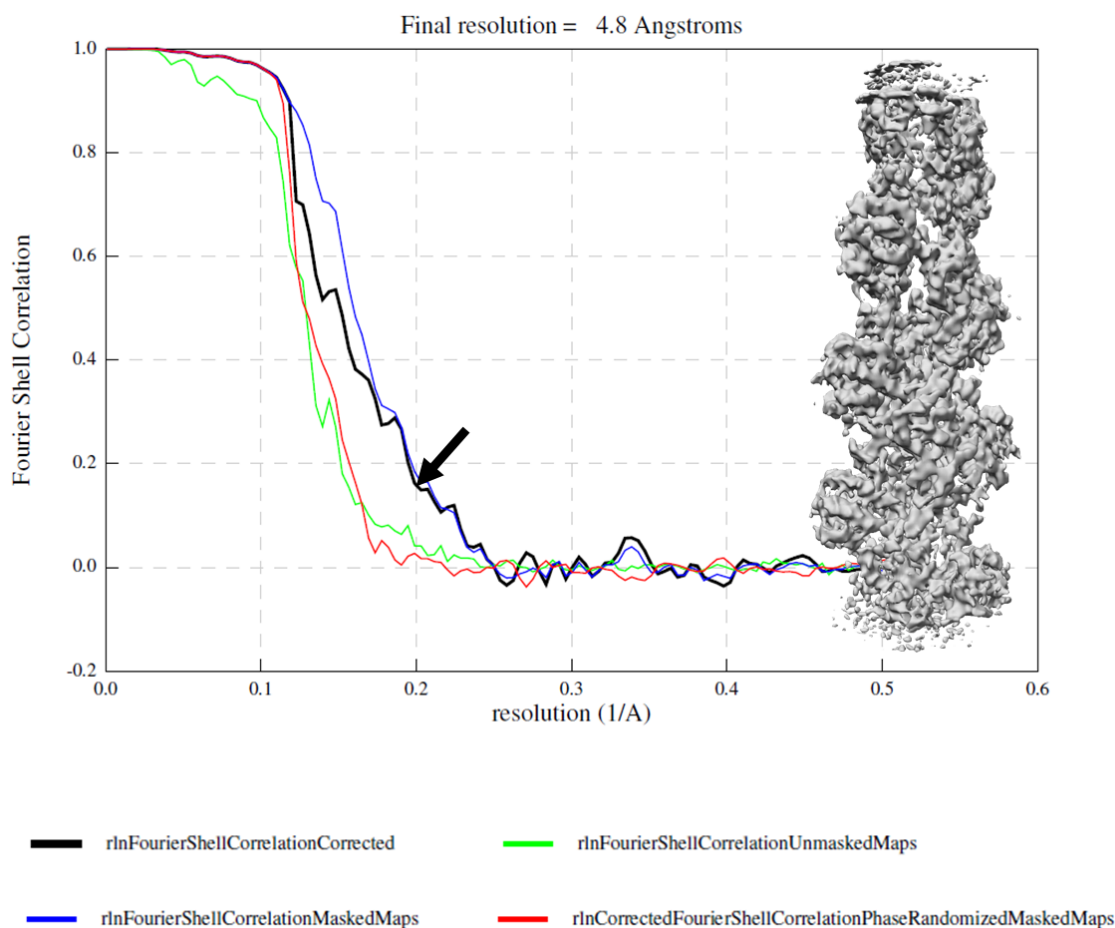


Figure 6.2: FSC curve and final map of yeast F-actin polymerized in the presence of Las17PP. Arrows indicate the point where the corrected FSC curve (black) crosses the threshold value of 0.143, which is the traditional method for determining maximum map resolution (Rosenthal and Henderson, 2003). Inset: the final, unmasked map.

3D classification with four classes was performed to detect any sub-populations of filaments with distinct structures. 3D classification was successful for this dataset, with two of the classes – Class003 and Class004 – displaying a characteristic F-actin structure, with a polar arrangement of subunits with a visible cleft (Figure 6.3A). Class004 protomers had an additional area of density that protruded from subdomain 4 (indicated on one of the protomers by an arrow). Interestingly, this extra density is adjacent to a cluster of residues previously demonstrated to be of importance for Las17PP-binding (Urbanek *et al.*, 2013; Figure 6.3B). Performing a 3D refinement using only the particles contributing to Class004 removed the extra density, so further investigation was not possible with this dataset.

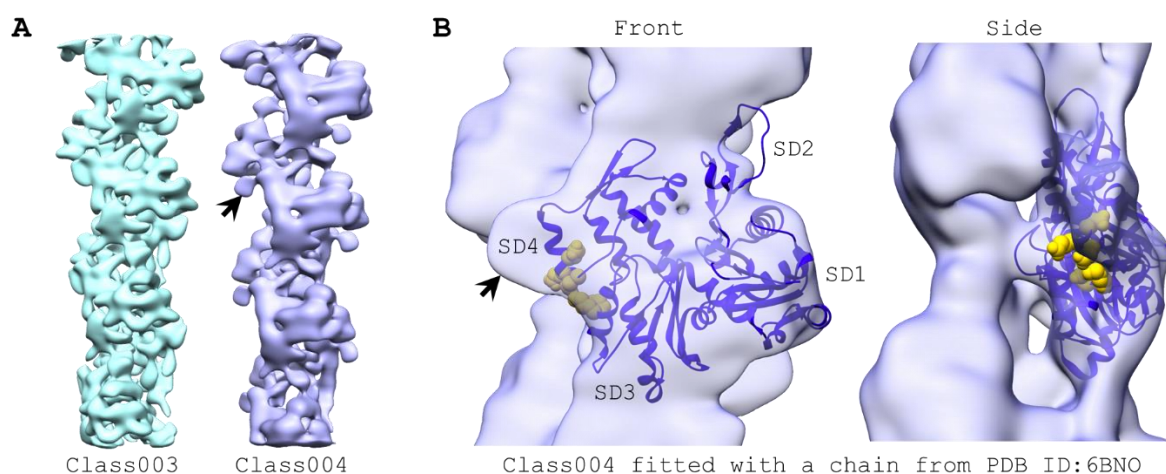


Figure 6.3: 3D Classification reveals extra density at the predicted binding site for Las17PP. **A)** The two successful classes from 3D classification, with 23,046 and 23,682 contributing particles, respectively. The extra density seen in the Class004 map is indicated by an arrow. **B)** Class004 fitted with a single actin protomer from PDB ID: 6BNO. Residues putatively involved in binding Las17PP (K315, E316, D222, E224 and E226; Urbanek *et al.*, 2013) are represented by gold spheres. Subdomains 1-4 (SD1-4) are indicated. A slightly lower contour threshold was applied here compared to panel A.

6.2.2 An Increased Las17PP Concentration Enhances Actin Polymerisation and Induces Filament Bundling

Las17PP had been undetectable in cryo-EM at the concentration used to generate the filaments in the dataset described above, which was a ~1:10 molar ratio Las17PP:G-actin. In an effort to increase the likelihood of detecting Las17PP bound to F-actin, the concentration was increased to equimolar Las17 and G-actin. However, screening negatively stained samples prepared using this greatly increased Las17PP concentration detected thick F-actin bundles rather than isolated, linear actin filaments.

To investigate this finding, samples of 5 μM G-actin were prepared with different nucleation conditions: A) no nucleator, B) KME, C) 0.5 μM Las17PP₃₀₀₋₅₃₆ and D) 5 μM Las17PP₃₀₀₋₅₃₆. All samples were incubated for ~1 hr at room temperature. For this experiment, TEM was paired with a high-speed pelleting (HSP) assay to quantitatively assess the proportion of actin in the monomeric and filamentous states. The speed used in an HSP assay ($\geq 100,000 \times g$) is sufficient to pellet F-actin, but not G-actin, so it can be used to assess the proportion of actin in the monomeric vs the polymeric state by comparing band densities for the supernatant and pellet. Condition A (actin in G-buffer) was used as a control for minimum polymerisation to confirm that the purified actin used in the experiment had not spontaneously polymerised prior to the experiment (Figure 6.4A). Condition B (actin in F-buffer; G-buffer + KME) was used as a control for maximum polymerisation to confirm that the actin used was polymerisation-competent (Figure 6.4B).

Increasing the concentration of Las17PP relative to actin increased the proportion of actin in the filamentous state, from ~50% to ~94% and induced the formation of sparsely distributed actin bundles, several filaments thick (Figure 6.4D), contrary to the dense actin mesh observed for the KME-nucleated actin sample (Figure 6.4B) and the filaments observed in the sample with a low concentration of Las17PP (Figure 6.4C). An additional observation is that in both C and D, the Las17PP₃₀₀₋₅₃₆ co-pelleted with F-actin, indicating F-actin binding.

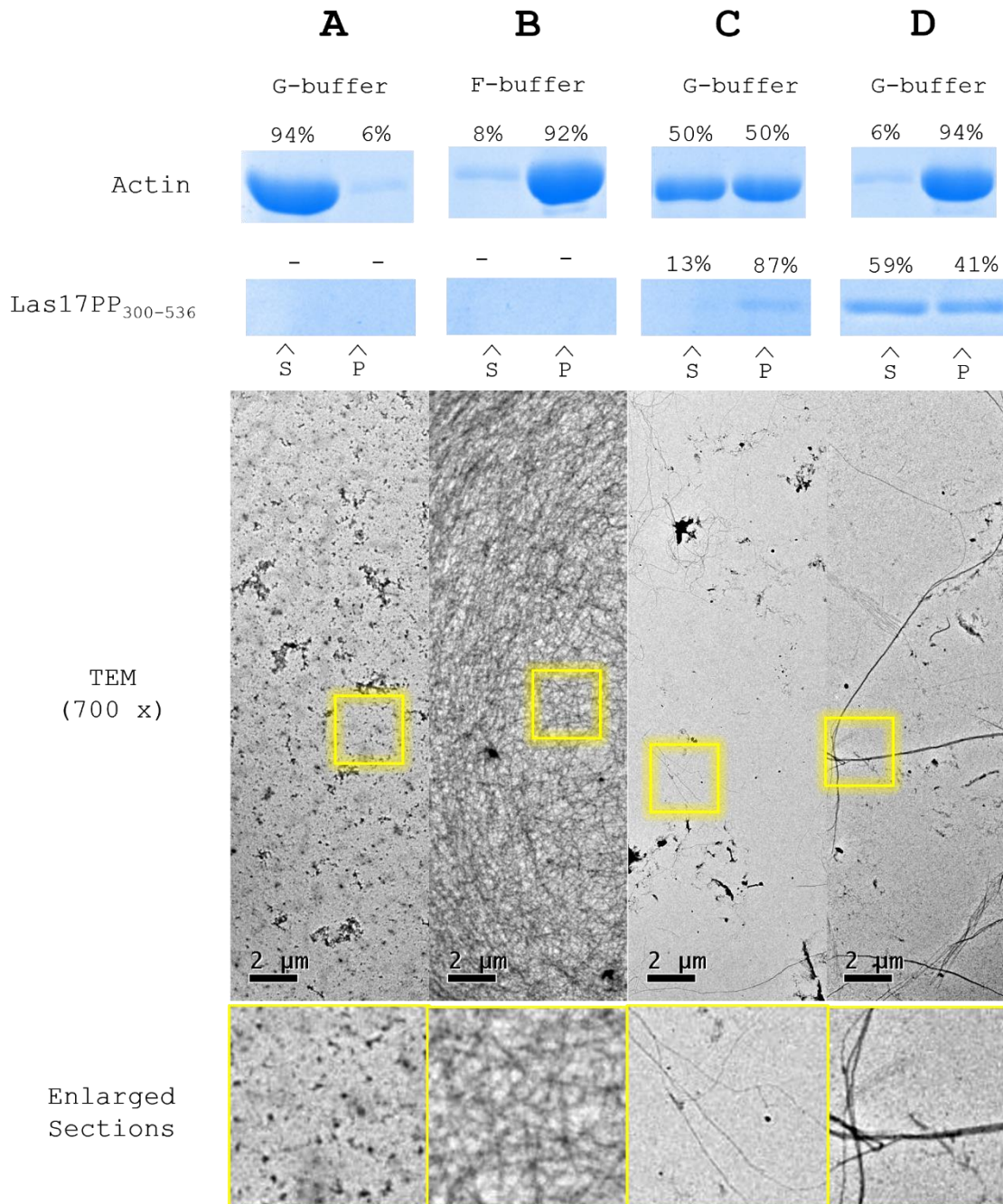


Figure 6.4: Pairing TEM with a high-speed sedimentation assay to investigate the effect of a high Las17PP concentration on the polymerisation of F-actin. Coomassie-stained SDS-PAGE gel bands for actin and Las17PP are shown at the top of the figure, with the supernatant (S) and pellet (P) indicated for each condition. TEM images of the same samples are shown below, with enlarged sections inset. **A)** G-actin in G-buffer, **B)** G-actin in F-buffer (G-buffer + KME), **C)** G-actin and 0.5 μM Las17PP₃₀₀₋₅₃₆ in G-buffer (1:10 ratio actin:Las17), **D)** G-actin and 5 μM Las17PP₃₀₀₋₅₃₆ in G-buffer (1:1 ratio actin:Las17). All samples used 5 μM rabbit skeletal muscle G-actin.

6.2.3 Assessing the Proportion of F-actin integrated in Bundles

While high speed pelleting assays ($\geq 100,000 \times g$) can be used to separate F-actin from G-actin, centrifugation at a much lower-speed ($\geq 14,000 \times g$) can be used to separate bundled F-actin from unbundled F-actin and G-actin. High-speed and low-speed pelleting (HSP and LSP) assays were run side-by-side to get an indication of the total proportion of actin in the F-actin state as well as the proportion of actin contained in actin bundles (Figure 6.5).

A sample containing only $4 \mu\text{M}$ G-actin in G-buffer (with no added nucleator) served as a negative control for both polymerisation and bundling. As expected, KME-nucleated F-actin remained unbundled, with no significant increase in the actin content of the low-speed pellet compared to the G-actin only control. In contrast, most of the F-actin nucleated by $4 \mu\text{M}$ Las17PP₃₀₀₋₅₃₆ was bundled (Figure 6.5; grey bars). This indicated that low-speed sedimentation was an appropriate assay to use for detecting the presence of Las17-induced actin bundles.

Assessment of Actin Bundling by Sedimentation Assays

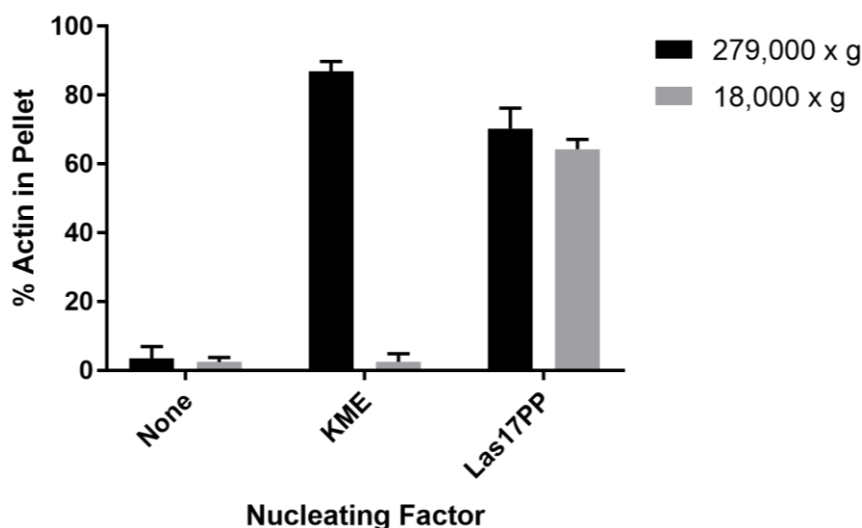


Figure 6.5: High-speed and low-speed sedimentation of actin incubated under different nucleating conditions. A bar graph summarising the average proportion of F-actin in the pellet when $4 \mu\text{M}$ recombinant yeast G-actin was incubated under three conditions: in G-buffer ($n = 3$), with $1 \times$ KME ($n = 3$), and with $4 \mu\text{M}$ GST-cleaved Las17PP₃₀₀₋₅₃₆ ($n = 2$). High-speed = $279,000 \times g$. Low-speed = $18,000 \times g$.

Using the LSP assay, four different Las17PP₃₀₀₋₅₃₆ concentrations (1, 2, 3 and 4 μM) were tested for their ability to induce actin bundle formation from a pool of 4 μM G-actin. The band volumes of actin and Las17PP in the supernatant (S) and resuspended pellet (P) for each sample were measured by densitometry, then the proportion of each protein in the pellet fraction compared to the total (S + P) was converted into estimated protein concentration (μM) and plotted in Figure 6.6B.

The results indicate that the lowest concentration of Las17PP used ($\sim 1 \mu\text{M}$) was sufficient to induce some actin bundling. Only a small proportion ($\sim 25\%$) of the Las17PP present co-pelleted with these bundles. Doubling the total concentration of Las17PP to $\sim 2 \mu\text{M}$ roughly doubled both the amount of bundled actin and the amount of Las17PP associated with the bundles. Further increase in Las17PP concentration did little to increase either the amount of actin in a bundled state or the amount of bundle-associated Las17PP, as evidenced by the flattening of both curves (Figure 6.6B). This is indicative that there is a saturation point at which maximum bundling is achieved; i.e. additional Las17PP does not induce further bundling or allow additional Las17PP binding to the existing bundles.

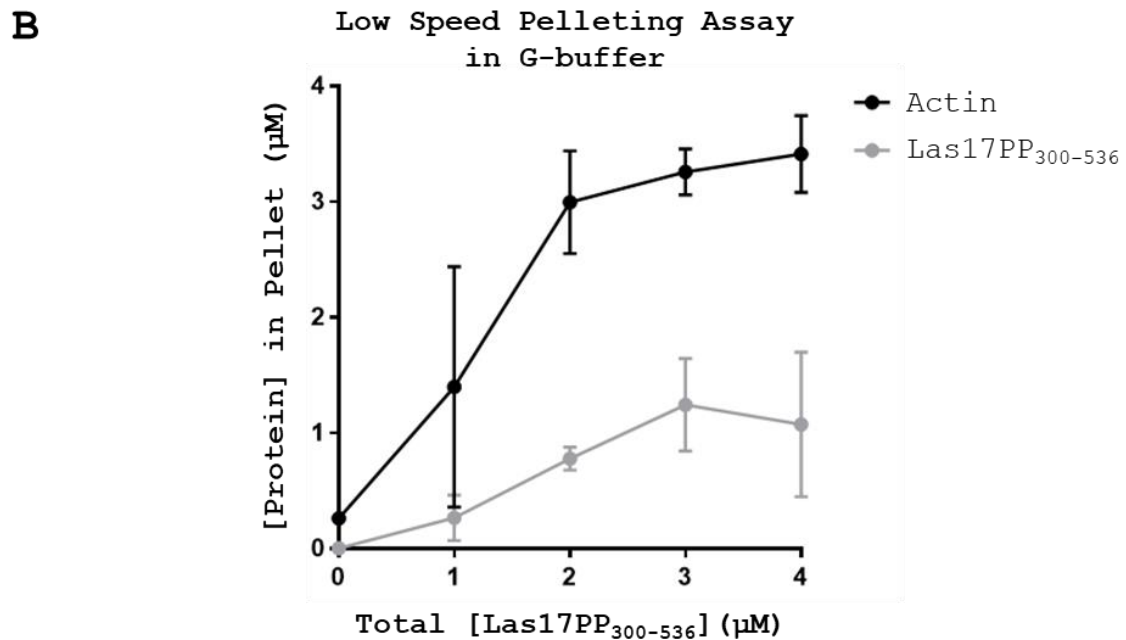
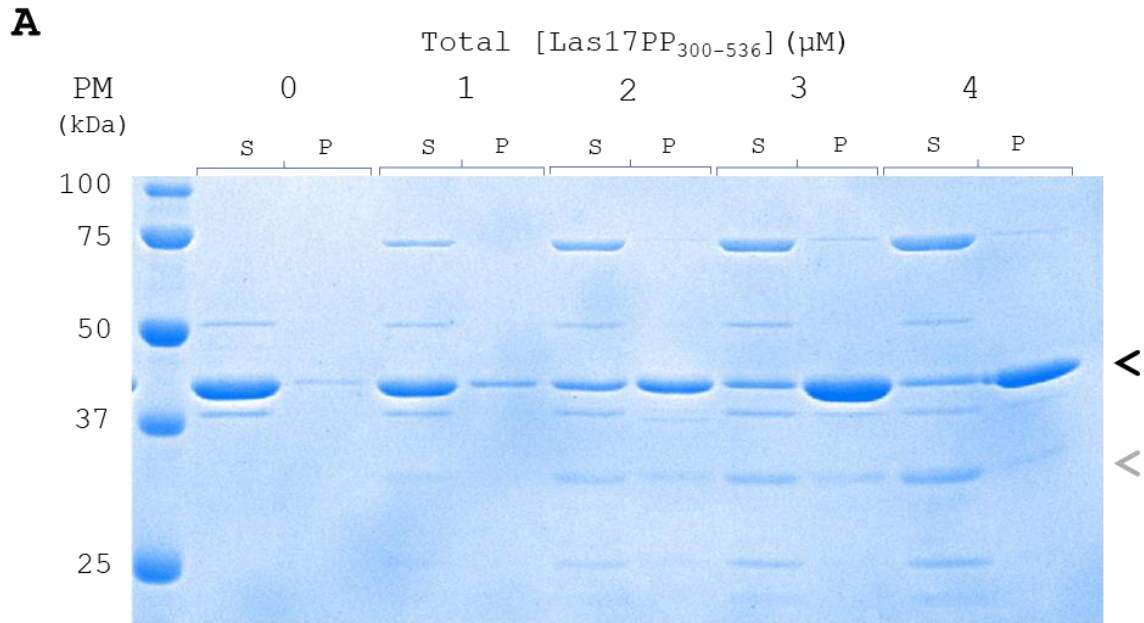


Figure 6.6: Low-speed sedimentation of actin bundles in the presence of increasing concentrations of Las17PP₃₀₀₋₅₃₆ in G-buffer. **A**) A representative gel used for quantification. Actin (black arrowhead) and Las17PP (grey arrowhead) bands are indicated. S = supernatant. P = pellet. **B**) The concentration of Las17 and actin in the low-speed (18,000 x g) pellet, indicating the amount of actin or Las17PP which is incorporated into or associated with F-actin bundles. The total concentration of actin present was 4 μM for all conditions. n = 2 for all conditions except 2 μM total Las17PP where n = 3.

6.2.4 The N-terminal Half of the Las17 Polyproline Region is Sufficient to Induce Actin Bundling

In order to investigate whether the region of Las17 responsible for bundling was the same as that responsible for nucleation, the experiments described in section 6.2.3 were repeated with a shorter fragment spanning residues 300-422 (Las17PP₃₀₀₋₄₂₂). This fragment has previously been shown to be both necessary and sufficient to induce nucleation (Urbanek *et al.*, 2015; Allwood *et al.*, 2016). Low-speed sedimentation assays indicated that this shorter portion of Las17PP was indeed sufficient to induce actin bundling in the presence and absence of salt (Figure 6.7). As seen for Las17PP₃₀₀₋₅₃₆, Las17PP₃₀₀₋₄₂₂ co-pelleted with the actin bundles, indicating actin binding.

A notable difference between the two Las17 fragments was that the curve for Las17PP₃₀₀₋₄₂₂ in the pellet did not plateau at higher Las17 concentrations: for every concentration tested, the Las17PP₃₀₀₋₄₂₂ band was found almost entirely in the pellet.

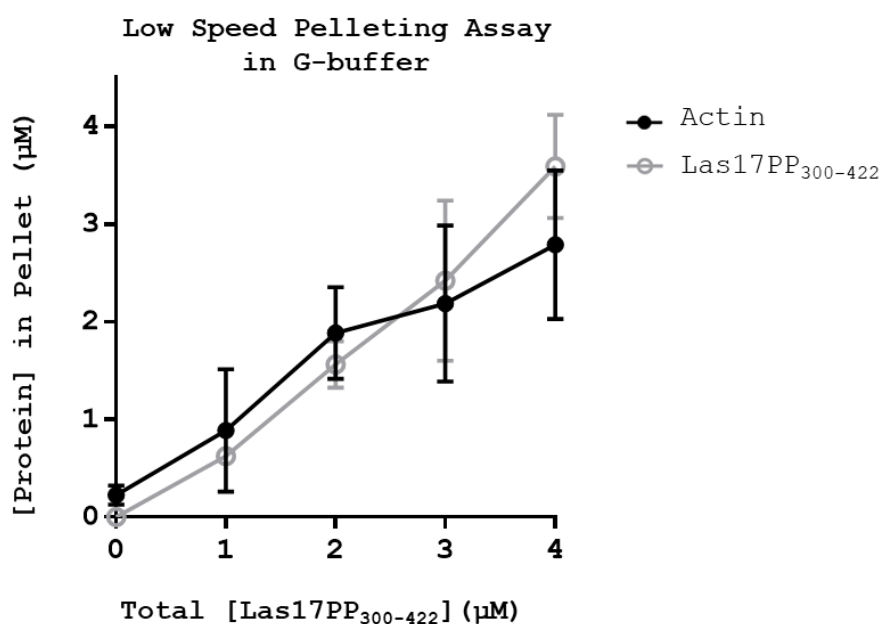


Figure 6.7: Low-speed sedimentation of actin bundles in the presence of increasing concentrations of Las17PP₃₀₀₋₄₂₂ in G-buffer. n=2 (The 3rd repeat was excluded because the Las17 band was not visible.)

6.2.5 Las17PP Bundling in the Presence of Salt

A much lower concentration of Las17PP₃₀₀₋₄₂₂ was required to bundle actin in the presence of KME than in its absence (Figure 6.8), which may be indicative of a larger pool of F-actin available for bundling. Additionally, a larger proportion of Las17PP remained in the supernatant in the presence of KME, indicating some disruption of its F-actin binding by the salt.

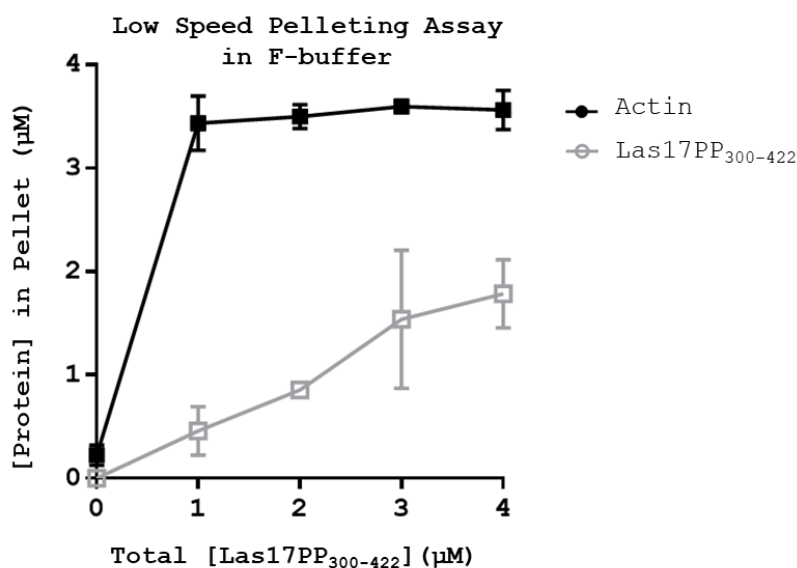


Figure 6.8: Low-speed sedimentation of actin bundles in the presence of increasing concentrations of Las17PP300-422 in F-buffer. F-buffer is G-buffer with added KME. n=2 (The 3rd repeat was excluded because the Las17 band was not visible.)

It was also investigated whether the bundling was a result of the way Las17PP was nucleating actin, or whether it could bundle pre-existing filaments. This is relevant because it provides insight into how Las17 might be binding F-actin, and how it might be mediating nucleation and bundling actin. In a former study by the KA lab, bundling of actin by the protein Ysc84, another *S. cerevisiae* protein involved in endocytosis, was found only capable of bundling actin if it was present from the nucleation stage, indicating that it was incorporated within the filaments rather than side-binding. Similarly, the tail domain of vinculin - a *de novo* nucleator and bundler of actin - was found incapable of bundling pre-formed F-actin (Wen *et al.*, 2009). In contrast to the above examples, we found that Las17PP *could* bundle pre-existing filaments that had been polymerised by the addition of KME (data not shown). Therefore, Las17PP does not require incorporation into actin filaments in order to induce bundling and is likely to bind to the sides of actin filaments.

6.2.6 Characterisation of Las17PP-Induced Actin Bundles using TEM

Optimisation of TEM sample preparation permitted visualisation of the arrangement of actin filaments within Las17PP-induced bundles. Individual filaments could be seen clearly within bundles in many places where staining provided sufficient contrast. Most bundles exhibited a tightly packed arrangement of filaments that strongly resemble the F-actin paracrystals induced by high concentrations (> 20 mM) of MgCl₂ (Francis and DeRosier, 1990) or by poly-lysine (Fowler and Aebi, 1982). In places, the F-actin had the appearance of neat parallel striations (Figure 6.9). This allowed quantification of centre-to-centre spacing of the filaments, which was on average 7 nm (Figure 6.10). The bundles had the same characteristics regardless of which Las17PP fragment has been used.

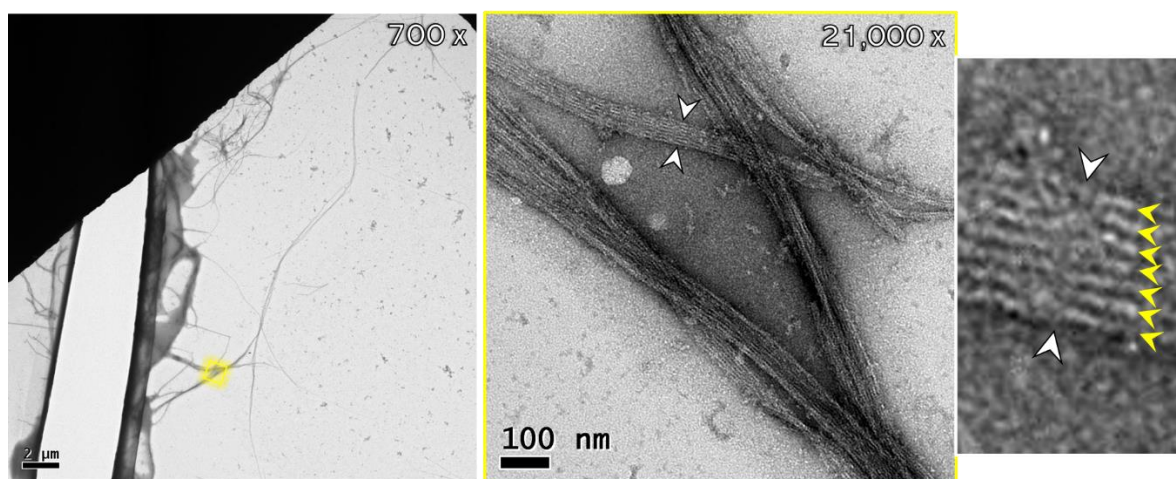


Figure 6.9: Filaments within the bundles are clearly visible when viewed at high magnification in negative stain TEM. Left: low magnification image showing several actin bundles at a tear in the carbon film. Right: higher magnification image of the area outlined by the yellow box in the low magnification image. An enlarged section of the image is inset, in which individual filaments are indicated by yellow arrowheads. 5 μM rabbit skeletal muscle actin with 5 μM GST-cleaved Las17PP₃₀₀₋₅₃₆ in G-buffer.

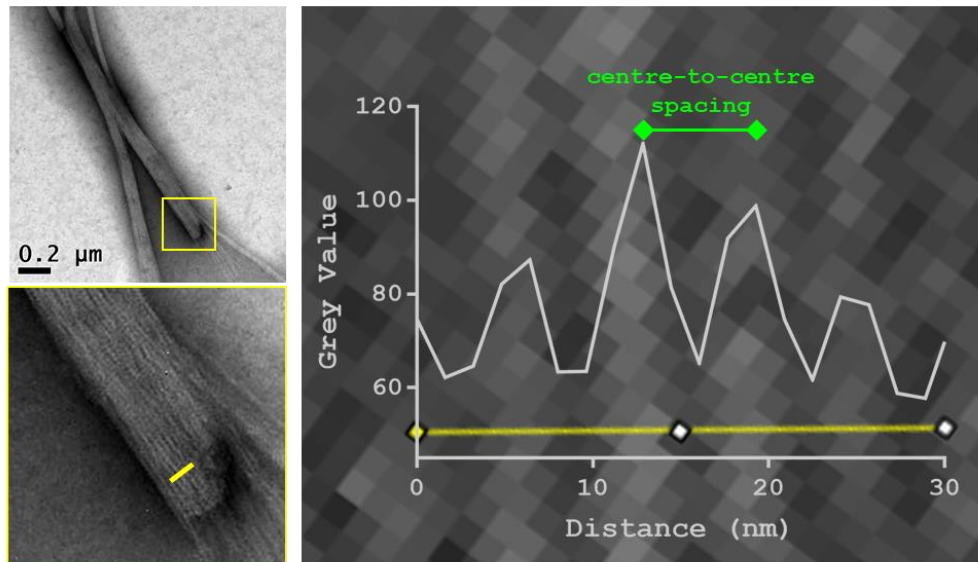
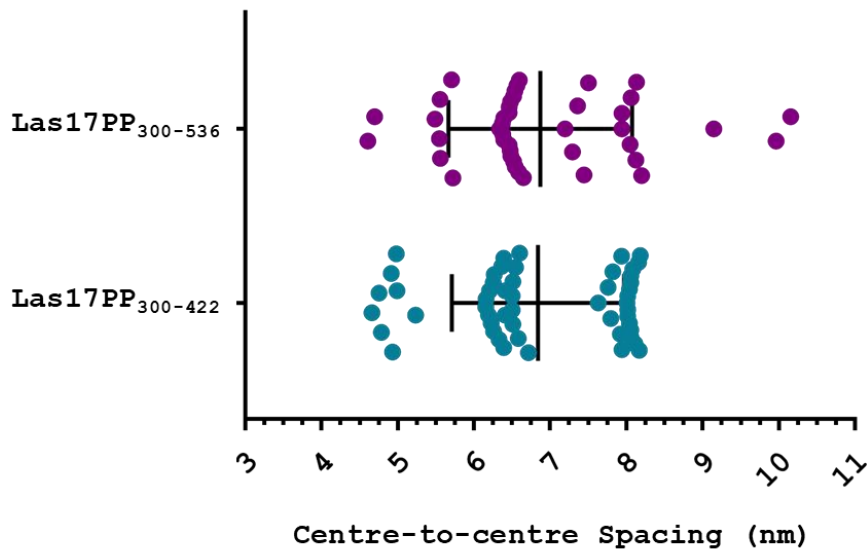
A**B**

Figure 6.10: Actin filaments in Las17PP-induced bundles have a centre-to-centre spacing of ~7 nm. Inter-peak distance measurements were used as centre-to-centre spacing of filaments in sections of the bundle where striations were clearly visible. The mean and standard deviation is shown for both Las17 fragments. Las17PP₃₀₀₋₄₂₂: inter-peak distance = 6.84 ± 1.13 (n=52). Las17PP₃₀₀₋₅₃₆: inter-peak distance = 6.87 ± 1.20 (n=42). A parametric unpaired t-test found the difference between the means to be non-significant ($p = 0.8919$; > 0.05).

2D classification confirmed the tight bundling of filaments. The averaged filaments did not have the characteristic fluctuating diameter of actin that would be expected of filaments arranged in a single layer (Figure 6.11). A multi-layered arrangement of filaments might have this arrangement if the filaments were staggered.

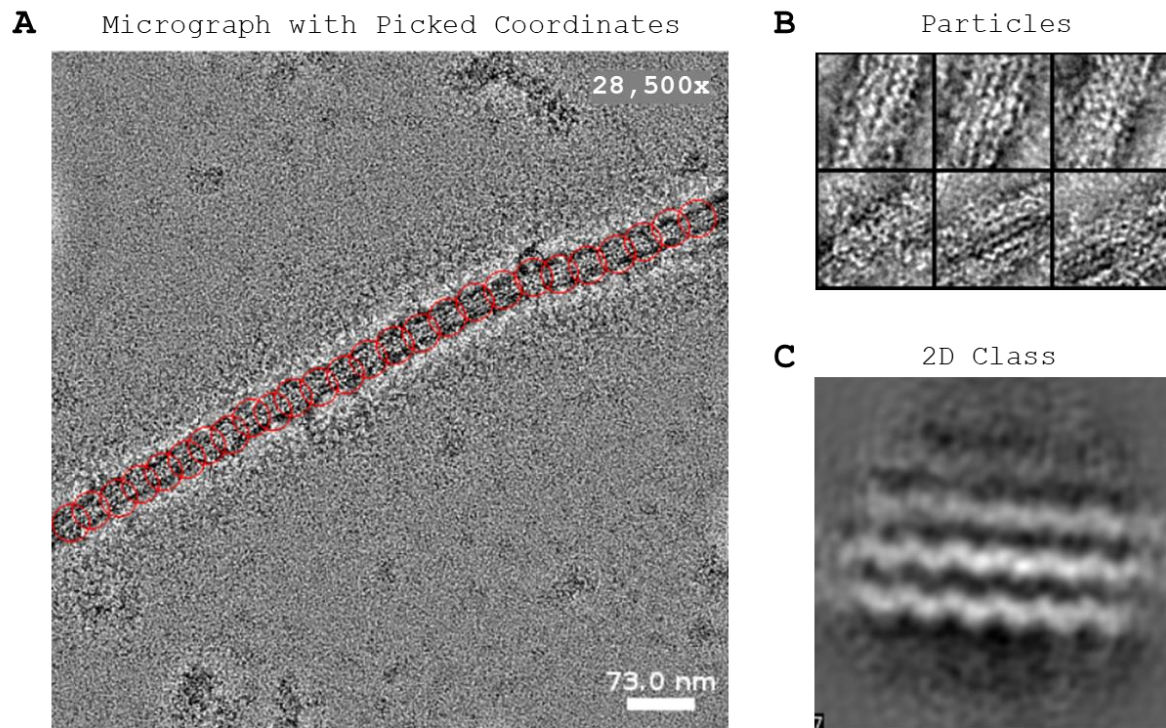


Figure 6.11: 2D classification of Las17PP-induced actin bundles. A) An example of a micrograph with picked particle co-ordinates. Particles are ringed in red. B) Examples of individual particles, each with a box width of 50.4 nm (70 pixels). C) Representative 2D class. The mask radius is 20 nm. This dataset used 4 μM recombinant yeast actin and 8 μM Las17PP₃₀₀₋₅₃₆ in G-buffer. 2D classification was performed in CisTEM. Particles were grouped into 8 classes in 20 iterations, starting with random assignment. Pixel size was 7.2 Å.

Bundle length was variable, with the longest bundles measuring tens of microns in length (>30 μm ; with larger measurements limited by the field of view). Similarly, bundle thickness was highly variable. The thickest bundles exceeded 100 nm in width and composed of 14 or more filaments, while the thinnest bundles present appeared to be composed of just two closely associated actin filaments. Thickness measurements of a population of 190 bundles were used to plot a frequency distribution of bundle thickness (Figure 6.12). Bundles with more-or-less unvarying width were measured only once where possible to avoid duplicate measurements. In instances where a thick bundle forked or splayed into two or more thinner bundles, one measurement was taken for the thick bundle and the widths of each fork were also recorded separately. Where present, individual actin filaments were also included in the measurements. While the average bundle thickness was 31.2 nm, the distribution was skewed towards thinner bundles: a frequency distribution with a binning of 4 nm indicates that the modal actin bundle thickness range measured was 18-22 nm, while the median bundle thickness was 24.7 nm.

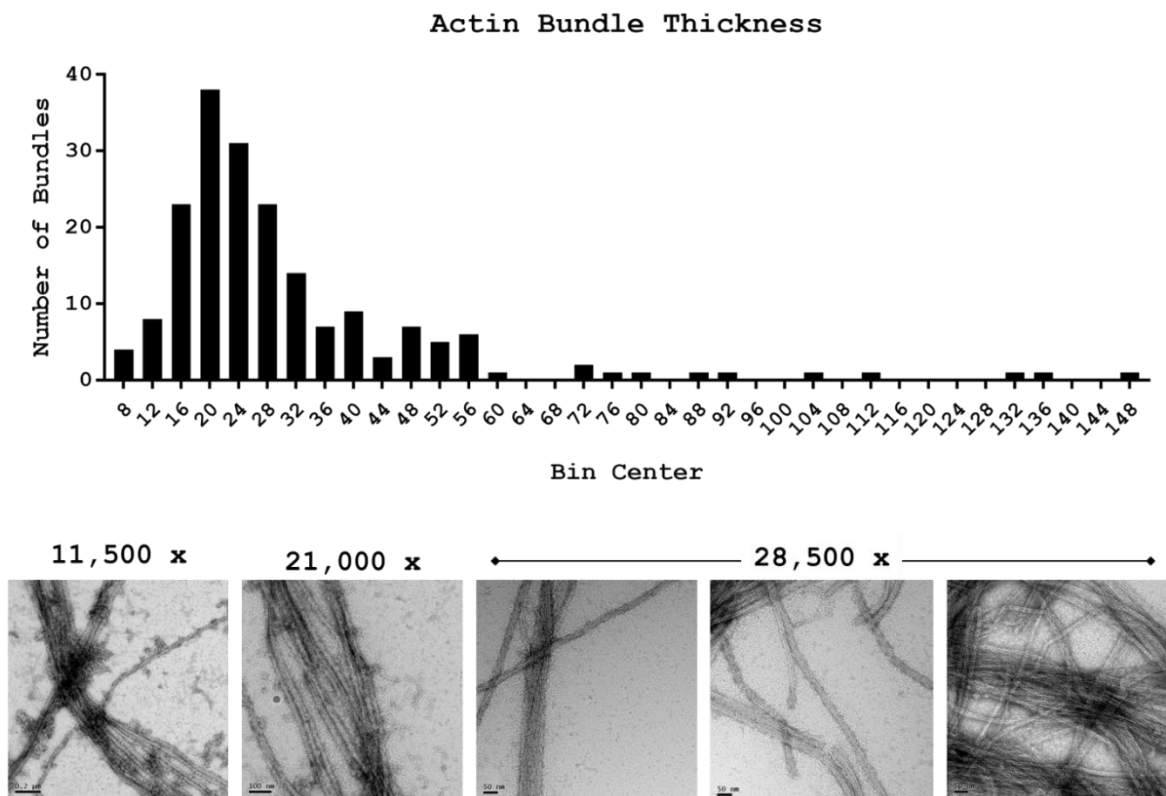


Figure 6.12: Frequency distribution of actin bundle thickness. Micrographs from a single grid with magnifications ranging from 6,600 x to 56,000 x were used for this analysis, some of which are displayed below the histogram. 190 measurements were recorded by measuring bundle width manually in FIJI. Sample = 5 μM rabbit actin and 5 μM Las17PP₃₀₀₋₅₃₆ (GST-cleaved) in G-buffer with fresh ATP and DTT.

It was not possible to use width and spacing measurements alone to predict how many actin filaments were contained in a bundle. Without knowing whether the bundles were flat sheets (monolayers) or cylindrical in shape, it was not possible to estimate how many filaments could be incorporated in a bundle of a given width. Two strategies for obtaining information about 3D bundle shape are explored in the next sections: cryogenic electron tomography and atomic force microscopy.

6.2.7 Assessing Bundle Shape with Cryogenic Electron Tomography

Cryo-electron tomography (cryo-ET) was employed as a method to provide information about the 3D shape of the actin bundles. Samples for cryo-ET, like samples for other classes of cryo-EM techniques, are embedded in a thin layer of vitreous ice (thin enough to be electron-transparent). Bundles were found to distribute poorly on holey carbon grids (data not shown), but Lacey grids were found to enable a good sample distribution (Figure 6.13).

The grid used for data collection had a reasonably even distribution of fiducial markers (10 nm BSA-coated gold nanoparticles), although it was observed that many of the bundles in this sample were much wider than samples made previously, with several measuring ~500 nm. Out of 9 tilt series collected, a single tilt series was selected for processing, chosen on the basis of several factors, including an absence of the following: tears in the carbon film; large jumps in the field of view; distortion from inconsistencies in the ice (seen as a ‘sparkling’ effect when moving through the frames of the tilt series).

Fiducial-based alignment resulted in a relatively smooth transition between planes in *z*, although artefacts could be seen as white streaks around the gold nanoparticles and duplication of gold particles when out of focus (Figure 6.14A). By observing the approximate path of filaments in each section of the tomogram, it was clear that filaments were multilayered within the flattened bundle, dismissing the possibility that the bundle was an ordered monolayer of F-actin. Low magnification, poor contrast and high signal-to-noise made it impossible to track individual actin filaments through the tomogram. However, the data was useful for a macro-examination of the overall

bundle shape (Figure 6.14B). The bundle was found to have a relatively flat structure with a height approximately 8-10% of its width. We suspect the flattened appearance is likely to have been squashed by the constraints of the ice rather than having a flattened shape prior to grid preparation. It was therefore decided that an alternative approach was required to obtain information about bundle shape, which is the topic of the next section.

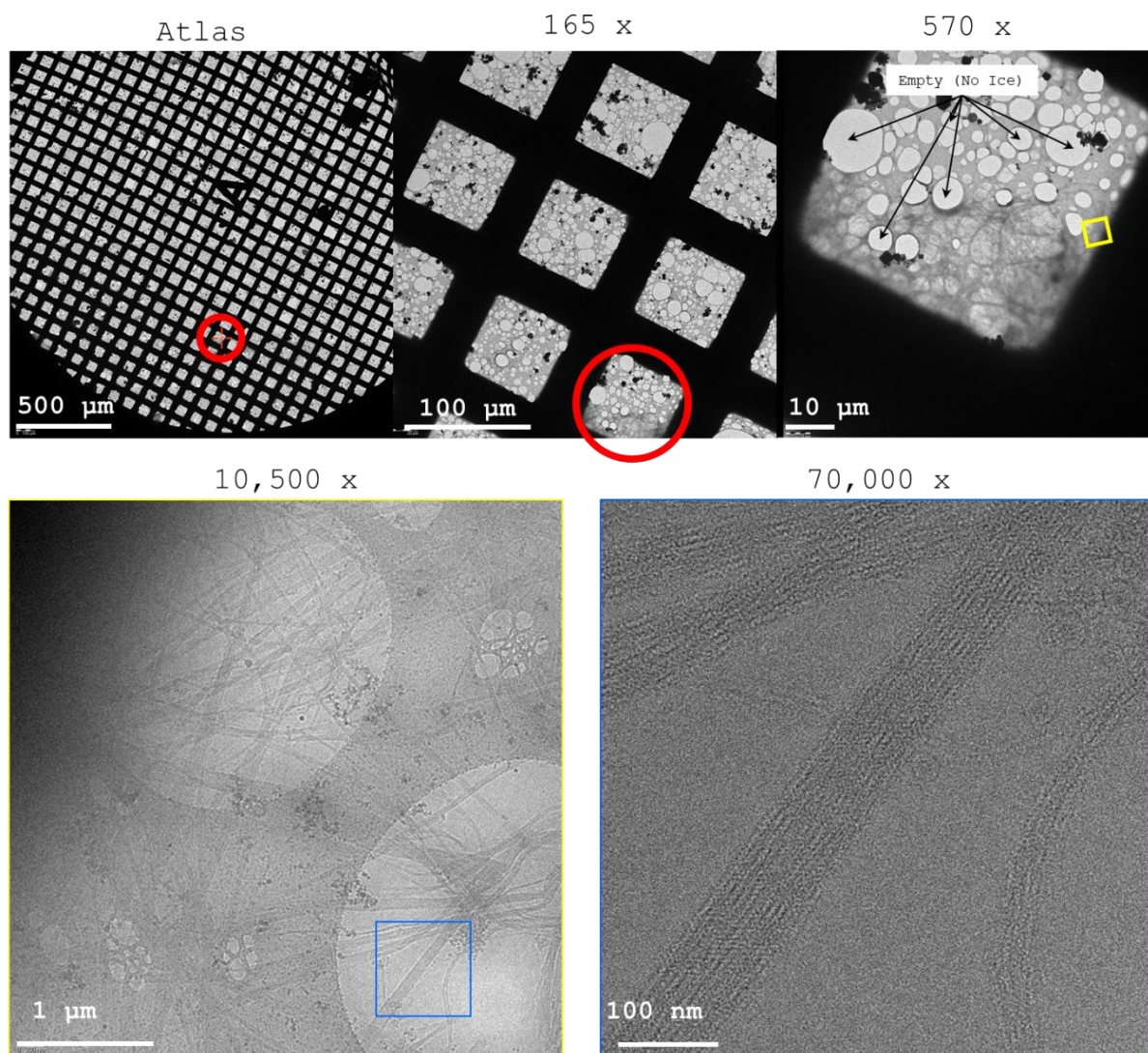


Figure 6.13: Appearance of bundles in ice on lacy grids. The holes in the carbon film of lacy grids have irregular size and distribution, which was well-suited for samples containing F-actin bundles. A range of magnifications is shown to indicate the appearance of F-actin bundles during the screening process.

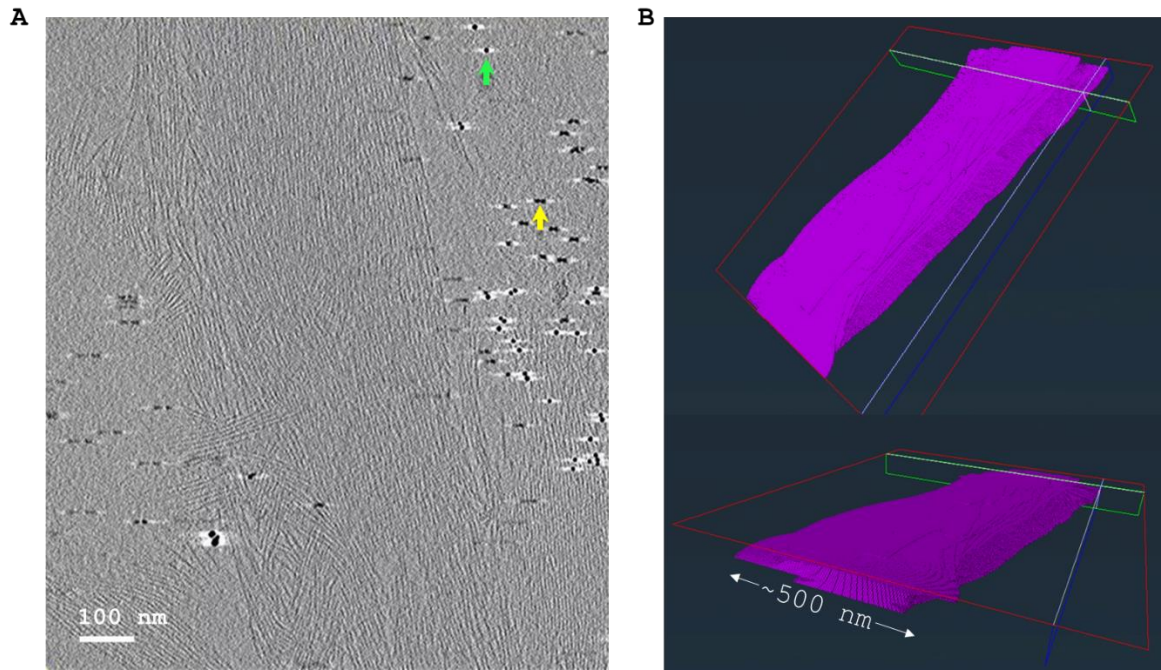


Figure 6.14: Visualising Las17PP-induced F-actin bundles in 3D using Cryo-ET. **A)** A slice of the aligned tomogram of a thick (~500 nm-thick) F-actin bundle and 10 nm gold nanoparticles. Gold nanoparticles were surrounded by white streak artefacts (e.g. green arrow) and were duplicated when out of focus (yellow arrow), indicating imperfect alignment. **B)** The segmented F-actin bundle.

6.2.8 Bundle Characterisation by Atomic Force Microscopy

As an alternative method to assess bundle shape, Las17PP₃₀₀₋₅₃₆-induced actin bundles were prepared for atomic force microscopy (AFM). AFM gives a height measurement as well as a width measurement, with height represented in the resulting image by intensity (grey value). An important consideration when making measurements with this technique is that lateral (width) measurements suffer from convolution with the cantilever tip. This cannot be corrected for because the tip shape is difficult to characterise, particularly because it can change shape throughout the course of the experiment (e.g. by picking up debris, or due to damage). In contrast, height measurements, as well as periodicity measurements of a sample with regular repeating features (e.g. helical pitch), do not suffer from this distortion.

Preliminary results, collected by Nic Mullin (The University of Sheffield) and analysed in Gwyddion (Nečas and Klapetek, 2012), support a multi-layered bundle organisation. For example, the bundle shown in Figure 6.15 was measured to have a height of 24 nm, which is more than 3 times the height of a single actin filament. A line profile was generated for a path along the length of a bundle. The periodicity along the length of a bundle was found to repeat every ~36 nm, which is the expected crossover length of the F-actin protofilaments. Interestingly, each repeat contained a second, smaller peak (Figure 6.15B).

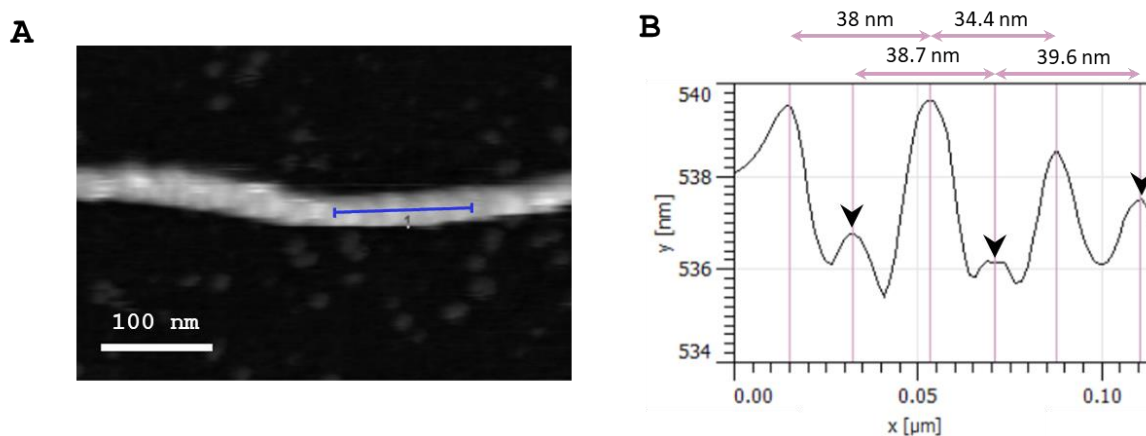


Figure 6.15: Periodicity of an F-actin Bundle. A) AFM image of an F-actin bundle induced by incubation with Las17PP₃₀₀₋₅₃₆. The blue line indicates the line profile area. B) The line profile from the area of bundle indicated in part A showing a repeating pattern of two peaks. The second, smaller peak, from each pair is labelled with an arrowhead. The periodicity is similar to the expected 36 nm for a single actin protofilament crossover.

6.3 Discussion

6.3.1 Findings from Single Particle Analysis

Single particle reconstruction of F-actin polymerised with Las17PP revealed no clear indication of either 1) density corresponding to Las17 or 2) any structural alteration of F-actin induced by Las17PP. It is possible, however, that the extra density seen in one of the 3D classes for this dataset does correspond to Las17PP, especially given its proximity to a potential Las17PP binding site that was identified through a yeast-two-hybrid assay with several actin mutants (Urbanek *et al.*, 2013). Interestingly, our observations reported in this chapter for Las17 have similarities to reports of a BAR domain protein called BIN1 that has been found to bundle actin (Dräger *et al.*, 2017), but has not been detected on single actin filaments by cryo-EM (Wang and Mim, 2021).

6.3.2 A Novel *in vitro* Ability of Las17PP

The KA lab has now demonstrated that both nucleation and bundling can be induced by the Las17 polyproline region *in vitro*. The minimal region tested to have both these abilities is aa300-422. It has been established here that Las17 is able to bundle preformed actin filaments. Importantly, this indicates that Las17 can associate and dissociate freely and does not rely on co-polymerisation with actin as a bundling mechanism. This also rules out another possibility we had considered: that Las17-nucleated filaments are more prone to bundling than KME-nucleated filaments, perhaps owing to a subtle structural difference.

The bundles formed by incubating Las17 with F- or G-actin were found to have tight packing, with centre-to-centre spacing of approximately one filament width (~7 nm). This extremely dense packing in the presence of Las17 fits with our current understanding of Las17PP structure as an extended linear protein, in contrast with the globular proteins fimbrin, villin and fascin which restrict how tightly the filaments can pack (~12 nm centre-to-centre spacing; Brown and McKnight, 2010; Yang *et al.*, 2013). Our cryo-ET and AFM results revealed that the Las17-induced actin bundles consist of multiple layers of filaments. We were unable to deduce the polarity of the filaments within the bundles (unipolar or bipolar), but this could be determined using the S1 fragment of

myosin, which has been shown effective for Mg^{2+} -induced actin paracrystals, despite the tight packing of filaments (Francis and DeRosier, 1990).

The tight packing of filaments may explain why a GST-tagged Las17PP fragment spanning most of this region (Las17_{aa300-404}) was previously found not to appreciably co-pellet with F-actin in a high-speed sedimentation assay (Feliciano *et al.*, 2015): a ~26 kDa GST tag is large enough to be expected to obstruct lateral contacts between filaments and therefore prevent bundling.

6.3.3 Implications About Bundle Organisation from AFM Data

The preliminary AFM data indicated a double-peaked height profile repeating every ~34-40 nm over the length of a bundle. A single actin filament would be expected to have a single peaked profile repeating after approximately the same distance. We hypothesise the second peak could be indicative of a staggered bundle formation (Figure 6.16B). 2D classification of TEM data also seemed to support a staggered arrangement of filaments within the bundles because of the absence of fluctuating width that is characteristic of actin filaments. This was observed in individual micrographs and was reinforced by 2D class averaging. The striations bear a strong resemblance to a projection of actin paracrystals induced to form by poly-lysine (Fowler and Aebi, 1982).

Another possible explanation for the second peak in the AFM line profile is the presence of regularly-bound Las17PP at the bundle surface. This could be tested by increasing the salt concentration in the buffer used for AFM (which was G-buffer for the data presented here). While bundle integrity did not appear to be compromised by KME, the amount of Las17 that co-sedimented with the bundles greatly diminished in the presence of this amount of salt. This salt-induced reduction in Las17PP binding may indicate that only a small proportion of Las17PP is integrated within the F-actin bundles, but low-salt conditions allow additional weak association between Las17PP and actin at the surface of the bundle.

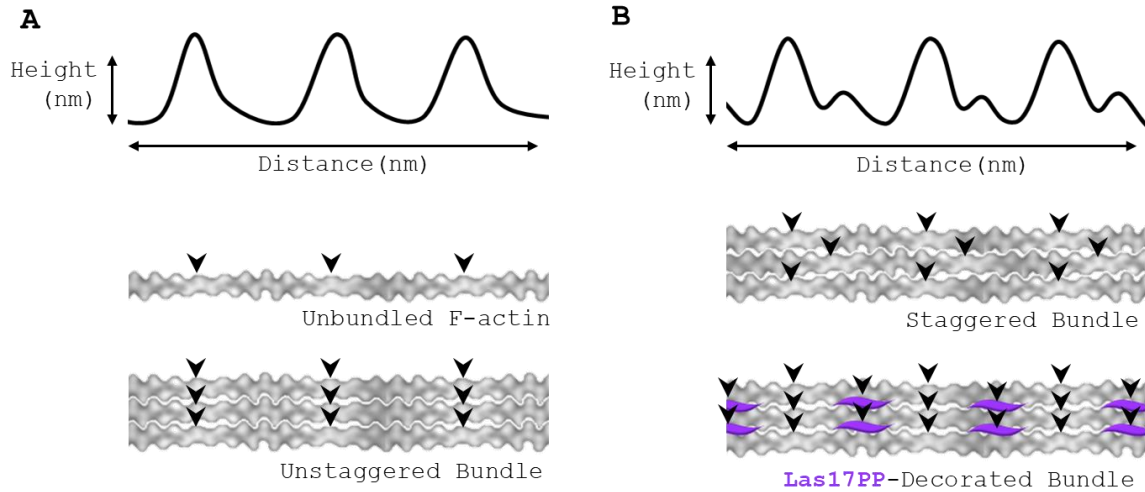


Figure 6.16: Proposed Arrangements of F-actin in Las17PP-induced bundles based on the double-peaked line profile observed in AFM. Schematic illustrations of actin filament and bundle organisations (viewed from the top) that would be expected to give **A**) single peak and **B**) the double peak line profile in AFM.

6.3.4 Could Non-Specific Interactions Enable Las17PP to Bundle F-Actin?

Mg^{2+} and polycations are understood to induce bundling by masking negative charges on the surface of actin filaments, thereby allowing a close lateral association that would otherwise be unfavourable due to electrostatic repulsion (Tang and Janmey, 1996). The Las17PP fragments used in this work have an overall positive charge owing to several arginine residues in the aa300-422 region (Figure 6.1). The predicted pI for both Las17PP fragments used is 12.4 while the pI for actin is 5.44 (*S. cerevisiae*) or 5.23 (vertebrate α -skeletal muscle isoform). All bundling experiments were performed in a buffer with a pH of 7.5-8.0. Therefore, one possibility to consider is that F-actin bundling could be the result of a non-specific, charge-based interaction. If bundling is wholly due to non-specific charge masking, the addition of 50 mM KCl in KME would be expected to disrupt the integrity of the bundles by competing with Las17 to mask charges on actin. This scenario is not supported by our LSP assay data, which demonstrated that KME did not compromise bundle integrity. Conversely, the proportion of bundle-associated actin increased in F-buffer (+KME) compared to G-buffer. An explanation for this is that KME and Las17PP combined were able to induce more actin filaments to form than Las17PP alone, and therefore less actin was in the G-actin state.

6.3.5 Are PP Tracts and Arginine Pairs Involved in Las17PP-Mediated Actin Bundling?

It has previously been proposed that the aa300-536 region consists of a tandem G-actin-binding region that nucleates actin, and an F-actin-tethering region that elongates and stabilises the nascent filament (Allwood *et al.*, 2016). In this model, F-actin tethering requires PP tracts 8 and 9, which have been found necessary for F-actin elongation *in vitro* and the disruption of which causes defects at the early stages of endocytosis *in vivo* (Urbanek *et al.*, 2013; Allwood *et al.*, 2016). Surprisingly, these two tracts (which were absent in the shorter Las17 fragment used in this work), were found to be non-essential for bundling. The fragment capable of bundling did however still contain 4 PP tracts (2-5). The importance of PP tracts for actin bundling could be tested by investigating whether PP tracts have F-actin bundling capability in the absence of the arginine-rich portion of Las17PP. This could be achieved by generating a new plasmid for ~aa423-536, which, like Las17₃₀₀₋₄₂₂, encompasses four PP tracts (6-9). Unlike Las17₃₀₀₋₄₂₂, this C-terminal portion of Las17PP is devoid of arginine residues and therefore is much less positively charged. If this fragment (pI 5.52) was found capable of bundling actin, it would also rule out the previously discussed possibility that bundling is simply due to a non-specific charge-based interaction.

The arginine pairs R349-350 and R382-383 are already known to bind G-actin (Feliciano *et al.*, 2015) and have been demonstrated to be essential for *de novo* nucleation of actin by Las17 (Allwood *et al.*, 2016). The importance of these arginine pairs for actin bundling could be investigated further by using the nucleation impaired Las17PP mutant in which these residues are all substituted for alanine (available in the KA lab plasmid collection).

7. Final Discussion

7.1 Developments in Actin Purification

Different approaches have been applied to the purification of actin, especially from non-muscle sources which have a lower actin content than skeletal and cardiac muscle sources. As covered in Chapter 3, one commonly used purification method utilises the actin-DNase I interaction (Cook *et al.*, 1991; Schafer *et al.*, 1998). Another affinity-based method for purifying native actin pulls down profilactin using profilin-binding polyproline motifs (Rozycki *et al.*, 1991). The recently developed recombinant actin purification method using *Pichia pastoris* offers an additional option that may be more suitable for certain applications. In particular, this method shows great potential in its versatility, for example it can be applied to any actin isoform, and has undergone further development to enable incorporation of specific PTMs (Hatano *et al.*, 2018, 2020).

We were able to use this method to produce enough good-quality *S. cerevisiae* G-actin for the biochemical and structural work presented in this thesis. However, we also identified an inefficient step in the purification process that compromises the yield and purity of the preparation that we predict could be easily circumvented by a simple sequence modification (discussed in section 3.3.3). This optimisation work is currently under development in the KA lab. Optimisation of the protocol in this way is expected to be particularly beneficial for the purification of the non-polymerisable actin mutants (introduced in section 3.2.7 and discussed in section 3.3.4), which cannot undergo the cycling step that is used at the final stages of WT actin purification for selectively enhancing polymerisation-competent actin.

7.2 Further Steps Towards Understanding Yeast F-actin Structure

This project has challenged earlier findings that yeast F-actin has structural differences to vertebrate skeletal muscle F-actin that are detectable at low-to-mid range resolution (Orlova *et al.*, 1997; Belmont *et al.*, 1999). It therefore seems that, in order to understand the structural basis of the

differential properties of these isoforms, it will be necessary to make a comparison in much more detail: on the level of individual sidechains. Future work will be to reconstruct a higher-resolution yeast F-actin structure to confirm and build on the observations made here, taking advantage of the continuing technological advances of cryo-EM. The best route forwards is to obtain a new, larger dataset with a smaller pixel size, using a more advanced microscope such as a 300 kV Titan Krios. This year has seen the first sub-3 Å resolution cryo-EM structures of F-actin deposited on EMDB: a 2.9 Å map of a cis-opto- jasplakinolide-8-bound rabbit skeletal muscle actin filament and a 2.6 Å map of a jasplakinolide-bound *P. falciparum* Act1 filament (Vahokoski *et al.*, *to be published*), demonstrating that this is already technically possible.

7.3 The Expanding Database of F-actin Structures

The number of published F-actin structures has increased substantially since the start of this PhD project in 2017, trending towards higher resolution (Figure 7.1). Despite the high number of solved structures, the protein used for high-resolution structural studies is almost exclusively the skeletal muscle actin isoform from vertebrates (Figure 7.2).

In some ways, using skeletal muscle F-actin as a canonical ‘model’ F-actin is beneficial as it allows comparison of the structural effects of different conditions such as nucleotide state (Merino *et al.*, 2018; Chou and Pollard, 2019), bound small molecules (Belyy *et al.*, 2020; Chou and Pollard, 2020; Kumari *et al.*, 2020; Pospich *et al.*, 2020), PTMs (Grintsevich *et al.*, 2017) and bound proteins (Von Der Ecken *et al.*, 2016; Menten *et al.*, 2018; Tanaka *et al.*, 2018; Huehn *et al.*, 2020; Kumari *et al.*, 2020; Shaaban *et al.*, 2020; Xu *et al.*, 2020). However, it is still poorly understood how actin isoform variation (within or between species) manifests different F-actin properties from a structural perspective, necessitating additional study of actin from different sources. This area of research has been improved by a recent increase in structures for F-actin from *P. falciparum*, which cannot form long, stable filaments in the absence of stabilising agents such as jasplakinolide. It was interesting that our map indicated that the helical twist of *S. cerevisiae* F-actin (which does not exhibit the same labile properties as *P. falciparum* actin) was more similar to *P. falciparum* actin than to the canonical twist of F-actin. As previously reported for *P. falciparum* F-actin (Pospich *et al.*, 2017), the

exaggerated twist in *S. cerevisiae* actin did not have an obvious effect on the stability of protomer-protomer interfaces.

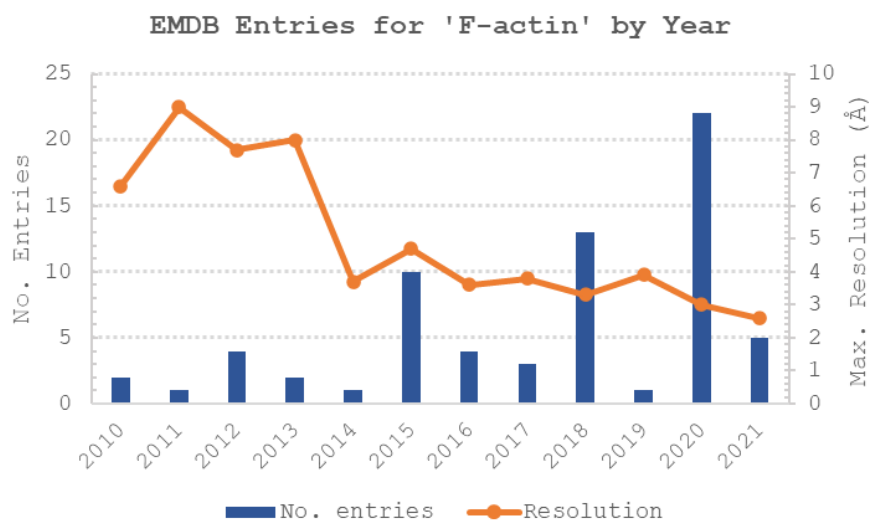


Figure 7.1: EMDB entries falling under the search term ‘F-actin’, arranged by year. For each year, the number of entries and the highest resolution achieved is plotted. The ‘resolution revolution’ enabled the first high resolution structure of F-actin to be published in 2014. Two 2021 entries (EMD-10587 and EMD-10588 that were not picked up by the search added manually).

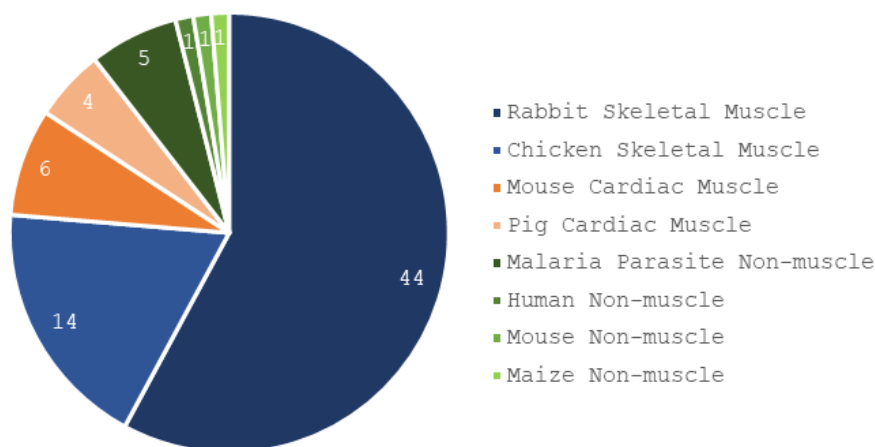


Figure 7.2: Diversity of Actin Isoforms in Structural Studies of F-actin. Actin sources for published F-actin structures with resolution better than 10 Å between January 2010 and August 2021. This includes F-actin with bound small molecules or proteins. (76 structures are shown in total.)

While cryo-EM is the best tool for studying the structure of F-actin at high resolution, cryo-ET is also rapidly advancing in its capabilities and expanding its applications to F-actin. High resolution structural studies of F-actin cannot currently be achieved *in situ*, though cryogenic electron tomography is a rapidly advancing technique that has already allowed visualisation of how actin filaments are arranged within subcellular actin architectures. Sub-tomogram imaging (a hybrid technique of tomography and single-particle reconstruction) can enable *in situ* structural studies of molecules within cells, but this is currently limited to ~ 10 Å resolutions and that is in a best-case scenario with a compatible molecule of interest. Crucially, cryo-ET offers a chance to study actin in its cellular context: *in situ*. The relatively recent sample preparation development of FIB-milling has permitted more varied sample types than was previously possible, as it can slice through frozen samples to etch away a section thin enough to be electron-transparent. Applying cryo-ET to the study of the cytoskeleton is reviewed in Chakraborty *et al.*, 2020. It seems likely that, with optimisation, cryo-ET could also be applied to actin bundles *in vitro*, as was attempted here (section 6.2.7). This would require a higher magnification than what was used in our study (16,000 x) and attention to bundle thickness in the sample to make sure bundle shape is not distorted in the thin ice layer.

7.4 Implications for Las17 at Endocytic Sites

Through the work in this project, it has been established that the polyproline region of Las17 is not only an NPF and actin nucleator, but also a bundling protein, at least *in vitro*. This finding explains previous observations of dense F-actin clusters in the presence of Las17PP in TIRF microscopy (Tyler, 2017).

During endocytosis, Las17 is known to remain in the plane of the plasma membrane (Mund *et al.*, 2018; Picco *et al.*, 2018), possibly tethered directly to membrane lipids via its N-terminal WH1 domain, with the PP and WCA regions extending into the cytoplasm (Allwood *et al.*, 2016). In addition to its role in actin monomer delivery, the WH2 domain in the WCA region has been found to weakly bind F-actin, implicating it in a tethering role (Bieling *et al.*, 2018). The ability of Las17PP to bind F-actin, as reported here, may serve to strengthen this tethering role. The ability

of Las17PP to bundle F-actin is indicative of this region being able to bind multiple actin filaments simultaneously. *In vivo*, this ability may serve to promote a high local concentration of short actin filaments that are readily available as substrates for Arp2/3.

Given that Las17 is tethered to the plasma membrane, any binding to F-actin *in vivo* would be limited to very short actin filaments, or to just the end section of longer filaments. It would therefore be interesting to find out where Las17 fragments are localised within actin bundles *in vitro*. During this project, steps were made towards a coarser examination of the Las17PP-F-actin interface. This was to be achieved by labelling Las17PP with 1.8 nm diameter gold particles to determine the position of Las17PP within F-actin bundles. The aim was to allow us to determine whether Las17 has, for instance, a regular lateral association with actin filaments, or whether bundling is mediated by aggregation of Las17 at a single point along the length of the bundle. An alternative approach would be to employ light microscopy for this investigation. Two-colour TIRF has been used successfully to this effect for other mediators of actin bundling in a comparison between the bundling protein fascin and the polycation polylysine (Kwon et al., 2006). This study revealed that, while fascin is found distributed along the length of the bundle, polylysine was concentrated to a disc-like distribution at a one point along the length of the bundle.

7.5 Towards Understanding Distinct Architectures in a Common Cytoplasm from the Perspective of Actin Nucleators

This project initially set out to investigate the hypothesis that the intrinsic structure of an actin filament can be influenced by the actin nucleator that initiated its polymerisation. This hypothesis concerns the broader question of how nucleators can collectively orchestrate such diversity of actin architectures (section 1.6). Our comparison of F-actin structures polymerised by the polyproline region of Las17 versus F-actin polymerised by the addition of salts did not reveal a difference in F-actin structure that was detectable at the relatively high resolution of 4.7-4.8 Å. This may indicate that Las17PP has no influence on F-actin structure, or otherwise that any structural influence is extremely subtle. Our work has addressed only a single actin nucleator, so this study would have to be extended to encompass other actin nucleators before a broader conclusion can be made. The

most suitable candidates for further work are yeast Arp2/3 and the yeast formins Bni1 and Bnr1, which together with Las17 would encompass all known actin nucleators in *S. cerevisiae*. Additionally, since we cannot rule out the possibility of more subtle structural differences between filaments (on the level of side-chain orientation), future work will require large, high-quality datasets from good samples, collected on more advanced microscopes, such as the 300 kV Titan Krios model that is available at many research facilities.

8. References

- Abe, A. *et al.* (2000) 'Acetylation at the N-Terminus of Actin Strengthens Weak Interaction between Actin and Myosin', *Biochemical and Biophysical Research Communications*, 268(1), pp. 14–19. doi: 10.1006/bbrc.1999.2069.
- Adrian, M. *et al.* (1984) 'Cryo-electron microscopy of viruses', *Nature*, 308(5954), pp. 32–36. doi: 10.1038/308032a0.
- Adzhubei, A. A., Sternberg, M. J. E. and Makarov, A. A. (2013) 'Polyproline-II Helix in Proteins: Structure and Function', *Journal of Molecular Biology*, 425(12), pp. 2100–2132. doi: 10.1016/j.jmb.2013.03.018.
- Afonine, P. V. *et al.* (2018) 'New tools for the analysis and validation of cryo-EM maps and atomic models', *Acta Crystallographica Section D: Structural Biology*, 74(9), pp. 814–840. doi: 10.1107/S2059798318009324.
- Aghamohammadzadeh, S. and Ayscough, K. R. (2009) 'Differential requirements for actin during yeast and mammalian endocytosis', *Nature Cell Biology*, 11(8), pp. 1039–1042. doi: 10.1038/ncb1918.
- Ahmed, S. S., Messali, Z. and Chouiter, M. (2013) 'Public software: TomoJ, eTomo and tomtoolbox for stem and EFTEM tomography of biological samples', *2013 8th International Workshop on Systems, Signal Processing and Their Applications, WoSSPA 2013*, (1), pp. 99–104. doi: 10.1109/WoSSPA.2013.6602344.
- Ahuja, R. *et al.* (2007) 'Cordon-Bleu Is an Actin Nucleation Factor and Controls Neuronal Morphology', *Cell*, 131(2), pp. 337–350. doi: 10.1016/j.cell.2007.08.030.
- Allwood, E. G. *et al.* (2016) 'Elucidating key motifs required for Arp2/3-dependent and independent actin nucleation by Las17/WASP', *PLoS ONE*, 11(9), pp. 1–21. doi: 10.1371/journal.pone.0163177.
- Amberg, D. C. (1998) 'Three-dimensional imaging of the yeast actin cytoskeleton through the budding cell cycle.', *Molecular biology of the cell*, 9(12), pp. 3259–62. doi: 10.1091/mbc.9.12.3259.
- Asakura, S. (1961) 'The interaction between G-actin and ATP', *Archives of Biochemistry and Biophysics*, 92(1), pp. 140–149. doi: 10.1016/0003-9861(61)90228-4.
- Aydin, F. *et al.* (2018) 'Gating mechanisms during Actin filament elongation by Formins', *eLife*, 7, pp. 1–27. doi: 10.7554/eLife.37342.
- Ayscough, K. R. *et al.* (1997) 'High rates of actin filament turnover in budding yeast and roles for actin in establishment and maintenance of cell polarity revealed using the actin inhibitor latrunculin-A [published erratum appears in J Cell Biol 1999 Sep 6;146(5):following 1201]', *Journal of Cell Biology*, 137(2), pp. 399–416. doi: 10.1083/jcb.137.2.399.
- Ayscough, K. R. (2000) 'Endocytosis and the development of cell polarity in yeast require a dynamic F-actin cytoskeleton', *Current Biology*, 10(24), pp. 1587–1590. doi: 10.1016/S0960-9822(00)00859-9.
- Beall, B. and Chalovich, J. M. (2001) 'Fesselin, a synaptopodin-like protein, stimulates actin nucleation and polymerization', *Biochemistry*, 40(47), pp. 14252–14259. doi: 10.1021/bi011806u.
- Behrmann, E. *et al.* (2012) 'Structure of the rigor actin-tropomyosin-myosin complex', *Cell*, 150(2), pp. 327–338. doi: 10.1016/j.cell.2012.05.037.
- Belmont, L. D. *et al.* (1999) 'A change in actin conformation associated with filament instability after Pi release.', *Proceedings of the National Academy of Sciences of the United States of America*, 96(1), pp. 29–34. doi: 10.1073/pnas.96.1.29.
- Belyy, A. *et al.* (2020) 'Structure of the Lifeact–F-actin complex', *PLOS Biology*. Edited by C. A. Parent, 18(11), p. e3000925. doi: 10.1371/journal.pbio.3000925.
- Berepiki, A., Lichius, A. and Read, N. D. (2011) 'Actin organization and dynamics in filamentous fungi', *Nature Reviews Microbiology*, 9(12), pp. 876–887. doi: 10.1038/nrmicro2666.
- Bieling, P. *et al.* (2018) 'WH2 and proline-rich domains of WASP-family proteins collaborate to accelerate actin filament elongation', *The EMBO Journal*, 37(1), pp. 102–121. doi: 10.15252/embj.201797039.

- Blanchoin, L. and Pollard, T. D. (2002) 'Hydrolysis of ATP by Polymerized Actin Depends on the Bound Divalent Cation but Not Profilin', *Biochemistry*, 41(2), pp. 597–602. doi: 10.1021/bi011214b.
- Boiero Sanders, M., Antkowiak, A. and Michelot, A. (2020) 'Diversity from similarity: cellular strategies for assigning particular identities to actin filaments and networks', *Open Biology*, 10(9), p. 200157. doi: 10.1098/rsob.200157.
- Boulant, S. *et al.* (2011) 'Actin dynamics counteract membrane tension during clathrin-mediated endocytosis', *Nature Cell Biology*, 13(9), pp. 1124–1131. doi: 10.1038/ncb2307.
- Brown, J. W. and McKnight, C. J. (2010) 'Molecular Model of the Microvillar Cytoskeleton and Organization of the Brush Border', *PLoS ONE*. Edited by J. M. Schnur, 5(2), p. e9406. doi: 10.1371/journal.pone.0009406.
- Bryan, K. E. and Rubenstein, P. A. (2005) 'An intermediate form of ADP-F-actin', *Journal of Biological Chemistry*, 280(2), pp. 1696–1703. doi: 10.1074/jbc.M410180200.
- Bubb, M. R. *et al.* (2002) 'Polylysine Induces an Antiparallel Actin Dimer That Nucleates Filament Assembly', *Journal of Biological Chemistry*, 277(23), pp. 20999–21006. doi: 10.1074/jbc.M201371200.
- Buttery, S. M., Yoshida, S. and Pellman, D. (2007) 'Yeast Formins Bni1 and Bnr1 Utilize Different Modes of Cortical Interaction during the Assembly of Actin Cables', *Molecular Biology of the Cell*. Edited by D. Lew, 18(5), pp. 1826–1838. doi: 10.1091/mbc.e06-09-0820.
- Buzan, J. M. and Frieden, C. (1996) 'Yeast actin: Polymerization kinetic studies of wild type and a poorly polymerizing mutant', *Proceedings of the National Academy of Sciences of the United States of America*, 93(1), pp. 91–95. doi: 10.1073/pnas.93.1.91.
- Campellone, K. G. and Welch, M. D. (2010) 'A nucleator arms race: Cellular control of actin assembly', *Nature Reviews Molecular Cell Biology*, 11(4), pp. 237–251. doi: 10.1038/nrm2867.
- Carrier, M. F. (1990) 'Actin polymerization and ATP hydrolysis.', *Advances in biophysics*, 26, pp. 51–73. doi: 10.1016/0065-227x(90)90007-g.
- Chakraborty, S., Jasnin, M. and Baumeister, W. (2020) 'Three-dimensional organization of the cytoskeleton: A cryo-electron tomography perspective', *Protein Science*, 29(6), pp. 1302–1320. doi: 10.1002/pro.3858.
- Chang, F., Drubin, D. and Nurse, P. (1997) 'cdc12p, a Protein Required for Cytokinesis in Fission Yeast, Is a Component of the Cell Division Ring and Interacts with Profilin', *Journal of Cell Biology*, 137(1), pp. 169–182. doi: 10.1083/jcb.137.1.169.
- Chen, M. J. G., Shih, C. L. and Wang, K. (1993) 'Nebulin as an actin zipper. A two-module nebulin fragment promotes actin nucleation and stabilizes actin filaments', *Journal of Biological Chemistry*, 268(27), pp. 20327–20334. doi: 10.1016/s0021-9258(20)80732-7.
- Chen, Q. and Pollard, T. D. (2013) 'Actin Filament Severing by Cofilin Dismantles Actin Patches and Produces Mother Filaments for New Patches', *Current Biology*, 23(13), pp. 1154–1162. doi: 10.1016/j.cub.2013.05.005.
- Chen, X. *et al.* (2013) 'Structural Basis of Actin Filament Nucleation by Tandem W Domains', *Cell Reports*, 3(6), pp. 1910–1920. doi: 10.1016/j.celrep.2013.04.028.
- Chereau, D. *et al.* (2008) 'Leiomodin Is an Actin Filament Nucleator in Muscle Cells', *Science*, 320(5873), pp. 239–243. doi: 10.1126/science.1155313.
- Chou, S. Z. and Pollard, T. D. (2019) 'Mechanism of actin polymerization revealed by cryo-EM structures of actin filaments with three different bound nucleotides', *Proceedings of the National Academy of Sciences*, 116(10), pp. 4265–4274. doi: 10.1073/pnas.1807028115.
- Chou, S. Z. and Pollard, T. D. (2020) 'Cryo-electron microscopy structures of pyrene-labeled ADP-Pi- and ADP-actin filaments', *Nature Communications*, 11(1), p. 5897. doi: 10.1038/s41467-020-19762-1.
- Cook, R. K. *et al.* (1993) 'Enhanced stimulation of myosin subfragment 1 ATPase activity by addition of negatively

- charged residues to the yeast actin NH2 terminus', *Journal of Biological Chemistry*, 268(4), pp. 2410–2415.
- Cook, R. K., Blake, W. T. and Rubenstein, P. A. (1992) 'Removal of the amino-terminal acidic residues of yeast actin. Studies in vitro and in vivo.', *The Journal of biological chemistry*, 267(13), pp. 9430–6. Available at: <http://www.ncbi.nlm.nih.gov/pubmed/1349604>.
- Cook, R. K., Sheff, D. R. and Rubenstein, P. A. (1991) 'Unusual metabolism of the yeast actin amino terminus', *Journal of Biological Chemistry*, 266(25), pp. 16825–16833.
- Cooke, R. and Morales, M. F. (1971) 'Interaction of globular actin with myosin subfragments', *Journal of Molecular Biology*, 60(2), pp. 249–261. doi: 10.1016/0022-2836(71)90291-9.
- Croll, T. I. (2018) 'ISOLDE : a physically realistic environment for model building into low-resolution electron-density maps', *Acta Crystallographica Section D Structural Biology*, 74(6), pp. 519–530. doi: 10.1107/S2059798318002425.
- Das, S. *et al.* (2020) 'D-loop Dynamics and Near-Atomic-Resolution Cryo-EM Structure of Phalloidin-Bound F-Actin', *Structure*, 28(5), pp. 586-593.e3. doi: 10.1016/j.str.2020.04.004.
- Depue, R. H. and Rice, R. V. (1965) 'F-actin is a right-handed helix', *Journal of Molecular Biology*, 12(1), pp. 302–303. doi: 10.1016/S0022-2836(65)80306-0.
- DeRosier, D. J. and Moore, P. B. (1970) 'Reconstruction of three-dimensional images from electron micrographs of structures with helical symmetry', *Journal of Molecular Biology*, 52(2), pp. 355–369. doi: 10.1016/0022-2836(70)90036-7.
- Dogterom, M. and Koenderink, G. H. (2019) 'Actin–microtubule crosstalk in cell biology', *Nature Reviews Molecular Cell Biology*, 20(1), pp. 38–54. doi: 10.1038/s41580-018-0067-1.
- Dräger, N. M. *et al.* (2017) 'Bin1 directly remodels actin dynamics through its BAR domain', *EMBO reports*, 18(11), pp. 2051–2066. doi: 10.15252/embr.201744137.
- Drubin, D. G., Jones, H. D. and Wertman, K. F. (1993) 'Actin structure and function: roles in mitochondrial organization and morphogenesis in budding yeast and identification of the phalloidin-binding site.', *Molecular Biology of the Cell*, 4(12), pp. 1277–1294. doi: 10.1091/mbc.4.12.1277.
- Dujon, B. (1996) 'The yeast genome project: what did we learn?', *Trends in Genetics*, 12(7), pp. 263–270. doi: 10.1016/0168-9525(96)10027-5.
- Von Der Ecken, J. *et al.* (2015) 'Structure of the F-actin-tropomyosin complex', *Nature*, 519(7541), pp. 114–117. doi: 10.1038/nature14033.
- Von Der Ecken, J. *et al.* (2016) 'Cryo-EM structure of a human cytoplasmic actomyosin complex at near-atomic resolution', *Nature*, 534(7609), pp. 724–728. doi: 10.1038/nature18295.
- Egelman (1985) 'The structure of F-actin', *Molecular Biology*, 151, pp. 129–151. doi: 10.1016/S0022-2836(63)80081-9.
- Egelman, E. H., Francis, N. and Derosier, D. J. (1982) 'F-actin is a helix with a random variable twist', *Nature*, 298(5870), pp. 131–135. doi: 10.1038/298131a0.
- van den Ent, F. *et al.* (2014) 'Bacterial actin MreB forms antiparallel double filaments', *eLife*, 2014(3), pp. 1–22. doi: 10.7554/eLife.02634.
- Feliciano, D. *et al.* (2015) 'A second Ias17 monomeric actin-binding motif functions in Arp2/3-dependent actin polymerization during endocytosis', *Traffic*, 16(4), pp. 379–397. doi: 10.1111/tra.12259.
- Fernandez-Leiro, R. and Scheres, S. H. W. (2017) 'A pipeline approach to single-particle processing in RELION', *Acta Crystallographica Section D: Structural Biology*, 73(6), pp. 496–502. doi: 10.1107/S2059798316019276.
- Fowler, W. E. and Aebi, U. (1982) 'Polymorphism of actin paracrystals induced by polylysine.', *Journal of Cell Biology*, 93(2), pp. 452–458. doi: 10.1083/jcb.93.2.452.
- Francis, N. R. and DeRosier, D. J. (1990) 'A polymorphism peculiar to bipolar actin bundles', *Biophysical Journal*, 58(3),

pp. 771–776. doi: 10.1016/S0006-3495(90)82419-X.

Frémont, S. *et al.* (2017) ‘Oxidation of F-actin controls the terminal steps of cytokinesis’, *Nature Communications*, 8(1), p. 14528. doi: 10.1038/ncomms14528.

Fujii, T. *et al.* (2010) ‘Direct visualization of secondary structures of F-actin by electron cryomicroscopy’, *Nature*, 467(7316), pp. 724–728. doi: 10.1038/nature09372.

Fujiwara, I. *et al.* (2018) ‘Latrunculin A Accelerates Actin Filament Depolymerization in Addition to Sequestering Actin Monomers’, *Current Biology*, 28(19), pp. 3183–3192.e2. doi: 10.1016/j.cub.2018.07.082.

Gałazkiewicz, B. *et al.* (1985) ‘Polymerization of G-actin by caldesmon’, *FEBS Letters*, 184(1), pp. 144–149. doi: 10.1016/0014-5793(85)80671-2.

Galkin, V. E. *et al.* (2002) ‘The bacterial protein sipa polymerizes g-actin and mimics muscle nebulin’, *Nature Structural Biology*, 9(7), pp. 518–521. doi: 10.1038/nsb811.

Galkin, V. E. *et al.* (2010) ‘Structural polymorphism in F-actin’, *Nature Structural & Molecular Biology*, 17(11), pp. 1318–1323. doi: 10.1038/nsmb.1930.

Galkin, V. E. *et al.* (2011) ‘Remodeling of actin filaments by ADF / cofilin proteins’, *Pnas*, 108(51), pp. 20568–20572. doi: 10.1073/pnas.1110109108/-/DCSupplemental.www.pnas.org/cgi/doi/10.1073/pnas.1110109108.

Galkin, V. E. *et al.* (2015) ‘Near-Atomic Resolution for One State of F-Actin’, *Structure*, 23(1), pp. 173–182. doi: 10.1016/j.str.2014.11.006.

Galletta, B. J., Chuang, D. Y. and Cooper, J. A. (2008) ‘Distinct roles for Arp2/3 regulators in actin assembly and endocytosis’, *PLoS Biology*, 6(1), pp. 0072–0085. doi: 10.1371/journal.pbio.0060001.

Gasteiger, E. *et al.* (2005) ‘Protein Identification and Analysis Tools on the ExPASy Server BT - The Proteomics Protocols Handbook’, in Walker, J. M. (ed.). Totowa, NJ: Humana Press, pp. 571–607. doi: 10.1385/1-59259-890-0:571.

Gautel, M. and Djinić-Carugo, K. (2016) ‘The sarcomeric cytoskeleton: From molecules to motion’, *Journal of Experimental Biology*, 219(2), pp. 135–145. doi: 10.1242/jeb.124941.

Geeves, M. A., Hitchcock-DeGregori, S. E. and Gunning, P. W. (2015) ‘A systematic nomenclature for mammalian tropomyosin isoforms’, *Journal of Muscle Research and Cell Motility*, 36(2), pp. 147–153. doi: 10.1007/s10974-014-9389-6.

Goddard, T. D. *et al.* (2018) ‘UCSF ChimeraX: Meeting modern challenges in visualization and analysis’, *Protein Science*, 27(1), pp. 14–25. doi: 10.1002/pro.3235.

Goode, B. L., Eskin, J. A. and Wendland, B. (2015) ‘Actin and endocytosis in budding yeast’, *Genetics*, 199(2), pp. 315–358. doi: 10.1534/genetics.112.145540.

Grant, T., Rohou, A. and Grigorieff, N. (2018) ‘cis TEM , user-friendly software for single- particle image processing’, pp. 1–24.

Greenfield, N. J. *et al.* (2006) ‘Solution NMR Structure of the Junction between Tropomyosin Molecules: Implications for Actin Binding and Regulation’, *Journal of Molecular Biology*, 364(1), pp. 80–96. doi: 10.1016/j.jmb.2006.08.033.

Greer, C. and Schekman, R. (1982) ‘Actin from *Saccharomyces cerevisiae*’, *Molecular and Cellular Biology*, 2(10), pp. 1270–1278. doi: 10.1128/mcb.2.10.1270-1278.1982.

Grintsevich, E. E. *et al.* (2017) ‘Catastrophic disassembly of actin filaments via Mical-mediated oxidation’, *Nature Communications*, 8(1), pp. 1–10. doi: 10.1038/s41467-017-02357-8.

Gunning, P. W. *et al.* (2015) ‘Tropomyosin - master regulator of actin filament function in the cytoskeleton’, *Journal of Cell Science*, 128(16), pp. 2965–2974. doi: 10.1242/jcs.172502.

Gurel, P. S. *et al.* (2014) ‘INF2-Mediated Severing through Actin Filament Encirclement and Disruption’, *Current Biology*, 24(2), pp. 156–164. doi: 10.1016/j.cub.2013.12.018.

- Haglund, C. M. *et al.* (2010) 'Rickettsia Sca2 is a bacterial formin-like mediator of actin-based motility', *Nature Cell Biology*, 12(11), pp. 1057–1063. doi: 10.1038/ncb2109.
- Hanson, J. and Lowy, J. (1963) 'The structure of F-actin and of actin filaments isolated from muscle', *Journal of Molecular Biology*, 6(1), pp. IN2–IN5. doi: 10.1016/S0022-2836(63)80081-9.
- Harris, E. S., Li, F. and Higgs, H. N. (2004) 'The Mouse Formin, FRL α , Slows Actin Filament Barbed End Elongation, Competes with Capping Protein, Accelerates Polymerization from Monomers, and Severs Filaments', *Journal of Biological Chemistry*, 279(19), pp. 20076–20087. doi: 10.1074/jbc.M312718200.
- Hartman, M. A. and Spudich, J. A. (2012) 'The myosin superfamily at a glance', *Journal of Cell Science*, 125(7), pp. 1627–1632. doi: 10.1242/jcs.094300.
- Hartwell, L. H. (1974) 'Saccharomyces cerevisiae cell cycle', *Bacteriological Reviews*, 38(2), pp. 164–198. doi: 10.1128/br.38.2.164-198.1974.
- Hatano, T. *et al.* (2018) 'Rapid production of pure recombinant actin isoforms in Pichia pastoris', *Journal of Cell Science*, 131(8), p. jcs213827. doi: 10.1242/jcs.213827.
- Hatano, T. *et al.* (2020) 'Pick-ya actin - A method to purify actin isoforms with bespoke key post-translational modifications', *Journal of Cell Science*, 133(2). doi: 10.1242/jcs.241406.
- He, S. and Scheres, S. H. W. (2017) 'Helical reconstruction in RELION.', *Journal of structural biology*, 198(3), pp. 163–176. doi: 10.1016/j.jsb.2017.02.003.
- Henderson, R. (2013) 'Avoiding the pitfalls of single particle cryo-electron microscopy: Einstein from noise', *Proceedings of the National Academy of Sciences of the United States of America*, 110(45), pp. 18037–18041. doi: 10.1073/pnas.1314449110.
- Herzik, M. A., Wu, M. and Lander, G. C. (2019) 'High-resolution structure determination of sub-100 kDa complexes using conventional cryo-EM', *Nature Communications*, 10(1), p. 1032. doi: 10.1038/s41467-019-08991-8.
- Higgins, D. R. (1995) 'Overview of Protein Expression in Pichia pastoris', *Current Protocols in Protein Science*, 2(1), pp. 1–16. doi: 10.1002/0471140864.ps0507s02.
- Holmes, K. C. *et al.* (1990) 'Atomic model of the actin filament', *Nature*, 347(6288), pp. 44–9. doi: 10.1038/347044a0.
- Huehn, A. *et al.* (2018) 'The actin filament twist changes abruptly at boundaries between bare and cofilin-decorated segments', *Journal of Biological Chemistry*, 293(15), pp. 5377–5383. doi: 10.1074/jbc.AC118.001843.
- Huehn, A. R. *et al.* (2020) 'Structures of cofilin-induced structural changes reveal local and asymmetric perturbations of actin filaments', *Proceedings of the National Academy of Sciences*, 117(3), pp. 1478–1484. doi: 10.1073/pnas.1915987117.
- Humphries, J. D. *et al.* (2007) 'Vinculin controls focal adhesion formation by direct interactions with talin and actin', *Journal of Cell Biology*, 179(5), pp. 1043–1057. doi: 10.1083/jcb.200703036.
- Hung, R.-J., Pak, C. W. and Terman, J. R. (2011) 'Direct Redox Regulation of F-Actin Assembly and Disassembly by Mical', *Science*, 334(6063), pp. 1710–1713. doi: 10.1126/science.1211956.
- Huxley, H. E. (1963) 'Electron microscope studies on the structure of natural and synthetic protein filaments from striated muscle', *Journal of Molecular Biology*, 7(3), pp. 281–308. doi: 10.1016/S0022-2836(63)80008-X.
- Iancu, C. V. *et al.* (2007) 'Electron cryotomography sample preparation using the Vitrobot', *Nature Protocols*, 1(6), pp. 2813–2819. doi: 10.1038/nprot.2006.432.
- Ishiwata, S. (1976) 'Freezing of Actin. Reversible Oxidation of a Sulfhydryl Group and Structural Change', *The Journal of Biochemistry*, 80(3), pp. 595–609. doi: 10.1093/oxfordjournals.jbchem.a131315.
- Jockusch, B. M. and Isenberg, G. (1981) 'Interaction of alpha-actinin and vinculin with actin: opposite effects on filament network formation.', *Proceedings of the National Academy of Sciences*, 78(5), pp. 3005–3009. doi: 10.1073/pnas.78.5.3005.
- Johnson, M. *et al.* (2008) 'NCBI BLAST: a better web interface', *Nucleic Acids Research*, 36(Web Server), pp. W5–W9. doi:

10.1093/nar/gkn201.

Johnson, M., East, D. A. and Mulvihill, D. P. (2014) 'Formins determine the functional properties of actin filaments in yeast', *Current Biology*, 24(13), pp. 1525–1530. doi: 10.1016/j.cub.2014.05.034.

Johnson, R. M. (2019) *Investigating the role of cryo-EM as a tool for structure-based drug design*. The University of Leeds.

Kabsch, W. *et al.* (1990) 'Atomic structure of the actin: DNase I complex', *Nature*, 347(6288), pp. 37–44. doi: 10.1038/347037a0.

Kaksonen, M., Sun, Y. and Drubin, D. G. (2003) 'A Pathway for Association of Receptors, Adaptors, and Actin during Endocytic Internalization', *Cell*, 115(4), pp. 475–487. doi: 10.1016/S0092-8674(03)00883-3.

Kalhor, H. R. *et al.* (1999) 'A Highly Conserved 3-Methylhistidine Modification Is Absent in Yeast Actin', *Archives of Biochemistry and Biophysics*, 370(1), pp. 105–111. doi: 10.1006/abbi.1999.1370.

Kang, H. *et al.* (2012) 'Identification of cation-binding sites on actin that drive polymerization and modulate bending stiffness', *Proceedings of the National Academy of Sciences*, 109(42), pp. 16923–16927. doi: 10.1073/pnas.1211078109.

Karashima, T. *et al.* (2012) 'Interaction of plectin and intermediate filaments.', *Journal of dermatological science*, 66(1), pp. 44–50. doi: 10.1016/j.jdermsci.2012.01.008.

Karlsson, R., Aspenström, P. and Byström, A. S. (1991) 'A chicken beta-actin gene can complement a disruption of the *Saccharomyces cerevisiae* ACT1 gene', *Molecular and Cellular Biology*, 11(1), pp. 213–217. doi: 10.1128/mcb.11.1.213-217.1991.

Keep, N. H. (2000) 'Structural comparison of actin binding in utrophin and dystrophin', *Neurological Sciences*, 21, pp. S929–S937. doi: 10.1007/s100720070006.

Kelpsch, D. J. and Tootle, T. L. (2018) 'Nuclear Actin: From Discovery to Function', *The Anatomical Record*, 301(12), pp. 1999–2013. doi: 10.1002/ar.23959.

Kim, E., Miller, C. J. and Reisler, E. (1996) 'Polymerization and in vitro motility properties of yeast actin: A comparison with rabbit skeletal α -actin', *Biochemistry*, 35(51), pp. 16566–16572. doi: 10.1021/bi9623892.

Kim, H.-R. *et al.* (2018) 'TAGLN2 polymerizes G-actin in a low ionic state but blocks Arp2/3-nucleated actin branching in physiological conditions', *Scientific Reports*, 8(1), p. 5503. doi: 10.1038/s41598-018-23816-2.

Kocks, C. *et al.* (1992) 'L. monocytogenes-induced actin assembly requires the actA gene product, a surface protein', *Cell*, 68(3), pp. 521–531. doi: 10.1016/0092-8674(92)90188-I.

Kühlbrandt, W. (2014) 'The Resolution Revolution', *Science*, 343(6178), pp. 1443–1444. doi: 10.1126/science.1251652.

Kumari, A. *et al.* (2020) 'Structural insights into actin filament recognition by commonly used cellular actin markers', *The EMBO Journal*, 39(14), pp. 1–13. doi: 10.15252/embj.2019104006.

De La Cruz, E. M. and Pollard, T. D. (1996) 'Kinetics and Thermodynamics of Phalloidin Binding to Actin Filaments from Three Divergent Species †', *Biochemistry*, 35(45), pp. 14054–14061. doi: 10.1021/bi961047t.

Lee Sweeney, H. and Holzbaur, E. L. F. (2018) 'Motor proteins', *Cold Spring Harbor Perspectives in Biology*, 10(5), pp. 1–17. doi: 10.1101/cshperspect.a021931.

Li, R. (1997) 'Bee1, a yeast protein with homology to Wiscott-Aldrich syndrome protein, is critical for the assembly of cortical actin cytoskeleton', *Journal of Cell Biology*, 136(3), pp. 649–658. doi: 10.1083/jcb.136.3.649.

Li, X. *et al.* (2013) 'Electron counting and beam-induced motion correction enable near-atomic-resolution single-particle cryo-EM', *Nature Methods*, 10(6), pp. 584–590. doi: 10.1038/nmeth.2472.

Lind, S. E. *et al.* (1986) 'Role of plasma gelsolin and the vitamin D-binding protein in clearing actin from the circulation.', *Journal of Clinical Investigation*, 78(3), pp. 736–742. doi: 10.1172/JCI112634.

- Lovell, S. C. *et al.* (2003) 'Structure validation by C α geometry: ϕ , ψ and C β deviation', *Proteins: Structure, Function, and Bioinformatics*, 50(3), pp. 437–450. doi: 10.1002/prot.10286.
- Löwe, J. *et al.* (2016) 'X-ray and cryo-EM structures of monomeric and filamentous actin-like protein MamK reveal changes associated with polymerization', *Proceedings of the National Academy of Sciences*, 113(47), pp. 13396–13401. doi: 10.1073/pnas.1612034113.
- Lu, R., Drubin, D. G. and Sun, Y. (2016) 'Clathrin-mediated endocytosis in budding yeast at a glance', *Journal of Cell Science*, 129(8), pp. 1531–1536. doi: 10.1242/jcs.182303.
- Machesky, L. M. *et al.* (1994) 'Purification of a Cortical Complex Containing Two Unconventional Actins from', *October*, 127(1), pp. 107–115.
- Mannherz, H. G., Brehme, H. and Lamp, U. (1975) 'Depolymerisation of F-Actin to G-Actin and Its Repolymerisation in the Presence of Analogs of Adenosine Triphosphate', *European Journal of Biochemistry*, 60(1), pp. 109–116. doi: 10.1111/j.1432-1033.1975.tb20981.x.
- Mastrorarde, D. N. and Held, S. R. (2017) 'Automated tilt series alignment and tomographic reconstruction in IMOD.', *Journal of structural biology*, 197(2), pp. 102–113. doi: 10.1016/j.jsb.2016.07.011.
- McGough, A. *et al.* (1997) 'Cofilin changes the twist of F-actin: Implications for actin filament dynamics and cellular function', *Journal of Cell Biology*, 138(4), pp. 771–781. doi: 10.1083/jcb.138.4.771.
- McKane, M. *et al.* (2005) 'A mammalian actin substitution in yeast actin (H372R) causes a suppressible mitochondria/vacuole phenotype', *Journal of Biological Chemistry*, 280(43), pp. 36494–36501. doi: 10.1074/jbc.M506970200.
- Mentes, A. *et al.* (2018) 'High-resolution cryo-EM structures of actin-bound myosin states reveal the mechanism of myosin force sensing', *Proceedings of the National Academy of Sciences*, 115(6), pp. 1292–1297. doi: 10.1073/pnas.1718316115.
- Merino, F. *et al.* (2018) 'Structural transitions of F-actin upon ATP hydrolysis at near-atomic resolution revealed by cryo-EM', *Nature Structural & Molecular Biology*, 25(6), pp. 528–537. doi: 10.1038/s41594-018-0074-0.
- Michelot, A. *et al.* (2010) 'Reconstitution and protein composition analysis of endocytic actin patches', *Current Biology*, 20(21), pp. 1890–1899. doi: 10.1016/j.cub.2010.10.016.
- Millonig, R., Salvo, H. and Aebi, U. (1988) 'Probing actin polymerization by intermolecular cross-linking.', *Journal of Cell Biology*, 106(3), pp. 785–796. doi: 10.1083/jcb.106.3.785.
- Mishra, M., Huang, J. and Balasubramanian, M. K. (2014) 'The yeast actin cytoskeleton', *FEMS Microbiology Reviews*, 38(2), pp. 213–227. doi: 10.1111/1574-6976.12064.
- Moore, P. B., Huxley, H. E. and DeRosier, D. J. (1970) 'Three-dimensional reconstruction of F-actin, thin filaments and decorated thin filaments', *Journal of Molecular Biology*, 50(2), pp. 279–296. doi: 10.1016/0022-2836(70)90192-0.
- Moseley, J. B. *et al.* (2004) 'A Conserved Mechanism for Bni1- and mDia1-induced Actin Assembly and Dual Regulation of Bni1 by Bud6 and Profilin', *Molecular Biology of the Cell*, 15(2), pp. 896–907. doi: 10.1091/mbc.e03-08-0621.
- Mund, M. *et al.* (2018) 'Systematic Nanoscale Analysis of Endocytosis Links Efficient Vesicle Formation to Patterned Actin Nucleation', *Cell*, 174(4), pp. 884-896.e17. doi: 10.1016/j.cell.2018.06.032.
- Nag, S. *et al.* (2013) 'Gelsolin: The tail of a molecular gymnast', *Cytoskeleton*, 70(7), pp. 360–384. doi: 10.1002/cm.21117.
- Nakamura, F., Stossel, T. P. and Hartwig, J. H. (2011) 'Organizers of cell structure and function The filamins', 5(2), pp. 160–169. doi: 10.4161/cam.5.2.14401.
- Nakane, T. *et al.* (2020) 'Single-particle cryo-EM at atomic resolution', *Nature*, 587(7832), pp. 152–156. doi: 10.1038/s41586-020-2829-0.
- Narasimhan, M. *et al.* (2019) 'Evolutionary unique mechanistic framework of clathrin-mediated endocytosis in plants', *bioRxiv*, pp. 1–30. doi: 10.1101/762906.

- Narita, A. *et al.* (2006) 'Structural basis of actin filament capping at the barbed-end: A cryo-electron microscopy study', *EMBO Journal*, 25(23), pp. 5626–5633. doi: 10.1038/sj.emboj.7601395.
- Narita, A., Oda, T. and Maéda, Y. (2011) 'Structural basis for the slow dynamics of the actin filament pointed end', *EMBO Journal*, 30(7), pp. 1230–1237. doi: 10.1038/emboj.2011.48.
- Nečas, D. and Klapetek, P. (2012) 'Gwyddion: an open-source software for SPM data analysis', *Open Physics*, 10(1), pp. 181–188. doi: 10.2478/s11534-011-0096-2.
- Oda, T. *et al.* (2009) 'The nature of the globular- to fibrous-actin transition', *Nature*, 457(7228), pp. 441–445. doi: 10.1038/nature07685.
- Oda, T., Aihara, T. and Wakabayashi, K. (2016) 'Early nucleation events in the polymerization of actin, probed by time-resolved small-angle x-ray scattering', *Scientific Reports*, 6(October), pp. 1–13. doi: 10.1038/srep34539.
- Oda, T., Namba, K. and Maéda, Y. (2005) 'Position and Orientation of Phalloidin in F-Actin Determined by X-Ray Fiber Diffraction Analysis', *Biophysical Journal*, 88(4), pp. 2727–2736. doi: 10.1529/biophysj.104.047753.
- Okada, K. *et al.* (2010) 'Adenomatous polyposis coli protein nucleates actin assembly and synergizes with the formin mDia1', *Journal of Cell Biology*, 189(7), pp. 1087–1096. doi: 10.1083/jcb.201001016.
- Orlova, A. *et al.* (1997) 'Modulation of Yeast F-Actin Structure by a Mutation in the Nucleotide-binding Cleft', pp. 235–243.
- Orlova, A. *et al.* (2001) 'Probing the structure of F-actin: cross-links constrain atomic models and modify actin dynamics 1 Edited by M. F. Moody', *Journal of Molecular Biology*, 312(1), pp. 95–106. doi: 10.1006/jmbi.2001.4945.
- Orlova, A. *et al.* (2004) 'Actin-destabilizing factors disrupt filaments by means of a time reversal of polymerization', *Proceedings of the National Academy of Sciences*, 101(51), pp. 17664–17668. doi: 10.1073/pnas.0407525102.
- Ostrowska-Podhorodecka, Z. *et al.* (2020) 'Tropomyosin isoforms regulate cofilin 1 activity by modulating actin filament conformation', *Archives of Biochemistry and Biophysics*, 682. doi: 10.1016/j.abb.2020.108280.
- Otomo, T. *et al.* (2005) 'Structural basis of actin filament nucleation and processive capping by a formin homology 2 domain', *Nature*, 433(7025), pp. 488–494. doi: 10.1038/nature03251.
- Pan, L. *et al.* (2018) 'Super-Resolution Microscopy Reveals the Native Ultrastructure of the Erythrocyte Cytoskeleton', *Cell Reports*, 22(5), pp. 1151–1158. doi: 10.1016/j.celrep.2017.12.107.
- Pardee, J. D. and Spudich, J. A. (1982) 'Chapter 18 Purification of Muscle Actin', in *Methods in Cell Biology*, pp. 271–289. doi: 10.1016/S0091-679X(08)60661-5.
- Pelaseyed, T. and Bretscher, A. (2018) 'Regulation of actin-based apical structures on epithelial cells', *Journal of Cell Science*, 131(20), pp. 1–10. doi: 10.1242/jcs.221853.
- Pettersen, E. F. *et al.* (2004) 'UCSF Chimera - A visualization system for exploratory research and analysis', *Journal of Computational Chemistry*, 25(13), pp. 1605–1612. doi: 10.1002/jcc.20084.
- Pettersen, E. F. *et al.* (2021) '<sc>UCSF ChimeraX</sc>: Structure visualization for researchers, educators, and developers', *Protein Science*, 30(1), pp. 70–82. doi: 10.1002/pro.3943.
- Picco, A. *et al.* (2015) 'Visualizing the functional architecture of the endocytic machinery', *eLife*, 4, pp. 1–29. doi: 10.7554/eLife.04535.
- Picco, A. *et al.* (2018) 'The contributions of the actin machinery to endocytic membrane bending and vesicle formation', *Molecular Biology of the Cell*, 29(11), pp. 1346–1358. doi: 10.1091/mbc.E17-11-0688.
- Pollard, T. D. (2016) 'Actin and Actin-Binding Proteins.', *Cold Spring Harbor perspectives in biology*, 8(8), pp. 1–18. doi: 10.1101/cshperspect.a018226.
- Pollard, T. D. and Borisy, G. G. (2003) 'Cellular Motility Driven by Assembly and Disassembly of Actin Filaments', *Cell*,

112(4), pp. 453–465. doi: 10.1016/S0092-8674(03)00120-X.

Pospich, S. *et al.* (2017) ‘Near-atomic structure of jaspilkinolide-stabilized malaria parasite F-actin reveals the structural basis of filament instability’, *Proceedings of the National Academy of Sciences*, p. 201707506. doi: 10.1073/pnas.1707506114.

Pospich, S. *et al.* (2021) ‘Cryo-EM Resolves Molecular Recognition Of An Optojasp Photoswitch Bound To Actin Filaments In Both Switch States’, *Angewandte Chemie International Edition*, 60(16), pp. 8678–8682. doi: 10.1002/anie.202013193.

Pospich, S., Merino, F. and Raunser, S. (2020) ‘Structural Effects and Functional Implications of Phalloidin and Jaspilkinolide Binding to Actin Filaments’, *Structure*, pp. 1–13. doi: 10.1016/j.str.2020.01.014.

Prochniewicz, E. and Thomas, D. D. (1999) ‘Differences in Structural Dynamics of Muscle and Yeast Actin Accompany Differences in Functional Interactions with Myosin †’, pp. 14860–14867.

Quinlan, M. E. *et al.* (2005) ‘Drosophila Spire is an actin nucleation factor’, *Nature*, 433(7024), pp. 382–388. doi: 10.1038/nature03241.

Rao, J. N., Madasu, Y. and Dominguez, R. (2014) ‘Mechanism of actin filament pointed-end capping by tropomodulin’, *Science*, 345(6195), pp. 463–467. doi: 10.1126/science.1256159.

RELION (2021) *RELION wiki*. Available at: <https://relion.readthedocs.io/en/latest/Reference/PixelSizeIssues.html> (Accessed: 16 June 2021).

Ren, Z. *et al.* (2019) ‘Cryo-EM Structure of Actin Filaments from Zea mays Pollen’, *The Plant Cell*, p. tpc.00973.2018. doi: 10.1105/tpc.18.00973.

Renault, L., Deville, C. and van Heijenoort, C. (2013) ‘Structural features and interfacial properties of WH2, β -thymosin domains and other intrinsically disordered domains in the regulation of actin cytoskeleton dynamics’, *Cytoskeleton*, 70(11), pp. 686–705. doi: 10.1002/cm.21140.

Ridley, A. J. (2011) ‘Life at the leading edge’, *Cell*, 145(7), pp. 1012–1022. doi: 10.1016/j.cell.2011.06.010.

Robert-Paganin, J. *et al.* (2021) ‘The actomyosin interface contains an evolutionary conserved core and an ancillary interface involved in specificity’, *Nature Communications*, 12(1), p. 1892. doi: 10.1038/s41467-021-22093-4.

Rodal, A. A. *et al.* (2003) ‘Negative Regulation of Yeast WASp by Two SH3 Domain-Containing Proteins’, *Current Biology*, 13(12), pp. 1000–1008. doi: 10.1016/S0960-9822(03)00383-X.

De Rosier, D. J. and Klug, A. (1968) ‘Reconstruction of three dimensional structures from electron micrographs’, *Nature*, 217(5124), pp. 130–134. doi: 10.1038/217130a0.

Rould, M. A. *et al.* (2006) ‘Crystal structures of expressed non-polymerizable monomeric actin in the ADP and ATP states’, *Journal of Biological Chemistry*, 281(42), pp. 31909–31919. doi: 10.1074/jbc.M601973200.

Rozsa, G., Szent-Györgyi, A. and Wyckoff, R. W. G. (1949) ‘The Electron Microscopy of F-Actin’, *Biochimica et biophysica acta*, 3, pp. 561–569.

Rozycki, M., Schutt, C. E. and Lindberg, U. (1991) ‘Affinity chromatography-based purification of profilin:actin’, in *Methods in Enzymology*, pp. 100–118. doi: 10.1016/0076-6879(91)96012-G.

Safer, D., Elzinga, M. and Nachmias, V. T. (1991) ‘Thymosin β 4 and Fx, an actin-sequestering peptide, are indistinguishable’, *Journal of Biological Chemistry*, 266(7), pp. 4029–4032. doi: 10.1016/S0021-9258(20)64278-8.

Schafer, D. A., Jennings, P. B. and Cooper, J. A. (1998) ‘Rapid and efficient purification of actin from nonmuscle sources.’, *Cell motility and the cytoskeleton*, 39(2), pp. 166–71. doi: 10.1002/(SICI)1097-0169(1998)39:2<166::AID-CM7>3.0.CO;2-4.

Scheres, S. H. W. (2012) ‘RELION: Implementation of a Bayesian approach to cryo-EM structure determination’, *Journal of Structural Biology*, 180(3), pp. 519–530. doi: 10.1016/j.jsb.2012.09.006.

Schwanhüsser, B. *et al.* (2011) ‘Global quantification of mammalian gene expression control’, *Nature*, 473(7347), pp.

337–342. doi: 10.1038/nature10098.

Schwayer, C. *et al.* (2016) ‘Actin Rings of Power’, *Developmental Cell*, 37(6), pp. 493–506. doi: 10.1016/j.devcel.2016.05.024.

Schwytter, D., Phillips, M. and Reisler, E. (1989) ‘Subtilisin-cleaved actin: polymerization and interaction with myosin subfragment 1’, *Biochemistry*, 28(14), pp. 5889–5895. doi: 10.1021/bi00440a027.

Senju, Y. *et al.* (2017) ‘Mechanistic principles underlying regulation of the actin cytoskeleton by phosphoinositides’, *Proceedings of the National Academy of Sciences*, 114(43), pp. E8977–E8986. doi: 10.1073/pnas.1705032114.

Shaaban, M., Chowdhury, S. and Nolen, B. J. (2020) ‘Cryo-EM reveals the transition of Arp2/3 complex from inactive to nucleation-competent state’, *Nature Structural and Molecular Biology*, 27(11), pp. 1009–1016. doi: 10.1038/s41594-020-0481-x.

Shartava, A. *et al.* (1995) ‘A posttranslational modification of beta-actin contributes to the slow dissociation of the spectrin-protein 4.1-actin complex of irreversibly sickled cells.’, *Journal of Cell Biology*, 128(5), pp. 805–818. doi: 10.1083/jcb.128.5.805.

Shemesh, T. *et al.* (2005) ‘A novel mechanism of actin filament processive capping by formin’, *Journal of Cell Biology*, 170(6), pp. 889–893. doi: 10.1083/jcb.200504156.

Shortle, D., Haber, J. E. and Botstein, D. (1982) ‘Lethal disruption of the yeast actin gene by integrative DNA transformation’, *Science*, 217(4557), pp. 371–373. doi: 10.1126/science.7046050.

Shvetsov, A. *et al.* (2008) ‘Actin Hydrophobic Loop 262–274 and Filament Nucleation and Elongation’, *Journal of Molecular Biology*, 375(3), pp. 793–801. doi: 10.1016/j.jmb.2007.10.076.

Stoddard, P. R. *et al.* (2017) ‘Evolution of polymer formation within the actin superfamily’, *Molecular Biology of the Cell*, 28(19), pp. 2461–2469. doi: 10.1091/mbc.E15-11-0778.

Straub, F. B. and Feuer, G. (1950) ‘Adenosinetriphosphate the functional group of actin’, *Biochimica et Biophysica Acta*, 4(September), pp. 455–470. doi: 10.1016/0006-3002(50)90052-7.

Suarez, C. *et al.* (2015) ‘Profilin Regulates F-Actin Network Homeostasis by Favoring Formin over Arp2/3 Complex’, *Developmental Cell*, 32(1), pp. 43–53. doi: 10.1016/j.devcel.2014.10.027.

Sun, Y., Martin, A. C. and Drubin, D. G. (2006) ‘Endocytic Internalization in Budding Yeast Requires Coordinated Actin Nucleation and Myosin Motor Activity’, *Developmental Cell*, 11(1), pp. 33–46. doi: 10.1016/j.devcel.2006.05.008.

Tanaka, K. *et al.* (2018) ‘Structural basis for cofilin binding and actin filament disassembly’, *Nature Communications*, 9(1), pp. 1–3. doi: 10.1038/s41467-018-04290-w.

Tang, G. *et al.* (2007) ‘EMAN2: An extensible image processing suite for electron microscopy’, *Journal of Structural Biology*, 157(1), pp. 38–46. doi: 10.1016/j.jsb.2006.05.009.

Tang, J. X. and Janmey, P. A. (1996) ‘The polyelectrolyte nature of F-actin and the mechanism of actin bundle formation’, *Journal of Biological Chemistry*, 271(15), pp. 8556–8563. doi: 10.1074/jbc.271.15.8556.

Tegunov, D. and Cramer, P. (2019) ‘Real-time cryo-electron microscopy data preprocessing with Warp’, *Nature Methods*, 16(11), pp. 1146–1152. doi: 10.1038/s41592-019-0580-y.

Terman, J. R. and Kashina, A. (2013) ‘Post-translational modification and regulation of actin’, *Current Opinion in Cell Biology*, 25(1), pp. 30–38. doi: 10.1016/j.ceb.2012.10.009.

Titus, M. A. (2018) ‘Myosin-Driven Intracellular Transport’, *Cold Spring Harbor Perspectives in Biology*, 10(3), p. a021972. doi: 10.1101/cshperspect.a021972.

Tyler, J. J. (2017) *Analysis of the Arp2/3-independent activity of the WASp family protein Las17*. University of Sheffield.

Tyler, J. J. *et al.* (2021) ‘Phosphorylation of the WH2 domain in yeast Las17/WASP regulates G-actin binding and protein

- function during endocytosis', *Scientific Reports*, 11(1), pp. 1–11. doi: 10.1038/s41598-021-88826-z.
- Tyler, J. J., Allwood, E. G. and Ayscough, K. R. (2016) 'WASP family proteins, more than Arp2/3 activators', *Biochemical Society Transactions*, 44(5), pp. 1339–1345. doi: 10.1042/BST20160176.
- Umeki, N. *et al.* (2019) 'K336I mutant actin alters the structure of neighbouring protomers in filaments and reduces affinity for actin-binding proteins', *Scientific Reports*, 9(1), pp. 1–10. doi: 10.1038/s41598-019-41795-w.
- Urbanek, A. N. *et al.* (2013) 'A novel actin-binding motif in Las17/WASP nucleates actin filaments independently of Arp2/3', *Current Biology*, 23(3), pp. 196–203. doi: 10.1016/j.cub.2012.12.024.
- Urbanek, A. N. *et al.* (2015) 'Distinct actin and lipid binding sites in Ysc84 are required during early stages of yeast endocytosis', *PLoS ONE*, 10(8), pp. 1–19. doi: 10.1371/journal.pone.0136732.
- Vahokoski, J. *et al.* (2021) *No Title*. doi: 10.2210/pdb6tu4/pdb.
- Vandekerckhove, J. and Weber, K. (1978a) 'At least six different actins are expressed in a higher mammal: An analysis based on the amino acid sequence of the amino-terminal tryptic peptide', *Journal of Molecular Biology*, 126(4), pp. 783–802. doi: 10.1016/0022-2836(78)90020-7.
- Vandekerckhove, J. and Weber, K. (1978b) 'Mammalian cytoplasmic actins are the products of at least two genes and differ in primary structure in at least 25 identified positions from skeletal muscle actins', *Proceedings of the National Academy of Sciences*, 75(3), pp. 1106–1110. doi: 10.1073/pnas.75.3.1106.
- Varland, S., Vandekerckhove, J. and Drazic, A. (2019) 'Actin Post-translational Modifications: The Cinderella of Cytoskeletal Control', *Trends in Biochemical Sciences*, 44(6), pp. 502–516. doi: 10.1016/j.tibs.2018.11.010.
- Vinson, V. K. *et al.* (1998) 'Interactions of Acanthamoeba Profilin with Actin and Nucleotides Bound to Actin †', *Biochemistry*, 37(31), pp. 10871–10880. doi: 10.1021/bi980093l.
- Vonck, J., Parcej, D. N. and Mills, D. J. (2016) 'Structure of alcohol oxidase from pichia pastoris by cryo-electron microscopy', *PLoS ONE*, 11(7), pp. 1–20. doi: 10.1371/journal.pone.0159476.
- Vorobiev, S. *et al.* (2003) 'The structure of nonvertebrate actin: Implications for the ATP hydrolytic mechanism', *Proceedings of the National Academy of Sciences of the United States of America*, 100(10), pp. 5760–5765. doi: 10.1073/pnas.0832273100.
- Wagner, A. R. *et al.* (2013) 'Dip1 defines a class of Arp2/3 complex activators that function without preformed actin filaments', *Current Biology*, 23(20), pp. 1990–1998. doi: 10.1016/j.cub.2013.08.029.
- Wang, Z. *et al.* (2021) 'The molecular basis for sarcomere organization in vertebrate skeletal muscle The molecular basis for sarcomere organization in vertebrate skeletal muscle', *Cell*, pp. 1–16. doi: 10.1016/j.cell.2021.02.047.
- Wang, Z. and Mim, C. (2021) 'CryoEM reveals BIN1 (isoform 8) does not bind to single actin filaments in vitro.', *microPublication biology*, 2021(isoform 8), pp. 25–28. doi: 10.17912/micropub.biology.000404.
- Weinberg, J. and Drubin, D. G. (2012) 'Clathrin-mediated endocytosis in budding yeast', *Trends in Cell Biology*, 22(1), pp. 1–13. doi: 10.1016/j.tcb.2011.09.001.
- Weissenberger, G., Henderikx, R. J. M. and Peters, P. J. (2021) 'Understanding the invisible hands of sample preparation for cryo-EM', *Nature Methods*, 18(5), pp. 463–471. doi: 10.1038/s41592-021-01130-6.
- Wen, K.-K., McKane, M. and Rubenstein, P. A. (2013) 'Importance of a Lys113–Glu195 Intermonomer Ionic Bond in F-actin Stabilization and Regulation by Yeast Formins Bni1p and Bnr1p', *Journal of Biological Chemistry*, 288(26), pp. 19140–19153. doi: 10.1074/jbc.M113.474122.
- Wen, K. K., Rubenstein, P. A. and DeMali, K. A. (2009) 'Vinculin nucleates actin polymerization and modifies actin filament structure', *Journal of Biological Chemistry*, 284(44), pp. 30463–30473. doi: 10.1074/jbc.M109.021295.
- Winder, S. J. and Ayscough, K. R. (2005) 'Actin-binding proteins', *Journal of Cell Science*, 118(4), pp. 651–654. doi: 10.1242/jcs.01670.

- Winder, S. J., Jess, T. and Ayscough, K. R. (2003) 'SCP1 encodes an actin-bundling protein in yeast', *Biochemical Journal*, 375(2), pp. 287–295. doi: 10.1042/bj20030796.
- Winkelman, J. D. *et al.* (2016) 'Fascin- and α -Actinin-Bundled Networks Contain Intrinsic Structural Features that Drive Protein Sorting', *Current Biology*, 26(20), pp. 2697–2706. doi: 10.1016/j.cub.2016.07.080.
- Wioland, H. *et al.* (2021) 'Actin filament oxidation by MICAL1 suppresses protections from cofilin-induced disassembly', *EMBO reports*, 22(2), pp. 1–11. doi: 10.15252/embr.202050965.
- Xu, K., Zhong, G. and Zhuang, X. (2013) 'Actin, Spectrin, and Associated Proteins Form a Periodic Cytoskeletal Structure in Axons', (January), pp. 452–457.
- Xu, X. P. *et al.* (2020) 'Structural basis of ae-catenin–f-actin catch bond behavior', *eLife*, 9, pp. 1–42. doi: 10.7554/ELIFE.60878.
- Xue, B. *et al.* (2014) 'Structural basis of thymosin- β 4/profilin exchange leading to actin filament polymerization', *Proceedings of the National Academy of Sciences of the United States of America*, 111(43), pp. E4596–E4605. doi: 10.1073/pnas.1412271111.
- Yamashita, A. (2003) 'Crystal structure of CapZ: structural basis for actin filament barbed end capping', *The EMBO Journal*, 22(7), pp. 1529–1538. doi: 10.1093/emboj/cdg167.
- Yang, S. *et al.* (2013) 'Molecular Mechanism of Fascin Function in Filopodial Formation', *Journal of Biological Chemistry*, 288(1), pp. 274–284. doi: 10.1074/jbc.M112.427971.
- Yates, L. D., Greaser, M. L. and Huxley, H. E. (1983) 'Quatitative determination of myosin and actin in rabbit skeletal muscle', *Journal of Molecular Biology*, 168(1), pp. 123–141. doi: 10.1016/S0022-2836(83)80326-X.
- Zechel, K. (1980) 'Dissociation of the DNase-I . actin complex by formamide', *European journal of biochemistry*, 110(2), pp. 337–41. doi: 10.1111/j.1432-1033.1980.tb04872.x.
- Zhang, K. (2016) 'Gctf: Real-time CTF determination and correction', *Journal of Structural Biology*, 193(1), pp. 1–12. doi: 10.1016/j.jsb.2015.11.003.
- Zheng, S. Q. *et al.* (2017) 'MotionCor2: anisotropic correction of beam-induced motion for improved cryo-electron microscopy', *Nature Methods*, 14(4), pp. 331–332. doi: 10.1038/nmeth.4193.
- Zuchero, J. B. *et al.* (2009) 'p53-cofactor JMY is a multifunctional actin nucleation factor', *Nature Cell Biology*, 11(4), pp. 451–459. doi: 10.1038/ncb1852.